

Nuclear Safety

ISBN 978-92-64-99113-2
NEA/CSNI/R(2010)1

Nuclear Fuel Behaviour Under Reactivity-initiated Accident (RIA) Conditions

State-of-the-art Report

© OCDE 2010
NEA No. 6847

NUCLEAR ENERGY AGENCY
ORGANISATION FOR ECONOMIC CO-OPERATION AND DEVELOPMENT

ORGANISATION FOR ECONOMIC CO-OPERATION AND DEVELOPMENT

The OECD is a unique forum where the governments of 30 democracies work together to address the economic, social and environmental challenges of globalisation. The OECD is also at the forefront of efforts to understand and to help governments respond to new developments and concerns, such as corporate governance, the information economy and the challenges of an ageing population. The Organisation provides a setting where governments can compare policy experiences, seek answers to common problems, identify good practice and work to co-ordinate domestic and international policies.

The OECD member countries are: Australia, Austria, Belgium, Canada, the Czech Republic, Denmark, Finland, France, Germany, Greece, Hungary, Iceland, Ireland, Italy, Japan, Korea, Luxembourg, Mexico, the Netherlands, New Zealand, Norway, Poland, Portugal, the Slovak Republic, Spain, Sweden, Switzerland, Turkey, the United Kingdom and the United States. The Commission of the European Communities takes part in the work of the OECD.

OECD Publishing disseminates widely the results of the Organisation's statistics gathering and research on economic, social and environmental issues, as well as the conventions, guidelines and standards agreed by its members.

This work is published on the responsibility of the Secretary-General of the OECD. The opinions expressed and arguments employed herein do not necessarily reflect the official views of the Organisation or of the governments of its member countries.

NUCLEAR ENERGY AGENCY

The OECD Nuclear Energy Agency (NEA) was established on 1st February 1958 under the name of the OEEC European Nuclear Energy Agency. It received its present designation on 20th April 1972, when Japan became its first non-European full member. NEA membership today consists of 28 OECD member countries: Australia, Austria, Belgium, Canada, the Czech Republic, Denmark, Finland, France, Germany, Greece, Hungary, Iceland, Ireland, Italy, Japan, Luxembourg, Mexico, the Netherlands, Norway, Portugal, Republic of Korea, the Slovak Republic, Spain, Sweden, Switzerland, Turkey, the United Kingdom and the United States. The Commission of the European Communities also takes part in the work of the Agency.

The mission of the NEA is:

- to assist its member countries in maintaining and further developing, through international co-operation, the scientific, technological and legal bases required for a safe, environmentally friendly and economical use of nuclear energy for peaceful purposes, as well as
- to provide authoritative assessments and to forge common understandings on key issues, as input to government decisions on nuclear energy policy and to broader OECD policy analyses in areas such as energy and sustainable development.

Specific areas of competence of the NEA include safety and regulation of nuclear activities, radioactive waste management, radiological protection, nuclear science, economic and technical analyses of the nuclear fuel cycle, nuclear law and liability, and public information.

The NEA Data Bank provides nuclear data and computer program services for participating countries. In these and related tasks, the NEA works in close collaboration with the International Atomic Energy Agency in Vienna, with which it has a Co-operation Agreement, as well as with other international organisations in the nuclear field.

Corrigenda to OECD publications may be found on line at: www.oecd.org/publishing/corrigenda.

© OECD 2010

You can copy, download or print OECD content for your own use, and you can include excerpts from OECD publications, databases and multimedia products in your own documents, presentations, blogs, websites and teaching materials, provided that suitable acknowledgment of OECD as source and copyright owner is given. All requests for public or commercial use and translation rights should be submitted to rights@oecd.org. Requests for permission to photocopy portions of this material for public or commercial use shall be addressed directly to the Copyright Clearance Center (CCC) at info@copyright.com or the Centre français d'exploitation du droit de copie (CFC) contact@cfcopies.com.

FOREWORD

The NEA Working Group on Fuel Safety (WGFS) is tasked with advancing the current understanding of fuel safety issues by assessing the technical basis for current safety criteria as well as their applicability to high burn-up and to new fuel designs and materials. The group aims to facilitate international convergence in this area, including on experimental approaches as well as interpretation and use of experimental data relevant for safety.

In 1986, a working group of the NEA Committee on the Safety of Nuclear Installations (CSNI) issued a state-of-the-art report on water reactor fuel behaviour in design-basis accident (DBA) conditions. The 1986 report was limited to the oxidation, embrittlement and deformation of pressurised water reactor (PWR) fuel in a loss-of-coolant accident (LOCA).

Since then, a considerable worldwide effort has been expended in experimental and numerical modelling of PWR and boiling water reactor (BWR) fuel behaviour under accident conditions, in particular for high burn-up fuel, which has allowed the updating of the 1986 report and expanding its scope to include other types of DBAs, such as reactivity-initiated accidents (RIAs). The WGFS issued a first update covering nuclear fuel behaviour under LOCA conditions in spring 2009. The present report addresses nuclear fuel behaviour under RIA conditions, and covers the following technical aspects:

- RIA scenarios for major types of reactors: BWRs, PWRs and to a lesser extent Canadian deuterium-uranium (CANDU) heavy water reactors.
- State of fuel and cladding at various burn-up levels.
- RIA phenomena needed to be addressed by experiments and modelling.
- RIA test methodologies.
- Specific phenomena under RIA conditions and their experimental basis.
- Results from integral tests and predictive code calculations.

ACKNOWLEDGEMENTS

The NEA Secretariat wishes to express its gratitude to Dr. Lars Olof Jernkvist and Dr. Ali R. Massih (Quantum Technologies AB) for their efforts in drafting the report, and to the Swedish Radiation Safety Authority (SSM) for supporting the work.

The following WGFS members and other experts from the industry also provided valuable input to various chapters of the report:

Toyoshi Fuketa, JAEA, Japan
Zoltán Hózer, KFKI, Hungary
Jan In de Betou, SSM, Sweden
Joelle Papin, IRSN, France
Marc Petit, IRSN, France
Motoe Suzuki, JAEA, Japan
Carlo Vitanza, NEA, France
John Voglewede, USNRC, United States
Ian Wilson, HSE, United Kingdom
Suresh Yagnik, EPRI, United States

TABLE OF CONTENTS

Foreword	3
List of figures.....	8
List of tables	11
Executive summary	13
1. Introduction	21
1.1 Background to reactivity-initiated accidents.....	21
1.2 Consequences of reactivity-initiated accidents	22
1.3 Regulatory acceptance criteria	22
1.4 Scope and outline of the report.....	23
2. Description of RIA scenarios for major types of reactors	27
2.1 Overview of reactivity insertion events.....	28
2.1.1 Control system failures	28
2.1.2 Control rod ejections.....	28
2.1.3 Coolant/moderator temperature and void effects.....	29
2.1.4 Dilution or removal of coolant/moderator poison.....	30
2.2 Power pulse characteristics	30
2.2.1 Pulse width and shape.....	31
2.2.2 Pulse amplitude	34
3. State of fuel and cladding at various burn-up levels	37
3.1 Fuel pellets	37
3.1.1 Fuel pellet composition.....	37
3.1.2 Radial distribution of burn-up and power	40
3.1.3 Microstructure – high burn-up restructuring.....	40
3.1.4 Solidus temperature.....	41
3.1.5 Thermal conductivity	43
3.1.6 Fission gas release.....	43
3.2 Cladding tubes.....	44
3.2.1 Radiation damage.....	44
3.2.2 Waterside corrosion	45
3.3 Pellet-clad gap.....	47
3.3.1 Gap gas composition and pressure.....	47
3.3.2 Pellet-clad contact and bonding	48

4. Phenomena that need to be addressed by experiments and modelling.....	51
4.1 Types of damage to fuel and cladding.....	51
4.2 Changes of temperature and geometry with influence on coolability	53
4.2.1 Clad ballooning	53
4.2.2 Fuel rod fragmentation.....	54
4.3 Mechanical energy generation.....	54
4.3.1 Thermal to mechanical energy conversion	55
4.3.2 Consequences of coolant pressure pulses	57
4.4 Radiological consequences.....	58
5. Overview of RIA testing methodology	65
5.1 Pulse reactor tests	65
5.1.1 Overview of pulse reactor tests	65
5.1.2 Typicality of test conditions.....	66
5.1.3 SPERT-CDC tests.....	67
5.1.4 PBF tests	67
5.1.5 IGR tests.....	68
5.1.6 BIGH tests	68
5.1.7 NSRR tests	68
5.1.8 CABRI tests	69
5.2 Separate effect tests	70
5.2.1 Cladding mechanical properties.....	70
5.2.2 Clad-to-coolant transient heat transfer	75
5.2.3 Fuel-coolant interaction	77
6. Specific phenomena under RIA and their experimental basis	79
6.1 Fuel pellets	79
6.1.1 Fuel pellet heat-up and melting.....	79
6.1.2 Fuel pellet transient fragmentation and swelling	82
6.1.3 Transient fission gas release	85
6.2 Cladding tubes.....	88
6.2.1 Cladding heat-up and melting	88
6.2.2 Cladding transient deformation.....	93
6.2.3 Cladding high-temperature oxidation	96
6.2.4 Oxide transient cracking and spallation	104
6.2.5 Cladding failure.....	105
6.2.6 Hydrogen-induced embrittlement	114
7. Summary of results from integral RIA testing programmes.....	123
7.1 Tests on fresh fuel rods	123
7.1.1 Cladding failure.....	124
7.1.2 Fuel dispersal and fuel-coolant interaction	125
7.2 Tests on pre-irradiated fuel rods.....	126
7.2.1 Cladding failure.....	126
7.2.2 Fuel dispersal and fuel-coolant interaction	128

8. Predictive computer codes	133
8.1 Core and fuel assembly codes	134
8.1.1 Codes for generation of homogenized cross-sections.....	134
8.1.2 Codes for core-wide neutron kinetics calculations	135
8.1.3 Codes for thermal-hydraulic analyses.....	136
8.2 Fuel rod codes	137
9. Results of energy and failure distribution calculations.....	141
9.1 Control rod ejection accidents in PWRs.....	141
9.2 Control rod drop accidents in BRWs	143
9.3 Summary remarks on energy and failure distribution calculations	145
10. Summary and conclusions	147
10.1 Experimental data.....	147
10.2 Computation methods.....	148
11. Nomenclature.....	151
11.1 Fundamental definitions	151
11.2 Latin symbols	152
11.3 Greek symbols.....	153
11.4 List of abbreviations.....	153
 Appendices	
A. Summary of pulse reactor tests on pre-irradiated LWR fuel rods	157
B. Overview of computer codes.....	175
C. References	183

List of figures

Figure 1.	Calculated pulse widths for HZP REA at EOC conditions, compiled from three-dimensional core kinetics analyses.....	32
Figure 2.	Calculated pulse shapes for HZP REA at EOC conditions, compiled from three-dimensional core kinetics analyses.....	33
Figure 3.	Calculated pulse widths for CZP RDA at EOC conditions, compiled from three-dimensional core kinetics analyses.....	34
Figure 4.	Calculated pulse shapes for CZP RDA at EOC conditions, compiled from three-dimensional core kinetics analyses.....	34
Figure 5.	Calculated maximum fuel enthalpy increase under HZP REA at EOC conditions, compiled from three-dimensional core kinetics analyses.....	36
Figure 6.	Calculated maximum fuel enthalpy increase under CZP RDA at EOC conditions, compiled from three-dimensional core kinetics analyses.....	36
Figure 7.	Change in fuel pellet average isotopic composition with burn-up, calculated with the TUBRNP model	38
Figure 8.	Influence of initial ²³⁵ U enrichment on radial power distribution in high-burn-up fuel pellets of UO ₂	39
Figure 9.	Width of restructured zone (“rim zone”) in UO ₂ fuel pellets of commercial PWR fuel rods, determined by optical microscopy.....	41
Figure 10.	Influence of restraining pressure from PCMI on the build-up of porosity in the high burn-up microstructure of UO ₂ fuel. Experimental data from eight studies	42
Figure 11.	Calculated variation in fuel melting temperature and burn-up across the pellet radius in a typical PWR fuel rod	42
Figure 12.	Radial cracks through the cladding oxide layer and subjacent hydride rim act as stress- and strain localisation sites. Photograph of the PWR fuel rod HBO-5, tested in the NSRR	46
Figure 13.	Hydrogen solubility versus reciprocal temperature, determined from experiments on hydride precipitation in un-irradiated Zircaloy cladding.....	46
Figure 14.	Possible mechanisms for fuel and cladding damage under an RIA	52
Figure 15.	Thermal-to-mechanical energy conversion ratio for fuel dispersal, measured in the NSRR	56
Figure 16.	Schemata of iodine transformations within the containment	62
Figure 17.	Schematic illustration of specimen design and load conditions in ring tensile tests.....	71
Figure 18.	Typical temperature (dashed line) and power (solid line) distribution in high-burn-up fuel, subjected to a fast (8.8 ms) power pulse	80
Figure 19.	Evolution of the fuel temperature profile in rod REP-N5, calculated with the SCANAIR-3.2 computer code	80
Figure 20.	Calculated variation in fuel temperature across the pellet radius at time of incipient fuel pellet melting in UO ₂ PWR fuel under a postulated HZP REA.....	80
Figure 21.	Best-estimate thresholds for UO ₂ fuel pellet melting under postulated BWR CZP RDA and PWR HZP REA.....	81
Figure 22.	Fuel pellet fragments observed after CABRI test REP-Na5	83
Figure 23.	Pellet average grain boundary gas content, in fraction of the total amount of gas created, versus pellet average burn-up in UO ₂ and MIMAS AUC MOX fuel.....	84
Figure 24.	Change of fuel pellet density versus peak radial average fuel enthalpy during pulse irradiation tests, carried out on ATR MOX fuel in the NSRR	85
Figure 25.	Measured transient fission gas release for pre-irradiated UO ₂ and MOX fuel rods, tested in CABRI, BIGH and the NSRR.....	85
Figure 26.	Measured transient fission gas release for pre-irradiated UO ₂ fuel rods, tested in CABRI, BIGH and the NSRR.....	87

Figure 27.	Calculated cladding temperature	88
Figure 28.	Mechanisms for boiling crisis in single phase liquid water under quasi-stationary and transient conditions.....	90
Figure 29.	Peak cladding surface temperatures, measured by thermocouples under RIA simulation tests in the NSRR	91
Figure 30.	Influence of coolant velocity and subcooling on the film-boiling conditions. Results from NSRR pulse-irradiation tests on fresh PWR fuel rods.....	92
Figure 31.	Peak values of cladding hoop residual strain, measured after pulse irradiation tests in BIGR, CABRI and the NSRR.....	93
Figure 32.	Peak values of cladding hoop residual strain for high-burn-up PWR fuel rods that did not experience DNB and high cladding temperature under pulse irradiation tests in CABRI and the NSRR. The fuel burn-up was 54-76, 47-65 and 39-71 MWd(kgHM) ⁻¹ for the considered CABRI UO ₂ , CABRI MOX and NSRR test rods, respectively	94
Figure 33.	Estimates of cladding stress biaxiality ratio under RIA, based on measured average ratios of axial-to-hoop plastic strains in CABRI tests	95
Figure 34.	Cladding hoop strain rate versus time	96
Figure 35.	Portion of the zirconium-oxygen binary phase diagram.	98
Figure 36.	Correlation between (ZrO ₂ + α -Zr)-layer thickness ξ and energy deposition.....	100
Figure 37.	Oxygen concentration profiles across β -Zr layer with moving-boundary, (ZrO ₂ + α -Zr)-layer thickness ξ ,	100
Figure 38.	Sawatzky <i>et al.</i> [246] transient oxidation experiment of Zircaloy-4 tube specimen in steam.....	101
Figure 39.	Schematic temperature-time histories used in one of the steam oxidation tests on Zircaloy-4 PWR clad performed by Pawel <i>et al.</i>	102
Figure 40.	Calculated total (average) oxygen concentration in β -Zr layer during two-sided oxidation of Zircaloy cladding in steam.....	103
Figure 41.	Calculated fraction of the β -Zr layer thickness (F_w) during oxidation of Zircaloy in steam.....	104
Figure 42.	Relation between azimuthal spacing of oxide cracks, oxide layer thickness and cladding hoop residual strain, observed in post-test examinations of pre-irradiated fuel rods from the CABRI REP-Na test series	104
Figure 43.	Post-test appearance of rodlet VA-1, which experienced PCMI-induced failure at a fuel enthalpy of 268 J(gUO ₂) ⁻¹ under an RIA simulation test in the NSRR	107
Figure 44.	Calculated evolution of clad temperature and deformation in the CABRI REP-Na1 and REP-Na4 pulse reactor test rods.....	108
Figure 45.	Effect of clad stress biaxiality on hoop total elongation, i.e. the hoop plastic strain to failure	109
Figure 46.	Fuel enthalpy increase versus burn-up for pre-irradiated UO ₂ fuel rods, tested in various pulse reactors.....	110
Figure 47.	Fuel enthalpy increase versus cladding oxide layer thickness for pre-irradiated UO ₂ fuel rods, tested in various pulse reactors	110
Figure 48.	High-temperature ballooning and pin-hole cladding failure of rod RT-9 tested in the BIGR	111
Figure 49.	Uranium dioxide fuel rods that have failed by high temperature clad ballooning and burst under RIA simulation tests in the NSRR, IGR and BIGR.....	112
Figure 50.	Schematic relation between relative ductility, temperature (T) and hydride volume fraction in zirconium alloys	115
Figure 51.	Ductile-to-brittle transition temperature for irradiated Zircaloy-4 cladding, estimated through axial tensile tests at two different strain rates.....	116

Figure 52. Measured (symbols) and calculated (dashed lines) time needed for complete dissolution of zirconium δ -hydride precipitates in un-irradiated Zircaloy-4	117
Figure 53. Cladding failure initiated at a hydride blister in the CABRI REP-Na8 test.....	119
Figure 54. Peak fuel enthalpy versus burn-up for pre-irradiated VVER fuel rods tested in the IGR and BIGR	126
Figure 55. Peak fuel enthalpy increase versus a) burn-up and b) clad oxide layer thickness for pre-irradiated PWR and BWR fuel rods, tested in RIA simulation experiments	127
Figure 56. Fuel dispersal observed for 25 pre-irradiated UO_2 fuel rods, all of which failed by PCMI under pulse reactor tests	129
Figure 57. Measured fuel loss in failed BWR and PWR high-burn-up UO_2 fuel rods.....	130
Figure 58. External (a) and internal (b) coupling of computer codes for neutron kinetics and thermal-hydraulics in core-wide transient analyses	134
Figure 59. Calculated distribution of peak fuel pellet enthalpy, in units of $\text{cal}(\text{gUO}_2)^{-1}$, resulting from the postulated HZP REA considered by Nakajima.....	142
Figure 60. Scatter plot of calculated peak fuel enthalpy increase versus fuel pellet average burn-up under the postulated HZP REA considered by Nakajima.....	143
Figure 61. Calculated distribution of peak fuel enthalpy, in units of $\text{cal}(\text{gUO}_2)^{-1}$, under the postulated CZP RDA considered by Nakajima.....	144
Figure 62. Calculated dependence of peak fuel enthalpy on fuel assembly burn-up and distance from the dropped control rod under the CZP RDA considered by Heck <i>et al.</i>	145

List of tables

Table 1.	Estimated pulse widths and core-wide maxima of fuel pellet radial average enthalpy and enthalpy increase for various scenarios of REA and RDA.....	31
Table 2.	Fraction of delayed neutrons, β , emitted in fissioning of isotopes relevant to nuclear fuel	38
Table 3.	Coolant conditions under fuel-coolant interaction experiments in the NSRR and the PBF, in comparison with typical BWR CZP, BWR HZP, and PWR HZP conditions ...	57
Table 4.	Groups of radionuclides	59
Table 5.	Radionuclides considered important in the reactor safety study consequence analysis, applicable to a 3 200 MW-t PWR	60
Table 6.	Selected radionuclides released to the environment from the Chernobyl accident.....	61
Table 7.	Overview of pulse reactor tests on pre-irradiated LWR fuel rods.....	66
Table 8.	Typical values of critical heat flux, critical surface temperature and film-boiling heat flux, measured in PATRICIA tests under RIA-like transients and steady-state conditions	76
Table 9.	Cumulative yields of stable isotopes of Xe and Kr	86
Table 10.	Overview of pulse reactor facilities used for RIA simulation tests on fresh fuel rods....	123
Table 11.	Enthalpy thresholds reported for limiting failure modes of fresh UO ₂ fuel rods	124
Table 12.	Enthalpy thresholds reported for fuel rod fragmentation, in comparison with those for cladding failure by quenching	125
Table 13.	Examples of lattice physics codes that can be used for generation of homogenized cross-sections	135
Table 14.	Examples of codes for three-dimensional neutron kinetics calculations.....	136
Table 15.	Examples of codes for core thermal-hydraulic calculations.....	137
Table 16.	Comparison of transient fuel rod analysis codes, applicable to analyses of reactivity-initiated accidents.....	138
Table 17.	Summary of computational studies of postulated control rod ejection accidents, in which calculated distributions of energy and failed fuel rods are reported.....	141
Table 18.	Summary of computational studies of postulated control rod drop accidents, in which calculated distributions of energy and failed fuel rods are reported.....	143
Table 19.	Typical composition of zirconium alloys used as cladding materials in LWRs	151

EXECUTIVE SUMMARY

In 1986, a Working Group of the Committee on the Safety of Nuclear Installations issued a state-of-the-art report (SOAR) on water reactor fuel behaviour in design basis accident conditions. The 1986 report was limited to the oxidation, embrittlement and deformation of pressurized water reactor fuel in a loss-of-coolant-accident. Since then, a considerable world wide effort has been expended in experimental and numerical modelling of PWR and BWR fuel behaviour in accident conditions, in particular for high burn-up fuel, which has allowed updating the State-of-the-Art Report and expanding its scope to include other types of DBAs, such as reactivity-initiated accidents.

The CSNI Working Group on Fuel Safety issued a State-of-the-art Report on fuel behaviour under LOCA conditions in spring 2009 [1], and has prepared a similar report for RIA. This report, here presented, is summarised below by chapter.

Chapter 1: Introduction

A reactivity-initiated accident is a nuclear reactor accident that involves an unwanted increase in fission rate and reactor power. The power increase may damage the reactor core, and in very severe cases, even lead to disruption of the reactor. Some scenarios for reactivity-initiated accidents were identified by regulatory bodies as design basis accidents.

The immediate consequence of a reactivity-initiated accident is a fast rise in fuel power and temperature. The power excursion may lead to failure of the nuclear fuel rods and release of radioactive material into the primary reactor coolant. In severe cases, the fuel rods may be shattered and large parts of the fuel pellet inventory dispersed into the coolant. The expulsion of hot fuel into water has potential to cause rapid steam generation and pressure pulses, which could damage nearby fuel assemblies, other core components, and possibly also the reactor pressure vessel. To prevent those potential consequences, safety criteria are usually set up to limit the energy injection into the fuel.

In the early 1990s, experimental programmes, in the form of pulse irradiation tests, were initiated in France, Japan and Russia to study the behaviour of high burn-up fuel under reactivity-initiated accidents. These test programmes were primarily intended to check the adequacy of regulatory acceptance criteria for RIA, which at the time were based largely on test results for un-irradiated or moderately irradiated fuel. Hence, an extension of the experimental database to higher fuel burn-up was needed.

The aforementioned pulse irradiation tests show that cladding failure occurs at lower fuel enthalpies for pre-irradiated than for fresh fuel rods, and that the susceptibility to failure increases with increasing fuel burn-up. Moreover, failures of pre-irradiated fuel rods usually occur at an early stage of the power surge, when the cladding temperature is low. The increased susceptibility to failure and the change from high temperature failures to a low temperature failure mode are attributed to the combined effects of clad tube embrittlement and aggravated pellet-clad mechanical interaction (PCMI) in high-burn-up fuel rods. It is also clear that the burn-up dependent state of the rod, and in particular the degree of cladding waterside corrosion, is very important for survivability of pre-irradiated fuel rods.

This report summarises the current understanding of fuel behaviour under reactivity-initiated accidents in light water reactors (LWRs). In the discussion of fuel behaviour, we consider the effects of fuel burn-up and residence time in the reactor to be particularly important, and consider that high-burn-up nuclear fuel rods may be characterised by:

- Embrittlement of the cladding tubes by radiation damage and waterside corrosion (including hydriding).
- Pellet-clad gap closure and bonding between the contacting materials.
- Changes in composition and distribution of fissile material within the fuel pellets.
- Retention of large amounts of gaseous fission products within the fuel pellets.
- Recrystallization and other changes to the fuel pellet microstructure.
- Depression of fuel pellet thermal conductivity and melting point.

The effects of these phenomena on the RIA fuel behaviour are in the report discussed in light of both experimental data and computer simulations.

Chapter 2: Description of RIA scenarios for major types of reactors

Three accident scenarios are of particular interest for RIA; (a) control rod ejection accidents in PWRs, (b) control rod drop accidents in BWRs, and (c) loss of coolant accidents in pressure tube heavy water reactors, such as the Canadian deuterium-uranium reactors. These are design basis accidents, which are used to define operational safety limits for each reactor type.

A control rod ejection accident (REA) can occur in PWRs by mechanical failure of the control rod drive mechanism. The accident results in rapid reactivity increase in a few fuel assemblies around the ejected control rod due to the local decrease of neutron absorption. Since the reactivity addition rates and the resulting power transients are much larger than for other conceivable RIA scenarios, these events are postulated accidents to establish the design and operation basis for PWRs.

The design basis reactivity accident in BWRs is the rod drop accident (RDA). The initiating event for an RDA is the separation of a control rod blade from its drive mechanism, to drop in a free fall. The rod ejection in an RDA is slower than in REA. The most severe RDA is deemed to occur at cold zero power (CZP) conditions, i.e. at a state with a strongly subcooled coolant, and nearly zero reactor power.

Inadvertent changes in coolant/moderator temperature and/or void fraction may add reactivity to the core. For LWRs, these events lead to additions of reactivity, which are generally slower relative to the control rod ejection or control rod drop accident, and they are classified as transients rather than accidents. On the other hand, the design of CANDU reactors, with heavy water and natural or low enriched uranium fuel, leads to a positive coolant void reactivity coefficient. Therefore, the loss-of-coolant-induced reactivity accidents are of particular interest and design basis accidents in CANDU reactors and they are mitigated by two independent, fast-acting shut down systems in CANDU reactors.

Chapter 3: State of fuel and cladding at various burn-up levels

The properties of fuel and cladding gradually change over a nuclear fuel rod life. Changes to the fuel pellets are due to transmutation of the material and radiation damage, whereas radiation damage in combination with waterside corrosion is responsible for the changes to the cladding tubes. With increasing burn-up, these mechanisms cause changes to the material properties, which are usually detrimental to the fuel behaviour under RIAs. In particular, corrosion of the cladding tubes has a twofold impact on the performance of LWR fuel. Firstly, the thermal and mechanical behaviour of the cladding tubes is directly affected by the formation of an external oxide (ZrO_2) layer at the metal-water interface. Secondly, the metal-water reactions liberate oxygen and hydrogen, part of which diffuse into the metal phase and cause gradual embrittlement of the material.

Chapter 4: Phenomena that need be addressed by experiments and modeling

The main safety concerns in RIAs are loss of long-term core coolability, possible damage to the reactor pressure boundary and the core through pressure wave generation. However, RIA experiments and modelling have traditionally focused on fuel rod failure, as this is a prerequisite for loss of coolable core geometry and pressure wave generation. In addition, some regulatory bodies require the number of failed fuel rods in the core to be calculated, so that the radiological consequences of the design basis RIA can be evaluated.

The fuel rod behaviour under an RIA is affected by the characteristics of the power pulse, core coolant conditions, burn-up-dependent state of the fuel rod, and fuel rod design. There are four potential failure modes for the fuel rod, one at low temperature:

- a) by PCMI under the early heat-up stage, which are relevant first and foremost to high-burn-up fuel rods with severely corroded cladding,

and three at high temperature:

- b) by cladding ballooning and burst, which occur as a consequence of film boiling and rod internal overpressure,
- c) by disruption of the cladding upon quenching from high temperature, which occurs as a consequence of embrittlement due to cladding oxidation under the film-boiling phase,
- d) by melting of the cladding and possibly also the fuel pellets.

Fuel rod fragmentation and loss of rod-like geometry may result from either PCMI-induced failure or quenching of fuel rods with overheated cladding. In the former case, the fuel dispersal is driven by gas-induced fragmentation, as observed for high-burn-up fuel rods. The degree of fuel-coolant interaction (FCI) is quantified with the energy conversion ratio, i.e. the ratio of the mechanical energy generated in the coolant to the thermal energy in the dispersed fuel. RIA tests on fresh fuel have shown that energy conversion ratios may reach up to about 1%. The conversion ratio increases with the rod internal gas overpressure and the energy injected into the fuel, and decreases with mean fragment size. Out-of-pile experiments on molten fuel dispersed into water have shown that FCI is affected by the pressure and subcooling of the coolant.

Chapter 5: Overview of RIA testing methodology

Our understanding of the fuel behaviour during reactivity-initiated accidents is based on the results of RIA simulation tests, performed on instrumented short-length rodlets in dedicated power pulse reactors, and separate effect tests, carried out on fuel or cladding samples out of pile.

To date, more than a thousand RIA simulation tests have been performed on fresh (un-irradiated) fuel rods, using pulse reactors in the USA, Japan, Russia, Kazakhstan and Romania. Later work has been focused on the behaviour of pre-irradiated fuel rods, and over the past 40 years, RIA simulation tests have been conducted on about 140 pre-irradiated light water reactor fuel rods in six different power pulse reactors:

- SPERT-CDC (Special Power Excursion Reactor – Capsule Driver Core, Scoville, ID, USA). Experiments performed in 1969-1970.
- PBF (Power Burst Facility, Scoville, ID, USA). Experiments performed in 1978-1980.
- IGR (Pulse Graphite Reactor, Kurchatov, Kazakhstan). Experiments performed in 1990-1992.
- BIGR (Fast Pulse Graphite Reactor, Sarov, Russia). Experiments performed in 1997-2000.

- NSRR (Nuclear Safety Research Reactor, Tokai, Japan). Ongoing experiments, carried out since 1975.
- CABRI (Cadarache, France). Experiments performed in 1993-2002 with sodium coolant loop. Tests with water coolant loop planned to start in the near future.

The results of these experiments are discussed in detail in the report. Direct application of the results from the pulse irradiation tests to LWR conditions is complicated by two key factors:

- The test conditions differ significantly between the aforementioned studies and also from the operational conditions in LWRs.
- The condition of fuel pellets and cladding of the tested fuel rods might be modified by re-fabrication of full-length LWR fuel rods into short-length rodlets for testing.

Hence, direct application of the results from pulse reactor tests to LWR conditions is difficult, but possible.

Additionally, mechanical tests of cladding tubes in support of RIA analyses have been carried out by many institutions; these include mainly:

- Burst tests, where cladding tube samples are subjected to internal pressure loading.
- Mandrel-type tests, where cladding tube samples are loaded internally by an expanding mandrel.
- Ring tensile tests, where ring-like cladding samples with two notched gauge sections are loaded in tension by inserts.

The most extensive test programme on cladding mechanical properties under RIA conditions is the French PROMETRA (PROpriétés MEcaniques en TRansitoire – Transient Mechanical Properties) programme. The tests are carried out mostly on irradiated cladding samples, taken from high-burn-up fuel rods, but also on unirradiated, artificially corroded samples. The results from PROMETRA show that the transient mechanical properties of cladding of high-burn-up fuel rods are influenced mainly by waterside corrosion. In particular, the tests have shown that cladding with spalled oxide can be severely embrittled by massive hydride blisters. At temperatures below 750 K, such cladding can fail without any plastic deformation, at a stress level that depends on the maximum depth of the hydride blisters.

Clad-to-coolant heat transfer under RIA-like conditions was studied in a series of experiments in the PATRICIA test loop of CEA, Grenoble, France. Two series of tests revealed significant kinetic effects in the clad-to-coolant heat transfer: The critical heat flux, i.e. the threshold heat flux at which a boiling crisis occurred, was significantly higher in the transient tests than under steady-state conditions. The same was true for the critical surface temperature, i.e. the surface temperature at which the transition to film-boiling took place.

In-pile separate effect tests have been carried out in the NSRR to study the interaction between solid fuel fragments and water. Fuel-coolant interaction is usually studied in connection with fuel rod failure in RIA simulation tests, but the tests were intended to separate the FCI phenomenon from the fuel rod failure mechanisms. In particular, the tests aimed to determine the relation between thermal-to-mechanical energy conversion ratio and the size of solid fuel particles.

Chapter 6: Specific phenomena under RIA and their experimental basis

Factors of particular importance to fuel rod behaviour under RIAs include:

- Fuel pellets: heat-up rates, melting, fragmentation, fission gas induced transient swelling and transient fission gas release.
- Cladding tubes: heat-up rates, melting, transient deformation, oxidation and failure.

Mixed oxide (MOX) fuel has also been examined, and it appears that local melting can occur at lower radial average fuel enthalpies in MOX than in pure UO_2 fuel. It is thought that this is associated with heat generation being concentrated in $(\text{U,Pu})\text{O}_2$ agglomerates, which also have lower melting points. Fuel rod failures under RIA simulation tests are usually divided into:

- Low-temperature, PCMI-induced fuel rod failures, which occur under the early heat-up phase of the accident.
- High-temperature failures, which occur at a later stage of the accident, as a result of film-boiling, degraded clad-to-coolant heat transfer and cladding overheating.

Low-temperature PCMI-induced clad failures under RIA may occur in high-burn-up fuel rods, but not in fresh fuel. This failure mode is more likely for accidents that initiate from conditions with low reactor power and/or significant subcooling than for accidents that occur at full reactor power. The PCMI-induced failures generally occur at significantly lower fuel enthalpies than high temperature failures.

It should be pointed out that the mode of PCMI-induced loading is much different from that of gas overpressure loading in cladding tubes. The PCMI-induced loading is displacement controlled, which means that the loads are relaxed when the cladding expands and yields. This leads to a stable mode of deformation, which is completely opposite to the deformation behaviour under gas pressure loading, where yielding is usually followed by immediate cladding failure through localised plastic deformation (necking). This unstable mode of failure is promoted by biaxial loading and also by the loss of strain hardening in embrittled materials. Due to the low level of corrosion and to cladding ductility, VVER fuel does not appear to undergo PCMI-induced failures at low temperature.

High-temperature fuel rod failures under RIA may occur by two different modes: clad ballooning and fuel rod disruption upon quenching. The first of these failure modes can be a limiting factor when there is a substantial gas overpressure in the fuel rod. Fuel rod disruption under quenching is due to cladding embrittlement by high temperature oxidation under the film-boiling phase. This failure mode was frequently observed in early pulse reactor tests on un-irradiated fuel rods, when the fuel enthalpy reached about $240 \text{ cal}(\text{gUO}_2)^{-1}$, i.e. about $1\,000 \text{ J}(\text{gUO}_2)^{-1}$. Early acceptance criteria for RIA in light water reactors were based largely on this threshold enthalpy.

Chapter 7: Summary of results from integral testing programmes

About 140 RIA simulation tests have to date been carried out on pre-irradiated LWR fuel rods. The majority of these tests were performed on UO_2 fuel rods, but 13 of the tests involved MOX fuel.

The pulse test data suggest a difference in the dominant failure mode for pre-irradiated fuel rods under RIA conditions for VVER and PWR or BWR fuel types. In contrast to the VVER rods, most pulse test failures of pre-irradiated PWR and BWR fuel rods are due to partially brittle fracture of the cladding, caused by pellet-clad mechanical interaction under the early stage of the power pulse. The apparent difference in failure behaviour between high-burn-up VVER fuel rods and PWR or BWR rods in pulse irradiation tests deserves attention and proposed explanations are related to the differences in cladding properties and fuel pellet design between VVER and PWR/BWR fuel rods.

As it was already mentioned, RIA simulation tests on fresh fuel rods in various pulse reactors result in fuel rod fragmentation and dispersal of fuel into the coolant, when the peak fuel enthalpy exceeds roughly $1\,000 \text{ Jg}^{-1}$. Pulse reactor tests on pre-irradiated fuel rods show that fuel may be dispersed into the coolant at significantly lower fuel enthalpy ($\approx 500 \text{ Jg}^{-1}$), when the fuel burn-up exceeds approximately $40 \text{ MWd}(\text{kgU})^{-1}$. The fuel dispersal occurs in connection with PCMI-type cladding failure; the ballooning and burst type of failure does not lead to significant fuel dispersal in the testing conditions investigated to date.

Chapter 8: Predictive computer codes

Modelling of reactivity-initiated accidents involves the simultaneous solution of equations for neutron transport, heat transport within the fuel rods and across the clad-to-coolant interface, mechanical behaviour of fuel and cladding, and coolant thermal-hydraulics. These equations are strongly related and depend on both space and time, and some simplifications may be necessary as it is difficult to solve the equations in full detail for core-wide applications, using conventional computer systems.

The neutron transport problem is normally simplified by applying a two-step procedure, where different computer codes are used for each step. The first step involves detailed preparatory calculations at the level of the fuel assemblies, whereas the second step involves core-wide calculations with more approximate methods.

Core-wide thermal-hydraulic calculations are typically done by considering each fuel assembly as a vertical flow channel. In analyses of BWRs, each fuel assembly can be treated by a one-dimensional model, since the assemblies are enclosed by fuel channels (boxes). Three-dimensional thermal-hydraulic models are on the other hand often needed in analyses of PWRs, due to lateral cross flow between assemblies.

Following the core-wide analyses, specifically designated codes can be used to analyse the thermo-mechanical behaviour of particular fuel rods in detail. Such codes have been verified and calibrated against experimental data from RIA simulation tests in the NSRR and/or CABRI. Some general conclusions from this work are:

- The codes are quite successful in reproducing measured fuel rod temperatures and deformations for cases in which the cladding tube remains at low temperature throughout the test.
- Also clad failures are captured with fair accuracy for these cases, provided that the degree of cladding corrosion is known and can be used as input to the analysis.
- For tests under which a boiling crisis occurs, neither temperatures nor deformations are reproduced with sufficient accuracy by the codes. Specific RIA clad-to-coolant heat exchange models that should improve the situation were developed recently, but the current experimental database is not large enough to allow complete code validation.

Fuel rod codes also usually fail to accurately predict fission gas release during simulated RIA transients. This is not surprising, because the physical mechanisms involved are complex. Model improvements are clearly required in this area.

Chapter 9: Results of energy and failure distribution calculations

To assess the consequences of an RIA, i.e. to estimate the number of failed fuel rods, it is necessary to first calculate the pulse amplitude and the resulting peak fuel enthalpy for each fuel rod. The peak fuel enthalpy of each rod is then compared with relevant failure criteria, in which the state (burn-up, internal gas overpressure, clad corrosion, etc.) of the fuel rod is considered.

Results of numerous three-dimensional core kinetics analyses of postulated REAs and RDAs show that only 10-20% of the fuel within a typical reactor core experiences a significant energy deposition under these accidents. On the whole, it appears that the energy deposition is too low to cause fuel rod failure, even under very severe postulated accidents, apart from the specific faults for a 6×6 to 8×8 array of fuel assemblies around the ejected or dropped control rod.

Chapter 10: Summary and conclusions

Our current knowledge of reactivity-initiated accidents in light water reactors and their consequences is based largely on two sources of information:

- Pulse irradiation tests of instrumented fuel rodlets, carried out in research reactors.
- Computer analyses of the reactor response to postulated accident scenarios.

The pulse irradiation tests show that there are two limiting failure modes for the fresh rods: fracture of the overheated and oxygen-embrittled cladding upon quenching, or clad ballooning and burst. The tests on pre-irradiated fuel rods show that irradiated rods are more susceptible to cladding failure than fresh rods, i.e. they fail at lower fuel enthalpy. The tests also suggest that high-burn-up fuel rods fail either by cladding high-temperature ballooning and burst, or at low temperature, by pellet-clad mechanical interaction during the early heat-up stage of the accident.

There are a number of questions regarding the pulse test conditions that may mean that the true fuel behaviour under reactivity-initiated accidents in light water reactors is not accurately reproduced:

- Many of the un-irradiated test rods were designed with high enrichments of ^{235}U . Parametric studies show that enrichment has an observable effect on the behaviour of fresh fuel rods under RIAs.
- Most tests, both on un- and pre-irradiated fuel rods, were done with cooling by water at room temperature, atmospheric pressure and low (or zero) flow. Whilst these conditions are fairly close to those at cold zero power in BWRs, they are very different to those associated with rod ejection accidents in PWRs. It is also noted that data for fuel rod post-failure behaviour, i.e. for fuel-coolant interaction and thermal-to-mechanical energy conversion ratios, originate almost exclusively from tests with water at ambient conditions and low or zero flow.
- About thirty of the pre-irradiated test rods, namely those in the SPERT and NSRR/JMTR tests, had atypical design and/or were pre-irradiated under atypical reactor conditions. Unfortunately, these tests make up the most of the database for the burn-up range of 10 to 40 MWd(kgU)-1.
- Pulse widths in the NSRR (4-7 ms FWHM) and the BIGH (2-3 ms) are much smaller than those expected for control rod ejection/drop accidents. The pulse width affects the PCMI failure mode, most importantly because it controls the time lag between mechanical loading and heating of the cladding tube; a narrow power pulse leads to mechanical loading at a time when the cladding is insignificantly heated from its initial temperature and therefore potentially more brittle.

Overall, it is believed that the failure behaviour of LWR fuel rods under reactivity-initiated accidents has been fairly well investigated experimentally and that the failure mechanisms are largely understood. However, it is recommended that further consideration be given to additional tests to evaluate some of the test uncertainties:

- RIA simulation tests should be made at cooling conditions and with power pulses that better reproduce light water reactor conditions.
- More attention should be paid to the role of pre-conditioning in tests on pre-irradiated fuel rods.
- Investigations of the post-failure behaviour of failed rods, and measurements of thermal-to-mechanical energy conversion ratios at other coolant conditions than room temperature and atmospheric pressure, are needed.

It is considered that this work should include tests on individual fuel rodlets and also fuel rod bundle tests, if possible.

Finally, the consistency of calculated results in reported state-of-the-art analyses of postulated control rod ejection/drop accidents suggest that current computational methods used to analyse these accidents are well established and reliable. However, improvements to the modelling of fuel rod thermo-mechanical behaviour, including transient fission gas release under RIA simulation tests on pre-irradiated fuel rods, would be desirable to aid our understanding the effect of transient release of gaseous fission products on the fuel rod internal gas pressure and possible threats to cladding integrity.

1. INTRODUCTION

1.1 Background to reactivity-initiated accidents

A reactivity-initiated accident is a nuclear reactor accident that involves an unwanted increase in fission rate and reactor power. The power increase may damage the reactor core, and in severe cases, even lead to disruption of the reactor. A few such accidents occurred in the early days of research reactors [2], e.g. the 1952 accident in the NRX reactor at Chalk River, Canada [3], and the 1961 SL-1 accident in Idaho Falls, USA [4]. These early reactivity-initiated accidents led to design improvements, which were implemented in later generations of research reactors and, more importantly, in commercial power generating reactors. The design philosophy was to reduce potential causes for RIAs to a minimum, and if an accident still occurred, to quickly terminate the power surge [5]. Moreover, some scenarios for reactivity-initiated accidents were identified by regulatory bodies as design basis accidents, i.e. they were classified as accidents that a reactor must be designed and built to withstand.

In current pressurised and boiling water reactors, which are the two most common types of power generating reactors worldwide [6], protection against reactivity-initiated accidents is afforded by engineered safety systems, but also by inherent reactor feedback mechanism. More precisely, the reactors are designed so that an unwanted power rise produces fast negative reactivity feedback through the increase in fuel and coolant temperature, and also by steam generation in the light water coolant. The negative feedback limits the peak power and provides time for the engineered safety systems to respond and shut the reactor down. No reactivity-initiated accident with severe consequences has so far occurred with the PWR and BWR reactor designs.

Historically, the worst reactivity-initiated accident took place on April 26 1986 in reactor 4 of the Chernobyl nuclear power plant in Ukraine [7]. The reactor, which was of light water graphite moderated pressure tube design (RBMK), was completely disrupted, and radioactively contaminated fallout spread over most of the northern hemisphere. The severe consequences of the Chernobyl accident were due to the fact that RBMKs lack not only a reactor containment, but also some of the inherent feedback mechanisms mentioned above for PWRs and BWRs [7]. It should also be remarked that the accident occurred under a reactor test, where normal operating guidelines were ignored and safety systems were made ineffective.

The Chernobyl accident reminded the nuclear community of the destructive potential of RIAs, and it prompted much research into the subject. Utilities and safety organisations in many countries undertook reviews of potential RIAs in their own power plants, and the results were shared through expert meetings and seminars arranged by international organisations, such as the International Atomic Energy Agency (IAEA) and the OECD Nuclear Energy Agency. In the early 1990s, experimental programs were also initiated in France, Japan and Russia to study the behaviour of highly irradiated nuclear fuel under reactivity-initiated accidents. These test programs were primarily intended to check the adequacy of regulatory acceptance criteria for RIA, which at the time were based largely on test results for un-irradiated or moderately irradiated fuel. Hence, an extension of the experimental database to higher fuel burn-up¹ was needed.

1. Fuel burn-up refers to the amount of energy generated per unit initial mass of heavy nuclides. See the nomenclature section for a definition.

1.2 Consequences of reactivity-initiated accidents

The immediate consequence of a reactivity-initiated accident is a fast rise in fuel power and temperature. The power excursion may lead to failure of the nuclear fuel rods and release of radioactive material into the primary reactor coolant. This material comprises gaseous fission products as well as fuel pellet solid fragments. In severe cases, the fuel rods may be shattered, and large parts of the fuel pellet inventory dispersed into the coolant. The expulsion of hot fuel into water has potential to cause rapid steam generation and pressure pulses, which could damage nearby fuel assemblies, other core components, and possibly also the reactor pressure vessel. Our understanding of these damage mechanisms is based on RIA simulation tests, carried out on short-length fuel rods in pulse reactors. To date, more than a thousand pulse irradiation tests of this kind have been carried out on fresh (un-irradiated) fuel rods, and about 140 tests have been done on pre-irradiated samples.

The damage mechanisms observed for fresh fuel rods in pulse irradiation tests are:

- Cladding ballooning and burst.
- Embrittlement and failure by high-temperature oxidation.
- Melting of fuel pellets and/or cladding.

These damage mechanisms are all related to high temperature, and the tests on fresh fuel rods show that the degree of fuel rod damage correlates well with the peak value of fuel pellet specific enthalpy,² the higher the enthalpy, the more extensive is the damage. Regulatory acceptance criteria for RIAs are for this reason traditionally formulated in terms of limits for the fuel radial average specific enthalpy (see Subsection 1.3).

Pulse irradiation tests generally show that cladding failure occurs at lower fuel enthalpies for pre-irradiated than for fresh fuel rods, and that the susceptibility to failure increases with increasing fuel burn-up. Moreover, failures of pre-irradiated fuel rods usually occur at an early stage of the power surge, when the cladding temperature is low. The increased susceptibility to failure and the change from high temperature failures to a low temperature failure mode are attributed to the combined effects of clad tube embrittlement and aggravated pellet-clad mechanical interaction in high-burn-up fuel rods. It is also clear that the burn-up dependent state of the rod, and in particular the degree of cladding waterside corrosion, is very important for survivability of pre-irradiated fuel rods. The correlation between fuel pellet enthalpy and cladding damage is not as clear for pre-irradiated rods as for fresh fuel rods.

1.3 Regulatory acceptance criteria

Acceptance criteria for reactivity-initiated accidents are defined by regulatory authorities to ensure integrity of the reactor coolant pressure boundary and maintenance of core coolability in the event of an accident. These criteria form the design basis for reactivity control systems, and usually, they also define safety limits that must not be transgressed under reactor operation. The acceptance criteria vary with country and reactor type, but they are generally formulated so that gross fuel rod shattering and mechanical energy generation by fuel-coolant interaction is precluded under any accident scenario. The concern is that the generation of a coolant pressure pulse could break the reactor coolant pressure boundary or damage the fuel and other core internals so that long-term cooling of the core would be impaired. Some fuel damage is generally tolerated, at least if the considered accident scenario is judged to occur with very low frequency. The acceptable amount of damage is settled by the requirements to meet regulatory limits on radiation dose to the public, and to ensure integrity of the coolant pressure boundary and long-term coolability of the fuel.

2. Specific enthalpy refers to the enthalpy per unit mass of the fuel material. See the nomenclature section for a definition.

The acceptance criteria are based on the results of RIA-simulation tests, conducted in dedicated research reactors. The criteria are commonly defined in terms of limits on the radially averaged fuel pellet specific enthalpy, or the increment of this property during the reactivity-initiated accident. Regulatory authorities usually postulate two kinds of enthalpy limits: (i) a definite limit for core damage, which must not be transgressed at any axial position in any fuel rod in the core, and (ii) fuel rod failure thresholds, that define whether a fuel rod should be considered as failed or not in calculations of radioactive release. The enthalpy thresholds for fuel rod failure are often supplemented with acceptance criteria for other parameters of importance to cladding failure, such as the clad-to-coolant local heat flux or the fuel rod internal gas overpressure. Reactor operators must verify that these acceptance criteria are met through computer analyses of postulated accident scenarios.

A review of national acceptance criteria for reactivity-initiated accidents is beyond the scope of this report. The reader is referred to [8], in which a recent review of fuel rod failure thresholds for RIAs in PWRs and BWRs can be found. The review covers currently applied as well as projected failure thresholds. It should be remarked that considerable differences exist between these thresholds, in particular as to how the effects of fuel burn-up and cladding waterside corrosion are accounted for.

In late 1993 and early 1994, two high-burn-up PWR fuel rods failed at remarkably low fuel enthalpies under RIA simulation tests in the French CABRI facility and the Japanese Nuclear Safety Research Reactor (NSRR). The test rods failed at fuel enthalpies far below existing thresholds for fuel rod failure, and thus called for revisions of the acceptance criteria. Since then, burn-up related effects on the enthalpy threshold for fuel rod failure have been extensively studied, and many RIA simulation tests on high-burn-up fuel rods have been conducted in France, Japan and Russia. As of today, regulatory authorities in Japan [9] and Switzerland [10] have revised their acceptance criteria for RIA based on this research, while revisions are under way in other countries, including the United States [11-12]. Hence, in the years to come, revised acceptance criteria for RIA are expected to gain legal force in many countries.

1.4 Scope and outline of the report

This report is intended to summarise the current understanding of fuel behaviour under reactivity-initiated accidents in light water reactors. This understanding is based largely on experiments on PWR, BWR and VVER³ fuels, and the presentation is therefore mostly concerned with these reactors and their fuel designs. However, Canadian deuterium-uranium heavy water reactors and their fuel are to some extent also considered in the report.

In the discussion of fuel behaviour, we consider in particular the effects of fuel burn-up and residence time in the reactor. In summary, high-burn-up nuclear fuel rods are characterised by:

- Embrittlement of the cladding tubes by radiation damage and waterside corrosion.
- Pellet-clad gap closure and bonding between the contacting materials.
- Changes in composition and distribution of fissile material within the fuel pellets.
- Retention of large amounts of gaseous fission products within the fuel pellets.
- Recrystallisation and other changes to the fuel pellet microstructure.
- Depression of fuel pellet thermal conductivity and melting point.

The effects of these phenomena on the RIA fuel behaviour are in the report discussed in light of both experimental data and computer simulations.

The fuel pellet material of primary concern is UO_2 , but the report covers also $(\text{U,Pu})\text{O}_2$ mixed oxide fuel, gadolinium-bearing burnable absorber fuel, and inert matrix fuel. Particular characteristics

3. Russian type pressurised water reactor.

of the non- UO_2 fuels are discussed, and their behaviour under reactivity-initiated accidents is compared with that of uranium dioxide fuel. The report includes experimental data and calculated results, published in open literature up to March 2009.

The outline of the report is as follows:

- Section 2 provides an introductory overview of scenarios for reactivity-initiated accidents in major types of reactors. Emphasis is placed on control rod ejection accidents in pressurised water reactors and control rod drop accidents in boiling water reactors, which are deemed to be the most challenging RIA scenarios for the reactor types mentioned. The power pulses caused by these accidents are discussed with regard to their shape, width and amplitude.
- Section 3 gives a background to burn-up related changes to fuel pellets, cladding tubes and the pellet-clad gap. Changes to the fuel pellets are due to transmutation of the material and radiation damage, whereas radiation damage in combination with waterside corrosion is responsible for the changes to the cladding tubes. Most of these changes are detrimental to the fuel rod behaviour under RIAs.
- Section 4 identifies phenomena that are important to the course of events of a reactivity-initiated accident and to its consequences. Possible failure modes for the fuel rods are identified, and the conditions under which each failure mode occurs are delineated. Moreover, the fuel rod post-failure behaviour is described. Of particular importance is the fuel-coolant interaction, i.e. the conversion of fuel thermal energy into mechanical energy by steam generation, and its potential to cause detrimental pressure pulses in the coolant. Also the radiological consequences of RIAs are discussed.
- Section 5 is an overview of tests and experiments that have been pursued to study the fuel rod behaviour under RIAs. Experimental programs with integral RIA simulation tests, performed in various research reactors, are reviewed. A more detailed account of the results of these tests is given in Appendix A. In addition, we summarise important out-of-pile separate effect tests with relevance to fuel behaviour in RIAs. These are tests on cladding mechanical properties, clad-to-coolant transient heat transfer and fuel-coolant interaction phenomena.
- Section 6 provides detailed discussions of phenomena with particular importance to the fuel rod behaviour under RIAs. For the fuel pellets, we treat heat-up, melting, fragmentation, fission gas induced transient swelling and transient fission gas release, and for the cladding tubes, we consider heat-up, melting, transient deformation, oxidation and failure. These phenomena are discussed in light of experimental data from integral RIA simulation tests as well as separate effect tests. When needed, computer simulations are used to interpret the tests and to illustrate particular phenomena.
- Section 7 is a summary of results from experimental programs with integral RIA simulation tests. The presentation is focused on reported fuel enthalpy thresholds for cladding failure and fuel dispersal. A distinction is made between test done on un-irradiated and pre-irradiated fuel rods, respectively.
- Section 8 deals with computer codes used for analyses of reactivity-initiated accidents. The presentation is intended to give a brief overview of state-of-the-art methods and models currently used for analyses of RIAs in light water reactors, rather than descriptions of individual codes. However, some of the most widely used codes for neutron kinetics calculations, thermal-hydraulics and fuel rod analyses in RIAs are reviewed. Details are given in Appendix B.

- Section 9 is a logical continuation to the preceding section on computer codes. Here, we summarise calculated results on core-wide distributions of energy and failed fuel rods under postulated control rod ejection and control rod drop accidents. All studies reviewed in this section were done with state-of-the-art three-dimensional neutron kinetics codes.
- Section 10 is a final summary, where we also try to identify knowledge gaps in experimental data and model deficiencies in computer codes.

The international system of units (SI) is used throughout the report, and symbols used in equations conform to prevalent nomenclature in international literature. All symbols and abbreviations are explained as they first appear in the text. However, to ease a non-linear reading of the report, a nomenclature is also provided in Section 11.

2. DESCRIPTION OF RIA SCENARIOS FOR MAJOR TYPES OF REACTORS

Let us first define some basic notions of reactor kinetics, relevant to reactivity-initiated accidents. Reactivity is a fundamental quantity, expressing the departure of a nuclear reactor from criticality, i.e. from a state where the number of neutrons released by fission is exactly balanced by the neutrons being absorbed or escaping the reactor core [13]. More precisely, static reactivity, ρ , is defined as the fractional departure from core criticality:

$$\rho = \frac{k-1}{k} \quad (1)$$

Here, k is the effective neutron multiplication factor, i.e. the ratio of neutron production to neutron absorption and leakage. A positive reactivity thus indicates a move towards supercriticality (power increase), whereas a negative reactivity corresponds to a move towards subcriticality (power decrease). Under reactor operation, the reactivity can be controlled, e.g. by movements of control rods or by addition/removal of soluble neutron absorbers in the coolant or moderator. However, reactivity is also affected by changes in fuel and moderator temperature, and by changes in the moderator steam (void) content. Hence, the reactivity rate of change may be written:

$$\dot{\rho} = \dot{\rho}_{CS} + \frac{\partial \rho}{\partial T_f} \dot{T}_f + \frac{\partial \rho}{\partial T_m} \dot{T}_m + \frac{\partial \rho}{\partial \alpha_m} \dot{\alpha}_m \quad (2)$$

where $\dot{\rho}_{CS}$ is the reactivity rate of change induced by reactivity control systems, \dot{T}_f and \dot{T}_m are the rates of temperature change for fuel and moderator, and $\dot{\alpha}_m$ is the rate of change for the moderator vapour phase (void) volume fraction [13-14]. Of the partial derivatives on the right hand side of equation (2), the fuel temperature (Doppler) coefficient $\partial \rho / \partial T_f$ is always negative, which means that the fuel temperature increase accompanying a rise in reactivity always provides negative feedback, to the benefit of reactor stability. The other partial derivatives, which are usually termed moderator temperature and void coefficients, can be either positive or negative, depending on reactor design and/or operating conditions.

There is a wide spectrum of scenarios for accidents and events that may result in inadvertent insertion of reactivity to nuclear power reactors. A general overview and classification of these scenarios in major types of reactors are given in Section 2.1. Three accident scenarios are of particular interest: (i) control rod ejection accidents in PWRs, (ii) control rod drop accidents in BWRs, and (iii) loss of coolant accidents in pressure tube heavy water reactors, such as the Canadian deuterium-uranium reactors. These are design basis accidents, i.e. postulated events of low probability, which would have serious consequences if they were not inherently accounted for in the design of the reactor and related safety systems. Section 2.2 deals with the power pulses that are generated in the aforementioned design basis accidents. We consider in particular the shape, amplitude and duration of the pulses, since these parameters are important to the fuel behaviour in an RIA.

2.1 Overview of reactivity insertion events

Reactivity insertion events in power reactors can be divided broadly into:

- Control system failures.
- Control element ejections.
- Events caused by coolant/moderator temperature and void effects.
- Events caused by dilution or removal of coolant/moderator poison.

Events belonging to each of these classes are discussed for major types of power reactors in the following subsections. The presentation is based largely on a study of reactivity accidents by the International Atomic Energy Agency [15].

2.1.1 Control system failures

All major types of power reactors use control elements (rods) for shutdown, and most reactors also use these rods for power control under normal operation. The control rods contain a neutron absorbing material, usually some of the elements B, Ag, Cd, In or Hf, which lowers the reactivity when the rods are inserted into the core. Inadvertent withdrawal of these rods, either due to control system faults or operator errors, is a possible cause to reactivity-initiated accidents in all types of power reactors. However, reactor control systems generally place constraints on allowable control rod movements, thereby excluding operator errors as long as the control systems function. Further protection is afforded by operating limits, known as rod insertion limits (RILs), which put restriction on the reactivity worth of each control element. Hence, should a control rod be inadvertently withdrawn, the RILs ensure that the reactivity addition will be manageable. Events involving inadvertent removal of control rods are generally not classified as accidents, but fall into the category of transients [15].

2.1.2 Control rod ejections

A control rod ejection can occur by mechanical failure of the control rod drive mechanism or its housing. As a consequence of the rod ejection, the reactivity of the core is rapidly increased due to decreasing neutron absorption. Since the reactivity addition rates and the resulting power transients are much larger for these events than for other accident scenarios, control rod ejections belong to the category of design basis accidents in light water reactors. This means that they are postulated, credible accidents with low probability that are used to establish the design basis for the reactor and to define safety limits for its operation. The postulated accident scenarios for control rod ejections in PWRs and BWRs are further described below.

In pressure tube heavy water reactors, such as CANDUs, control rod ejections are excluded by the core design. Control rods in a CANDU are actually termed shutoff rods, since they are used only for safe shutdown of the reactor. Reactivity control under normal operation is facilitated by on-power refuelling and by water level adjustment in a system of light water zone controllers.

2.1.2.1 Rod ejection accidents in PWRs

The design basis reactivity accident in pressurised water reactors is the rod ejection accident. This accident is caused by mechanical failure of a control rod mechanism housing, such that the coolant pressure ejects a control rod assembly completely out of the core. The consequence of the rod ejection is a rapid positive reactivity addition, which results in a core power excursion with large localised relative power increase [16]. The rod ejection and its associated addition of reactivity to the core occur within about 0.1 s in the worst possible scenario; the actual time depends on reactor coolant pressure and the severity of the mechanical failure.

The nuclear design of the core affects the severity of the accident via the reactivity worth, location and grouping of control rods. During normal operation of a PWR at full power, only one bank (group) of control rods is positioned in the core, and these rods are for safety reasons only partially inserted in the top of the core. This positioning is possible because reactivity changes under operation, e.g. caused by core depletion and xenon transients, are in a PWR compensated for by changes in the soluble boron concentration rather than by control rod movements. The amount of reactivity that is added by the ejection of a control rod during normal full power operation is thereby limited. At lower power, PWRs are allowed to operate with more banks and control rods further inserted. With respect to reactivity addition, the most severe REA would therefore occur at hot zero power (HZIP) conditions,⁴ i.e. with the coolant at normal reactor operating temperature and pressure, but with nearly zero reactor power [16]. This accident scenario is further discussed in Section 2.2.

2.1.2.2 Rod drop accidents in BWRs

The design basis reactivity accident in boiling water reactors is the rod drop accident. The initiating event for this accident is the separation of a control rod blade from its drive mechanism. The separation is assumed to take place when the blade is fully inserted in the core, and the detached blade remains stuck in this position until it suddenly becomes loose and drops out of the core in a free fall. Hence, the control rod is removed from the core due to gravity, and in contrast to the REA in PWRs, the accident can occur at any reactor operating condition, independent of coolant pressure, and the coolant pressure does not influence the rod ejection rate. The rod ejection is also slower in RDAs than in REAs. For this reason, and because of the coarser core lattice (lower ratio of fissile to non-fissile core material) for BWRs in comparison with PWRs, the power surge is generally somewhat slower in RDAs than in REAs (see Section 2.2.1).

The power surge is terminated mainly by the negative fuel temperature feedback, i.e. by the second term on the right hand side of Equation 2, but if the coolant is saturated or close to saturation, additional negative feedback from coolant heating and vapour generation will help mitigate the power excursion. However, the reactivity feedback provided by changes in coolant temperature and vapour content is slower than the fuel temperature effect, since there is a time lag in fuel-to-coolant heat transfer. With respect to reactivity addition, the most severe RDA is deemed to occur at cold zero power conditions, i.e. at a state with a strongly subcooled coolant, and nearly zero reactor power [17-19]. This accident scenario is further discussed in Section 2.2.

2.1.3 Coolant/moderator temperature and void effects

As indicated by Equation 2, inadvertent changes in coolant/moderator temperature and/or void fraction may add reactivity to the core. Since the moderator temperature coefficient ($\partial\rho/\partial T_m$) and void coefficient ($\partial\rho/\partial\alpha_m$) can have both positive and negative sign, scenarios for reactivity addition through moderator temperature and void effects vary significantly between reactors.

2.1.3.1 PWRs

Pressurised water reactors are generally operated with a negative moderator temperature coefficient, although the coefficient may turn positive in cases where the coolant is strongly borated and at low temperature. With the exception of these rare cases, reactivity can thus be inserted by a decrease in coolant temperature. Possible scenarios for such an inadvertent event are the start-up of an inactive reactor coolant pump in an idle steam generator loop, or a sudden increase in heat removal by the

4. With respect to potential fuel damage, however, other operating conditions than HZIP could be more challenging.

secondary side [15]. These events lead to relatively slow additions of reactivity, and they are classified as transients rather than accidents.

2.1.3.2 BWRs

Boiling water reactors are operated with negative reactivity feedback from moderator temperature and void fraction, meaning that a reduction of these quantities results in reactivity addition to the core. Possible scenarios for reactivity events in BWRs include loss of feedwater heating, leading to coolant temperature reductions, and accidental operation of emergency core cooling systems or various over-pressurisation transients, resulting in void collapse [15]. These events are classified as transients, since they lead to relatively slow reactivity additions, which are unable to cause prompt criticality (Section 2.2.1).

2.1.3.3 CANDUs

The design of CANDU reactors, i.e. the combination of a low temperature heavy water moderator, a high temperature heavy water coolant within the pressure tubes, and natural or low enriched ($<1\%$ by weight ^{235}U) uranium fuel, leads to a positive coolant void reactivity coefficient [20]. Hence, coolant boiling, e.g. caused by inadvertent heating of the feedwater or a reduction of coolant flow, results in reactivity insertion in CANDU reactors [21]. Loss of coolant accidents (LOCAs) are therefore of particular interest in CANDU reactors, and they are obvious design basis accidents. A guillotine break of a large diameter header to a loop of the heat transport system is one of the most severe postulated scenarios with respect to reactivity insertion rate. For this scenario, the core average power may raise to 3-4 times its nominal value. The power surge is terminated by the shutoff system, and the pulse width is typically about 1 s [22]. The time scale for a LOCA-induced power pulse in a CANDU reactor is thus much longer than that for a PWR REA or a BWR RDA, as will be shown in Section 2.2.

2.1.4 Dilution or removal of coolant/moderator poison

Both light and heavy water reactors use soluble neutron absorbers (poisons) in the coolant/moderator as a safety shutdown system, in complement to the control rods. Once this safety system is actuated, positive reactivity may be inadvertently added if the poisoned coolant/moderator is diluted with unpoisoned water. Scenarios for this kind of reactivity insertion events, which thus take place after reactor shutdown, often involve injection of unpoisoned water by the emergency core cooling system [15]. Finally, it should be remarked that PWRs use neutron absorbing boron in the primary coolant system as a means of reactivity control also under normal reactor operation. A malfunction of the chemical and volume control system (CVCS) could therefore lead to inadvertent reactivity addition also under normal operation for PWRs.

2.2 Power pulse characteristics

Among the reactivity insertion scenarios reviewed in Section 2.1, the control rod ejection accident in PWRs and the control rod drop accident in BWRs are of particular concern, since they may lead to fast and significant power excursions in fuel elements close to the failed control rod. The characteristics of the power pulse depend on the accident scenario – most importantly the reactivity worth of the ejected control rod, but also on the core and fuel design, reactor operating state, and the time at which the accident occurs under the fuel cycle [23]. The reactivity worth of the ejected control rod depends on its position and insertion depth in the core, the core axial power shape and the fuel burn-up distribution close to the ejected rod. A control rod ejected from a position dominated by high-burn-up fuel gives a lower reactivity addition than if the rod is ejected from a position with fresh (un-irradiated) or low-burn-up fuel.

Since the REA and the RDA are design basis accidents in PWRs and BWRs, respectively, these accident scenarios have over the years been closely analysed by use of computer codes and models. The

rigour of the applied computational models varies greatly, but they usually include neutron kinetics calculations coupled with calculations of fuel rod thermomechanics and coolant thermal-hydraulics, in order to capture the reactivity feedback effects from fuel and coolant heating. Moreover, a gradual shift from codes with lower dimensionality to three-dimensional models have taken place during the last decade, since the REA and RDA involve localised reactivity addition to the core. State-of-the-art computer codes for analyses of reactivity-initiated accident are discussed in Section 8 of the report.

In Table 1, we summarise estimated values for the pulse width and maximum fuel pellet specific enthalpy under REAs and RDAs. The data are taken from realistic and moderately conservative analyses of postulated accident scenarios, which have been carried out with state-of-the-art computer codes and reported in open literature. The fuel pellet enthalpies reported in Table 1 pertain to the core-wide maximum of radial average specific enthalpy and the core-wide maximum of enthalpy increase. As will be shown in the following subsections, the pulse width and fuel enthalpy under an REA or RDA depend strongly on the reactivity worth of the ejected/dropped control rod. For this reason, the range of rod worths used in the calculations is also given in Table 1. It is clear from the table that REAs initiating from hot full power conditions have considerably wider pulses than accidents that occur at zero reactor power. Also, the maximum fuel enthalpy increase is moderate for the REA at HFP.

Table 1. Estimated pulse widths and core-wide maxima of fuel pellet radial average enthalpy and enthalpy increase for various scenarios of REA and RDA

The data are compiled from realistic and moderately conservative computer analyses.

Reactor, accident scenario	Pulse width [ms]	Max fuel enthalpy [J(gUO ₂) ⁻¹]	Max ent. increase [J(gUO ₂) ⁻¹]	Rod worth [10 ⁻⁵]	Literature sources [references]
PWR:					
REA HZP	25-65	140-320	80-250	600-850	16,17,24-26
REA HFP	400-4 500	230-350	10-130	40-200	17,24,27-29
BWR:					
RDA CZP	45-75	140-460	130-450	700-1 300	17,18,24,30
RDA HZP	45-140	160-400	90-320	600-1 300	17,30,31

HZP: Hot zero power, **HFP:** Hot full power, **CZP:** Cold zero power

In the following subsections, power pulse characteristics from recent three-dimensional neutron kinetics analyses of REAs and RDAs are evaluated and compared. Of particular interest to the fuel behaviour are the width, shape and amplitude of the power pulse. The width and shape do not vary significantly with position in the core, and can thus be treated approximately as core-wide parameters under an REA or RDA. The pulse amplitude, on the other hand, is a local property.

2.2.1 Pulse width and shape

If the reactivity addition under an REA or RDA is larger than the fraction of delayed neutrons, the reactor becomes prompt critical, meaning that the reactor is critical on prompt neutrons alone.⁵ The power will then rise rapidly until the negative fuel temperature feedback terminates the power rise within a few hundredths of a second [13]. Additional negative reactive feedback is obtained from coolant heating, and possibly also from coolant void generation, but these effects are much slower than the fuel temperature feedback.

The adiabatic Nordheim-Fuchs model gives simple analytical expressions for the pulse width and pulse shape under conditions of prompt criticality [13]. This is a simple point-kinetic model, in which

5. Prompt neutrons are released immediately in fission, in contrast to the delayed neutrons, which are emitted from nuclei produced in beta decay of the original fission fragments.

adiabatic fuel heating and a linear negative fuel temperature feedback on reactivity are assumed. Other feedback effects, as well as the effects of delayed neutrons, are neglected. According to the model, for a step-like insertion of reactivity $\Delta\rho$, the full width at half maximum (FWHM), τ , of the power pulse is approximately given by:

$$\tau = \frac{4 \cosh^{-1}(\sqrt{2}) \Lambda}{\Delta\rho - \beta} = \frac{3.5255 \Lambda}{\Delta\rho - \beta} \quad (3)$$

provided that $\Delta\rho > \beta$, where β is the effective fraction of delayed neutrons. Here, Λ is the effective neutron lifetime, i.e. the mean time between the birth of a fission neutron and its subsequent absorption, leading to another fission. In ordinary UO_2 fuel, β depends on the initial content of ^{235}U and fuel burn-up (see Section 3.1.1). The adiabatic Nordheim-Fuchs model also gives an approximation to the pulse shape under a prompt critical event. More precisely, the pulse shape is given by:

$$P(t) = P_{\max} \text{sech}^2 \left(\frac{(\Delta\rho - \beta)(t - t_{\max})}{2\Lambda} \right) \quad (4)$$

where P_{\max} and t_{\max} are the maximum power and the time at which the maximum is obtained, respectively.

Although the adiabatic Nordheim-Fuchs model is very simple, the pulse widths and pulse shapes provided by Equations 3 and 4 are in fair agreement with those obtained from state-of-the-art three-dimensional core kinetics analyses of REA. This is illustrated in Figure 1, which is a compilation of calculated pulse widths for HZP REA at end-of-cycle (EOC) conditions, obtained from several independent three-dimensional core kinetics analyses. In the figure, $\Delta\rho$ corresponds to the reactivity worth of the ejected control rod. Equation 3, with an effective neutron lifetime (Λ) of $20 \mu\text{s}$, is plotted for comparison. The agreement between Equation 3 and the results obtained with state-of-the-art methods is surprisingly good.

Figure 1. **Calculated pulse widths for HZP REA at EOC conditions, compiled from three-dimensional core kinetics analyses reported in [16,23-26,32]**
The adiabatic Nordheim-Fuchs model with $\Lambda = 20 \mu\text{s}$ is also included for comparison.

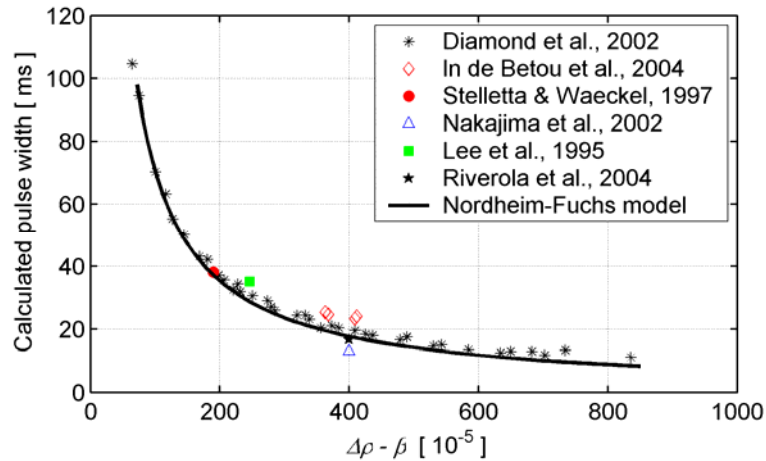


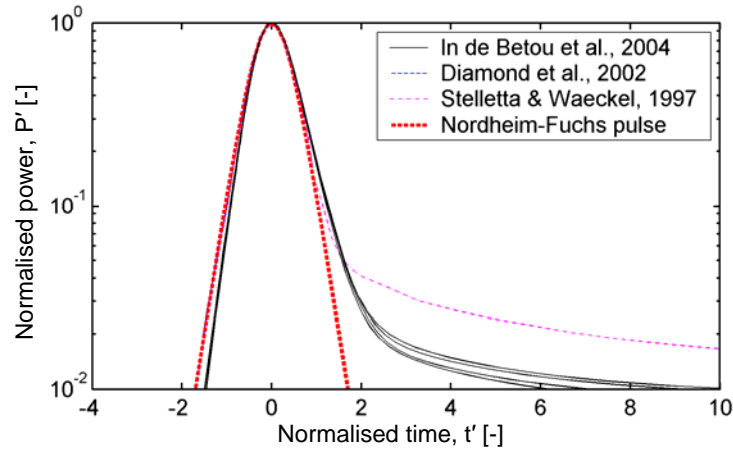
Figure 2 is a comparison of pulse shapes, obtained by use of state-of-the-art three-dimensional models in analyses of HZP REA at EOC. In order to allow a comparison of the calculated pulse shapes, each pulse in Figure 2 is normalised by use of the relations:

$$P' = \frac{P}{P_{\max}} \quad (5)$$

$$t' = \frac{t - t_{\max}}{\tau} \quad (6)$$

where P_{\max} , t_{\max} and τ have already been defined. The Nordheim-Fuchs pulse shape, defined by Equation (4) is also included in Figure 2 for comparison. Obviously, there is very little variation in the ascending flank among the calculated pulses, and all pulses from the three-dimensional analyses are close to the Nordheim-Fuchs pulse. However, the tails of the calculated pulses differ significantly, and they also depart from the Nordheim-Fuchs pulse shape. As a consequence of delayed neutrons, the power does not return to zero, but remains at about 1% of the peak value for a considerable period of time. It should be emphasised, that this power level is still significant with respect to energy deposition in the fuel. Eventually, the power returns to zero as more negative reactivity is added by moderator feedback effects and by the insertion of fault-free control rods due to reactor trip. This later phase is not shown in Figure 2.

Figure 2. Calculated pulse shapes for HZP REA at EOC conditions compiled from three-dimensional core kinetics analyses reported in [16,24,26]



In Figures 3 and 4, similar comparisons of calculated pulse widths and pulse shapes are given for CZP RDA. As before, the pulses were calculated for EOC conditions by use of state-of-the art three-dimensional core kinetics models. From Figure 3, we first note that the calculated pulses for CZP RDA are wider than those for HZP REA at comparable reactivity additions. This is partly due to the fairly slow rod ejection in the RDA, but also to the coarser core lattice for BWRs in comparison with PWRs, resulting in a longer effective neutron lifetime. Secondly, the trend in calculated pulse widths is not particularly well captured by the Nordheim-Fuchs relation in Equation 3, where an effective neutron lifetime, Λ , of 60 μ s has been used in this case.

The calculated pulse shapes for CZP RDA in Figure 4 are similar to those for the HZP REA in Figure 2, but the tails of the pulses are higher. Following the peak of the power pulse, the power remains at about 10% of its peak value, until negative reactivity feedback from the coolant temperature rise and void generation finally terminates the power excursion. The ascending flank of all calculated pulses is close to that of the Nordheim-Fuchs pulse, in similarity to the calculated pulses for HZP REA in Figure 2. Hence, it seems that the pulse shapes under HZP REA as well as CZP RDA can be fairly well described solely by the parameters P_{\max} , t_{\max} and τ , as long as we consider only the first part of the pulse. From Figures 2 and 4, we conclude that the calculated pulses, normalised with the above mentioned parameters, are practically identical for $t' < 1$, or by use of Equation 6, for $t < t_{\max} + \tau$. Up to this point in time, the pulse shape is controlled by the reactivity addition and the negative feedback from the fuel temperature rise. For $t \geq t_{\max} + \tau$, other feedback effects come into play, and the tail of the pulse therefore shows a much stronger case-to-case variation.

Figure 3. **Calculated pulse widths for CZP RDA at EOC conditions, compiled from three-dimensional core kinetics analyses reported in [18,24,32]**
The adiabatic Nordheim-Fuchs model with $\Lambda = 60 \mu\text{s}$ is also included for comparison.

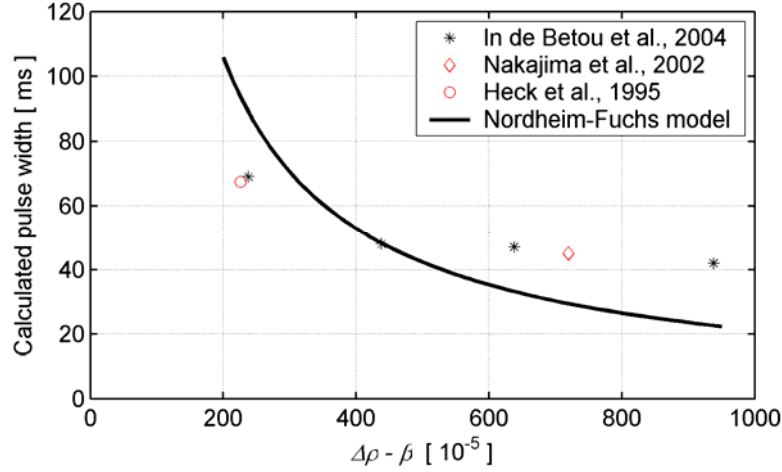
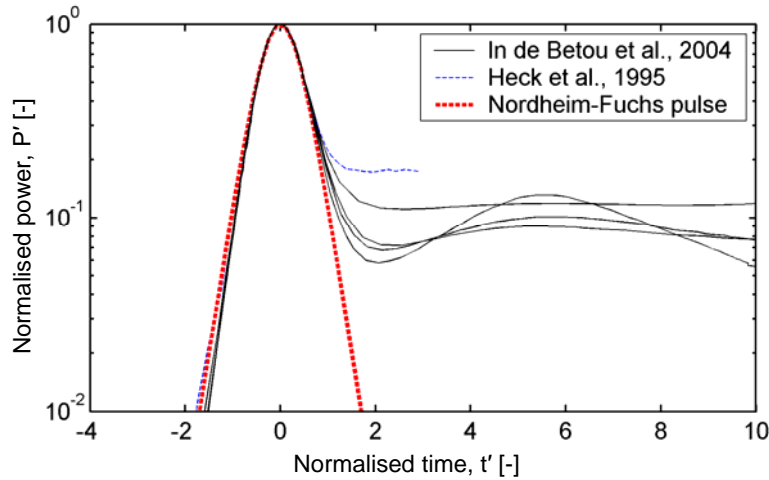


Figure 4. **Calculated pulse shapes for CZP RDA at EOC conditions, compiled from three-dimensional core kinetics analyses reported in [18,24]**



2.2.2 Pulse amplitude

Of the characteristic pulse parameters described above, τ and t_{max} do not vary significantly with position in the core under an REA or RDA. The pulse amplitude, P_{max} , is however a local property, which falls off with increasing distance from the ejected control rod, and it also depends on fuel burn-up. In short, the local power generation within a specific fuel pellet is controlled by a reactive component and a driven component. The reactive component reflects the reactivity of the considered fuel pellet itself, which depends on its burn-up dependent content of fissile isotopes (see Section 3.1.1). The driven component stems from the external neutron flux, which depends on the burn-up dependent composition of fissile isotopes in nearby fuel assemblies and the distance from the ejected control rod. Consequently, the local value for P_{max} depends on fuel burn-up, core loading pattern, the distance from the ejected control rod, and the reactivity worth of the ejected rod. The same is true for the local fuel enthalpy, as will be further discussed in connection with the core energy distribution under RIA (see Section 9).

The adiabatic Nordheim-Fuchs model, discussed in Section 2.2.1, gives a simple analytical approximation to the pulse amplitude (in units of watt per fuel mass):

$$P_{max} \approx -\frac{c_f (\Delta\rho - \beta)^2}{2\Lambda (\partial\rho/\partial T_f)} \quad (7)$$

Here, c_f is the specific heat capacity of the fuel material, and $\partial\rho/\partial T_f$ is the fuel temperature coefficient, as defined in Equation 2. These material properties are thus of fundamental importance to the pulse amplitude. The adiabatic Nordheim-Fuchs model also gives a simple approximation to the total energy deposition in the fuel under the power pulse:

$$E_{tot} \approx -\frac{2 c_f (\Delta\rho - \beta)}{\partial\rho/\partial T_f} \quad (8)$$

where E_{tot} is in units of joule per fuel mass. It should be noted that, while the prompt reactivity insertion, $\Delta\rho - \beta$, is quadratic in the expression for P_{max} in Equation 7, it is only linear in the expression for total energy deposition in Equation 8. Hence, the peak power increases more quickly with respect to reactivity insertion than the deposited energy. The reason is that if the reactivity addition is larger, the pulse is also terminated more quickly (see Equation 3).

For now, we will consider only the core-wide maximum of fuel enthalpy increase under RIA, i.e. the largest increase of fuel pellet radial average enthalpy that is experienced by any fuel pellet in the core. This is an important parameter for assessment of fuel integrity, and a key result in any analysis of RIA. Figure 5 shows a compilation of open-literature data on maximum fuel enthalpy increase, obtained from three-dimensional core kinetics analyses of HZP REA at EOC conditions. The data are plotted with respect to prompt reactivity insertion, $\Delta\rho - \beta$. For $\Delta\rho - \beta$ less than about 3×10^{-3} , the data are fairly consistent, and seem to follow a nearly linear trend with respect to the reactivity insertion. This trend is also what we expect from the approximate expression for the total energy deposition in equation (8). However, the fuel enthalpy increase is generally lower than the total deposited energy, since some heat transfer from the fuel to the cladding takes place during the accident. For $\Delta\rho - \beta$ beyond 3×10^{-3} , there is an increasing spread in the calculated results. This is probably due to the fact that the results are sensitive to the unrealistic assumptions for model parameters and input data that are needed to achieve these very high reactivity additions in three-dimensional core kinetics calculations.

The core-wide maxima of fuel enthalpy increase in Figure 5 are calculated at EOC conditions. The enthalpy increase under an REA at beginning-of-cycle (BOC) is usually somewhat higher than at EOC for a given $\Delta\rho - \beta$, since there are fresh fuel assemblies with high reactivity in the core. On the other hand, the fraction of delayed neutrons, β , is larger at BOC than at EOC, which means that for a given reactivity insertion $\Delta\rho$, the fuel enthalpy increase is usually larger in an REA at EOC than at BOC. Hence, the most challenging conditions with respect to pulse amplitude under REA are generally deemed to exist at EOC.

In scenarios for rod drop accidents in BWRs, one has to consider the effects of burnable absorbers, usually gadolinium mixed with UO_2 , that are frequently used in BWR fuel designs to reduce power peaking and reactivity in fresh fuel assemblies. The gadolinium isotopes ^{155}Gd and ^{157}Gd have large cross sections (probabilities) for absorption of thermal neutrons. During reactor operation, these isotopes are gradually consumed (burnt) by transmutation to ^{158}Gd , which has a much smaller cross section for neutron absorption [33]. At EOC, the exposure in once-burned fuel assemblies corresponds roughly to the burn-up at which all the neutron absorbing gadolinium has been consumed, and the assemblies are near their maximum reactivity. Hence, also for RDAs, the most challenging conditions with respect to pulse amplitude are usually found at EOC. Figure 6 summarises results on

maximum fuel enthalpy increase, calculated for CZP RDA at EOC conditions by use of three-dimensional state-of-the-art methods. Apparently, there is a nearly linear relationship between the core-wide maximum enthalpy increase and the prompt reactivity addition for this accident scenario. Moreover, for a given $\Delta\rho\text{-}\beta$, the maximum fuel enthalpy increase seems to be larger in CZP RDA than in HZP REA (see Figures 5 and 6).

Figure 5. Calculated maximum fuel enthalpy increase under HZP REA at EOC conditions, compiled from three-dimensional core kinetics analyses reported in [16-17,23-26,32,34]

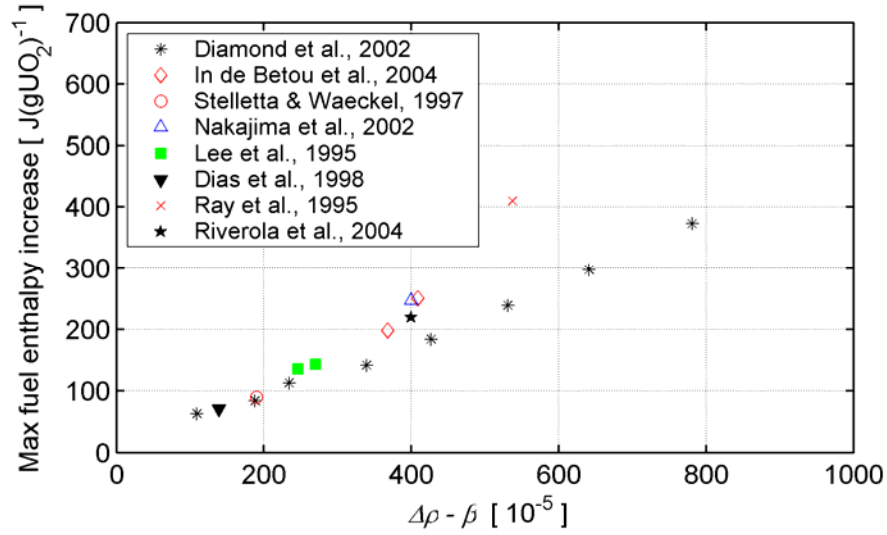
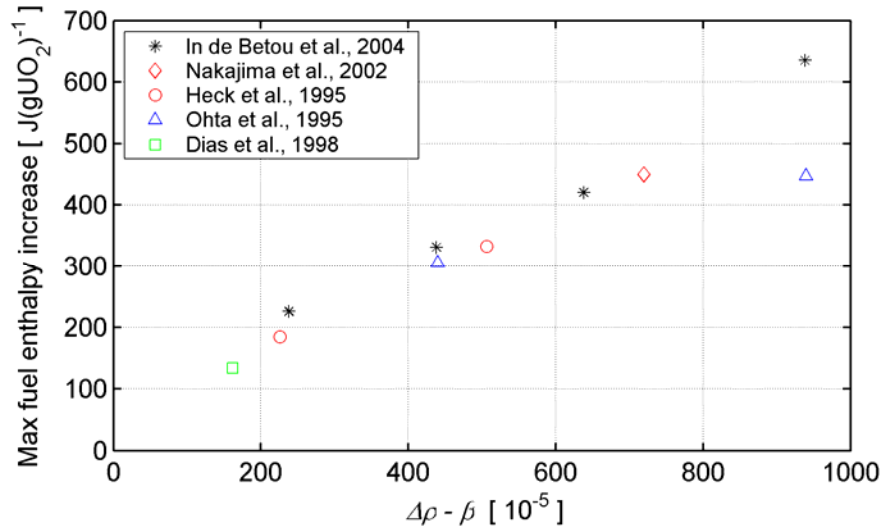


Figure 6. Calculated maximum fuel enthalpy increase under CZP RDA at EOC conditions, compiled from three-dimensional core kinetics analyses reported in [17,18,24,32,35]



3. STATE OF FUEL AND CLADDING AT VARIOUS BURN-UP LEVELS

The microstructure and chemistry of fuel and cladding changes gradually over the life of a nuclear fuel rod. Changes to the fuel pellets are due to transmutation of the material and radiation damage, whereas radiation damage in combination with waterside corrosion is responsible for the changes to the cladding tubes. With increasing burn-up, these mechanisms cause changes to the macroscopic material properties, which are usually detrimental to the fuel behaviour under RIAs. In the following sections, important burn-up effects on the fuel pellet, the cladding tube and the pellet-clad gap are discussed.

3.1 Fuel pellets

Most thermo-physical properties of the fuel pellets change as a result of in-reactor operation. Properties like fuel thermal conductivity and melting temperature decline notably with increasing exposure. Another effect of interest to the fuel behaviour under RIAs at high burn-up is the transmutation of fissile isotopes, which leads to a gradual change in neutronic behaviour and also to the generation and release of volatile gases. The transmutation does not occur uniformly in the fuel, and in uranium bearing fuel, there is an enhanced local buildup of fissile plutonium isotopes and fission products at the fuel pellet periphery. This phenomenon leads to a radial power distribution in high-burn-up fuel, which is strongly peaked to the pellet surface. It also leads to the formation of a porous microstructure at the pellet rim, which has the potential to affect fuel deformation behaviour and fission gas release at high burn-up.

3.1.1 Fuel pellet composition

The fuel pellet as-fabricated composition is important to the fuel behaviour in RIAs, and it also has an impact on how the fuel properties change with increasing burn-up. Here, we will consider UO_2 fuel, burnable absorber (BA) fuel, mixed oxide (MOX) fuel and inert matrix fuel (IMF).

In standard UO_2 fuel, the most important compositional parameter is the enrichment of ^{235}U . The enrichment affects the effective fraction of delayed neutrons, β , since the fissionable isotopes of U and Pu have different yields of delayed neutrons (see Table 2). In a light water reactor loaded with fresh UO_2 fuel, about 90% of the fissions take place in ^{235}U , and the remaining part in ^{238}U . The effective fraction of delayed neutrons is then about 0.0077. This number decreases with increasing burn-up, as ^{235}U is consumed and fissioning of plutonium isotopes becomes significant. The rate at which β declines with increasing burn-up depends inversely on the as-fabricated enrichment. The change in β influences the dynamic behaviour of the reactor under transients and perturbed conditions (see e.g. Section 2.2.1).

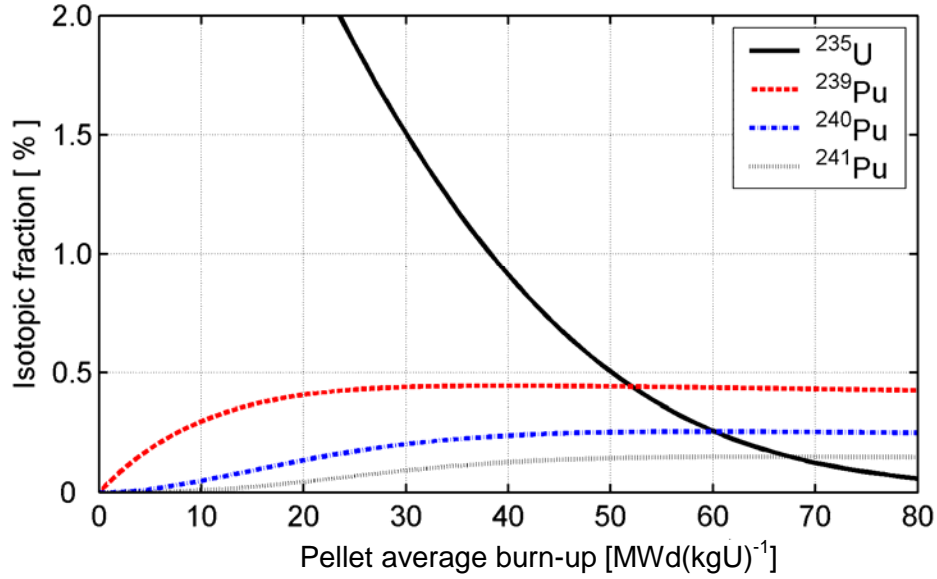
Another important property that changes with burn-up is the fuel temperature coefficient, $\partial\rho/\partial T_f$ in Equation 2. This coefficient increases (becomes less negative) with increasing burn-up, since production of ^{239}Pu in the fuel during irradiation gives a positive contribution. However, as shown in Figure 7, the concentration of ^{239}Pu saturates at a pellet average burn-up of about $40 \text{ MWd}(\text{kgU})^{-1}$ in LWR fuel, and hence, $\partial\rho/\partial T_f$ does not change significantly beyond this burn-up [36].

Table 2. Fraction of delayed neutrons, β , emitted in fissioning of isotopes relevant to nuclear fuel [14]

Isotope			
^{235}U	^{238}U	^{239}Pu	^{241}Pu
0.0067	0.0164	0.0022	0.0054

The data are for fissioning by thermal neutrons, except for ^{238}U .
Only fissioning by fast neutrons is relevant for that particular isotope.

Figure 7. Change in fuel pellet average isotopic composition with burn-up, calculated with the TUBRNP model [37]



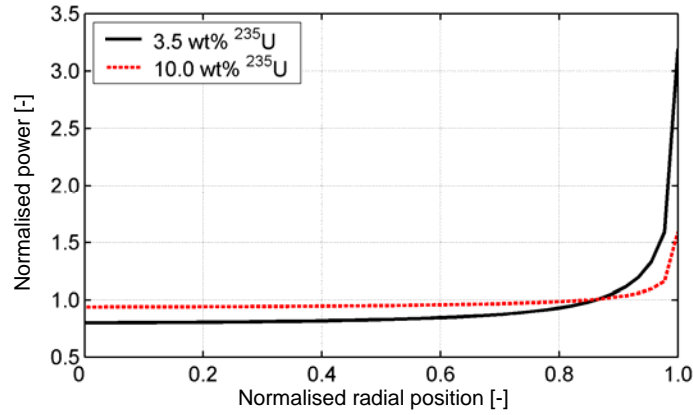
A 96% theoretically dense UO_2 fuel pellet with radius 4.1 mm and an initial ^{235}U enrichment of 4.5 wt% was assumed in the calculations.

The enrichment of ^{235}U also affects the fuel reactivity, which determines the amplitude of the power pulse experienced by the fuel under an RIA. A high enrichment of ^{235}U increases the energy deposition in the fuel pellets. Moreover, the enrichment also affects the radial distribution of power and thereby the radial temperature profile in the fuel pellets during the accident (see Section 4.2). The temperature profile, in turn, affects the pellet deformation behaviour and fission gas release.

The enrichment of ^{235}U in commercial LWR fuel is typically in the range 2.5 – 5.0% by weight, and the fuel rod behaviour under RIA is not significantly affected by variations in fuel enrichment within this narrow range. However, as shown in Section 5.1, many RIA simulation tests have been performed on fuel enriched to 10 and even 20 wt% ^{235}U , and one should not expect the behaviour of this fuel to be representative of commercial LWR fuel with significantly lower enrichment. This is particularly true for high-burn-up fuel, in which the shape of the radial power profile is strongly affected by the initial ^{235}U enrichment. This is illustrated in Figure 8, which shows the radial power profile at a pellet radial average burn-up of 60 MWd(kgU)^{-1} for two fuel pellets with different initial enrichments.⁶ The profiles are calculated with the TUBRNP model by Lassmann *et al.* [37]. As shown in Section 3.1.2, the radial temperature profile in the pellet agrees very closely to the power profile during the initial heat-up phase of an RIA.

6. It should be remarked that, for fresh and low-burn-up fuel, the relation is opposite to that shown in the figure. Hence, in fresh fuel, the power profile is more uniform for the lower enrichment.

Figure 8. **Influence of initial ^{235}U enrichment on radial power distribution in high-burn-up fuel pellets of UO_2**



The fuel pellet radius is 4.5 mm and the radial average burn-up is $60 \text{ MWd}(\text{kgU})^{-1}$ in both cases shown.

Fuel additives in the form of Al_2O_3 and SiO_2 , which are known to “soften” UO_2 and thereby reduce cladding stresses induced by pellet-cladding mechanical interaction under normal fuel operation, have proven ineffective under RIA [38]. This is hardly surprising, since the beneficial effect of these additives is due to enhanced UO_2 fuel creep, whereas the time scale of a typical RIA is too short for any noticeable creep deformation to take place in the material.

Burnable absorber fuel, which usually contains 3-8 wt% Gd_2O_3 , has a radial power distribution at low burn-up that is much distorted from that in pure UO_2 fuel. However, the neutron-absorbing isotopes of gadolinium are generally consumed during the first reactor cycle, and the distortion in radial distribution of power and burn-up later in life is fairly weak. Addition of Gd_2O_3 to UO_2 also lowers the fuel thermal conductivity, although the depression seems moderate at temperatures above 1 500 K [39]. Little is known about the effect of gadolinium on fuel melting point, but the data at hand show no noticeable difference between pure UO_2 and fuel with up to 2 wt% Gd_2O_3 [40]. Pulse reactor tests on fresh fuel rods with Gd_2O_3 additions were done in the 1980s [41]. The tests were carried out with high energy injections, leading to fuel rod failure by local melting of the clad tube at fuel enthalpies between 1 110 and 1 150 $\text{J}(\text{gUO}_2)^{-1}$. The observed failure threshold and failure behaviour were not notably different from those of fresh UO_2 fuel rods. To our best knowledge, no pulse reactor tests have yet been performed on pre-irradiated BA fuel rods.

Mixed oxide fuel is used in many LWRs. The fissile material in MOX fuel is mostly the plutonium isotopes ^{239}Pu and ^{241}Pu , and the fuel pellets are usually produced by mixing plutonium oxide powder into natural (non-enriched) uranium oxide powder, followed by pelletizing and sintering. Since plutonium isotopes have a lower yield of delayed neutrons than ^{235}U , the effective fraction of delayed neutrons is lower for MOX than for UO_2 fuel (see Table 2). More importantly, prevalent manufacturing processes for MOX fuel create a heterogeneous material, with plutonium oxide (PuO_2) agglomerates embedded in a matrix of natural UO_2 [42]. Since fissions occur predominantly in the agglomerates, they may reach very high local burn-up, although the volume average burn-up is moderate [43]. At high burn-up, the heterogeneous distribution of power, burn-up and retained gaseous fission products in MOX fuel lead to higher fission gas release and fission gas induced swelling than for UO_2 fuel under comparable RIA transients [44-45]. For this reason, high-burn-up MOX fuel rods are usually deemed to be more susceptible to failure under RIA than UO_2 fuel rods (see Sections 6.1.2 and 6.1.3).

Inert matrix fuel contains fissile plutonium embedded in a uranium-free (inert) matrix, which allows Pu to burn without breeding new plutonium through resonance capture of epithermal neutrons

by ^{238}U . The use of IMF in light water reactors is therefore a possible way for final disposal of the increasing stockpile of plutonium. The inert matrix is usually yttria-stabilised zirconia, which is a rock-like material, and the fuel is also alluded to as rock-like oxide (ROX) fuel.

The absence of ^{238}U in inert matrix fuel leads to a very small negative reactivity feedback from increase in fuel temperature, since ^{238}U provides the most significant contribution to this effect [36]. As discussed in Section 2, the fuel temperature feedback is important to terminate the power surge under RIA, and the weak Doppler feedback in IMF is therefore a disadvantage. In addition, the melting temperature and other thermo-physical properties of IMF are different from those of uranium-bearing fuel, and the behaviour of IMF under normal operating conditions as well as RIAs is not comparable to that of UO_2 or MOX fuels [46-47]. The behaviour of un-irradiated inert matrix fuel under RIA has been studied in pulse reactor tests [48-49].

3.1.2 Radial distribution of burn-up and power

As UO_2 nuclear fuel is taken into operation, there is a successive change not only in the fuel average isotopic composition, but also in the radial distribution of fissile material, power and fission products within the fuel pellets. In fresh UO_2 fuel, the fissile material consists predominantly of ^{235}U , which is usually uniformly distributed in the fuel pellets. Hence, both power and fission products are generated with a relatively small variation along the fuel pellet radius. However, with increasing burn-up, there is a non-uniform build-up of fissile plutonium isotopes through resonance capture of epithermal neutrons by ^{238}U and subsequent β -decays into ^{239}Pu and heavier fissile isotopes of plutonium [14]. Since the neutron capture takes place mainly at the pellet surface, the distributions of fissile material, fission rate and fission products will develop marked peaks at the pellet surface as fuel burn-up increases. The shapes of these distributions are dependent not only on irradiation time, but also on the fuel initial content of ^{235}U , pellet radius and the neutron energy spectrum of the reactor. This was illustrated in Figure 8 (Section 3.1.1).

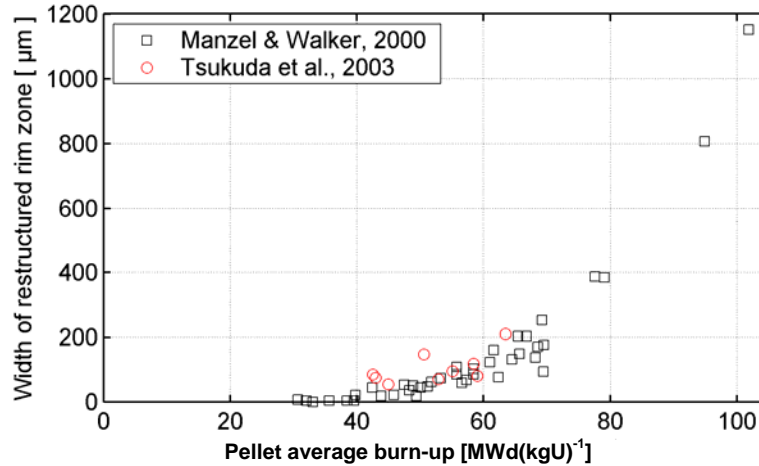
3.1.3 Microstructure – high burn-up restructuring

As a consequence of accumulated fission products, enhanced local burn-up and fission rate in combination with low temperature, a restructuring of the fuel material takes place at the pellet peripheral rim in high-burn-up fuel. The restructuring is characterised by a simultaneous reduction in grain size, increase in porosity and depletion of fission gas from the UO_2 matrix [50-51]. The resulting microstructure is usually referred to as the “rim zone structure”, which is somewhat misleading, since the microstructure is related to enhanced local burn-up and fission rate in combination with low temperature at the pellet rim, rather than to the radial position in itself. Consequently, we will use the term ‘high burn-up structure’, as proposed by Lassmann *et al.* [52], to denote the restructured part of the fuel material.

There is ample experimental evidence [53] that the high burn-up structure starts to form at a *local* burn-up of $60\text{-}70 \text{ MWd}(\text{kgU})^{-1}$ by subdivision of grains at the fuel pellet outer surface and at pores and bubbles close to the surface. At conditions typical of LWR fuel, the pellet *radial average* burn-up is about $45 \text{ MWd}(\text{kgU})^{-1}$ when this restructuring starts at the pellet rim. However, these numbers are approximate. Distinct thresholds cannot be defined, since the fuel restructuring is a gradual process, and restructured grains may co-exist with original, untransformed grains up to a local burn-up of $120 \text{ MWd}(\text{kgU})^{-1}$. The burn-up threshold for restructuring is also influenced by the original grain size of the material, and large-grain UO_2 materials have markedly higher resistance to restructuring than small-grained materials [54]. The progression of the re-structuring process, i.e. the inward propagation of the restructured zone towards the pellet centre, is controlled by the radial distributions of both fissile material and temperature. In commercial LWR fuel, the radial width of the restructured zone at the pellet rim is usually less than $200 \mu\text{m}$, which means that it constitutes less than 10% of the total fuel volume. However, as shown in Figure 9, the restructured zone may extend much deeper, if the

pellet radial average burn-up increases beyond $70 \text{ MWd}(\text{kgU})^{-1}$, which is a typical peak pellet radial average burn-up reached today in LWRs.

Figure 9. Width of restructured zone (“rim zone”) in UO_2 fuel pellets of commercial PWR fuel rods, determined by optical microscopy [57-58]



An important aspect of the fuel restructuring with respect to fuel behaviour under RIAs is the transfer of fission gas from nanometre-sized intragranular bubbles to micron-sized pores [55]. Spino *et al.* [51] reported that the micron-sized pores form early in the restructuring process, and that the pores are surrounded by a shell with recrystallised material that grows thicker as the restructuring proceeds. They also reported that the mean pore size remains constant, whereas the pore number density increases as the restructuring process proceeds. In fully restructured material, the porosity may reach 20 vol% and higher, but it is considerably lower in fuel that experiences mechanical restraint from pellet-clad mechanical interaction. Hence, rim zone porosity above 10 vol% is rarely observed in fuel subjected to PCMI. This is clear from Figure 10, which shows data on the porosity of restructured UO_2 fuel, compiled from eight different experimental investigations by Une *et al.* [54,56]. There is a distinct difference between fuel samples irradiated to high burn-up without mechanical constraints, and samples taken from high-burn-up fuel rods, in which the fuel pellets have been subjected to a restraining mechanical pressure from PCMI. The spread in measured porosities in Figure 10 is due to the fact that the fuel as-fabricated porosity ranged from 2 to 5 vol% in the eight considered studies. Moreover, the porosity of the restructured material was measured by different methods for quantitative image analysis, and the samples were irradiated at various fission rates and temperatures [54,56].

Under normal reactor operation, the fuel temperature in the rim zone is generally below 800 K, and the highly porous material is mechanically stable. However, under the initial phase of an RIA, the temperature profile is peaked to the pellet rim (Section 4.2). The mechanical stability of the material may then be lost, either through fragmentation or by fission gas induced swelling (Section 6.1.1).

3.1.4 Solidus temperature

The melting (solidus)⁷ temperature of fresh UO_2 fuel is $3120 \pm 30 \text{ K}$; see the review of data in [59]. Build-up of fission products in the fuel material leads to a depression of the melting temperature with increasing burn-up. Experimental data from the 1960s, e.g. the work of Christensen *et al.* [60],

7. When heated, the material changes gradually from being totally solid to being totally liquid over an extended temperature range. The lower and upper temperatures of this range are called solidus and liquidus, respectively.

showed that the depression was significant. More recent data show that the depression is much weaker, and early data on the melting temperature of irradiated UO_2 are today considered to be misleading, due to inadequate experimental techniques, see e.g. the work by Adamson *et al.* [61], and the reviews in [59,62,63]. However, it is difficult to completely rule out the early works, since contemporary investigations on nuclear fuel melting are focused on $(\text{U,Pu})\text{O}_2$ mixed oxide fuel rather than UO_2 . In these investigations, melting temperatures are usually measured on a series of irradiated fuel materials with various Pu/U fractions, and the melting temperature of pure UO_2 is determined by extrapolating the results to zero plutonium content. Direct measurements on irradiated UO_2 fuel with accurate experimental methods are rare, but some experimental data of this kind are presented by Komatsu *et al.* [64]. In their work, a correlation for the burn-up dependent melting temperature of UO_2 and $(\text{U,Pu})\text{O}_2$ is also given. The correlation is used in Figure 11 to illustrate the radial variation in fuel melting temperature in a high-burn-up fuel pellet. The calculated melting point is slightly below 3 000 K at the pellet rim, i.e. about 100 K lower than in fresh UO_2 .

Figure 10. **Influence of restraining pressure from PCMI on the build-up of porosity in the high burn-up microstructure of UO_2 fuel. Experimental data from eight studies [54,56]**

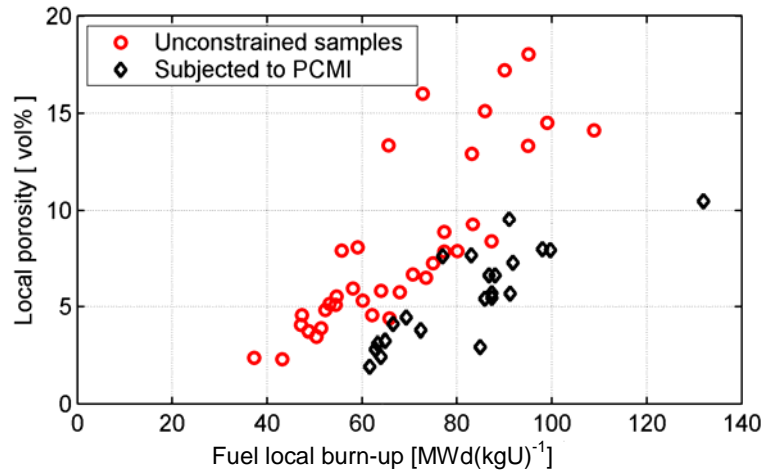
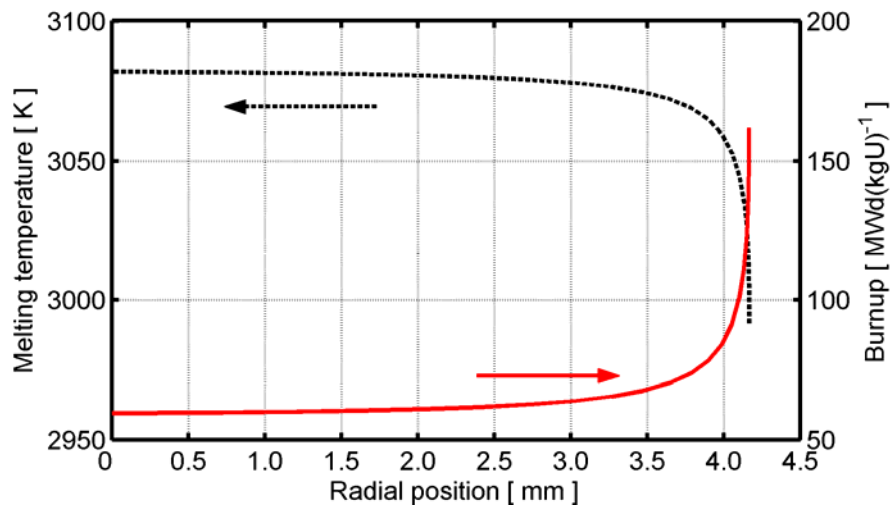


Figure 11. **Calculated variation in fuel melting temperature and burn-up across the pellet radius in a typical PWR fuel rod**



In the example, the pellet radial average burn-up is 68 MWd(kgU)^{-1} and the as-fabricated enrichment of ^{235}U is 3.8%. The melting temperature is calculated through the correlation by Komatsu *et al.* [64], based on a burn-up distribution calculated with the TUBRNP model [37].

3.1.5 Thermal conductivity

An important aspect of high fuel burn-up and the formation of a high burn-up microstructure is the degradation of fuel thermal conductivity. The degradation is primarily caused by an increased resistance to phonon heat transport, as radiation damage and fission products accumulate in the crystal lattice [65]. Theoretical models for thermal conductivity of solids, by which the effects of porosity, grain size and lattice defects can be evaluated, indicate that the thermal conductivity should decrease in the restructured fuel material as a consequence of grain subdivision and increased porosity [66]. However, recent laser flash measurements of thermal conductivity in high burn-up UO_2 fuel show that the restructuring has a negligible effect on thermal conductivity [67]. It seems that the negative effects of grain subdivision and increased porosity on thermal conductivity are compensated by elimination of lattice damage and nanometre-sized fission gas bubbles from the restructured material.

The thermal conductivity degradation in high-burn-up fuel hinders the radial heat transfer, and leads to an undesired increase in fuel temperature under steady-state reactor operation. The effects of fuel thermal conductivity degradation on fuel rod behaviour under RIA are largely unknown. However, from tests performed in the NSRR, it is known that the occurrence of boiling crises at the clad-to-coolant interface is affected by changes in heat transfer properties of the fuel rod [68]. A boiling crisis, or burnout, is a transition from efficient clad-to-coolant heat transfer to a regime with film-boiling and impaired heat transfer at a certain critical heat flux [69]. The transition is termed departure from nucleate boiling (DNB) when the coolant is a single phase liquid (PWRs), and dry-out when the coolant comprises both liquid and steam (BWRs) [70]. It has been found that boiling crises are suppressed or delayed, when radial heat transfer is hindered by e.g. a large pellet-clad gap or a thick layer of oxide at the cladding surface (see Section 5.2.2). Although direct experimental evidence on this subject is lacking, the degradation of fuel thermal conductivity may have a similar effect on the occurrence of boiling crises.

3.1.6 Fission gas release

Gaseous fission products are inevitably released from the fuel pellets, when the fuel is operated with long residence times in the core. The noble gases xenon and krypton are generated during fission of uranium and plutonium isotopes, and a fraction of these gaseous fission products is released into the free volume of the fuel rod, thereby increasing the internal fuel rod gas pressure. In addition, the released gas degrades the thermal conductance of the gas in the gap, causing higher fuel temperature. Fission gas release is generally considered to be a potentially life-limiting (burn-up-limiting) factor, because of its consequences to fuel rod pressure build-up and clad tube integrity. The fuel rod internal gas pressure is also important to fuel rod survivability in the event of reactivity-initiated accidents (see Section 6.2.5.2). Here, we will consider long-term fission gas release under normal fuel operation. Transient fission gas release under RIAs is treated in Section 6.1.3.

Several physical processes contribute to the long-term fission gas release (FGR) from UO_2 under steady-state operation. The processes are usually divided into thermal and athermal release mechanisms [71]. The former are driven by highly temperature dependent processes and have potential for large release fractions. These processes include gas diffusion to grain boundaries, grain growth, grain boundary saturation and release. Athermal release takes place by recoil and knockout of fission gas atoms by energetic fission fragments. Since these mechanisms generally result in release of less than 1% of the fission gas produced within the fuel pellets, athermal release alone is generally not considered a potential problem for excessive fuel rod pressure build-up with the discharge burn-ups reached today in LWRs. Yet, the fuel restructuring described in Section 3.1.3 has potential to significantly enhance the athermal fission gas release fraction at high fuel burn-up.

Some investigators have proposed that the enhancement of athermal fission gas release at high burn-up occurs as a direct and immediate consequence of the fuel restructuring [72]. However, studies of restructured fuel material with X-ray fluorescence (XRF) and secondary ion mass spectrometry (SIMS) techniques have revealed that no appreciable fission gas release occurs as a direct result of restructuring [73-74]. The same conclusion has also been drawn from measurements on the fission gas content of restructured UO₂ fuel samples by use of high-temperature annealing [67].

Other investigators have argued that the enhanced athermal gas release is an indirect effect of the restructuring. For instance, it has been suggested that the usual athermal mechanisms for fission gas release, recoil and knockout, are enhanced by an increase in the specific surface (S/V) of the porous restructured material [75]. This hypothesis seems plausible, but according to several experimental observations, the rim zone porosity is not interconnected, and should therefore not significantly increase the fuel specific surface [51,76]. An alternative hypothesis to the increased fission gas release rate from the restructured material is due to Lassmann et al [77], who recognised that irradiation enhanced athermal diffusion from the interior of the small restructured grains to the grain boundaries is sufficiently fast to explain the observed matrix depletion of gas, and that the same mechanism could possibly contribute to enhanced fission gas release from the pellet rim zone. Hence, there is currently no general consensus on how the enhanced fission gas release from the high-burn-up structure occurs.

3.2 Cladding tubes

Changes to the cladding properties with increasing burn-up result mainly from radiation damage and waterside corrosion, i.e. oxidation and hydrogen pickup. These phenomena, which have a detrimental effect on clad ductility, are briefly described below.

3.2.1 Radiation damage

Radiation damage in zirconium alloy cladding tubes is caused mainly by incident neutrons with high energy, which cause microstructural damage to the material through knockout and recoil processes [78-79]. The neutron energy, E_n , is up to several hundreds of MeV, and the resulting material damage is in the form of point defects, small dislocations loops, short line dislocations and dislocation entanglements. These defects raise the yield strength and reduce the ductility of zirconium alloys by hindering dislocation movements, which is the mechanism responsible for plastic deformation and creep in metals. In irradiated cladding, plastic deformation does not take place uniformly in the material, but the dislocation movements are confined to small regions. This localisation phenomenon, known as dislocation channelling, has been identified as a likely promoter of axial (longitudinal) crack propagation in irradiated cladding [80].

Irradiation-induced loss of ductility is observable at fairly low neutron fluences: for material irradiated at 600 K, typically at 10^{24} m^{-2} ($E_n \geq 1 \text{ MeV}$), and the embrittlement generally saturates already under the first reactor cycle of fuel operation. In the absence of other embrittling phenomena, such as hydride precipitation, zirconium alloys seem to reach a ductility minimum at a fast neutron fluence of about $2\text{-}3 \times 10^{25} \text{ m}^{-2}$, which corresponds to a rod burn-up of about $10 \text{ MWd}(\text{kgU})^{-1}$ and a lattice damage of about 5-7 dpa (displacements per atom) [80]. Further loss of clad ductility beyond this neutron fluence is thus due to embrittling phenomena other than pure radiation damage. If the material is held at elevated temperature, the microstructural defects responsible for irradiation embrittlement are annealed, and some of the ductility thus recovered. The annealing of radiation damage is a time and temperature dependent process, which is comparatively fast: experiments have shown that significant annealing takes place in less than 15 s at a clad temperature of 823 K [81]. Thermal annealing of radiation damage may therefore occur under an RIA, if the cladding is held at elevated temperature as a result of a boiling crisis. Temperature excursions experienced by the cladding tubes under RIAs are discussed in Section 6.2.1.

Irradiation may also induce microchemical changes to the material. For instance, irradiation induced dissolution and dispersal of intermetallic precipitates can change the corrosion behaviour of cladding materials [82].

3.2.2 Waterside corrosion

Waterside corrosion of the cladding tubes has a twofold impact on the performance of LWR fuel. Firstly, the thermal and mechanical behaviour of the cladding tubes is directly affected by the formation of an external oxide (ZrO_2) layer at the metal-water interface. Secondly, the metal-water reactions liberate oxygen and hydrogen, part of which diffuse into the metal phase and cause gradual embrittlement of the material.

The clad corrosion rate depends on alloy composition and thermomechanical treatment under manufacturing, accumulated neutron dose, coolant temperature and chemistry, and the clad-to-coolant heat flux [83]. The higher coolant temperatures in PWRs in comparison with BWRs aggravate clad corrosion, and the potential for degradation of the clad strength and ductility by oxidation and hydrogen pickup is therefore larger in PWRs than in BWRs. Another important difference between PWRs and BWRs is that the coolant temperature in the former rises with axial elevation in the core. The clad embrittlement due to corrosion is therefore more pronounced in the upper part of PWR fuel rods [84].

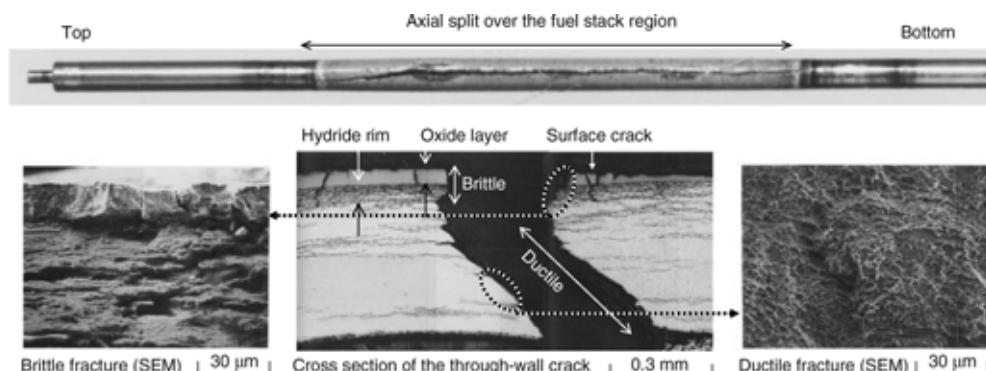
3.2.2.1 Direct effects of clad oxide layer

Due to its poor thermal conductivity ($\approx 2 \text{ W(mK)}^{-1}$), the external oxide layer affects the clad and fuel temperature. Under steady-state fuel operation with a typical linear heat generation rate of 20 kWm^{-1} , the clad temperature increases by approximately 0.3 K per micrometer external oxide. Hence, if spallation of a 100 μm thick oxide layer takes place, there can be temperature differences of up to 30 K between spalled regions and regions still covered with oxide. These local cold spots in clad tubes with spalled oxide have a strong effect on migration of hydrogen and precipitation of hydrides under steady-state reactor operation, as discussed in Section 6.2.6.3.

Moreover, the oxide layer affects the clad tube mechanical behaviour under accident conditions. Variations in oxide layer thickness along the circumferential as well as the longitudinal direction of the cladding tube promote localised plastic deformation under RIA. From post-test examinations of fuel rods subjected to pulse reactor tests, it has been reported that transient plastic deformation of the cladding occurs preferentially at regions with thicker oxide [85-86]. This effect can be understood from the local reduction in the load-bearing clad wall thickness, in combination with the local reduction in yield stress that results from a slightly higher temperature at regions with thicker oxide.

Another important localisation effect is due to cracks in the oxide layer. When a corroded cladding tube is subjected to a tensile stress in its hoop (circumferential) direction, radial cracks initiate through the entire thickness of the oxide layer, as shown in Figure 12. Since the oxide is brittle, the cracks form readily under plastic deformation of the metal beneath the oxide. Once the oxide cracks have formed, they may act as initiation sites for further crack propagation through the subjacent hydride-rich metal. Unless the oxide layer de-laminates from the underlying material and flakes off, the sharp oxide cracks lead to significant concentration of stress and strain to the crack tip region, and further ductile crack propagation can therefore take place through the metal with very limited observable plastic deformation at the macroscopic scale. Hence, clad tubes with an external oxide layer and/or a distinct outer rim with densely hydride material may exhibit macroscopically brittle behaviour, although the material closer to the cladding inner surface may be fairly ductile [87-90]. Since the stress concentration rises with increasing crack length, the localisation effect increases with growing thickness of the oxide layer and hydride rim [91]. The same localisation effect has also been observed for hydride blisters in the cladding [92-93].

Figure 12. **Radial cracks through the cladding oxide layer and subjacent hydride rim act as stress- and strain localisation sites**



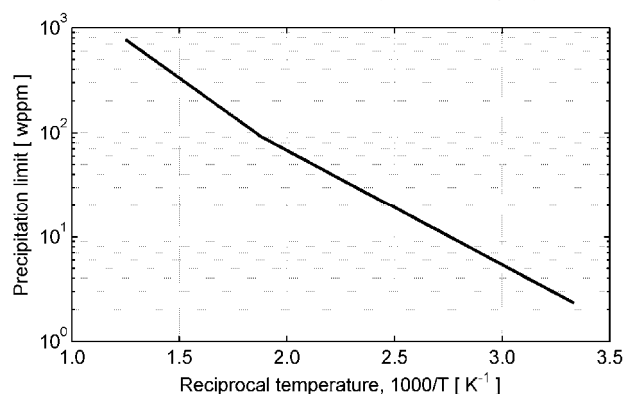
Photograph of the PWR fuel rod HBO-5, tested in the NSRR [91] (see Section A.5 in Appendix A). Picture reproduced from [91] with permission of the AESJ (CY-RT-002).

Finally, separate effect tests as well as pulse reactor tests on high-burn-up fuel rods show that clad-to-coolant heat transfer is affected by the clad oxide layer not only under steady-state conditions, but also under the RIAs [68,94]. In particular, it seems that transition to film-boiling is suppressed or delayed by oxidized cladding in comparison with un-oxidized or spalled cladding. To this end, it should be noticed that excessive *transient* spallation of the oxide has been observed in pulse reactor tests on highly corroded fuel rods in the CABRI facility [85,95]. This phenomenon, which will be further discussed in Section 6.2.4, may introduce debris into the coolant channels in a very short time under an RIA. The consequences of transient oxide spallation to global core coolability are unknown, but the local effects on clad-to-coolant heat transfer are significant.

3.2.2.2 Effects of hydrogen

Hydrogen is produced in the metal-water reaction at the clad outer surface, i.e. the reaction $\text{Zr} + 2\text{H}_2\text{O} \rightarrow \text{ZrO}_2 + 2\text{H}_2$. Depending on alloy composition and heat treatment under manufacturing of the material, 5-25% of this hydrogen enters the metal, and as the oxidation proceeds, it will precipitate as zirconium hydrides. The precipitation takes place when the hydrogen concentration exceeds the terminal solid solubility for hydrogen in the material. The solubility of hydrogen in zirconium base materials depends strongly on temperature, and to a lesser extent on alloy composition, irradiation effects and stress state. Figure 13 shows the terminal solid solubility of hydrogen versus temperature, as determined in hydride precipitation experiments on Zircaloy cladding.

Figure 13. **Hydrogen solubility versus reciprocal temperature, determined from experiments on hydride precipitation in un-irradiated Zircaloy cladding by Une and Ishimoto [97]**



As long as the hydrogen is dissolved in the metal, it has only a minor embrittling effect on zirconium-base alloys. In un-irradiated cladding, significant degradation of strength and ductility is thus only observed in materials with precipitated hydrides [96]. In contrast to the irradiation-induced embrittlement described in Section 3.2.1, the degradation due to hydriding does not saturate.

Hydrogen dissolved in the metal migrates by thermo-diffusion towards cold regions of the cladding, and will thus accumulate close to the comparatively cold outer surface of the clad tube [98]. When the local hydrogen concentration exceeds the terminal solid solubility, zirconium hydrides precipitate. In cladding tubes subjected to normal reactor operating conditions, the precipitates are platelet-shaped, with a thickness of a few microns [99]. These hydrides have a face-centred cubic (fcc) crystallographic structure, termed δ -phase, and a non-stoichiometric composition that range from $\text{ZrH}_{1.5}$ to $\text{ZrH}_{1.67}$. The zirconium δ -hydride is brittle, and it embrittles the cladding as it precipitates in the metal. The degree of embrittlement depends on the amount of hydrogen in excess of the solubility limit, as well as on size, orientation and distribution of the hydrides. Hydride-induced embrittlement is a complex matter, and several mechanisms come into play, depending on the hydride concentration, temperature, irradiation dose and stress state in the material. A separate subsection of the report (6.2.6) is devoted to these mechanisms.

3.2.2.3 Effects of oxygen

Oxygen is an alloying element in zirconium alloys, which is added in quantities up to 1 200 wppm in order to increase the material strength. At concentrations above about 1 800 wppm, oxygen has a detrimental effect on ductility and fracture toughness, especially in irradiated materials [100]. Some investigators, e.g. Chung and Kassner [101], have stated that the clad oxygen concentration increases with fuel rod burn-up under normal reactor operation, due to long-term diffusion of oxygen from the oxide-metal interface into the subjacent metal. Hence, in cladding tubes of high-burn-up fuel rods, the material directly beneath the oxide layer is expected to have reduced ductility and fracture toughness due to the locally dissolved oxygen. However, the possibility of oxygen thermal diffusion under normal cladding operating temperatures seems unlikely and is certainly a matter of dispute. The phenomenon is poorly investigated, and the detrimental effects of oxygen under normal reactor operation are usually neglected in comparison with the effects of hydrogen.

Cladding embrittlement as a result of high-temperature oxidation under accident conditions, such as LOCA, are much more important and therefore better studied. Excessive high-temperature oxidation of zirconium base cladding materials, in combination with rapid high-temperature diffusion of oxygen into the metal, may lead to complete loss of ductility and failure of the cladding, when it is cooled to normal temperature after a high-temperature excursion. Cladding high-temperature oxidation and oxygen-induced embrittlement are further discussed in Section 6.2.3.

3.3 Pellet-clad gap

3.3.1 Gap gas composition and pressure

Light water reactor fuel rods are manufactured with pure helium as a high thermal conductivity fill gas in the pellet-clad gap and fuel rod plena. The helium gas is usually filled to a pressure of 0.2-0.8 MPa (BWR) or 1-3 MPa (PWR) at room temperature. The internal gas pressure is chosen such that it partially balances the outside coolant pressure, when the fuel rod is operated at nominal power. Under operation, the gas composition and pressure change as a result of fission gas release from the fuel pellets. The released gases, notably xenon and krypton, degrade the thermal conductance of the gas within the pellet-clad gap. This degradation has little effect on pellet-clad heat transfer when the pellet and cladding are in mechanical contact, e.g. under the early phase of an RIA in high-burn-up fuel. However, if the RIA leads to high cladding temperatures as a result of a boiling crisis, and the rod gas pressure exceeds the coolant

pressure, the pellet-clad gap may open as a result of high-temperature cladding deformation. In this case, the burn-up-dependent composition and pressure of the gap gas are important to the fuel rod behaviour, and in particular, to the risk for clad tube ballooning and subsequent ductile failure. High-temperature cladding failure following boiling crises is further discussed in Section 6.2.5.2.

It may also be conjectured that the build-up of fuel rod gas pressure with increasing burn-up would promote dispersal of fuel fragments into the coolant, should the cladding fail. It is known from RIA simulation tests in the NSRR that high initial gas pressures promote fuel dispersal and aggravate fuel-coolant thermal interaction [102]. This is further discussed in Section 4.3.1.

3.3.2 Pellet-clad contact and bonding

The most severe scenarios for RIA in light water reactors take place at zero or very low fuel rod power. For these scenarios, there will be a certain radial gap between pellet and cladding at onset of the transient, and only the fuel expansion occurring after closure of this gap need be accommodated by expansion of the cladding tube. Consequently, the PCMI-induced loading under HZP or CZP RIA depends on pre-transient gap size, which in turn depends on the as-fabricated gap size, fuel swelling and clad creep-down. The latter phenomena depend on fuel rod design, reactor operating conditions and fuel residence time in the reactor, which means that the pre-transient gap size varies with burn-up.

At high burn-up, however, the gap is closed and the pellet-clad contact state tends to an equilibrium under steady-state operation, i.e. to a balance between fuel swelling and clad creep. This means that the pellet-clad contact state in high-burn-up fuel rods is largely unaffected by burn-up. In a high-burn-up fuel rod, the zero power gap size is therefore controlled predominantly by the difference in thermal contraction of fuel and cladding under reactor shutdown. Hence, the degree of PCMI under a CZP or HZP reactivity accident in high-burn-up fuel depends on the fuel power before reactor shutdown; a low final power leads to a more severe PCMI under the RIA.

Pellet clad bonding is a prominent phenomenon in high-burn-up fuel, with potential to aggravate the clad loading conditions under power excursions. In-reactor experiments have shown that the static coefficient of friction between pellet and cladding increases significantly with the dwell time in contact [103], meaning that the two interacting materials are gradually bond together. The bond formation was earlier thought to result from deposition and condensation of volatile fission products, notably Cs, at the clad inner surface. This hypothesis was later refuted by Nogita and Une [104], who extensively examined the crystallographic structure and chemical composition of the pellet-clad bonding layer in commercial BWR fuel rods with pellet average burnups between 15 and 49 MWd(kgU)⁻¹. The rods were operated at low power, and the release of Cs and other fission products from the fuel pellets was therefore negligible. For burn-ups above 40 MWd(kgU)⁻¹, Nogita and Une observed bonding layers that were typically 10-20 µm thick. The layers consisted mainly of cubic ZrO₂, but there was also a ≈5 µm thick transition layer at the pellet surface, consisting of a solid solution of (U,Zr)O₂, in which the concentrations of UO₂ and ZrO₂ changed continuously. The concentration of Cs and other fission products in the layer was less than 1 at%. Hence, the detailed measurements by Nogita and Une show that a pellet-clad bonding layer forms also in absence of fission products.

The role of Cs in bond formation has also been studied by Wesley *et al.* [105], who made post-irradiation examinations of PWR fuel rods with a pellet burn-up slightly greater than 62 MWd(kgU)⁻¹. These high-burn-up rods were ramped to peak power levels in excess of 40 kWm⁻¹, leading to large release of Cs and other fission products from fuel pellets located at the peak power region of the rod. Wesley and co-workers compared the bonding layer in these regions with that in low-power regions, where the deposition of Cs was negligible. They found that the pellet-clad bonding layer was in fact *weaker* in the Cs-rich part of the rod, thus suggesting a checking effect of Cs on the bond strength.

The formation of a bonding layer leads to improved transfer of both heat and mechanical contact forces across the pellet-clad gap. Of particular importance is the prevention of sliding between the pellet and cladding, both in circumferential and axial direction of the cylindrical contact surface, which aggravates the PCMI-induced loading under the early stage of RIA in high-burn-up fuel. This is further discussed in Section 6.2.5.1.

From power ramp tests on fuel rods with various fuel pellet geometries, it is known that the ratio between pellet length and diameter has a strong impact on pellet-clad mechanical interaction [106]. Under normal operating conditions, the parabolic temperature profile across the fuel pellets, and the non-uniform thermal expansion that comes with it, lend an hourglass shape to the originally cylindrical pellets, which causes cladding stress concentrations at pellet-pellet interfaces. These stress concentrations are mitigated by chamfering the pellets and reducing their length to diameter ratio. However, as shown in Section 3.1.2, the radial temperature profile in high-burn-up fuel under the initial phase of an RIA is strongly peaked to the pellet periphery, i.e. opposite to the profile under normal operation, and the deformed shape of a fuel pellet, expected from thermal expansion alone, is that of a barrel. Consequently, pellet chamfering is expected to be less beneficial to PCMI under an RIA than under operational overpower transients. However, gas-induced fuel swelling from growth of pressurised pores and fission product gas bubbles may add to the thermal expansion under RIA, and modify this barrel shape in an unknown manner. Pulse reactor tests on high-burn-up 17×17 PWR fuel rods with two different pellet geometries have been conducted within the TK and HBO test series at the NSRR facility in Japan [107]. Differences in terms of pellet deformation mode and fission gas release between the two fuel designs were observed, but these differences could not be attributed to the disparate pellet geometries alone, since also the pellet fabrication process was different for the two fuel designs.

Fuel pellets in VVER fuel rods are manufactured with a central hole, in contrast to the solid pellets used in other types of light water reactor fuel. The annular pellets may have a beneficial effect on PCMI under RIA, since additional free volume for fuel expansion could possibly be afforded by the central hole. PCMI-induced failures are usually not observed in RIA simulation tests on VVER fuel rods, which supports this hypothesis. However, the observed resistance to PCMI failures is more likely a consequence of the low cladding corrosion of the tested VVER rods (see Section 6.2.5.2). Differences in failure behaviour between VVER and PWR/BWR observed in RIA simulation tests on high-burn-up fuel rods are further discussed in Section 7.2.1.

4. PHENOMENA THAT NEED TO BE ADDRESSED BY EXPERIMENTS AND MODELLING

As mentioned in Section 1, the main safety concerns in reactivity-initiated accidents are loss of long-term core coolability and possible damage to the reactor pressure boundary and the core through pressure wave generation. Fuel failure, i.e. loss of clad tube integrity, is in itself generally not considered a safety concern, since fuel failures do not necessarily imply loss of coolable geometry or generation of harmful pressure waves. Nonetheless, RIA experiments and modelling have historically been focused on fuel rod failure, for several reasons:

- Fuel rod failure is a prerequisite for loss of coolable core geometry and pressure wave generation.
- The mechanisms for fuel rod failure are more easily studied, both experimentally and analytically, than those for gross core damage.
- Regulatory bodies require that the number of failed fuel rods in the core should be calculated in evaluations of radiological consequences to design basis RIA.

In the following subsections, we identify phenomena with relevance to fuel and core damage under RIA, without ranking their relative importance. In an international study from 2001, such a ranking was indeed made for phenomena contributing to PCMI-induced clad failure in high-burn-up fuel under hot zero power rod ejection accidents in PWRs [108]. Phenomena judged to be relevant to this particular failure mechanism and accident scenario were identified and ranked with respect to their relative importance by an international panel of experts. The uncertainty in the knowledge and understanding of each phenomenon was also ranked, with the aim to identify important but vaguely known phenomena that should be given priority in future research.

4.1 Types of damage to fuel and cladding

From RIA simulation experiments in power pulse reactors, it has been found that the fuel rod behaviour under a reactivity-initiated accident is affected primarily by the:

- Characteristics of the power pulse, in particular the amplitude and pulse width.
- Core coolant conditions, i.e. the coolant pressure, temperature and flow rate.
- Burn-up-dependent state of the fuel rod. Among the most important properties are the pre-accident width of the pellet-clad gap, the degree of cladding waterside corrosion, the internal gas overpressure in the fuel rod, and the distribution of gaseous fission products in the fuel pellets.
- Fuel rod design. Parameters of particular importance are the internal fill gas pressure, clad tube wall thickness, fuel pellet composition ($\text{UO}_2/\text{PuO}_2/\text{Gd}_2\text{O}_3$, enrichment) and the fuel pellet geometrical design (solid/annular).

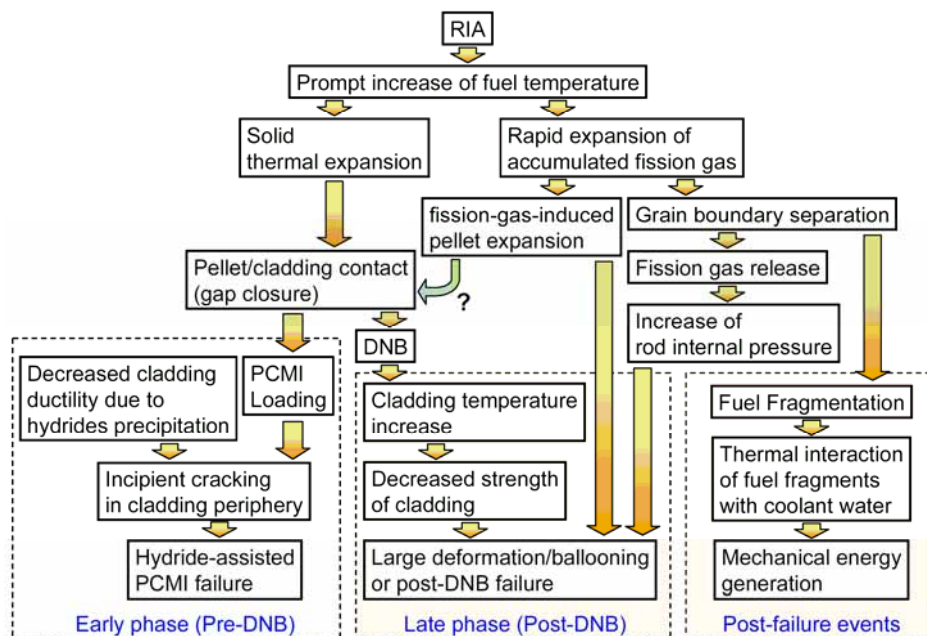
These factors are important to the fuel rod behaviour during an RIA, and they also control what kind of damage is inflicted to the fuel rod under the accident. Possible damage mechanisms are schematically presented in Figure 14. As shown in the figure, the rapid increase in power under the RIA leads to nearly adiabatic heating of the fuel pellets, which immediately deform by solid thermal expansion. If gaseous fission products are retained in the fuel, the expansion of the accumulated gas

will add to the solid pellet deformation. In case the pellet-clad gap is narrow or closed, which is normally the case for high-burn-up fuel, pellet clad mechanical interaction will lead to rapid and biaxial mechanical loading of the cladding tube. At this early stage of the accident, the cladding material is still at a fairly low temperature, and the thrust imposed by the expanding fuel pellets may therefore cause a partially brittle mode of clad failure [101]. This low-temperature failure mode is commonly observed in pulse irradiation tests on high-burn-up fuel rods.

At a later stage of the transient, heat transferred from the pellets may bring the cladding to such a high temperature that a boiling crisis occurs. If so, experience from pulse irradiation tests shows that the cladding material can remain at high temperature for up to about 15 s, until re-wetting takes place. This fairly long period at elevated temperature may lead to clad ballooning and creep rupture, in cases where significant pressure differences exist across the cladding wall. As indicated in Figure 14, transient release of accumulated fission gas increases the internal pressure loading. Another mode of high-temperature failure may occur during re-wetting of the overheated clad tube, since thermal stresses under the abrupt quenching may cause brittle fracture and disruption of the cladding material. This failure mode is imminent if the clad tube is embrittled by high temperature oxidation during the film-boiling phase.

Finally, if the energy deposited to the fuel is very high, the cladding and possibly also the fuel pellets may melt. Melting has been observed in pulse irradiation experiments on test rods charged with highly enriched fuel (10-20 wt% ^{235}U). The melting generally leads to cladding failure and violent thermal interaction between molten material and the coolant, causing pressure pulses in the coolant. For typical LWR fuel, the enrichment is significantly lower (<5%), and the energy deposition required for melting cannot be achieved in the experimental facilities at hand. This pertains in particular to high-burn-up fuel.

Figure 14. Possible mechanisms for fuel and cladding damage under an RIA [109]



However, thermal interaction between non-molten fuel fragments and the coolant may occur, as indicated in the rightmost column of Figure 14. This process is important to high-burn-up fuel, in which decohesion of the gas-filled grain boundaries turns the outer part (rim) of the fuel pellet into fine fragments during the RIA. Fuel coolant interaction and its consequences are further discussed in Section 4.3 below.

In summary, we have four potential failure modes for the fuel rod under an RIA:

- Low-temperature failures by PCMI under the early heat-up stage of the accident. This failure mode is relevant first and foremost to high-burn-up fuel rods with severely corroded cladding, which are subjected to a narrow power pulse, initiating from zero power conditions.
- High-temperature failures by cladding ballooning and burst. The failures occur as a consequence of film boiling and significant rod internal overpressure.
- Failures by disruption of the cladding upon quenching from high temperature. The failures occur as a consequence of oxygen-induced embrittlement due to high-temperature cladding oxidation under the film-boiling phase.
- High-temperature failures by melting of the cladding and possibly also the fuel pellets.

For narrow power pulses, typical of BWR RDAs and PWR REAs, which initiate from zero power conditions, pulse reactor experiments show that the first of the above failure modes is usually the most restricting for high-burn-up fuel rods, whereas either the second or the third failure mode is limiting for fresh and low-burn-up fuel - the fuel design and coolant conditions decide whether clad ballooning or oxidation-induced embrittlement is most likely to cause the failure in this case. An attempt has recently been made to construct a failure map for UO_2 fuel rods under RIA, which demarcates the various failure modes in terms of peak fuel enthalpy and pulse width [110]. Failure limits for different failure modes were constructed by evaluating the outcome of pulse reactor tests with simple analytical models. The failure limits were then used to create a failure map, defined in terms of fuel enthalpy and pulse width, in which the region of interest for each failure mode could be identified. Although the approach in [110] is interesting, it follows from our discussion that a general failure map must contain not only the peak fuel enthalpy and pulse width as parameters, but also the coolant conditions as well as burn-up-dependent properties, such as pellet-clad gap width and cladding corrosion.

4.2 Changes of temperature and geometry with influence on coolability

As mentioned in Section 1, acceptance criteria for RIA in light water reactors are intended to ensure long-term core coolability and to preclude damage to the reactor pressure vessel. Scenarios for loss of long-term core coolability after an RIA involve loss of coolable fuel geometry, for instance by ballooning or fragmentation of the fuel rods. A coolable fuel geometry may also be lost even if a rod-like geometry is preserved, in case large amounts of fuel pellet fragments are dispersed into the coolant under RIA. The dispersed fuel particles may block flow channels and impair long-term cooling, or simply pile up at the bottom of the core in a configuration not amenable to cooling. In the following, we discuss these scenarios for loss of coolable fuel geometry.

4.2.1 Clad ballooning

In Section 4.1, it was stated that clad tube ballooning and burst is a possible failure mode, if clad-to-coolant heat transfer is impaired by a boiling crisis and the fuel rod internal gas pressure exceeds the coolant pressure. The extent of high temperature ballooning that the cladding can sustain depends primarily on the time histories of temperature and pressure loading, and the state of the cladding material. Cladding hoop strains up to 123% have been reached in RIA simulation tests on fresh fuel rods in the NSRR [111], but irradiated rods are known to balloon significantly less: the maximum hoop strain measured in pulse reactor tests on pre-irradiated rods is merely 25% (see Section 6.2.2).

The rod pitch and diameter in current PWR and BWR fuel designs allow a clad hoop strain of 30-40% before rod-to-rod contact is reached, if neighbouring rods are assumed to deform similarly and each rod deforms axisymmetrically. Although a very hypothetical mode of deformation, the strain

values give some indication on the amount of clad ballooning needed for flow blockage in a fuel assembly [112]. In view of the maximum cladding strains measured in pulse reactor tests, flow blockage by clad ballooning under RIA can probably be ruled out for all but fresh fuel assemblies.

However, another important aspect of clad ballooning is that the area of metal exposed to high-temperature oxidation increases, giving a higher rate of oxygen-induced embrittlement. This, in combination with the wall thinning associated with ballooning, makes ballooned fuel rods vulnerable to thermal shock loads under quenching (see Section 6.2.3).

4.2.2 Fuel rod fragmentation

For LWR fuel rods subjected to an RIA, extensive fuel rod fragmentation and loss of rod-like geometry is a possible consequence of:

- PCMI-induced failure of fuel rods with severely corroded and embrittled cladding. This kind of fragmentation has been observed for both BWR and PWR high-burn-up fuel rods that have been tested in the NSRR. The fragmentation occurred in tests with peak fuel enthalpies as low as $373 \text{ J(gUO}_2\text{)}^{-1}$ (see Section 7.2.2 and Appendix A, Section A.5).
- Quenching of fuel rods with overheated cladding, which has been severely oxidized and embrittled as a consequence of film-boiling and high temperature under the RIA. The phenomenon has been observed for un-irradiated as well as pre-irradiated fuel rods, tested in the SPERT, PBF and NSRR [111,113]. The fragmentation occurred in tests with peak fuel enthalpies of $1\,005 \text{ J(gUO}_2\text{)}^{-1}$ and higher (see Section 7.1.2).

Fuel rod fragmentation due to PCMI-induced cladding failure has been observed to occur by long axial splits, in some cases in combination with guillotine breaks, i.e. cracks extending along the circumference of the cladding tube (see Section 7.2.2). The fuel dispersal is driven by the gas-induced fragmentation and grain boundary decohesion that takes place in high-burn-up fuel under RIA (see Section 6.1.2).

The extent of fuel rod fragmentation upon quenching is known to depend on the quenching temperature and the degree of high temperature oxidation and embrittlement experienced by the cladding tube under the film-boiling phase, and hence, on the peak fuel enthalpy [111,113]. Fuel rods tested in the SPERT, PBF and NSRR at peak fuel enthalpies around $1\,005\text{--}1\,045 \text{ J(gUO}_2\text{)}^{-1}$ merely broke up into decimetre-long segments of the fuel rod, but higher enthalpies resulted in finer fragments. This failure mode is further discussed in Sections 6.2.5.2 and 7.1.2.

The consequences of fuel rod fragmentation on mechanical energy generation have been studied experimentally, and will be discussed in the following subsection. Questions regarding long-term coolability of fragmented fuel rods, on the other hand, have not been addressed experimentally, and it seems that there is a consensus among regulatory bodies to equate loss of rod-like geometry under an RIA with loss of coolable geometry. Whether long-term coolability can indeed be maintained with fragmented fuel rods should, however, depend on the extent of damage and the fuel assembly design.

4.3 Mechanical energy generation

A major safety concern in reactivity-initiated accidents is that the thermal energy of fuel particles, expelled into the coolant from failed fuel rods, is rapidly converted to mechanical energy in the form of destructive pressure pulses. The coolant pressure pulses may damage nearby fuel assemblies, other core internals and ultimately also the reactor pressure vessel.

4.3.1 Thermal to mechanical energy conversion

By convention, the degree of fuel-coolant interaction is quantified with the energy conversion ratio, which is the ratio of the mechanical energy generated in the coolant to the thermal energy in the dispersed fuel. This ratio can be determined in pulse reactor tests, where the mechanical energy generated in the coolant is estimated by measuring the motion of the water column in the test rig, as it is raised by rapid expansion of steam bubbles around dispersed fuel fragments. The thermal energy of the fuel dispersed in the test can also be estimated: often, but not always, investigators use the total energy deposited in the fuel rod as a rough estimate to this property.

Energetic FCI, known as vapour explosions, may take place when molten fuel is dispersed into water. In vapour explosions, the timescale for heat transfer from the molten fuel to the coolant is shorter than the timescale for pressure relief. Therefore, the local surge in coolant pressure forms a shock wave, which propagates with a velocity greater than the characteristic speed of sound in the coolant ahead of the shock front [114]. The key feature of a vapour explosion is that the shock wave propagation through the coolant drives the rapid fuel fragmentation and associated heat transfer to the coolant, on the analogy of shock heating in a chemical detonation. In practise, fuel-coolant interaction does not generally exhibit these shock wave characteristics. The fragmentation of dispersed fuel particles is not necessarily linked to shock wave propagation, and the rapid boiling phenomenon propagates slower than the speed of sound. Although the character of the FCI is not explosive in this case, a large amount of vapour may be produced and detrimental pressure transients generated.

An upper limit for the energy conversion ratio under FCI can be calculated from thermodynamics, by assuming ideal mixing and isentropic expansion of the fuel-coolant mixture [115]. The ideal energy conversion ratio depends on the ratio between fuel and coolant volumes involved in the process, but for molten UO_2 fuel dispersed into water at typical PWR conditions, the ideal conversion ratio is greater than 10% for a wide range of fuel-to-coolant volume ratios. Much lower values are generally obtained in experiments [114]. In particular, early RIA simulation tests on fresh fuel have shown that energy conversion ratios may reach up to about 1%, when molten fuel is dispersed into water [102,116-117]. The conversion ratio correlates with the rod internal gas overpressure, and it is conjectured that the jet of molten fuel from the failed fuel rod is accelerated by the gas pressure, thereby leading to more efficient fuel-coolant interaction [102]. The energy conversion ratio for molten fuel dispersed into water also increases with the energy injected into the fuel under the accident, since higher energy injections result in fragmentation into finer fuel particles with larger surface to volume ratio [116].

Figure 15 shows the energy conversion ratio versus fuel fragment mean diameter, measured in the NSRR by various investigators. The mean diameter, d_{32} , of the fuel fragments is defined as the ratio of the total volume of fragments to the total surface, as measured after the test. The measurements by Tsuruta *et al.* [116] and Fuketa & Fujishiro [102] pertain to dispersal of molten fuel from un-irradiated fuel rods, whereas the data of Sugiyama & Fuketa [118] are for solid fuel, dispersed from high-burn-up fuel rods. The energy conversion ratio is here calculated by dividing the mechanical energy generated in the coolant with the energy deposited in the entire fuel volume.⁸

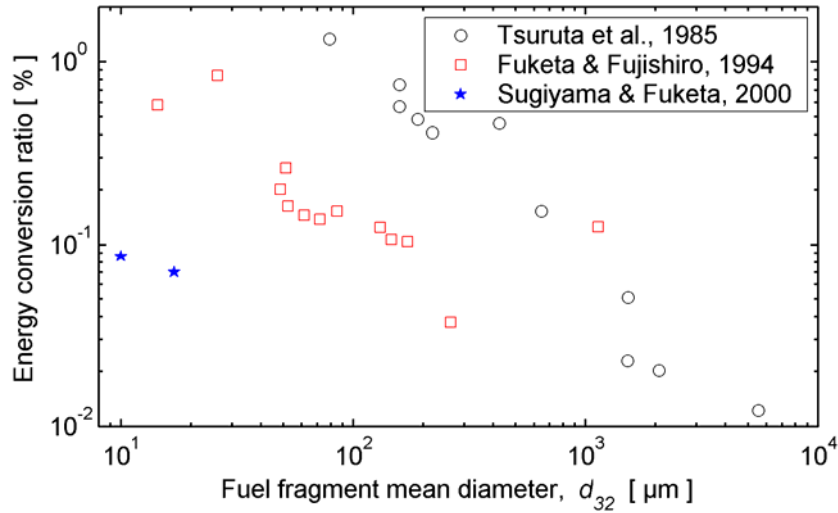
Three conclusions can be drawn from Figure 15: firstly, there are large differences between the datasets, but each dataset shows an inverse relationship between energy conversion ratio and mean fragment size. Secondly, solid fuel particles expelled from high-burn-up fuel rods are much smaller

8. In the paper by Sugiyama & Fuketa, the mechanical energy is divided by the estimated thermal energy of the dispersed fuel, which means that the energy conversion ratios reported in their paper are about an order of magnitude larger than those presented here.

than the fragments created when molten fuel are dispersed into the coolant from un-irradiated fuel rods. Thirdly, the energy conversion ratio associated with dispersal of solid fuel particles is lower than for molten fuel. This is believed to be an effect of particle temperature: the lower temperature of the solid particles result in slower fuel-to-coolant heat transfer. It should be remarked, that data on the energy conversion ratio for small ($<10\mu\text{m}$) fuel fragments are unavailable. Such data are warranted, because some of the fragments that emanate from the high burn-up microstructure at the rim of high-burn-up fuel pellets are smaller than $10\mu\text{m}$.

Figure 15. **Thermal-to-mechanical energy conversion ratio for fuel dispersal, measured in the NSRR**

The measurements by Tsuruta *et al.* [116] and Fuketa & Fujishiro [102] pertain to dispersal of molten fuel from un-irradiated fuel rods, whereas the data of Sugiyama & Fuketa [118] are for solid fuel, dispersed from high-burn-up fuel rods.



The data presented in Figure 15 stem from pulse irradiation tests in the NSRR. Energy conversion ratios measured in the PBF are not much different from those measured in the NSRR, which is somewhat surprising, considering that the coolant conditions are much different in these two facilities (see Table 3). Out-of-pile experiments on melted fuel dispersed into water have shown that the fuel-coolant interaction is affected by the pressure and subcooling⁹ of the coolant [114]. Energetic interaction in the form of vapour explosions is known to become less likely when the coolant pressure increases and the subcooling decreases. In both cases, this is explained by increased stability of the vapour film that encloses the hot fuel fragments. This vapour film serves as a thermal barrier, which hinders fuel-to-coolant heat transfer during the initial phase of fuel dispersion. Moreover, the coolant pressure strongly affects the volume of steam bubbles, generated by the fuel-coolant thermal interaction.

Typical coolant conditions for BWR cold and hot zero power as well as PWR hot zero power operation are included in Table 3 for comparison. The coolant velocity, pressure and temperature in the NSRR are similar to the BWR CZP conditions, and the PBF conditions are close to those of a BWR at hot zero power. However, the coolant conditions in both the NSRR and the PBF are far from those at PWR HZP. It is reasonable to believe that the higher pressure in the PWR may have a constraining effect on the expulsion of fuel fragments into the water. This assumption follows directly from the observed correlation between gas overpressure and energy conversion ratio [102]. Moreover, it follows from Table 3 that if a certain mass of water is vaporised, the steam volume will be 173 times larger in the

9. The subcooling is the difference between the saturation temperature and the actual temperature of the water.

NSRR than in the PWR at hot zero power conditions. Another distinct difference between the cooling conditions at PWR HZP and in the NSRR is the heat needed per unit mass for vaporisation of the coolant. Due to the lower subcooling and the higher pressure in the PWR at HZP conditions, only about half the heat is needed for vaporisation, in comparison with the NSRR. Considering these differences, it is likely that the fuel-coolant interaction could be much different in a PWR at HZP than in the NSRR. Pulse tests, carried out at typical PWR HZP cooling conditions, are needed to elucidate this issue.

Table 3. Coolant conditions under fuel-coolant interaction experiments in the NSRR and the PBF, in comparison with typical BWR CZP, BWR HZP, and PWR HZP conditions

Coolant property		NSRR	PBF	BWR CZP	BWR HZP	PWR HZP
Axial velocity	[ms ⁻¹]	0.0	0.4	0.7	2.0	5.1
Pressure	[MPa]	0.1	6.45	0.1	7.0	15.5
Temperature	[K]	298	538	303	513	565
Saturation temperature	[K]	373	554	373	559	618
Subcooling	[K]	75	16	70	46	53
Total heat for vaporisation	[J(gH ₂ O) ⁻¹]	2 570	1 620	2 550	1 730	1 300
Specific volume of saturated steam	[m ³ (kg) ⁻¹]	1.69	3.0×10 ⁻²	1.69	2.7×10 ⁻²	9.8×10 ⁻³

4.3.2 Consequences of coolant pressure pulses

Coolant pressure pulses with amplitudes up to 30-35 MPa have been reported in RIA simulation tests with large energy depositions, which resulted in dispersal of molten fuel into the coolant [102,117]. These peak pressure pulses are very short, typically a few tenths of a millisecond, and they are accompanied by a series of pressure pulses with lower amplitude, which occur over a period of about 10 ms upon fuel rod failure. The pressure pulses are too narrow to be explained by steam generation, and are believed to be the result of collapse (implosion) of steam bubbles.

Wider pressure pulses may occur by release of the plenum gas inventory from failed fuel rods. However, experiments have shown that mechanical energy deposition from leaking gas is moderate in comparison with that from thermal interaction between dispersed fuel and the coolant [118]. Pressure pulses caused by steam generation are even slower, but the generated steam has the potential to accelerate slugs of liquid coolant to high velocities. These slugs, known as water hammers, may cause substantial damage when they impinge on structural components.

An attempt to study the possibility of multi-rod failure by propagation of coolant pressure pulses was made in the RIA 1-4 test, carried out on a 3×3 array of pre-irradiated fuel rods in the PBF [119]. The rods were subjected to a 11 ms wide power pulse in the PBF, resulting in peak radial average fuel enthalpies in the range of 980 to 1 160 J(gUO₂)⁻¹. All the rods failed by axial cracks, induced by pellet-clad mechanical interaction, and one of the rods also experienced partial melting of the clad tube. However, no fuel material was dispersed into the coolant and damaging pressure pulses were therefore not generated. Consequently, the test failed to demonstrate the propagation of fuel rod damage from a failed rod to its neighbours by fuel dispersal and pressure pulse generation.

Two similar tests were done on un-irradiated fuel rods in the NSRR [120]. Two fuel assemblies, each comprising a central waterlogged PWR fuel rod surrounded by four intact rods and a flow shroud, were subjected to a pulse energy deposition of 890 and 1 020 J(gUO₂)⁻¹, respectively. It is well known that waterlogged fuel rods fail more violently than intact rods, and the purpose here was to clarify the damaging effects of waterlogged rod rupture on adjacent fuel rods and a BWR fuel channel box. The latter was in the tests represented by the flow shroud. In both tests, the central waterlogged rod burst, and almost all of the fuel pellets were dispersed into the coolant. The coolant pressure pulse caused large deformation (ballooning) of the flow shroud, while it had little influence on adjacent fuel

rods. These results were attributed to the difference in loading; while only the local pressure gradient in the coolant acted on the fuel rods, total pressure acted on the flow shroud that enclosed the pressure source. Hence, it was concluded that a coolant pressure pulse generated by the rupture of a single fuel rod is unlikely to damage adjacent fuel rods. On the other hand, a BWR fuel channel box may deform by the same pressure pulse. In a BWR, the ballooned fuel channel could block the insertion of control rods after an RIA, which would delay termination of the power excursion.

The damaging effects of coolant pressure pulses and water hammers on other core structures than fuel rods and fuel channels have, to the best of our knowledge, not yet been studied experimentally. However, recent analyses of scenarios for RIA in BWRs by use of computational fluid dynamics show that fluid viscosity in combination with tortuous flow paths lead to rapid dissipation of the coolant kinetic energy [121]. The computations show that mechanical loads on the reactor pressure vessel from the pressure pulse are weak, and the same is true for loads on core internals that are far away from the location where the pressure pulse is generated. The head of the core shroud is identified as the core internal that experiences the highest mechanical loads [121].

4.4 Radiological consequences

The worst-case consequence of a reactivity-initiated accident would be the release of radioactive fission products to the environment. Reactor accidents are usually analysed in relation to the probability of two distinct aspects of the accidents, namely (i) the probability of reactor *core damage*, in particular the (partial) meltdown of the reactor core, and (ii) the probability of a *large radiation release*, or radioactive transfer, emanating from the failure of so-called multiple-barriers, provided by the fuel rod cladding, the reactor pressure vessel and the reactor containment [6]. We should point out that the discourse in this section is mostly relevant to the worst case consequence of core damage in a postulated RIA, caused by fuel melting, rapid expulsion of molten fuel from the fuel rods, energetic fuel-coolant interaction and vapour explosions, leading to a severe accident and a high activity release [122]. As will be shown in Section 9 of the report, state-of-the art computer analyses of LWR RIAs indicate that less than 1% of the fuel rods are deemed to fail during the accident, without fuel melting. Unless these failures lead to subsequent core damage, one should expect that just a small fraction of the gaseous and volatile fission products in the core will be released to the primary coolant under an RIA.

The key attribute of a reactor accident is defined by the accident source term, Q , which is referred to the inventory of radionuclides released to the outside environment, in contrast to the inventory of radionuclides in the fuel rod enclosed by the cladding. The source term is often expressed as a fraction of radionuclide inventory in units of curie (Ci) in the core. More precisely, $Q = fI$, where I is the total inventory and f is the release fraction [123]. For example, for the hazardous I-131 and other iodine isotopes, the source term of the 1986 Chernobyl RBMK accident was essentially the total core inventory ($Q \approx I$), whereas in the 1979 Three Mile Island 2 (TMI-2) PWR accident, the source term for ^{131}I was negligible ($Q \approx 0$), namely 18 Ci^{10} out of 64 MCi [123].

It has been pointed out that the low release of iodine from TMI-2 was because of the existence of more caesium than iodine in the core inventory and the iodine mostly formed caesium iodide (CsI), rather than volatile gas I_2 . The difference in abundances emanates from the recurrent decay of ^{131}I with a half life of $t_{1/2} = 8.05$ days in the early months of reactor operation, whilst ^{137}Cs with $t_{1/2} = 30$ years keeps increasing in amount [6]. The CsI in TMI-2 was then trapped by dissolution in water or deposition on surfaces [6]. Various studies [123] indicate that in most cases, the source term will be substantially less than the core inventory. In conclusion, if the source term will be sufficiently low, then there is no large release of radionuclides.

10. For convenience, we use curie (Ci) rather than becquerel (Bq) for activity. $1 \text{ Ci} = 3.7 \times 10^{10} \text{ Bq}$.

Among the various environmental impacts that could result from a nuclear reactor accident (and its subsequent source terms), the biological effects to a population, as a consequence of the radiation dose, are of the utmost concern. The radiation dose at a given place as a result of release of a particular radionuclide depends on the amount released, its radiological characteristics, the weather conditions, the duration of exposure and the conformation between the receptor and the source. The dose from each nuclide is proportional to the mass of nuclides released. For a more thorough account of release consequences, in particular doses, radiation sources, effluent dispersion, etc. refer to Wilson *et al.*'s comprehensive review article [123] and references therein. Accident source terms for regulatory application for LWRs are described in the US NRC document NUREG-1465 [124]. In this document, the source term is expressed in terms of times and rates of appearance of radioactive fission products into the reactor containment, the types and quantities of species released, and other important quantities, such as the chemical forms of iodine.

It is customary to classify various radionuclides into groups, according to their physical-chemical properties. The groups are related, in parts, to the vapour pressure of the radionuclides at the temperature of the damaged core of the reactor. The groups utilised are the noble gases, the halogens, the alkali metals and the tellurium group, the barium and strontium group, the noble metals, volatile oxides or ruthenium group, non-volatile oxides or lanthanides, and the cerium group (see Table 4).

Table 4. Groups of radionuclides [124]

Group	Designation	Elements
1	Noble gases	Xe, Kr
2	Halogens	I, Br
3	Alkali metals	Cs, Rb
4	Tellurium group	Te, Sb, Se
5	Barium, strontium	Ba, Sr
6	Noble metals	Ru, Rh, Pd, Mo, Tc, Co
7	Lanthanides	La, Zr, Nd, Eu, Nb, Pm, Pr, Sm, Y, Cm, Am
8	Cerium group	Ce, Pu, Np

The relative contributions of each of the four major factors to doses in environment, namely, cloud dose, inhalation dose (a dose caused by the inhalation of radionuclides of the cloud), ground dose and food pathway dose, vary much depending on the nature of accident and the meteorological conditions. These effects, as well as the biological effects of irradiation, are detailed in [123]. Table 5 shows important radionuclides for the consequence analysis of the US NRC Reactor Safety Study, also known as the WASH-1400 study. The half-life and shutdown inventory values are taken from the later American Physical Society study [123]. The data shown in Table 5 are applicable to release from LWRs only, and include the most important isotopes at the time of an accident [123].

As an example of “worst-case” radionuclide release from a reactivity-initiated accident, we already mentioned the Chernobyl RBMK accident in 1986. In that accident, the release was not all immediate. It occurred over a time span of about 10 days with 24% the first day, 28% over the next 5 days and 48% over the following 4 days. The release mainly included volatile nuclides, such as noble gases, iodine, and caesium. The release of non-volatile nuclides, such as strontium, was much less. Table 6 presents the estimated release fractions and the total release for some of the important radionuclides [6,125]. The radioactive cloud from Chernobyl spread over most of the northern hemisphere, depositing radionuclides widely. The amount deposited decreased with increasing distance from the damaged reactor [126].

As a comparison to the Chernobyl accident, it may be informative to refer to an RIA that occurred in a PWR-1 type reactor on board a Russian Echo-II submarine at the Chazhma Bay near Vladivostok, Russia, on 10 August 1985 [127]. The fuel in this kind of PWR is reported to be a U-Al

alloy with 20% enrichment of ^{235}U , which is clad with a Zr-Nb alloy [127]. The total amount of ^{235}U in a fresh core is about 50 kg. The accident was caused by inadvertent rapid withdrawal of all control rods due to an external event during reactor refuelling [127]. The rapid reactivity insertion caused a hefty power pulse, followed by a steam explosion. Takano *et al.* [127] report that directly upon the explosion, a fire broke out, which was brought under control after four hours. The fire caused continuous release of radioactive elements from the damaged submarine for 7 h, and contaminated an area within 50 to 100 m from the submarine.

Table 5. Radionuclides considered important in the reactor safety study consequence analysis, applicable to a 3 200 MW-t PWR [123]

Radionuclides	Half-life [days]	Shutdown inventory [MCi]
1) Noble gases		
$^{85}\text{Kr}^*$	3950	0.56
$^{85\text{m}}\text{Kr}^*$	0.183	24
$^{87}\text{Kr}^*$	0.0528	47
$^{88}\text{Kr}^*$	0.117	68
^{133}Xe	5.28	170
^{135}Xe	0.384	34
2) Halogens		
^{131}I	8.05	85
^{132}I	0.0958	120
^{133}I	0.875	170
^{134}I	0.0366	190
^{135}I	0.28	150
3) Alkali metals		
^{134}Cs	750	7.5
^{136}Cs	13	3
^{137}Cs	11000	4.7
$^{86}\text{Rb}^*$	18.7	0.026
4) Tellurium group		
$^{127}\text{Te}^*$	0.391	5.9
$^{127\text{m}}\text{Te}$	109	1.1
$^{129}\text{Te}^*$	0.048	31
$^{129\text{m}}\text{Te}$	0.34	5.3
$^{131\text{m}}\text{Te}$	1.25	13
^{132}Te	3.25	120
^{127}Sb	3.88	6.1
^{129}Sb	0.179	33
5) Barium and strontium group		
^{89}Sr	52.1	94
^{90}Sr	11030	3.7
^{91}Sr	0.403	110
^{140}Ba	12.8	160
6) Noble metals		
$^{58}\text{Co}^*$	71	0.78
$^{60}\text{Co}^*$	1920	0.29
^{99}Mo	2.8	160
$^{99\text{m}}\text{Tc}^*$	0.25	140
^{103}Ru	39.5	110
$^{105}\text{Ru}^*$	0.185	72
^{106}Ru	366	25
$^{105}\text{Rh}^*$	1.5	49
7+8) Lanthanides and cerium group		
$^{90}\text{Y}^*$	2.67	3.9
^{91}Y	59	120
^{95}Zr	65.2	150
^{97}Zr	0.71	150
^{95}Nb	35	150
^{140}La	1.67	160
^{141}Ce	32.3	150
$^{143}\text{Ce}^*$	1.38	130
^{144}Ce	284	85
^{143}Pr	13.7	130
$^{147}\text{Nd}^*$	11.1	60
^{239}Np	2.35	1640
^{238}Pu	32500	0.057
^{239}Pu	8.90E+06	0.021
^{240}Pu	2.40E+06	0.021
^{241}Pu	5350	3.4
$^{241}\text{Am}^*$	1.50E+05	0.0017
^{242}Cm	163	0.5
^{244}Cm	6630	0.023

The radionuclides marked with an asterisk are negligible contributors to health effects [123].

Table 6. Selected radionuclides released to the environment from the Chernobyl accident [6,125]

Isotope	Half-life ($t_{1/2}$)	Inventory [MCi]	Release [MCi]	Fractional release
⁸⁵ Kr	10.8 years	0.89	0.89	1.00
¹³³ Xe	5.28 days	176	175.70	1.00
¹³¹ I	8.05 days	86	48.65	0.57
¹³⁴ Cs	2.07 years	4.60	1.46	0.32
¹³⁷ Cs	30.1 years	7.03	2.32	0.33
⁹⁰ Sr	28.8 years	5.95	0.27	0.05

According to Takano and co-workers [127], ten people were killed immediately upon the accident. Moreover, among the 2000 workers that participated in terminating the accident and in decontamination, 200 persons were exposed to radiation of more than 50 mSv. The activity of short-lived radioactive noble gases was estimated to be 74 PBq (2MCi) of the total of 259 PBq (7MCi), according to Takano and colleagues [127]. Since the core was loaded entirely with fresh fuel when the accident occurred, the inventory of hazardous radioactive nuclides, such as ¹³⁷Cs, ¹³⁴Cs and ⁹⁰Sr, was negligible from the standpoint of radioecology [127]. After the decay of radioactive nuclides with short half-lives, the radioactive iodine was considered to be the major cause of radiation dose [127]. Thanks to a favourable wind direction, resulting from sea breeze, most of the radioactive material was trapped by thick forests on the slopes of nearby hills. In this local area, a 3.5 km long and 200-650 m wide radioactive trace was created [127].

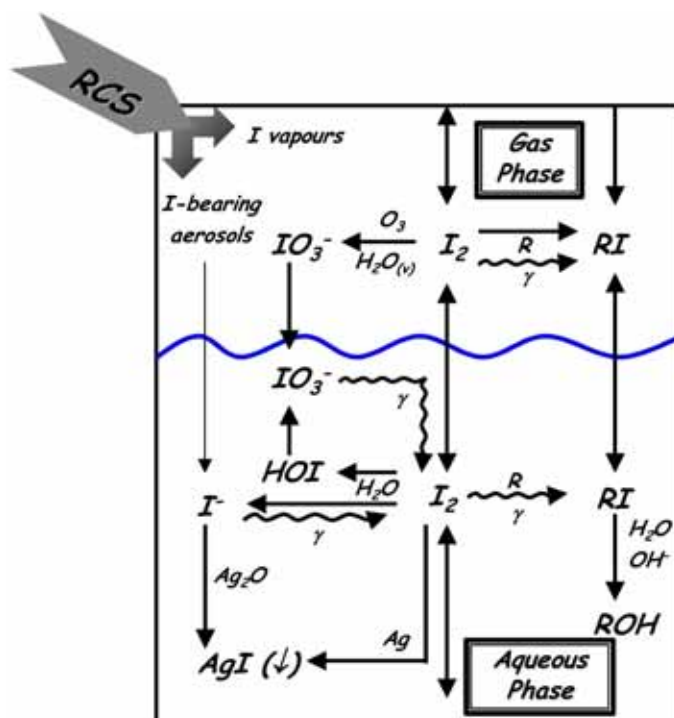
Various experimental programs on source terms of fission products and actinides have been conducted since the comprehensive study by the American Physical Society in 1985 [123]. The aim of these programs has been to promote understanding for the mechanisms that lead to release of fission products in postulated severe water reactor accidents. The programs include the HI/VI tests in USA [128], the CRL tests in Canada [129], the VEGA tests in Japan [130-131], and the HEVA [132] and VERCORS [133] experiments in France. Moreover, the in-reactor integral experiments PHEBUS Fission Products (FP) conducted in France have intended to simulate the core melt-down sequence and the ensuing source term [134-135]. These programs have provided a comprehensive database on source terms. For example, the HEVA/VERCORS program, which was primarily intended to generate data on volatile and low-volatile fission products, has also extended the database to include fuel melting and transuranic elements [133]. The generated data are valuable for improving severe accident computer models and codes, which are used for safety studies and accident management planning.

Among the radionuclides, the isotopes of iodine are considered to be the most hazardous that could be released from the fuel during a severe accident. This is due to a combination of several effects: (i) There exists an ample inventory of iodine in nuclear fuel (Table 5), (ii) the isotope of greatest radiological impact, ¹³¹I, has a half-life of eight days (Table 5), (iii) iodine has an affinity for chemical reaction that could lead to formation of volatile species, and hazardous biological effects [136]. For these reasons, extensive studies have been made to elucidate the chemistry of iodine and its transport under accident conditions [136-140].

There is a general consensus among iodine chemistry experts [136,140], that under most accidents, the iodine released from fuel to reactor coolant system (RCS) would be mainly in the form of alkaline halides such as caesium iodide (CsI) or rubidium iodide (RbI). These compounds are initially dissolved in water as non-volatile I, stemming from the discharged reactor coolant and any safety systems that are in operation. Upon an accident, due to the presence of high radiation fields, I could be oxidized by radiolytic-controlled processes to form volatile molecular iodine (I₂) that could become airborne. Molecular iodine in the aqueous phase would decompose into the gas phase and could be further

oxidized to other non-volatile iodine oxides (such as IO_3); or could be reduced back into its original non-volatile I state by thermal or radiolytic processes [136-137]. Moreover, iodine species in solution could also react with organic iodides (commonly denoted by RI) that could afterward decompose to I or transform into gas phase. The deposition of both gaseous and aqueous iodine species on surfaces could change the concentration of iodine species or induce surface-catalysed transformations. A simplified diagram of the redox (reduction oxidation) process provided by Clément *et al.* [140] is reproduced in Figure 16.

Figure 16. Schemata of iodine transformations within the containment after Clément *et al.* [140]



Finally, one noted element that could affect iodine chemical behaviour in the sump is silver. This element or its oxide Ag_2O can readily react with I_2 and I to yield silver iodide (AgI), which would precipitate in the sump. The release of silver into the containment vessel was observed in the PHEBUS FP tests [135] as a result of control rod melting.¹¹ As discussed by Clément, *et al.* [140], silver is likely to be released as Ag aerosols rather than Ag_2O from the reactor system. Once released into the oxidizing containment atmosphere (composed of radiation and air), Ag would be oxidized in the gas phase while reacting with iodine. The stability of AgI in the radiation field (in-situ β -radiation and external γ -radiation) has been investigated by Güntay and co-workers [141]. Small to significant decomposition of AgI in terms of the production of volatile and non-volatile species has been measured, whereas no effect of γ -radiation on AgI has been found [140].

Regarding other neutron absorber materials, such as B_4C , which is commonly used in BWRs, no study to our knowledge regarding its interaction with iodine and its transport in the RCS has been performed. According to Clément *et al.* [140], decomposition products of B_4C may modify the iodine speciation within the RCS and containment milieu, especially in the presence of radiation.

11. The control rods consisted of silver-indium-cadmium (80Ag-15In-5Cd in wt%) neutron absorber material in 304L type stainless steel cladding housed in Zircaloy guide tubes.

The iodine system in the post-accident containment is far from thermal equilibrium, due to continuous production of chemicals by radiolysis. Thus, chemical thermodynamic computations are not sufficient to assess iodine speciation, and therefore, the kinetics of individual reactions needs to be taken into account [136]. The determination of the rates of chemical reactions under post-accident containment conditions is an involved process, description of which is beyond the scope of our report; the interested reader can refer to the cited references, especially [136]. An interesting overview by Wren [137] delineates the needs for impending iodine chemistry research.

5. OVERVIEW OF RIA TESTING METHODOLOGY

Our understanding of the fuel behaviour during reactivity-initiated accidents is based on the results of RIA simulation tests, performed on instrumented short-length rodlets in dedicated power pulse reactors, and separate effect tests, carried out on fuel or cladding samples out of pile. The pulse reactor tests are done at conditions that approximate those expected in power reactors under RIA, and they provide valuable information on the integral fuel rod behaviour under the accident. However, these integral tests are costly, and it is also difficult to investigate the role of particular parameters, such as clad corrosion, by in-pile experiments. Out-of-pile separate effect tests, performed under well-controlled conditions, are therefore needed to investigate e.g. clad mechanical properties, clad-to-coolant heat transfer and fuel fission gas release under conditions expected in RIAs. The following subsections provide an overview of RIA integral and separate effect tests, performed up to March 2009.

5.1 Pulse reactor tests

5.1.1 Overview of pulse reactor tests

A large number of RIA simulation tests have been performed on fresh (un-irradiated) fuel rods, using pulse reactors in the USA, Japan, Russia, Kazakhstan and Romania. These tests, which were carried out predominantly from the sixties to the eighties, were used by national regulatory bodies to define RIA design requirements for the power plants that were built at the time. Also, the effects of differences in design parameters on failure propensity and thermo-mechanical behaviour under RIA were studied in these tests on fresh fuel. The results of these experiments on fresh fuel rods are summarised in Section 7.1 and early reviews, e.g. [111,113,142-143]. Later work has been focused on the behaviour of pre-irradiated fuel rods. Under the past four decades, RIA simulation tests have been conducted on pre-irradiated light water reactor fuel rods in six different power pulse reactors:

- SPERT-CDC (Special Power Excursion Reactor – Capsule Driver Core, Scoville, ID, USA)
Experiments performed in 1969-1970.
- PBF (Power Burst Facility, Scoville, ID, USA)
Experiments performed in 1978-1980.
- IGR (Pulse Graphite Reactor, Kurchatov, Kazakhstan)
Experiments performed in 1990-1992.
- BIGR (Fast Pulse Graphite Reactor, Sarov, Russia)
Experiments performed in 1997-2000.
- NSRR (Nuclear Safety Research Reactor, Tokai, Japan)
Ongoing experiments, carried out since 1975.
- CABRI (Cadache, France)
Experiments performed in 1993-2002 with sodium coolant loop. Tests with water coolant loop planned to start in the near future.

The test conditions, as well as the investigated fuel rods, differ significantly between these studies. This is shown in Table 7, which summarises test conditions and key test rod properties in each

experimental programme. It should be noticed that the pulse irradiation tests performed on pre-irradiated fuel rods are confined to UO₂ and MOX fuel. Burnable absorber and inert matrix fuels have so far been tested only in un-irradiated state [41,49].

Table 7. Overview of pulse reactor tests on pre-irradiated LWR fuel rods

The peak- and failure enthalpies are axial peak, radial average values for the fuel pellet. It should be noted that tests on fuel rods pre-irradiated in the JMTR are not included in the NSRR data (Section A.5, Appendix A).

	SPERT US	PBF US	IGR KZ	BIGR RU	NSRR JP	CABRI FR
Test conditions						
Coolant medium	Stagnant water	Flowing water	Stagnant water	Stagnant water	Stagnant water	Flowing sodium
Coolant temperature [K]	293	538	293	293	293*	553
Coolant pressure [MPa]	0.1	6.45	0.1	0.1	0.1*	0.5
Power pulse width [ms]	13-31	11-16	600-950	2-3	4-7	9 - 75
Fuel rods tested						
Number of tests (PWR/BWR/VVER/MOX)	10 (0/10/0/0)	17 (17/0/0/0)	13 (0/0/13/0)	12 (0/0/12/0)	58 (32/17/0/9)	14 (10/0/0/4)
Burn-up [MWdkg ⁻¹ HM ⁻¹]	1-32	0-6.1	47-49	47-60	20-77	33-76
Clad oxide thickness [μm]	0-65	0-5	5	3-7	4-73	10-126
Rod active length [mm]	132	≈ 1000	150	140-150	122-135	440-1000
Peak fuel enthalpy [Jg ⁻¹] (calg ⁻¹)	570-1 180 (137-282)	770-1190 (185-285)	255-1 051 (61-251)	481-787 (115-188)	155-657 (37-157)	343-832 (82-199)
Lowest failure enthalpy [Jg ⁻¹] (calg ⁻¹)	356 (85)	586 (140)	737 (176)	687 (164)	222 (53)	117-151 (28-36)

* Standard cooling conditions, used in most of the NSRR tests on pre-irradiated fuel. A new test capsule, allowing high coolant temperature and pressure, has just recently been taken into operation.

5.1.2 Typicality of test conditions

As shown in Table 7, the coolant conditions in PBF were close to those expected at HZP in BWRs, but the coolant conditions in the other pulse reactors are different from those in light water reactors. In particular, they differ from the conditions at HZP in PWRs, i.e. flowing water at a temperature of about 570 K and 15 MPa pressure. This non-typicality makes it difficult to directly transfer the results of pulse reactor tests to LWR conditions. Unfortunately, there are also other differences between the pulse reactor tests and the conditions expected under RIA in LWRs. For instance, from the results of three-dimensional core kinetics analyses of LWR RIA scenarios compiled in Section 2.2.1, it is clear that many pulse reactor tests have been performed with unrealistically narrow pulses. Moreover, power pulses generated in pulse reactors generally have a weaker tail than the pulses expected in LWRs under RIA.

The pulse irradiation tests are usually carried out on single rods. For pre-irradiated fuel, the only exception to this rule is the RIA 1-4 test, which was done on a 3×3 array of pre-irradiated PWR fuel rods in the PBF (Section 5.1.4). Moreover, all pulse reactor tests are done on short-length rodlets, and in all but the PBF and CABRI reactors, the test rods are subjected to a nearly uniform axial power profile throughout the entire transient. The length of the rod, and also the distribution of power along the rod as a function of time, could affect the transfer of axial forces from the expanding fuel pellets to the cladding. Hence, the cladding stress state in pulse reactor rodlets may not be the same as in full-length LWR rods. However, the PBF tests were nearly prototypical in this respect.

In addition to the non-prototypical test conditions, there is also non-typicality in fuel rod design and pre-irradiation conditions. In particular, it should be noted that the design of the SPERT rodlets

was very different from that of LWR fuel rods. The fuel enrichment was increased and the fuel and cladding diameters were reduced in order to increase the attainable energy deposition. Some of the SPERT rodlets were pre-irradiated in the Engineering Test Reactor (ETR), at very high power levels, resulting in fuel restructuring and central hole formation. Also some of the NSRR test rods were pre-irradiated under non-prototypical conditions in the Japanese Material Test Reactor (JMTR) facility, inasmuch as they were irradiated in an un-pressurised helium environment, and therefore not subjected to clad creep-down and waterside corrosion (Section A.5 in Appendix A). Due to the non-prototypical pre-irradiation conditions and the high (10-20 wt% ^{235}U) enrichment of the JMTR fuel rods, they are not considered representative of LWR fuel and therefore not included in Table 7.

Finally, it should be mentioned that re-fabrication of full-length LWR fuel rods into short-length rodlets for testing in pulse reactors may modify the state of both fuel pellets and cladding. Firstly, the pellet-clad gap state is altered through fuel fragment relocation when the rods are handled and manipulated. Unless the rodlets are pre-conditioned at normal operating power in the test reactor for a sufficiently long time to reach a new equilibrium pellet-clad contact state, PCMI under the subsequent power pulse will be aggravated by this relocation. A recent assessment of pulse reactor test data, made by the US NRC, indicates that fuel rods tested in the CABRI facility are probably sufficiently pre-conditioned before the pulse tests, whereas rods tested in the NSRR are not sufficiently pre-conditioned to reach an equilibrium pellet-clad contact state before the transient [144]. This is further discussed in Section 6.2.2. Since pre-conditioning at power is only possible in tests loops with a flowing coolant, it is likely that also the tests in SPERT, IGR and BGR were done on fuel rods having a perturbed pellet-clad contact state. Secondly, the cladding microstructure may be altered during the re-fabrication process, which usually involves heat input from cutting, welding and thermocouple attachment. Possible effects of these processes on the cladding properties of pulse reactor test rods have been identified and discussed by Garde [145].

5.1.3 SPERT-CDC tests

The SPERT-CDC test programme included tests on both un-irradiated test rods and rods that were pre-irradiated in the Engineering Test Reactor to rod average burn-ups in the range of 1 to 32 MWd(kgU)⁻¹. A total of ten pre-irradiated rodlets were tested in a sealed capsule, which was equipped with a pressure transducer and contained stagnant water at atmospheric pressure and room temperature. The rodlets were not instrumented, but the pressure transducer in the test capsule was used to detect coolant pressure spikes. In this way, it was possible to determine the approximate time and fuel enthalpy at which a test rod failed. Results from the SPERT-CDC tests on pre-irradiated fuel rods are summarised in Section A.1 of Appendix A.

5.1.4 PBF tests

The PBF tests simulated hot start-up conditions in a BWR, i.e. a coolant temperature of 559 K and a pressure of 7.0 MPa, using individually shrouded test rodlets with relatively low burn-up [113]. The reactor consisted of an annular driver core in a light water pool, with a pressurised water loop located in the central experimental cavity. In the tests, power excursions were initiated by a fast-acting drive system that moved control rods at a velocity of 9.5 ms⁻¹ through the test reactor core, giving a reactivity insertion time of about 50 ms. This is well above the BWR maximum free-fall control rod velocity of about 6.0 ms⁻¹, and the reactivity insertion time is much shorter than that for a RDA, which is about 1.0-1.5 s.

Three series of tests were performed on irradiated PWR fuel rods: the RIA 1-1, RIA 1-2 and RIA 1-4 tests [119,146-148]. Tests RIA 1-1 and RIA 1-2 each contained four test rods, but the rods were in individual flow shrouds such that they behaved as single-rod tests. The test rods were selectively instrumented with cladding surface thermocouples, elongation sensors and internal pressure transducers.

Test RIA 1-4 was a true multi-rod test with a 3×3 array of rodlets. The main objective of test RIA 1-4 was to investigate core coolability of clustered pre-irradiated rods for comparison with results of the RIA 1-1 tests.

Section A.2 in Appendix A summarises test conditions and results for all rods in these tests. Deposited energies were relatively high in the PBF test series, because the programme was designed to examine fuel behaviour near the US NRC 280 cal(gUO₂)-1 (1172 J(gUO₂)-1) fuel enthalpy core coolability limit.

5.1.5 IGR tests

The IGR is a homogeneous uranium-graphite pulse reactor with a natural pulse width of 500-900 ms. The reactor core contains a central experimental channel, where a test capsule with short-length test rodlets can be placed. The capsule contains stagnant water as coolant. From 1983 to 1990, a large number of RIA simulation tests were carried out on un-irradiated VVER fuel rods, and from 1990 to 1992, thirteen tests were also done on pre-irradiated rods [149]. Rodlets for the latter series of tests were re-fabricated from full-length VVER rods with burn-ups in the range of 47 to 49 MWd(kgU)⁻¹. Upon re-fabrication, the high-burn-up fuel pellets were replaced with fresh pellets in five of the rodlets. Hence, these rodlets contained un-irradiated fuel in irradiated cladding tubes. All re-fabricated test rods were back-filled with pure helium to a pressure of 1.7 MPa.

The cladding oxide layer was only about 5 µm thick for the pre-irradiated test rods, in spite of their fairly high burn-up. The low corrosion of the E110 cladding material used for the VVER fuel rod design contrasts with the severe corrosion of high-burn-up PWR fuel rods with Zircaloy-4 cladding, which have been tested in the NSRR and CABRI. Finally, it should be pointed out that none of the pre-irradiated test rods were instrumented in the IGR, since for safety reasons, instrument penetrations to the test capsule were not allowed in tests on irradiated specimens. The main results of IGR tests on pre-irradiated fuel rods are summarised in Section A.3, Appendix A.

5.1.6 BGR tests

The BGR is another uranium-graphite pulse reactor that has been used for RIA simulation tests of VVER fuel rods. The core height and diameter is 670 and 760 mm, respectively, and the reactor has a natural pulse width of 2-5 ms, which is the shortest pulse among all experimental facilities. A sealed test capsule with short-length rodlets, surrounded by stagnant water, is located at the periphery of the core [150]. As for the IGR, tests on pre-irradiated fuel rods are for safety reasons done without instrumentation in the test capsule.

Pulse irradiation tests were carried out on un-irradiated fuel rods in the BGR from 1994 to 1997, and from 1997 to 2000, twelve tests were carried out on pre-irradiated fuel. The rodlets for the latter series of tests were sampled from full-length VVER fuel rods, ranging in burn-up between 47 and 60 MWd(kgU)⁻¹ [151]. The re-fabricated rodlets were back-filled with pure helium to pressures between 0.1 and 2.1 MPa. The rodlets and the test results are further described in Section A.4, Appendix A.

5.1.7 NSRR tests

A large-scale RIA test programme has over the years been carried out at the Nuclear Safety Research Reactor by the Japan Atomic Energy Agency (JAEA), which was formerly the Japan Atomic Energy Research Institute (JAERI). Ishikawa and Shiozawa [111] have reviewed in detail the NSRR studies up to 1980, which were performed on un-irradiated fuel rods. Ishikawa *et al.* [152] have reviewed and evaluated the NSRR results up to 1989. In addition, there have been several more recent overviews by Fujishiro *et al.* [153] and Fuketa *et al.* [84,107] on PWR test rods, by Nakamura [154]

and Nakamura *et al.* [68,155-156] on BWR rods, and by Sasajima *et al.* [45] on MOX rods. Overviews of both PWR and BWR tests have been presented by Fuketa [157], Fuketa *et al.* [44] and Nakamura *et al.* [158]. The main results from the NSRR tests are summarised in Section A.5 of Appendix A.

The NSRR is a modified TRIGA-ACPR¹² pool reactor, the core of which consists of 149 uranium-zirconium hydride fuel-moderator elements. The reactor and reactivity control system yield pulses with full width at half maximum in the range of 4.4 to 7 ms. Until recently, all RIA simulation tests on pre-irradiated fuel rods were carried out in a test capsule containing stagnant water at atmospheric pressure, and most of the tests were carried out with the coolant initially at room temperature. Today, tests are also made at high coolant pressure and temperature by use of a modified test capsule [159]. The test capsule is placed in a hole, 220 mm in diameter, at the centre of the reactor core. The instrumentation for recording the response of the test rod and coolant during the transient is also placed within the test capsule. It should be pointed out that many of the NSRR tests have been done on extensively instrumented rodlets.

The test rods used in the NSRR tests can be separated into four main groups: (i) PWR test rods, (ii) BWR test rods, (iii) ATR MOX test rods, and (iv) Japanese Material Test Reactor (JMTR) rods. The first two groups of rods were sampled from full-length commercial fuel rods, which were irradiated in commercial power plants and then re-fabricated into short-length test rodlets. The third group of rods were re-fabricated from fuel rods operated in the Advanced Thermal Reactor (ATR), Japan.

Rodlets used in the first three groups of tests were re-fabricated by cutting segments with an active length of about 120 mm from full-length fuel rods. Top and bottom end fittings were welded to the segments, and the rodlets were back-filled with either pure helium, or a mixture of helium and other noble gases with lower thermal conductivity, to pressures ranging from 0.1 to 5.1 MPa in order to simulate the range of gas conditions representing end-of-life gas composition and pressure. The fourth group of test rods, which were pre-irradiated in the JMTR, were manufactured as short-length test rodlets, and directly inserted into the test capsule after pre-irradiation in the JMTR. A more detailed presentation of the tests performed on these rods is given in Section A.5.4 of Appendix A.

5.1.8 CABRI tests

The CABRI test reactor is a pool-type light water reactor with UO₂ fuel, designed with a central flux area that can accommodate the insertion of a test device [160]. The central flux area of the reactor contains a test loop. Since the loop is originally intended for research on fuel for liquid metal fast breeder reactors (LMFBR), it uses liquid sodium as coolant. This loop has been used in all RIA simulation tests performed to date, but it is currently being replaced with a pressurised water loop, which will be taken into operation in the next few years.

The test rods are placed inside a shrouded test rig, which also houses the in-reactor instrumentation used to monitor the fuel behaviour during the transient. The power transients are initiated from zero power, and pulse widths between 9.5 ms to 75 ms have been used in the RIA simulation tests. Although the coolant medium and pressure (0.5 MPa) are different from those in LWRs, the coolant conditions are considered as representative for situations where the cladding temperature increase is limited. Hence, the clad-to-coolant heat transfer is expected to be similar to that in LWRs during the first part of the transient, which is crucial to PCMI-induced clad failures. The coolant and fuel cladding temperature in CABRI is 553 K at start of the transient, which is close to that of a PWR at hot stand-by. The same is true for the coolant velocity, which is about 5 ms⁻¹.

12. TRIGA-ACPR: Training, Research, Isotopes General Atomics – Annular Core Pulse Reactor. TRIGA is a class of small research reactors, designed and manufactured by General Atomics, USA.

An international test programme, named REP¹³ Na, was launched in 1992 to study the validity of the RIA acceptance criteria on high-burn-up 17×17 PWR fuel, with emphasis on the behaviour of fuel during the early stage of the transient and fuel failure by PCMI [86,95]. A total of twelve tests have been conducted within the programme. Eight of the tests were performed on UO₂ fuel and four tests on MOX fuel, pre-irradiated to burn-ups ranging from 28 to 65 MWd(kgU)⁻¹. Except for rods REP-Na2 and REP-Na3, all test rods in the CABRI REP-Na series were taken from 17×17 PWR fuel rods irradiated under prototypical conditions in commercial PWRs, which were re-fabricated into short-length rodlets. Rod REP-Na2 was a test reactor rod, pre-irradiated in the Belgian Reactor 3 (BR3) test reactor, Mol, Belgium, and REP-Na3 was pre-irradiated in a commercial PWR as part of a segmented fuel rod. The cladding material was standard Zircaloy-4, except for rods REP-Na3 and REP-Na9 with low-tin (1.3 wt%Sn) Zircaloy-4, REP-Na2 with BR3 Zircaloy-4 cladding, and REP-Na11 with M5 cladding.

A follow-up to the REP-Na test series was launched in 2000. The new test series, named CABRI International Program (CIP), is to be carried out in the pressurised water coolant loop that is under construction. However, two pilot tests to CIP were performed in the existing sodium loop in November 2002. The PWR test rods, denoted CIP0-1 and CIP0-2, were manufactured with ZIRLO and M5 cladding, respectively, and had burn-ups around 75 MWd(kgU)⁻¹. The basic data on the 14 PWR rods tested to date in CABRI, along with the main results of the tests, are summarised in Section A.6 of Appendix A.

5.2 Separate effect tests

5.2.1 Cladding mechanical properties

The cladding strength and ductility are of fundamental importance to fuel rod survivability under reactivity-initiated accidents, and many separate effect test programs have been conducted to study these properties in detail. The objective has been to understand and quantify the observed degradation in fuel rod survivability at high burn-up, and most tests have therefore been focused on the embrittling effects related to cladding waterside corrosion, i.e. cladding oxidation and hydrogen uptake. These effects have been investigated by testing in-reactor corroded cladding, taken from high-burn-up fuel rods, as well as un-irradiated samples that have been artificially oxidized and hydrided under well-controlled laboratory conditions. Tests on the latter kind of samples provide a valuable supplement to the tests on irradiated cladding, which are costly and time consuming. Moreover, the hydride distribution in artificially corroded samples can be controlled in detail, which makes it possible to investigate the importance of e.g. hydride blisters to the cladding embrittlement.

Mechanical testing of materials is generally divided into three categories:

- Standardised tests for determination of strength parameters such as yield strength, ultimate tensile strength or fracture toughness. These tests are carried out on specimens with standardised geometries, according to standardised testing procedures.
- Tests for determination of constitutive parameters, i.e. parameters in material models, such as Young's modulus or creep properties. The testing methods are not standardised, and usually adapted to the constitutive relation (material model) at hand. Moreover, the loading and environment conditions are adapted to the expected operating conditions.
- Tests of components. Complete components are loaded to failure under typical loading and environment conditions.

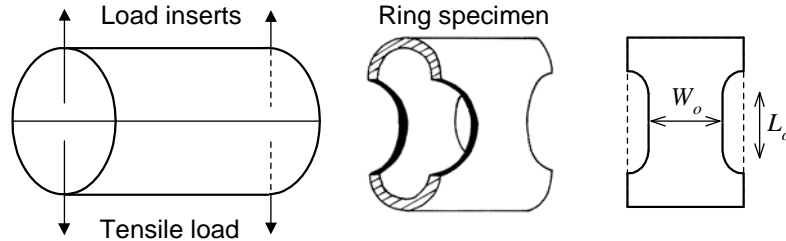
Nearly all of the separate effect tests that have been carried out to investigate cladding mechanical properties under RIA fall into the second category of tests. Hence, non-standard testing methods and specimen designs have been used, which makes it difficult to compare the results of various test series.

13. REP is a French abbreviation for pressurised water reactor (PWR).

Cladding low-temperature failure by PCMI is usually assumed to occur by a two-stage process, where the first stage involves radial propagation of flaws in the cladding external oxide layer, or the brittle hydride-rich material beneath the oxide layer, into short through-wall defects, and the second stage is a matter of axial propagation of these primary defects into axial splits. The material property of interest for the first stage is the cladding ductility in the hoop direction, i.e. the ability of the cladding to expand radially without rupture, and most out-of-pile mechanical tests performed in connection with RIA have been focused on this particular parameter. The tests have been carried out as:

- Burst tests, where cladding tube samples are subjected to internal pressure loading. The tube ends are normally closed, which gives a biaxial stress state with $\sigma_{zz}/\sigma_{\theta\theta}=1/2$ in the clad material. Some burst tests are carried out with open ends of the tube, which gives a uniaxial stress state, $\sigma_{zz}/\sigma_{\theta\theta}=0$. As will be shown in Section 6.2.5.1, the stress biaxiality ratio is important to the deformation behaviour of the cladding. Cladding ductility in burst tests is defined by the hoop plastic strain to failure, which is evaluated from post-test measurements of the relative elongation of the clad tube circumference.
- Mandrel-type tests, where cladding tube samples are loaded internally by an expanding mandrel. This kind of loading, which has historically been widely used to simulate PCMI, leads to a cladding stress state that is largely unknown. Cladding ductility is usually defined as in the aforementioned burst tests.
- Ring tensile tests, where ring-like cladding samples with two notched gauge sections are loaded in tension by inserts. These inserts also prevent bending and distortion of the cladding circular cross-section (see Figure 17). The stress state in the notched gauge sections is non-uniform, and depends on the sample geometry. When $W_o/L_o \ll 1$, the stress state is nearly uniaxial, whereas plane strain conditions prevail when $W_o/L_o > 1$. The specimen geometry is known to have a strong impact on the results for this kind of tests [161].

Figure 17. Schematic illustration of specimen design and load conditions in ring tensile tests



Another difficulty with ring tensile tests is that cladding ductility is usually defined as the total elongation of the gauge length, L_o . The gauge length influences the total elongation results, which can be understood by recognising that the total elongation of a test specimen is the sum of uniform elongation and localised deformation, usually referred to as necking.

Hence, for a specimen with gauge length L_o , the total elongation, ε_{te} , can be written:

$$\varepsilon_{te} = \frac{\Delta L}{L_o} = \frac{\delta + \varepsilon_{ue} L_o}{L_o} = \frac{\delta}{L_o} + \varepsilon_{ue}, \quad 9$$

where δ is the localised extension from necking. The uniform elongation, ε_{ue} , is practically independent of specimen geometry. The necking, on the other hand, depends on specimen geometry as well as on material properties. Barba [162], empirically found that δ is proportional to the linear dimensions of the cross-sectional area of the tensile specimen, A_o . The relation:

$$\delta = \kappa \sqrt{A_o} \quad 10$$

is therefore known as Barba's law. Here, κ is a parameter related to the local ductility of the material, i.e. the material's ability to deform plastically at the microscopic level. By combining Equations 9 and 10, we have:

$$\varepsilon_{te} = \kappa \frac{\sqrt{A_o}}{L_o} + \varepsilon_{ue} \quad 11$$

from which it is evident that the total elongation depends on both the length and cross-sectional area of the gauge section. Hence, the total elongation is not a true material property.

The rapid loading under a LWR RIA may lead to cladding strain rates up to about 1 s^{-1} (see Section 6.2.2). In tests of cladding mechanical properties that are focused on RIA behaviour, the loading rates are always adapted so that these exceptional strain rates are reached. For comparison, we note that standard tensile tests are conducted with a strain rate of $8.33 \times 10^{-5} \text{ s}^{-1}$ [163]. Also the heating of the cladding is very fast during the initial phase of an RIA, with peak heating rates in the range of 10^3 to 10^4 K s^{-1} . Although some tests in the PROMETRA experimental programme have been done with cladding heating rates of $100\text{-}200 \text{ K s}^{-1}$, mechanical tests on cladding materials are usually carried out at constant and uniform temperature. The temperature conditions in the majority of tests are thus very much different from those expected under an RIA, where the temperature varies with respect to both space and time. Hence, possible effects of a radial temperature gradient across the clad on local material properties and thermal stresses are overlooked in the mechanical property tests, and the same is true for time-dependent effects on e.g. hydride dissolution and brittle-to-ductile transition.

5.2.1.1 PROMETRA tests

The most extensive test programme on cladding mechanical properties under RIA conditions is the French PROMETRA programme, which has been carried out jointly by Institut de Radioprotection et de Sûreté Nucléaire (IRSN), Electricité de France (EDF) and Commissariat à l'Énergie Atomique (CEA) since 1993 [164]. The programme is intended to provide data for calibration of constitutive models for PWR cladding behaviour under RIA, and comprise tests on standard and low-tin (1.3 wt%Sn) Zircaloy-4, ZIRLO and M5 cladding materials. The tests are carried out mostly on irradiated cladding samples, taken from high-burn-up fuel rods, but also on un-irradiated, artificially corroded samples. Strain rates range from 10^{-3} to 5 s^{-1} , and testing temperatures are between 293 and 1 373 K. Some forty-odd tests have also been done under transient heating, with heating rates of either 100 or 200 K s^{-1} .

Three laboratories are engaged in the testing, and different methods and specimen geometries are used: axial tensile tests, ring tensile tests, mandrel-type tests and burst tests. Finite element methods are used to evaluate these tests, and also to fit parameters in constitutive relations by inverse modelling. This is necessary, since the specimens used for axial tensile tests and ring tensile tests give rise to complex and non-uniform stress states [165]. The results from PROMETRA show that the transient mechanical properties of cladding of high-burn-up fuel rods are influenced mainly by waterside corrosion. In particular, the tests have shown that cladding with spalled oxide can be severely embrittled by massive hydride blisters. At temperatures below 750 K, such cladding can fail without any plastic deformation, at a stress level that depends on the maximum depth of the hydride blisters. Moreover, the ductility of ZIRLO and M5 cladding is clearly higher than that of Zircaloy-4, up to a temperature of about 900 K. Further information on the PROMETRA programme can be found in [164-169]. A novel constitutive relation for Zircaloy-4 cladding under RIA loading conditions, based on data from the PROMETRA programme, is presented in [170].

5.2.1.2 GNF tests

Open-end burst tests have been carried out on Zircaloy-2 cladding in a joint programme between Global Nuclear Fuel-Japan, Toshiba Corporation and Japanese utilities [171]. The tests were done at room temperature and very high strain rate, with the intention to simulate the conditions expected

under a CZP RDA in a boiling water reactor. Thirteen tests were performed on samples fabricated from irradiated Zircaloy-2 cladding tubes with zirconium liner. The material was taken from fuel rods that had been irradiated to $7\text{--}61 \text{ MWd}(\text{kgU})^{-1}$ in commercial BWRs, and the average hydrogen content of the cladding samples ranged from 40 to 135 wppm. The irradiated samples were tested at strain rates from about 1 to 3 s^{-1} , and the hoop plastic strain to failure ranged between 0.1 and 5.8%. There was a clear inverse relationship between cladding ductility and hydrogen content.

In addition, 33 tests were done on un-irradiated cladding samples that were hydrogen-charged to average hydrogen concentrations up to 1 140 wppm. Gas-phase hydriding at 623 K was used to obtain uniform hydride distributions. All un-irradiated samples were made of standard Zircaloy-2, but in contrast to the irradiated samples, the cladding had no liner. Moreover, the material was not annealed after the final heat treatment, in order to produce a material with strength and ductility comparable to irradiated materials. The un-irradiated samples were tested at strain rates of 10^{-3} to 8 s^{-1} . The hoop plastic strain to failure for samples with more than 210 wppm hydrogen showed no strain rate dependence, whereas the failure strain of specimens with lower hydrogen concentrations dropped significantly with increasing strain rate. Moreover, un-irradiated samples with more than 210 wppm hydrogen had very low ductility, with hoop plastic strains to failure $\approx 1\%$.

It should be mentioned that about 50 additional tests have been done, using about the same materials and testing procedures as described above. However, the gaseous hydrogen charging was in some cases followed by a hydride re-orientation or re-distribution step, to obtain radial hydrides or hydride rims in the cladding samples. These tests were carried out under the auspices of the Electric Power Research Institute (EPRI) within the Nuclear Fuel Industry Research Group Program IV (NFIR-IV), and the results are proprietary [172].

5.2.1.3 JAEA tests

Burst tests have been performed on un-irradiated, hydrogen-charged cladding tubes at the Japan Atomic Energy Agency [173]. The tests were done at low temperature and with high loading rates, to simulate the conditions in a high-burn-up fuel rod under the early stage of an RIA. The material under study was low tin (1.3 wt%Sn) Zircaloy-4 cladding, which is commonly used in Japanese PWRs. The samples were hydrogen-charged to average hydrogen concentrations between 150 and 1 050 wppm in a mixture of hydrogen and argon gas at about 600 K. A uniform hydrogen distribution was introduced in most of the samples, but some samples were given pronounced hydride rims, 50-170 μm thick, at the clad tube outer surface [44,173]. Most of the burst tests were carried out at room temperature, but some of the samples, including those with hydride rims, were tested at 620 K. The strain rate ranged from 1.7×10^{-4} to $2.6 \times 10^{-1} \text{ s}^{-1}$. These strain rates are estimated from the rate of internal pressure increase under the tests, assuming elastic behaviour of the clad tube. In the plastic regime, the true strain rate is probably significantly higher.

At room temperature, the hoop plastic strain to failure for the uniformly hydrided samples dropped significantly in samples with more than 200 wppm hydrogen, which is in agreement with the GNF test results described above. At 620 K, uniformly hydrided samples showed a ductile behaviour up to at least 600 wppm hydrogen. However, the ductility of samples with hydride rims thicker than 110 μm was very low even at 620 K. The influence of hydride distribution on the failure behaviour in these tests has been studied theoretically by Kuroda *et al.* [174-175].

5.2.1.4 ANL and PSU tests

The influence of non-uniform hydride distribution on the cladding failure behaviour under RIA has been studied also by researchers at the Argonne National Laboratory (ANL) and the Pennsylvania

State University (PSU), United States. These research groups have developed novel techniques for tensile testing in both the hoop and axial direction of cladding tubes, by which the constitutive properties and failure behaviour of the material can be determined at high strain rates [176]. In particular, they have proposed a modified sample geometry for ring tensile tests, named ring stretch test (RST) specimens, in which $W_o/L_o \approx 3$ (see Figure 17). In contrast to standard ring tensile specimens, there is negligible contraction of the gauge section in the RST specimens, and a near plane-strain deformation condition in the tube axial direction is achieved [177].

In a series of tests reported by Daum and co-workers [178] at ANL, un-irradiated Zircaloy-4 cladding was tested at room temperature and 573 K, with strain rates ranging from 10^{-3} to 0.2 s^{-1} . The RST specimens were hydrogen-charged to average hydrogen concentrations up to 1800 wppm in a mixture of hydrogen and argon gas at about 600 K. The samples were given pronounced hydride rims, 20-270 μm thick, at the clad tube outer surface. The results were similar to those obtained in the JAEA tests mentioned above. More precisely, the cladding ductility in the hoop direction was found to be very sensitive to the thickness of the hydride rim at both room temperature and 573 K. The cladding was ductile when the hydride rim thickness was less than 90 μm , but brittle for hydride rims thicker than about 140 μm [178].

At PSU, tests have been done on un-irradiated Zircaloy-4 sheet material, in which solid hydride blisters with various depths were created by gaseous hydriding [92-93]. The solid hydride blisters were brittle at all test temperatures examined, from room temperature to 673 K. Failure of the sheets were attributed to a strain driven process, in which cracks are initiated through the brittle blisters at roughly the yield strain of the ductile substrate beneath the blister. As the load is increased, the crack through the blister blunts, before it eventually propagates into the substrate. The degree of blunting, and hence, the degree of resistance to fracture, was found to increase significantly with temperature.

5.2.1.5 KAERI tests

Ring tensile tests on artificially corroded, un-irradiated, low-tin Zircaloy-4 cladding have been performed at the Korean Atomic Energy Research Institute (KAERI) [90]. The tests were done at room temperature and with strain rates ranging from 10^{-2} to 1 s^{-1} . To study the effect of hydrogen on the cladding mechanical properties, samples were hydrogen-charged by the Sievert method to average hydrogen concentrations up to 1 000 wppm. The hydrogen distribution obtained in the samples was fairly uniform. To study the effect of an oxide layer, other samples were oxidized in a muffle furnace at a temperature of 740 K. In this manner, oxide thicknesses up to 100 μm were created, without notably introducing hydrogen in the samples. The cladding ultimate tensile strength and strain to failure were determined at room temperature. The latter parameter was measured by dividing the crosshead displacement at time of failure with the initial gauge length of the ring tensile specimens, L_o . The tests on both hydrided and oxidized cladding samples showed a significant effect of strain rate on cladding ductility; the higher the strain rate, the lower is the strain to failure. Moreover, the investigators concluded that the embrittling effect of the cladding oxide layer was more significant than that of the uniformly distributed hydrides [90].

In addition, results from rapid burst tests on hydrogen-charged, un-irradiated specimens of Zircaloy-4 and HANA-4 cladding have been reported by KAERI [179]. The latter alloy is a modified Zircaloy-4 material, which is developed by KAERI. It contains 1.5 wt% Nb and has a lower content of Sn than standard Zircaloy-4 cladding (see Table 19, Section 11.1). The specimens were gaseously hydrogen-charged to nominal hydrogen contents of 300 and 600 wppm. Burst tests were carried out at room temperature, 473 and 623 K, with an estimated hoop strain rate of 1 s^{-1} . In the paper by Kim *et al.* [179], results are presented in terms of hoop ultimate stress and its variation with respect to hydrogen content, testing temperature and alloy composition. Quantitative results in terms of ductility measures are not given, but the investigators report that only the samples with 600 wppm hydrogen,

when tested at room temperature, failed in a brittle mode. For lower hydrogen contents or higher temperatures, the samples were ductile. Moreover, the HANA-4 cladding was more ductile than that of Zircaloy-4, when tested at 600 wppm hydrogen and room temperature [179].

5.2.1.6 Studsvik tests

A mandrel-type of mechanical test, known as the Expansion-Due-to-Compression (EDC) test, has been developed by Studsvik Nuclear, Sweden, to measure the ductility of irradiated cladding at hoop strain rates as high as 1 to 10 s⁻¹. During testing, a piece of cladding tube is circumferentially loaded in tension due to the expansion of a polymer pellet, which is axially compressed inside the tube. From the load-displacement curve, it is possible to estimate the critical strain energy density (CSED) of the cladding, i.e. the mechanical energy per unit volume of the material, absorbed up to the point of failure [180-181]. The critical strain energy density is a measure of material ductility, which has been proposed as a cladding ductility parameter to be used in cladding failure criteria for RIA [182].

An obvious drawback with the EDC test is that the cladding axial stresses under testing are unknown, and may vary over the test section as a result of friction between the polymer pellet and the cladding and also because of bending (ballooning) of the cladding tube [183]. However, the results of EDC tests can be used for qualitative comparisons of cladding materials with respect to their ductility and survivability under RIA. A comparison of irradiated Zircaloy-4 and ZIRLO cladding was reported by Grigoriev *et al.* [184]. The material was sampled from fuel rods that had been irradiated to burn-ups of 50 to 54 MWd(kgU)⁻¹ in commercial PWRs. The average hydrogen content of the cladding samples ranged from 125 to 650 wppm, and the tests were carried out at temperatures from 298 to 613 K. Although the test series was limited to merely 9 samples, the comparison indicates that ZIRLO has superior ductility to Zircaloy-4 at comparable concentrations of hydrogen.

5.2.1.7 Kurchatov Institute tests

Four test series aimed to determine the mechanical properties of E110 cladding under RIA conditions have been carried out at the Kurchatov Institute, Russia:

- Ring tensile tests at temperatures from 293 to 1 200 K and strain rates from 0.002 to 0.5 s⁻¹.
- Burst tests at temperatures from 900 to 1 400 K, using gas as pressure medium.
- Biaxial burst tests at temperatures from 293 to 723 K, using a liquid as pressure medium.
- Axial tension tests at temperatures from 293 to 1 200 K and a strain rate of 0.002 s⁻¹.

The biaxial burst tests were carried out with two different stress biaxiality ratios, $\sigma_{zz}/\sigma_{\theta\theta}=1/2$ and $\sigma_{zz}/\sigma_{\theta\theta}=1$. Tests were done on both un-irradiated and highly irradiated material. High strain rates were used in tests carried out at low temperature, in order to simulate the rapid PCMI loading conditions under RIA. Results of the first two test series are reported in [149], and the results of the last two test series are documented in [185].

5.2.2 Clad-to-coolant transient heat transfer

Due to the rapid heating and deformation of the cladding tube, it is expected that clad-to-coolant heat transfer is much different during RIAs than under steady-state operating conditions or slow overpower transients. Both out-of-pile and in-pile tests have been carried out to investigate this issue. Of particular concern is the occurrence of a clad-to-coolant boiling crisis, i.e. a transition to a regime with film-boiling and low heat transfer at the clad-to-coolant interface. As will be shown in Section 6.2.5.2, if film-boiling and the high cladding temperatures that come with it are maintained for a sufficient period of time, the fuel rod may fail through cladding ballooning and burst, or through cladding disruption by thermal shock upon quenching.

5.2.2.1 PATRICIA tests

Clad-to-coolant heat transfer under RIA-like conditions was studied in a series of experiments in the PATRICIA test loop of CEA, Grenoble, France. This thermo-hydraulic test loop can be operated at nominal PWR conditions, and it comprises a test section in which an electrically heated and instrumented tube can be placed [94,186]. A 0.6 m long tube of Inconel, with an outer diameter of 9.5 mm, was used in the tests of interest. The tube was instrumented with thermocouples, welded to the tube inner surface at four different axial levels. The geometry of the test section was such that the flow channel cross-sectional area and equivalent heated diameter were the same as for an interior fuel rod in a 17×17 PWR fuel assembly. The hydraulic diameter, however, was different.

A first series of tests were carried out with coolant conditions corresponding to PWR inlet conditions, i.e. a pressure, temperature and axial velocity of 15 MPa, 553 K and 4 ms⁻¹, respectively. The heating rate of the tube was 2 200-4 900 Ks⁻¹. Another series of tests were done with coolant conditions typical of the NSRR, i.e. with stagnant water at 0.1 MPa and 293-317 K. The heating rate was also increased to 6 000-12 000 Ks⁻¹, in order to simulate the narrow power pulses in the NSRR. Both series of tests revealed significant kinetic effects in the clad-to-coolant heat transfer: The critical heat flux, i.e. the threshold heat flux at which a boiling crisis occurred, was significantly higher in the transient tests than under steady-state conditions. The same was true for the critical surface temperature, i.e. the surface temperature at which the transition to film-boiling took place. In the film-boiling regime, the magnitude of the heat flux was much different than under steady-state conditions. Typical values for these properties, measured in the transient tests as well as under steady-state conditions, are summarised in Table 8. It seems that the kinetic effects are most pronounced at NSRR conditions, probably as a consequence of the very high heating rate in these tests.

Table 8. Typical values of critical heat flux, critical surface temperature and film-boiling heat flux, measured in PATRICIA tests under RIA-like transients and steady-state conditions [94,187]

Measured parameter	PWR		NSRR	
	Steady-state	Transient	Steady-state	Transient
Critical heat flux [MWm ⁻²]	3	4-6	1	12
Critical temperature [K]	630	670	400	470-570
Film-boiling heat flux [MWm ⁻²]	3	1-2	0.2	1-5

It should be remarked that all PATRICIA tests were carried out with an air-filled Inconel tube as a proxy for a true fuel rod. The Inconel tube was free from surface oxide, in contrast to most fuel rods. The effect of a surface oxide layer on the clad-to-coolant heat transfer is strong, according to tests carried out in the NSRR. The same conclusion has been drawn from sensitivity studies, carried out with the SCANAIR computer code [94,187]. It has recently also been shown that irradiation enhances clad-to-coolant heat transfer, at least under steady-state conditions. The effect is known as radiation induced surface activation (RISA) [188]. Another atypical feature of the PATRICIA tests is that the Inconel tube was filled with air, and Joule heated by an electric current through the material. A cladding tube, on the other hand, is heated by a radial heat flux from the pellets. The importance of this difference in heating mode, as well as other atypical test conditions in the PATRICIA experiments, is discussed in [94].

5.2.2.2 NSRR tests

The first separate effect tests on clad-to-coolant heat transfer in the NSRR were performed out-of-pile in the late 1970s. The tests were done by dropping a heated Zircaloy-4 cylindrical rod¹⁴ into a pool with stagnant water, which had various degrees of subcooling [189]. The resulting heat-transfer phenomena were observed and recorded by high-speed photography, while at the same time,

14. Although not explicitly spelled out in the work by Mori et al, it seems that the rod was solid.

thermocouple measurements were made of the rod surface temperature. These tests showed a strong effect of coolant subcooling on the transient heat transfer: as the subcooling increased, the time with high cladding temperature and film boiling became shorter, while the quenching temperature increased [189].

Exactly the same effect of coolant subcooling was later observed under in-pile pulse irradiation tests on fresh PWR type fuel rods in the NSRR [190]. A large number of tests were carried out at the same energy deposition of $795 \text{ J(gUO}_2\text{)}^{-1}$, but with various coolant temperatures and flow rates. While the flow rate had a strong effect on the peak cladding temperature, the film boiling duration and the quenching temperature were controlled mainly by the subcooling [190]. These results are further discussed in Section 6.2.1.

In later pulse irradiation tests performed in the NSRR, it has been observed that, for comparable energy injections, corroded fuel rods show lower cladding surface temperatures than fresh rods without a surface oxide layer. A possible explanation to the temperature difference is that the oxide layer increases wettability of the cladding surface, thereby improving clad-to-coolant heat transfer. In order to verify this hypothesis, a series of pulse irradiation tests were done in the NSRR, using un-irradiated PWR fuel rods of 17×17 design with three different surface states: fresh test rods without oxide, autoclaved rods with 1 μm oxide thickness, and rods with 10 μm oxide. All test rods were instrumented with cladding surface thermocouples [191]. Transient records of the cladding surface temperature showed that the critical heat flux and the minimum heat flux were generally higher for the pre-oxidized than for the non-oxidized rods. Moreover, the duration of film-boiling was shorter for the pre-oxidized rods. However, no significant difference could be seen between rods with 1 μm and 10 μm oxide. Based on the latter observation, it was proposed that the oxide-induced improvement of surface wettability is caused by a change in chemical potential rather than a change in surface roughness [191].

The transient heat transfer mechanisms observed in the NSRR under standard cooling conditions (stagnant water at room temperature and atmospheric pressure) are discussed in a recent paper [192], where also a computer model for the heat transfer is proposed. It should also be mentioned that researchers at the JAEA have recently done out-of-pile experiments to study the kinetics of steam generation under RIA [193]. Fast-response impedance techniques and X-ray techniques were applied to measure the evolution of local void fraction around a simulated fuel rod during a CZP RIA. Although the experiment was intended primarily to verify models for transient vapour generation in neutronic/thermal-hydraulic computer codes for analyses of RIA, the results have implications to transient clad-to-coolant heat transfer.

5.2.3 Fuel-coolant interaction

In-pile separate effect tests have been carried out in the NSRR to study the interaction between solid fuel fragments and water [118]. Fuel-coolant interaction is usually studied in connection with fuel rod failure in RIA simulation tests, but the tests in [118] were intended to separate the FCI phenomenon from the fuel rod failure mechanisms. In particular, the tests aimed to determine the relation between thermal-to-mechanical energy conversion ratio and the size of solid fuel particles.

A vinyl bag, containing water and 30 g of un-irradiated 10 wt% enriched UO_2 particles with a specific size, was placed in a water filled and instrumented test capsule. The sample was pulse irradiated in the NSRR to a peak fuel enthalpy of about $500 \text{ J(gUO}_2\text{)}^{-1}$. The peak fuel temperature was estimated to be about 1 900 K, i.e. well below the fuel melting point. The generated mechanical energy was measured from the kinetic energy of the jumping water column in the test capsule. Results from four tests with particle diameters in the range of 20 to 250 μm clearly showed the typical inverse relationship between thermal-to-mechanical energy conversion ratio and fuel particle size; confer the data presented in Section 4.3.1. The highest energy conversion ratio, 0.41%, was obtained for the 20 μm particles. The particles with a diameter of 250 μm gave a conversion ratio of merely 0.04% [118].

6. SPECIFIC PHENOMENA UNDER RIA AND THEIR EXPERIMENTAL BASIS

In the following subsections, we describe phenomena with particular importance to fuel rod behaviour under RIAs. For the fuel pellets, we treat heat-up, melting, fragmentation, fission gas induced transient swelling and transient fission gas release, and for the cladding tubes, we consider heat-up, melting, transient deformation, oxidation and failure. In a separate subsection, we consider how the cladding tube behaviour is influenced by hydrogen-induced embrittlement. The phenomena are discussed in light of experimental data as well as computer simulations. Unless otherwise stated, the SCANAIR-3.2 fuel rod analysis programme [194] is used for the computations (see Section 8.2 for a brief description of this programme).

6.1 Fuel pellets

6.1.1 Fuel pellet heat-up and melting

The melting (solidus) temperature of un-irradiated UO_2 is 3120 ± 30 K and the enthalpy to melt is about $1\,150 \text{ J(gUO}_2\text{)}^{-1}$ [59,195]. This enthalpy threshold defines the *local* enthalpy associated with incipient melting of un-irradiated UO_2 , and it is therefore not directly comparable to the *radial average* fuel enthalpy that we are otherwise concerned with in this report. Since the radial temperature distribution in the fuel pellet is non-uniform, incipient melting of UO_2 fuel generally occurs at radial average fuel enthalpies lower than $1\,150 \text{ J(gUO}_2\text{)}^{-1}$. This is further discussed below.

Under the initial phase of an RIA, the fuel is heated almost adiabatically, i.e. without heat transfer taking place either inside the fuel pellets or across the pellet-clad gap. During this initial heat-up phase, the radial temperature profile in the pellet therefore agrees very closely to the radial power profile; the faster the energy deposition, the closer is the agreement. This is illustrated in Figure 18, which shows the calculated radial temperature distribution for the REP-Na5 rod in the CABRI pulse reactor; see section A.6 in appendix A for details on this test. The temperature distribution is calculated at the peak power axial position and at the time of maximum power by use of the SCANAIR-3.2 programme. The normalised radial power profile is shown for comparison. Due to the high burn-up of the fuel, $64.4 \text{ MWd(kgU)}^{-1}$ pellet radial average value, the power and temperature profiles are strongly peaked to the pellet surface. Figure 19 shows how the radial power profile evolves with time in the REP-Na5 test rod. For reference, $t=0$ defines the time at which maximum power is reached. According to our calculations, the fuel temperature reaches a local maximum about 7 ms later for this particular case, in which the pulse width is 8.8 ms. When the power excursion is terminated, heat conduction lowers the pellet surface temperature, and the temperature distribution approaches its normal, almost parabolic, shape.

Due to the surface-peaked temperature distribution in combination with the burn-up-induced depression of fuel melting temperature at the pellet periphery (see Figure 11), fuel melting under rapid RIAs, such as REAs and RDAs, will first occur at a radial position approximately 0.2-0.5 mm beneath the pellet surface. The peak temperature position moves slightly outward with increasing burn-up, as a result of the change in radial power distribution. This burn-up dependent change in radial temperature profile is illustrated in Figure 20, which shows the calculated temperature profile across the pellet radius at time of incipient fuel melting in low- and high-burn-up UO_2 fuel.

Figure 18. **Typical temperature (dashed line) and power (solid line) distribution in high-burn-up fuel, subjected to a fast (8.8 ms) power pulse**

Simulation of the CABRI REP-Na5 pulse reactor test, by use of the SCANAIR-3.2 computer code. The results refer to the peak power axial position and time.

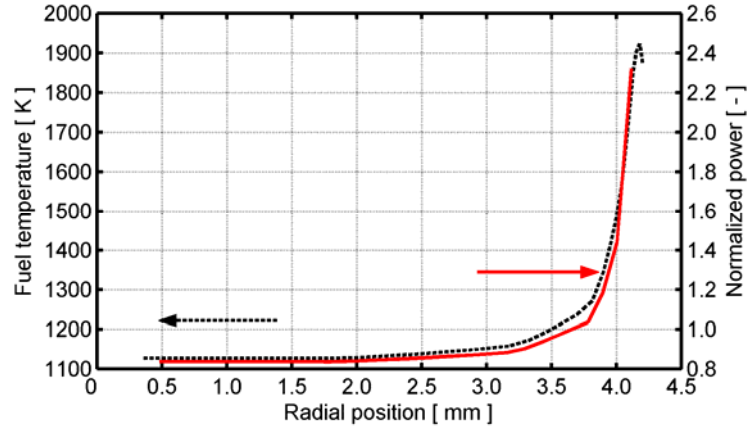


Figure 19. **Evolution of the fuel temperature profile in rod REP-Na5, calculated with the SCANAIR-3.2 computer code. In the calculations, $t=0$ defines the time at which maximum power is reached.**

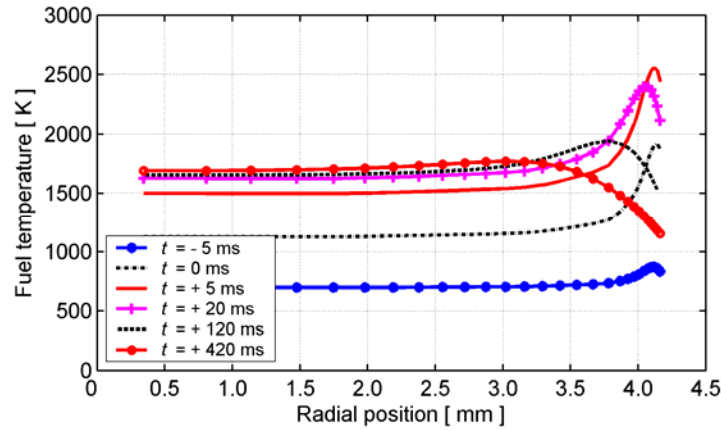
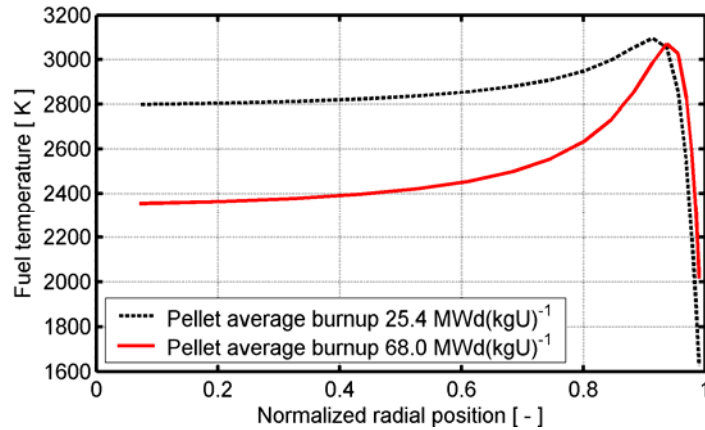


Figure 20. **Calculated variation in fuel temperature across the pellet radius at time of incipient fuel pellet melting in UO_2 PWR fuel under a postulated HZP REA [196-197].**

The power pulse applied in the calculations had Gaussian shape, and the pulse width (FWHM) was 25 ms.

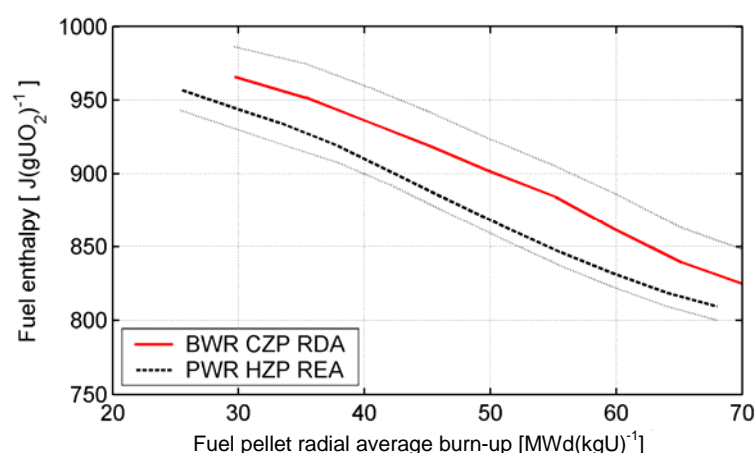


As shown in Figure 20, the temperature profile at high burn-up is strongly peaked to the pellet periphery, which means that a certain peak temperature is reached at a lower radial average fuel enthalpy at high burn-up than at low burn-up. The burn-up dependent change in radial distribution of power and temperature within the fuel pellet, together with the burn-up-related depression of fuel melting temperature, as described in Section 3.1.4, implies that the radial average enthalpy for fuel incipient melting decreases with burn-up. To study this phenomenon in detail, calculations have been made with best-estimate computer codes that consider the burn-up effects on both radial power profile and melting temperature of typical UO_2 fuel [196,198]. An example is given in Figure 21, which shows enthalpy thresholds for incipient fuel melting, calculated with SCANAIR-3.2 for a typical CZP RDA and HZP REA [196]. The thresholds are given in terms of peak radial average fuel enthalpy, plotted with respect to fuel pellet radial average burn-up. The calculated enthalpy thresholds drop moderately with increasing fuel burn-up, and notwithstanding the differences in fuel rod designs and postulated accident scenarios between the RDA and the REA, the calculated fuel melting thresholds for these two events are similar. The threshold for the RDA is 10-20 $\text{J}(\text{gUO}_2)^{-1}$ higher, mainly as a result of the wider power pulse. The wider power pulse in the postulated RDA (45 ms) in comparison with the REA (25 ms) leads to a somewhat more uniform temperature profile across the fuel pellet radius. Consequently, for the same radial peak temperature, the pellet radial average fuel enthalpy will be higher under the RDA than under the REA.

It is interesting to extrapolate the calculated fuel pellet melting thresholds in Figure 21 to zero burn-up. From the nearly constant slopes of the curves, we expect the radial average enthalpy to melt for fresh UO_2 fuel to be about $1\,070\text{ J}(\text{gUO}_2)^{-1}$. This value is in fair agreement with the enthalpy to melt observed in early pulse reactor tests on fresh UO_2 fuel rods [111,113]. However, direct comparisons with these tests are difficult, since the fuel enrichment in the test rods was exceptionally high (10-20 wt% ^{235}U), and the tests were carried out with narrow power pulses. These factors promote peaking of the temperature profile towards the fuel pellet periphery, which tends to lower the radial average enthalpy to melt. The lowest radial average fuel enthalpy, for which incipient fuel pellet melting has been observed experimentally, is, to the authors' best knowledge, $975\text{ J}(\text{gUO}_2)^{-1}$. This value pertains to rod CDC-504, a fresh UO_2 fuel rod with an enrichment of 10.5 wt% ^{235}U , which was tested in the SPERT [113].

Figure 21. Best-estimate thresholds for UO_2 fuel pellet melting under postulated BWR CZP RDA and PWR HZP REA [196]

The uncertainty band, indicated by the thin dotted lines, corresponds to $\pm 30\text{ K}$ uncertainty in fuel melting point prediction.



To extend the discussion on fuel melting from pure UO_2 fuel to $(\text{U,Pu})\text{O}_2$ mixed oxide fuel, it is necessary to consider:

- The effect of plutonium on the solidus temperature of $(\text{U,Pu})\text{O}_2$.
- The heterogeneous chemical composition of MOX fuel pellets.
- The effect of plutonium on the radial distribution of power and temperature in MOX fuel pellets.

The solidus temperature T_s of MOX fuel decreases monotonously with increasing fraction of Pu, and for un-irradiated $(\text{U,Pu})\text{O}_2$, it can be correlated to the fuel mole fraction, y , of PuO_2 through [199]:

$$T_s = 3120 - 655.3 y + 336.4 y^2 - 99.9 y^3, \quad 12$$

where T_s is in kelvin.

The bulk mole fraction of PuO_2 in typical light water reactor MOX fuel is 0.05-0.07. According to Equation 12, the bulk melting temperature of the material would thus be 30-45 K lower than that of pure UO_2 . However, one has to consider that the plutonium is not uniformly distributed in the most common type of MOX fuel. The heterogeneous chemical composition results from the fuel fabrication processes, in which $(\text{U,Pu})\text{O}_2$ particles are blended into a matrix of depleted UO_2 . The particles range up to several tens of microns in size, and they contain 25-30% PuO_2 . This leads to two phases in the fresh MOX fuel: $(\text{U,Pu})\text{O}_2$ agglomerates with $y=0.25-0.30$, and a depleted UO_2 matrix with $y=0$ [42].

From Equation 12, we estimate that the solidus temperature of Pu-rich agglomerates is about 140-170 K lower than for UO_2 . Moreover, heat generation is concentrated to the agglomerates, since they contain most of the fissile material. The combination of a high local temperature and a low local melting point makes the agglomerates preferential sites for fuel melting, and it is reasonable to believe that local melting can occur at lower radial average fuel enthalpies in MOX fuel than in pure UO_2 . However, there is no clear experimental evidence for this hypothesis. Some indication of local melting of Pu-rich particles is reported from tests on fresh MOX fuel rods in the NSRR [200], which were done on MOX fuel with large (400-1100 μm) PuO_2 particles artificially embedded at the surface of the MOX fuel pellet. Local melting of these large particles, as well as some adjacent material, was observed [200]. The total energy deposition ranged from 737 to 988 Jg^{-1} in the tests, and it is not clear from [200] whether local melting was observed over the entire energy range, or only for the highest energy depositions. The main conclusion of the work was that the artificially implanted PuO_2 particles had no significant effect on the fuel rod failure behaviour. Similar experiments in the SPERT, however, indicated an increased sensitivity to cladding failure due to large PuO_2 particles in MOX fuel [201].

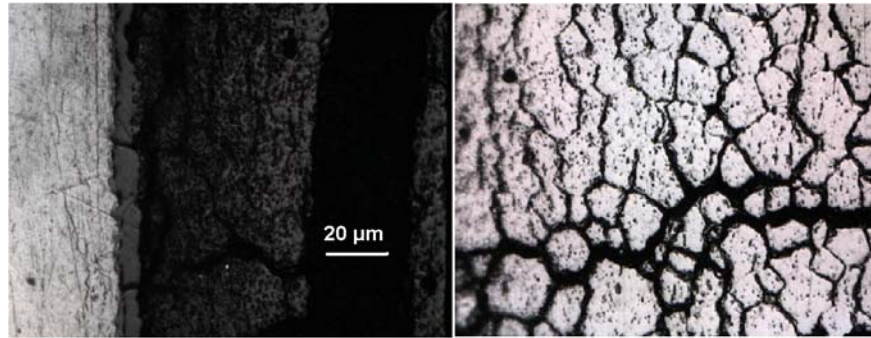
Finally, it should be remarked that no local fuel melting was observed for the REP-Na9 MOX fuel rod from the REP-Na test series in CABRI [86], even though the peak radial average fuel enthalpy reached 824 Jg^{-1} . This would suggest that the radial average fuel enthalpy threshold for incipient melting of MOX fuel is fairly close to the threshold for UO_2 fuel, but additional tests on MOX fuel are needed to draw a definite conclusion on this issue.

6.1.2 Fuel pellet transient fragmentation and swelling

In ceramographic examinations of high-burn-up fuel, which has undergone a simulated RIA in pulse reactors, it is usually found that the outermost part of the pellet is fragmented [44,202]. Typically, a large number of radial cracks are seen at the pellet surface, and these cracks extend a few millimetres towards the pellet centre, i.e. well beyond the re-structured rim zone. These cracks are probably caused by tensile hoop stresses during cool-down of the pellet periphery, i.e. the cracks nucleate late in the transient. In some cases, circumferential cracks are also found at the boundary between the re-structured rim zone and the subjacent part of the pellet. These cracks are attributed to tensile radial stresses during the early heat-up phase.

The radial and circumferential cracks described above create fairly large ($\approx 500\ \mu\text{m}$) fuel pieces, but in most RIA simulation tests on high-burn-up fuel in CABRI and the NSRR, much finer ($< 50\ \mu\text{m}$) fragments have also been observed in post-test examinations (see Figure 22). These fragments are found predominantly in the external part of UO_2 fuel pellets, whereas in MOX fuel, they occur close to Pu-rich agglomerates over large parts of the pellet [86]. The fine fragments are most likely a result of grain boundary decohesion, caused by overpressurisation of gas-filled pores and intergranular bubbles under rapid rise in temperature [203]. The internal gas pressure induces high tensile stresses, which may break the grain boundaries and/or result in swelling of the material.

Figure 22. Fuel pellet fragments observed after CABRI test REP-Na5. Cladding and fuel rim region to the left, and fuel sample from a position $200\ \mu\text{m}$ beneath pellet surface to the right [204]



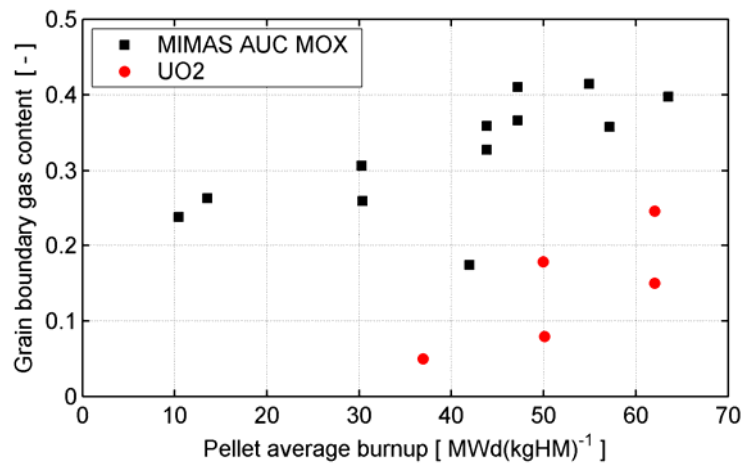
If the grain boundaries break, the resulting fuel fragments are small and can therefore be easily expelled through cladding cracks in a failed fuel rod [84,202]. Hence, post-failure fuel dispersal is promoted by this fragmentation mechanism for high-burn-up fuel (see Section 7.2.2). Moreover, grain decohesion is also believed to aggravate fuel-coolant interaction, due to the large surface-to-volume ratio of the small fragments (see Section 4.3.1). Another consequence of grain boundary decohesion is the burst release of helium and gaseous fission products, notably Xe and Kr, which are stored in intergranular bubbles and pores. This is further discussed in Section 6.1.3 below.

The phenomena of grain boundary decohesion and swelling are principally governed by the fuel temperature and the concentration of fission gas in grain boundaries. As shown in Section 6.1.1, the pellet temperature profile in high-burn-up UO_2 fuel is strongly peaked to the pellet surface under the early heat-up phase of an RIA. Consequently, the high-burn-up microstructure at the pellet rim, with its high density of grain boundaries and gas filled pores, is believed to play an important role for grain decohesion and transient swelling under RIA. In UO_2 fuel with $60\text{--}65\ \text{MWd}(\text{kgU})^{-1}$ pellet average burn-up, it has been estimated that the high-burn-up microstructure at the pellet rim answers to about half of the total grain boundary gas inventory, and to about 10% of the total gas inventory of the pellet [86]. In MOX fuel, the major portion of grain boundary gas is located in large pores within the $(\text{U,Pu})\text{O}_2$ agglomerates.

Figure 23 shows estimates of the grain boundary gas content, based on measurements on irradiated PWR UO_2 and MOX fuel [86,205]. In spite of the large scatter observed in the results, it is clear that the grain boundary gas concentration is higher in MOX than in UO_2 fuel at similar burn-up. The difference is pronounced at low and medium burn-up, i.e. below $30\text{--}40\ \text{MWd}(\text{kgHM})^{-1}$, but decreases at higher burn-up because of the decreasing influence of Pu-rich agglomerates in the MOX fuel and the increasing fraction of re-structured material at the pellet rim in the UO_2 fuel. The difference in grain boundary gas content, shown in Figure 23, suggests that MOX fuel has a stronger propensity for grain boundary decohesion and transient swelling under RIA than UO_2 fuel. However, one has to consider not only the *average concentration* of grain boundary gas in the pellet, but also its *radial distribution* in comparison with the radial temperature profile.

Fuel transient swelling from growth of over-pressurised pores and bubbles could possibly add to the thermal expansion, and thus aggravate the pellet-clad mechanical interaction in high-burn-up fuel. However, the current view seems to be that gaseous swelling is too slow to contribute to PCMI loading under the early heat-up phase of an RIA in UO_2 fuel rods, but that the phenomenon may play a role for MOX fuel. If gaseous swelling does occur in UO_2 fuel, it is believed to follow *after* the power pulse, at a time when the cladding is heated and the material therefore able to withstand large plastic deformation without rupture [156,206]. This conclusion is based mainly on the observation that computer codes for analyses of fuel rod behaviour under RIA are able to accurately reproduce fuel rod deformations in most RIA simulation tests merely by considering thermal expansion of the fuel pellets. The codes fail to reproduce deformations only in tests where a boiling crisis occurs, and the fuel rod is held at high temperature for a considerable period of time (>10 s).

Figure 23. Pellet average grain boundary gas content, in fraction of the total amount of gas created, versus pellet average burn-up in UO_2 and MIMAS AUC MOX fuel [86,205]



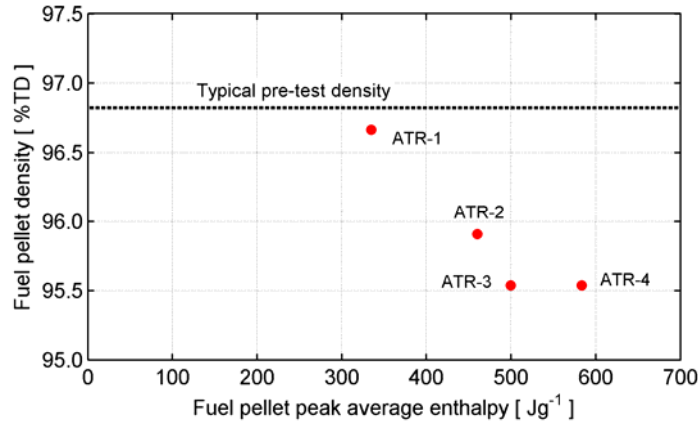
Possible differences between high-burn-up MOX and UO_2 fuel with respect to PCMI loading under the early heat-up phase of an RIA have been studied on the basis of results from the CABRI REP-Na test series by Vitanza and Conde-Lopez [207]. The investigators found no significant difference in PCMI behaviour between MOX and UO_2 fuel, at least not for transient fuel enthalpy increments lower than 500 Jg^{-1} . It should also be remarked that fuel transient swelling has been confirmed by post-test ceramography for only two rods in the CABRI REP-Na test series: REP-Na2 (UO_2) and REP-Na9 (MOX) [86]. As shown in Section A.6, Appendix A, these rods experienced the highest radial fuel enthalpies in the REP-Na test series, 832 and 824 Jg^{-1} , respectively.

Transient swelling of irradiated MOX fuel under RIAs has also been studied in pulse irradiation tests of ATR MOX fuel rods in the NSRR (see Section A.5.3 in Appendix A). These tests, most of which were performed on fuel with an average pellet burn-up of $20 \text{ MWd(kgHM)}^{-1}$, show that transient fission gas swelling is more pronounced in MOX fuel than in UO_2 fuel at similar burn-ups [44-45]. The degree of transient swelling was determined by post-test measurements of fuel pellet density, and the results are shown in Figure 24. The decrease of fuel density under the test, i.e. the volumetric transient swelling, is about 1% for the tests with peak fuel enthalpies above 450 Jg^{-1} . This corresponds to a linear expansion of roughly 0.3%, if one assumes that the fuel swelling is isotropic. For comparison, the linear *thermal* expansion of the fuel at an enthalpy of 450 Jg^{-1} is about 1.8%, which means that the contribution from transient gaseous swelling to the total fuel pellet deformation was moderate. However, the tested fuel had fairly low burn-up, and a more substantial contribution from gaseous swelling is expected in high-burn-up fuel, due to its higher fission gas content. One could also argue that the fuel gaseous swelling at hot fuel conditions is probably larger than the residual swelling that is measured at room temperature in post-

test examinations. To this end, it should be remarked that it is impossible to determine from post-test examinations of pulse irradiated fuel rods whether the fuel swelling occurred early during the transient, and thus contributed to the PCMI, or if it took place at a later stage.

Figure 24. **Change of fuel pellet density versus peak radial average fuel enthalpy during pulse irradiation tests, carried out on ATR MOX fuel in the NSRR [45].**

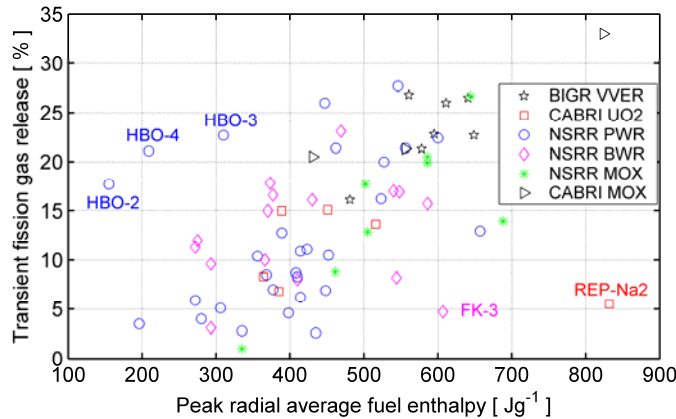
The pellet average burn-up was $20 \text{ MWd}(\text{kgHM})^{-1}$ for all tests shown in the figure (see Section A.5.3 in Appendix A).



6.1.3 Transient fission gas release

Transient release of gaseous fission products, retained in the fuel pellets, may increase the fuel rod internal gas pressure. The transient release of retained fission gas under RIA simulation tests on high-burn-up UO_2 fuel rods is generally high, typically in the range from 5 to 25% of the gas produced and accumulated in the fuel, and the release fraction correlates with peak fuel enthalpy under the tests [68,107,203]. This is shown by Figure 25, in which the transient fission gas release is plotted with respect to peak fuel enthalpy for pre-irradiated UO_2 and MOX fuel rods that have been tested in CABRI, BGR and the NSRR (see Appendix A).

Figure 25. **Measured transient fission gas release for pre-irradiated UO_2 and MOX fuel rods, tested in CABRI, BGR and the NSRR (see Appendix A). The release is given in percent of the produced gas.**



The correlation between transient fission gas release fraction and peak fuel enthalpy is fair, except for the five outliers marked in Figure 25. No explanations to the exceptional behaviour of these five rods can be found in literature, but there is some evidence that transient gas release under RIA is

influenced by the steady-state power history experienced by the fuel prior to the transient. Fuel rods operated at high steady-state linear heat generation rate (LHGR) have shown large gas release, not only under steady-state reactor operation, but also under subsequent pulse reactor tests in the NSRR [44]. This could have two possible explanations:

- The distribution of fission gas within the fuel pellet, in particular the partitioning of gas between intra- and intergranular bubbles, is affected by the conditions under steady-state pre-test operation. It is likely that irradiation conditions that result in a high fraction of intergranular gas lead to high release fractions under both steady-state operation and under the subsequent RIA simulation test.
- Release paths for the fission gas, generated during steady-state operation, may play a role also for transient fission gas release under the RIA simulation test.

The last hypothesis is less credible, since transient gas release under RIA takes place predominantly by other mechanisms than the thermal diffusion process that is operative under normal steady-state operation. As already mentioned in Section 6.1.2, fuel fragmentation through grain boundary decohesion provides a mechanism for prompt release of gas from intergranular bubbles, which is particular to RIA [203,208]. It has been concluded that this release mechanism dominates the fuel transient fission gas release under RIAs [86]. A fairly recent review of burst release phenomena and related data can be found in [209].

The non-uniform buildup of fissile plutonium isotopes in the fuel pellets, as described in Section 3.1.2, can be used to trace the radial location in the fuel, from which released fission gas originates. As shown in Table 9, the fractional yields of stable isotopes of Xe and Kr differ between ^{235}U , ^{239}Pu and ^{241}Pu , which are the dominant fissile isotopes in irradiated UO_2 fuel. Gas released from the plutonium-rich rim zone of the pellet has therefore a higher Xe/Kr ratio than gas released from the pellet centre, and the radial location where fission gas is released can thus be estimated by measuring the Xe/Kr-ratio of released gas [210].

**Table 9. Cumulative yields of stable isotopes of Xe and Kr.
From the OECD/NEA database through White [211].**

The fractional yield refers to the fraction of fissions resulting in production of the isotope.

Stable isotope	Fractional yield		
	^{235}U	^{239}Pu	^{241}Pu
^{131}Xe	0.02887	0.03867	0.03067
^{132}Xe	0.04273	0.05263	0.04078
^{134}Xe	0.07749	0.07562	0.07599
^{136}Xe	0.06270	0.06940	0.06714
Total Xe	0.21179	0.23632	0.21458
^{83}Kr	0.00549	0.00288	0.00200
^{84}Kr	0.01006	0.00474	0.00350
^{85}Kr	0.00287	0.00130	0.00085
^{86}Kr	0.01964	0.00770	0.00606
Total Kr	0.03807	0.01662	0.01241
Xe/Kr	5.56	14.22	17.29

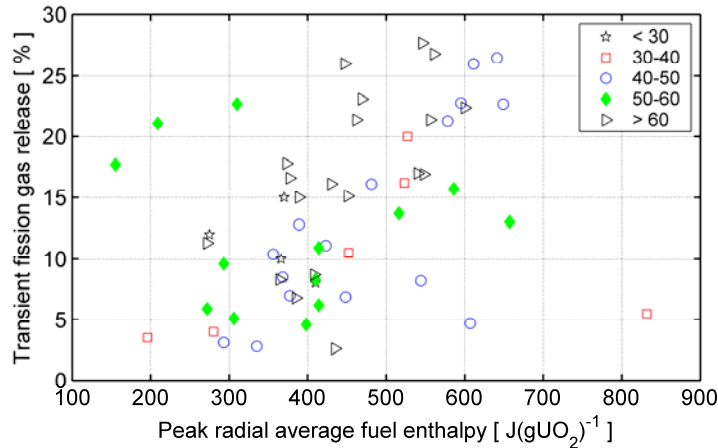
Isotopic gas analyses have been applied to study transient fission gas release in five pre-irradiated PWR fuel rods, tested in the NSRR [212]. The rods, HBO-2/3/4/6 and 7, had similar burn-ups in the range of 49 to 50 $\text{MWd}(\text{kgU})^{-1}$ (see Section A.5.1.2 in Appendix A). The isotopic analyses showed that

the fission gas was released from the peripheral region of the fuel pellet in two tests (HBO-3 and HBO-4) where fine radial cracks formed at the pellet periphery under the pulse irradiation. For the other three tests, where peripheral radial cracks did not form in the pellet, the isotopic analyses revealed that the fission gas was uniformly released from the whole pellet. The transient fission gas release was also significantly lower for these tests. In conclusion, the results from the isotopic analyses of the HBO test rods confirm the hypothesis that fuel fragmentation and cracking play an important role for transient fission gas release under RIAs.

Isotopic gas analyses have also been conducted on pre-irradiated BWR fuel rods, tested in the NSRR [68,156,213]. The burn-up of these rods ranged from 41 to 61 MWd(kgU)⁻¹, and the transient fission gas release during the tests ranged from 3 to 17%. According to the results of these isotopic gas analyses, the high-burn-up structure at the pellet rim did not significantly contribute to the gas release.

Figure 26 shows the transient fission gas release for pre-irradiated UO₂ fuel rods. The data have been divided into five groups, according to fuel pellet average burn-up in the tested rod. There is no obvious correlation between fission gas release fraction and fuel burn-up. This is somewhat inconsistent with the assumption that transient fission gas release under RIAs takes place by grain boundary opening: from the estimation of UO₂ grain boundary gas content in Figure 23, one would expect an increasing release fraction with increasing burn-up. It is also interesting to note that the highest fission gas release fractions observed in the tests on UO₂ fuel rods is about 25%. According to Figure 23 in Section 6.1.2, this would correspond to the release of practically all the fission gas that is accumulated in grain boundaries.

Figure 26. **Measured transient fission gas release for pre-irradiated UO₂ fuel rods, tested in CABRI, BGR and the NSRR (see Appendix A)**
The legend denotes fuel pellet burn-up in MWd(kgU)⁻¹.



From simultaneous on-line measurements of clad deformation and rod internal gas pressure under pulse reactor tests in the NSRR, it is clear that the pressure loading from fission gas release comes into play somewhat later than the PCMI-induced loading from the thermally expanding fuel pellets [68,214]. Hence, transient fission gas release is probably too slow to contribute to clad mechanical loading under the critical heat-up phase of an RIA, but still, it increases the risk for clad high temperature rupture later in the transient (see Section 6.2.5.2). The observed delay in fission gas release can be explained by the fact that compressive stresses, imposed on the fuel pellet from mechanical contact with the cladding tube, have to be relaxed for the grain boundaries to open and let the gas escape to the pellet-cladding gap. This phenomenon is well known from experiments with on-line measurements of fission gas release, in which significant gas release is often observed when the pellet-clad gap re-opens as a result of reduced fuel rod power [209].

It has recently been pointed out that also the burst release of helium from fuel grain boundaries may contribute to fuel rod internal pressure loading under RIA [205]. Some helium migrates from the pellet-clad gap into the fuel pellet by thermodiffusion, but the major part of helium occluded in high-burn-up fuel is produced within the fuel itself by neutron reactions with alpha particles during and after in-reactor operation. These reactions are more pronounced in MOX fuel than in UO_2 [205]. It has been estimated that the release of helium in the CABRI REP-Na test series corresponded to up to 30% of the released fission gases, both for UO_2 and MOX fuel [86]. Further studies on the role of helium release from high-burn-up fuel under RIA are therefore warranted.

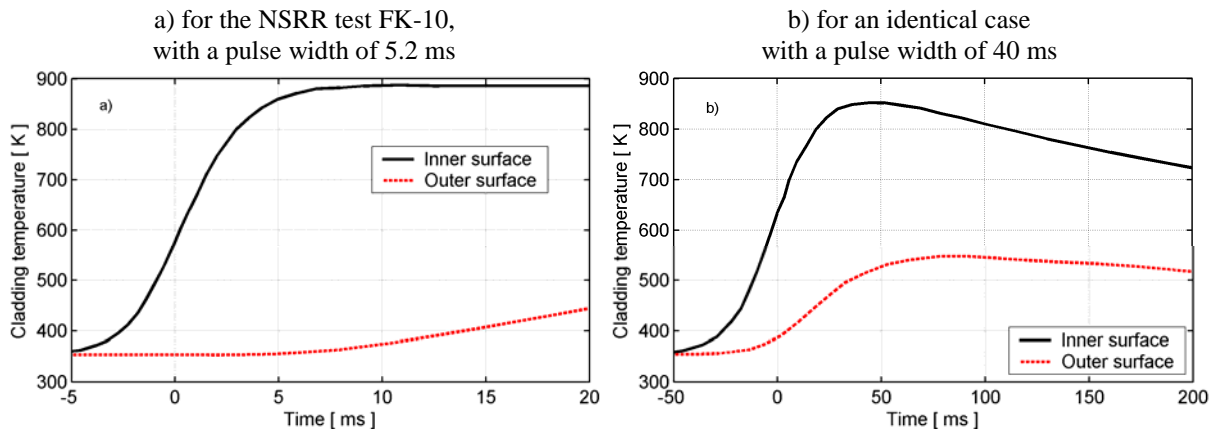
6.2 Cladding tubes

6.2.1 Cladding heat-up and melting

The cladding tube is heated primarily by heat conduction from the fuel pellets, but there is also a heat source stemming from attenuation of gamma radiation in the cladding material. The gamma heating takes place immediately upon a rise in fission rate, and the heating is practically uniform throughout the cladding material. The heat conduction from the pellets, on the other hand, is delayed by the pellet-clad gap. The time lag between a rise in fission rate and the heat flux arriving at the clad inner surface depends on the gap state: a wide open gap constitutes a significant barrier to the pellet-clad heat flow, whereas a closed gap with pellet-clad contact and bonding has very little thermal resistance [71].

Another important difference between prompt heating from gamma ray attenuation and delayed heating by conduction across the pellet-clad gap is that the latter leads to non-uniform heating of the cladding tube. This is illustrated in Figure 27a, which shows the calculated time-temperature history of the cladding inner and outer surfaces under the RIA simulation test FK-10. This is one of the most recent tests on high-burn-up BWR fuel rods conducted in the NSRR (see Section A.5.2.2 in Appendix A). The calculations were made by Suzuki *et al.*, using the RANNS code, and Figure 27 is extracted from their work [215]. The calculated temperature difference between the inner and outer surface of the cladding is striking in Figure 27a. To study the effect of pulse width, Suzuki and co-workers repeated the calculations with a wider pulse, keeping the peak radial average fuel enthalpy and all other properties unchanged [215]. The results are shown in Figure 27b. According to the calculations, the cladding inner surface temperature reaches 850-900 K, irrespective of pulse width, but the radial temperature gradient across the cladding wall is significantly milder for the wider power pulse.

Figure 27. Calculated cladding temperature



The plots are created from the results in [215], defining $t=0$ as the time at which peak power is reached. The temperature difference between the inner and outer surfaces reaches more than 500 K for the narrow pulse, and about 350 K for the wider pulse.

The non-uniform temperature distribution under the cladding heat-up phase is important to the cladding behaviour for several reasons. Firstly, since temperature has a strong effect on cladding mechanical properties, the material's response to transient mechanical loading will vary significantly across the cladding wall thickness. In particular, the material at the hot inner surface of the cladding will have lower yield strength and higher ductility than the material at the cold outer surface.

In high-burn-up fuel, this trend is further enhanced by the non-uniform distribution of hydrogen in the material. As discussed in Section 6.2.5.1, fractographic examinations of high-burn-up fuel rods that have failed by PCMI in RIA simulation tests generally show a ductile behaviour of the inner part of the cladding, also when the cladding is highly corroded. This is most likely an effect of high local temperature.

Secondly, the radial temperature gradient across the cladding thickness gives rise to thermo-elastic stresses, which add to the mechanical loading. The thermo-elastic hoop stress is tensile at the cold cladding outer surface and compressive at the hot inner surface. For reasons of mechanical equilibrium, the absolute magnitude of the hoop stress is nearly equal at the inner and outer surface, and the magnitude depends almost linearly on the temperature difference across the cladding wall. A simple analysis, in which only thermal loads and thermo-elastic deformation of the cladding tube are considered, shows that the hoop thermo-elastic stress reaches about 250 MPa at the cladding outer surface for the case shown in Figure 27aa, and about 175 MPa for the case in Figure 27b. These results, which are obtained through Equation 15 in Section 6.2.5.2, suggest that cladding thermo-elastic stresses should be accounted for in analyses of the early heat-up phase of an RIA. However, once the cladding has started to yield by plastic deformation or high-temperature creep, or heat conduction has reduced the radial temperature gradient, the analyses by Suzuki *et al.* [215] show that thermo-elastic stresses lose their importance.

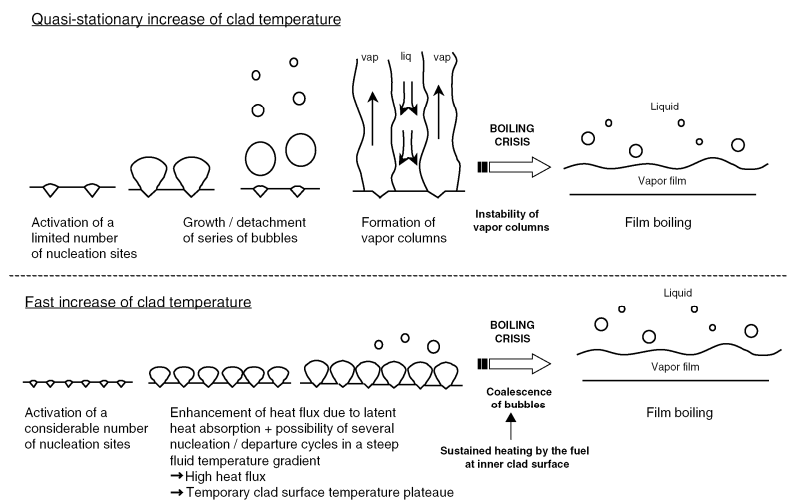
Thirdly, the significant difference between inner and outer surface temperature makes partial melting of the cladding wall possible. Melting of the inner part of the cladding wall has been observed in RIA simulation tests on fresh and low-burn-up UO_2 fuel rods, carried out with peak radial average fuel enthalpies between approximately 860 and 950 $\text{J(gUO}_2\text{)}^{-1}$ in the SPERT and the NSRR [113,152]. Hence, incipient clad melting seems to occur at slightly lower fuel enthalpy levels than incipient fuel pellet melting (see Section 6.1.1). The melting (solidus) temperature of the cladding depends on alloy composition and the material's content of oxygen and hydrogen. For example, the solidus temperature of Zircaloy-4 is about 2035 K in as-fabricated state, but may increase by hundreds of kelvin as a result of oxygen uptake under high-temperature accident conditions [216].

The peak cladding temperature reached under a LWR RIA depends on whether or not a boiling crisis occurs at the clad-to-coolant interface. As already mentioned in Section 5.2.2, separate effect tests have revealed that there are significant kinetic effects involved in the clad-to-coolant heat transfer under fast power transients, and the boiling crisis under RIA therefore differs from that under quasi-stationary conditions. As shown in Table 8, the critical heat flux, i.e. the threshold heat flux at which a boiling crisis occurs, is significantly higher under fast transients than under stationary conditions, and the film boiling heat flux is also much different. Figure 28 gives a schematic view of the mechanisms behind a boiling crisis (DNB) under a fast RIA in comparison with the mechanisms under quasi-stationary heat transfer conditions [192]. The illustration of the transient mechanisms in Figure 28 is based on visual observations of clad-to-coolant heat transfer under RIA simulation tests on fresh fuel rods in the NSRR [217]. In these tests, a periscope allowed observations of the cladding surface during the pulse irradiation, and a high-speed camera was used to capture the vapour film formation. The temperature history of the cladding surface was simultaneously recorded by use of thermocouples.

Although little is known about the nature of boiling crises under RIA conditions typical for LWRs, the data at hand from pulse reactor tests and separate effect tests indicate that the energy

deposition to the fuel, the coolant subcooling, the pellet-clad gap size and the cladding oxide layer thickness decide whether a boiling crisis will occur or not [94,186,218]. Significant energy depositions are needed for a boiling crisis to occur at high initial subcooling, whereas lower energies are needed when the coolant is close to saturation. The pellet-clad gap size is also known to affect the threshold energy deposition; a narrow or closed gap promotes the boiling crisis [111]. Likewise, the boiling crisis seems to cause higher cladding temperatures for fuel rods with a thin or spalled clad oxide layer than for rods with thick and uniform oxide [191]. The positive effects of the cladding oxide layer on clad-to-coolant heat transfer under RIA are attributed to an increase of surface wettability, as described in Section 5.2.2.2. In conclusion, film boiling and high cladding temperature are therefore more likely for LWR RIAs that initiate from hot operating conditions, and particularly for fuel rods with closed pellet-clad gap and thin or spalled oxide.

Figure 28. **Mechanisms for boiling crisis in single phase liquid water under quasi-stationary and transient conditions**



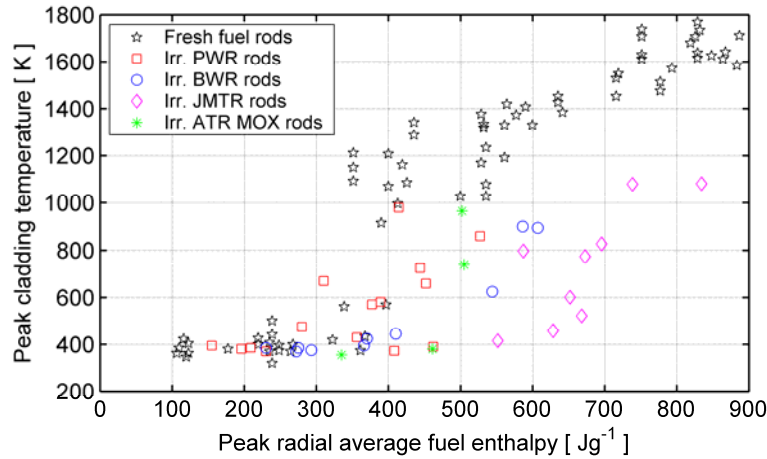
The picture is reproduced from [192] with permission of the AESJ (CY-RT-003).

Many pulse irradiation tests in the NSRR have been carried out on fuel rodlets with 2-3 thermocouples spot-welded to the cladding surface, and on-line measurements of the cladding outer surface temperature are available for these tests. Figure 29 summarises the peak cladding surface temperatures, recorded in NSRR tests on fresh and pre-irradiated fuel rods. All tests were done with near-zero initial rod power and enthalpy. The coolant was stagnant water at ambient temperature and atmospheric pressure. The sources of data for pre-irradiated PWR, BWR and ATR rods are defined in Section A.5 of Appendix A, data for fresh fuel rods are taken from [48], and data for rods pre-irradiated in the JMTR are from [68].

The data in Figure 29 illustrate the aforementioned influence of pellet-clad gap width on the enthalpy threshold for boiling crisis. Due to differences in burn-up, coolant overpressure and rate of cladding creep-down, fuel rods pre-irradiated in the JMTR have the widest pellet-clad gaps, whereas PWR-irradiated rods have the narrowest gaps; the pre-irradiated BWR rods fall in between. It is clear from Figure 29 that the boiling crisis occurs at significantly higher fuel enthalpies for the JMTR rods than for the PWR and BWR rods. It is also clear from Figure 29 that fresh fuel rods behave differently from pre-irradiated rods. The enthalpy threshold at which a boiling crisis occurs is more distinct, and the peak cladding surface temperature under film boiling is generally higher than for pre-irradiated fuel. These differences have been studied in depth by conducting pulse-irradiation tests on fresh fuel rods with pre-oxidized cladding in the NSRR [191]. The tests have shown that zirconium oxide has a better wettability than bare metal, which is the principal explanation to the lower cladding temperatures of pre-irradiated

fuel rods (see Section 5.2.2). Other possible contributions to the observed differences in transient thermal behaviour between fresh and pre-irradiated rods are discussed in [68]. Effects of pre-transient changes to the state of fuel and cladding are identified, such as cladding corrosion, fuel cracking and fragment relocation, and changes to the thermal conductivity of the fuel pellet and the pellet-clad gap.

Figure 29. Peak cladding surface temperatures, measured by thermocouples under RIA simulation tests in the NSRR. The coolant is stagnant water at ambient temperature and atmospheric pressure.



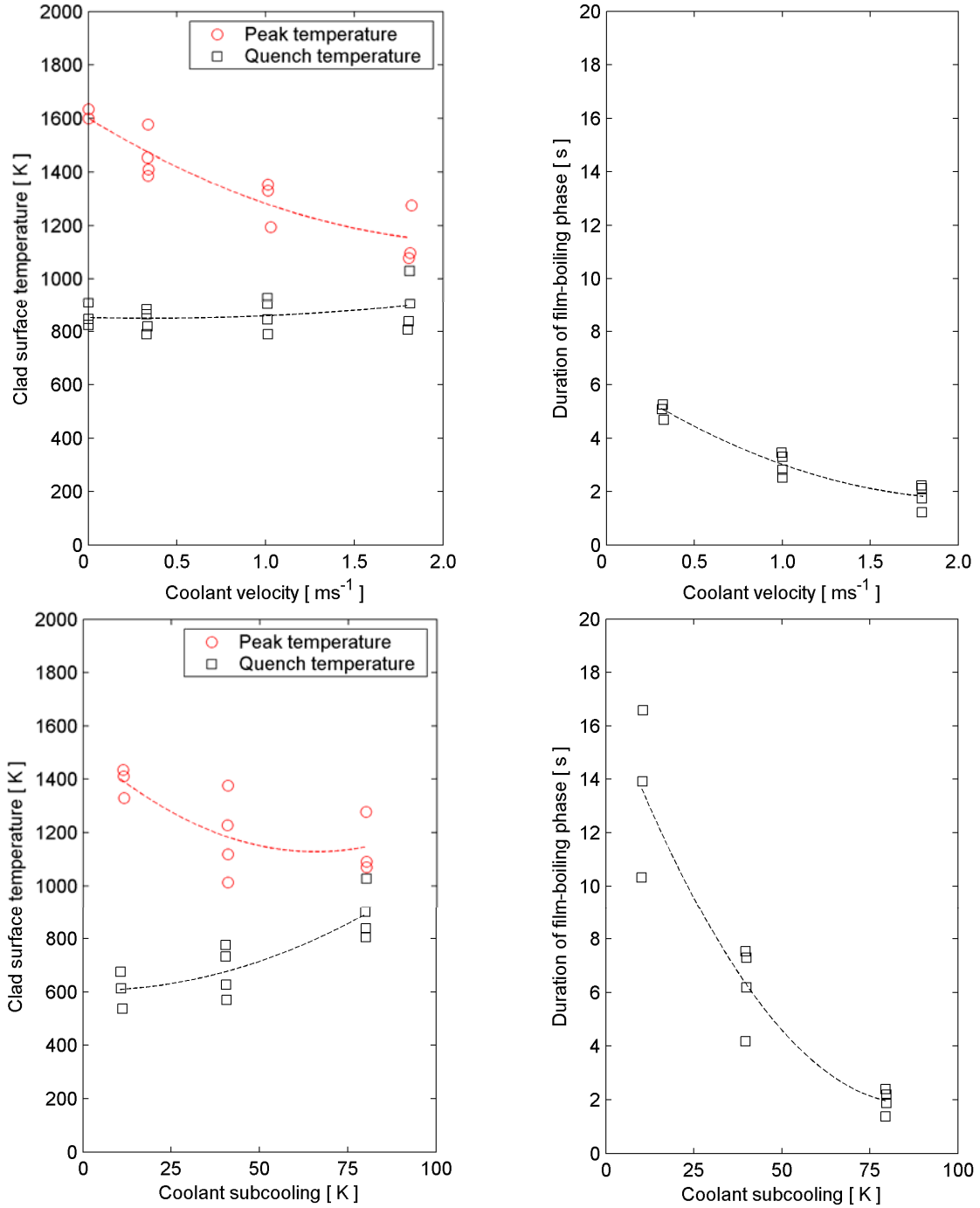
If a boiling crisis occurs, the peak cladding temperature is correlated to the energy deposition, as shown in Figure 29, and the same is true for the duration of the film-boiling phase. A film-boiling phase with high cladding temperature for 2-15 s is reported from the RIA simulation tests on instrumented rodlets in the NSRR [107,111,190]. The peak cladding temperature and the time at high temperature decrease with increasing coolant flow rate and subcooling. This is illustrated in Figure 30, which summarises results of a series of pulse irradiation tests on fresh PWR fuel rods of identical design, carried out in the NSRR with different cooling conditions [190]. The same energy deposition, $795 \text{ J(gUO}_2\text{)}^{-1}$, was used in all tests. The most remarkable result in Figure 30 is the strong effect of subcooling on the duration of the film-boiling phase. Figure 30 also includes data on the cladding quench temperature, also known as the minimum temperature for stable film boiling or Leidenfrost temperature [219].

It defines the cladding surface temperature at which the continuous vapour film breaks, the coolant re-establishes contact with the hot cladding surface, and the material is rapidly cooled (quenched). The quench temperature is important to fuel rod survivability, since it affects the thermal stresses induced in the cladding under re-wetting (see Section 6.2.5.2). As shown in Figure 30, the quench temperature is largely unaffected by flow rate, but it increases with increasing subcooling. Later tests in the NSRR on pre-oxidized fuel rods indicate that the quench temperature increases also with cladding oxide layer thickness [192]. An increase of quench temperature implies that the film-boiling phase with high cladding temperatures becomes shorter, but that the thermal stresses induced by the quench are higher. This is further discussed in Section 6.2.5.2.

There is a final case to be made on the in-reactor surface temperature measurements on pre-irradiated fuel rods in the NSRR: the film boiling under RIA seems to be a very local phenomenon. Measured temperatures often differ by several hundreds of kelvin between thermocouples, although their spacing is just a few centimetres. Post-test measurements of Vickers hardness of the cladding also bear witness to large axial and circumferential variations in peak cladding temperature during the transient [68]: since softening of irradiated cladding by annealing of radiation damage occurs in about 10-15 s at

temperatures above 850 K, it is possible to determine whether a boiling crisis has occurred during the test by the change in Vickers hardness [81]. It should be remarked that these measurements often indicate peak cladding temperatures that are higher than those measured by thermocouples [68]. Hence, the peak cladding temperatures for pre-irradiated fuel rods shown in Figure 29 may be underestimated.

Figure 30. **Influence of coolant velocity and subcooling on the film-boiling conditions.**
Results from NSRR pulse-irradiation tests on fresh PWR fuel rods [190]



The energy deposition was $795 \text{ J(gUO}_2\text{)}^{-1}$ in all tests. The upper figures show results for a fixed subcooling of 80 K, and the lower figures show results for a fixed coolant velocity of 1.8 ms^{-1} .

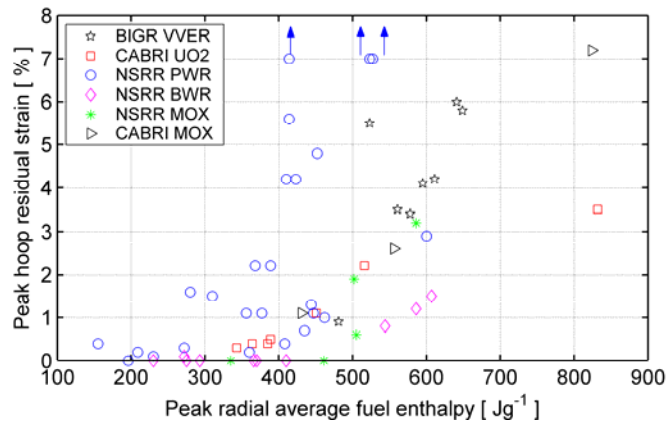
There is a final case to be made on the in-reactor surface temperature measurements on pre-irradiated fuel rods in the NSRR: the film boiling under RIA seems to be a very local phenomenon. Measured temperatures often differ by several hundreds of kelvin between thermocouples, although their spacing is just a few centimetres. Post-test measurements of Vickers hardness of the cladding also bear witness to large axial and circumferential variations in peak cladding temperature during the transient [68]: since softening of irradiated cladding by annealing of radiation damage occurs in about 10-15 s at temperatures above 850 K, it is possible to determine whether a boiling crisis has occurred during the test by the change in Vickers hardness [81]. It should be remarked that these measurements often indicate peak cladding temperatures that are higher than those measured by thermocouples [68]. Hence, the peak cladding temperatures for pre-irradiated fuel rods shown in Figure 29 may be underestimated.

6.2.2 Cladding transient deformation

Transient deformation of the cladding tube under an RIA is caused by thermal expansion and mechanical loading from the internal/external pressure difference. Pellet-clad mechanical interaction may also contribute to the mechanical loading, especially in high-burn-up fuel rods, where the pellet-clad gap is closed (see Section 3.3.2). The loading conditions are thus fairly complex, and the relative importance of thermal expansion, pressure loading and PCMI to the overall loading differs from one case to another, depending on fuel rod gap state, coolant conditions and pulse shape. Moreover, the relative importance of these loading mechanisms changes with time during an RIA: pellet-cladding mechanical interaction often dominates the loading during the early phase of the accident, whereas pressure loading may control the cladding deformation at a later stage.

Experimental data on cladding transient deformation under RIA simulation tests are mostly in the form of post-test measurements of cladding dimensional changes. By comparing the pre- and post-test dimensions of the cladding tube, it is possible to determine the irreversible deformations from the combined actions of plasticity and creep. An average value for the axial strain is obtained from the relative elongation of the rod, whereas local hoop strains are calculated by comparing pre- and post-test diameter traces. Figure 31 summarises peak values of cladding hoop residual strain, measured in post-test examinations of pre-irradiated fuel rods that have survived RIA simulation tests. The hoop residual strain is below 0.5% for peak fuel enthalpies below 280 Jg⁻¹. The residual deformation at higher fuel enthalpies depends on both fuel rod design and the facility in which the test is done. The largest deformations, and also the largest scatter, are found in the data for PWR fuel rods, tested in the NSRR.

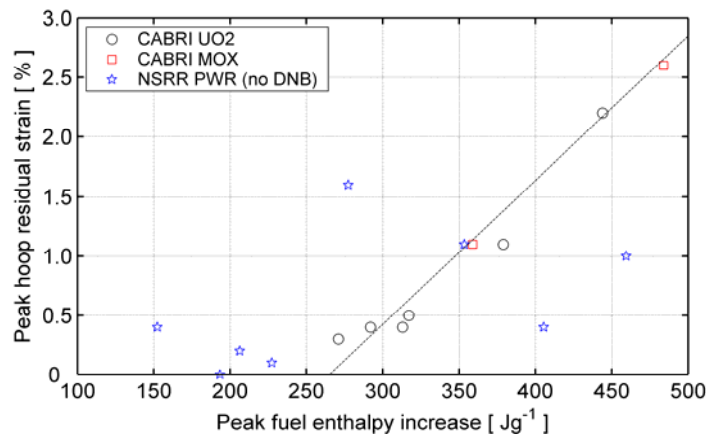
Figure 31. **Peak values of cladding hoop residual strain, measured after pulse irradiation tests in B1GR, CABRI and the NSRR**



The plot summarises data for pre-irradiated fuel rods that survived testing. Note that three of the NSRR PWR rods, here indicated by arrows in the plot, have hoop cladding strains in the range of 14.6 to 25%; (see Section A.5.1 in Appendix A).

To explain the scatter in Figure 31, one must consider the differences in burn-up and pre-transient fuel enthalpy between test rods, and one should also separate fuel rods that experienced a boiling crisis from those that maintained a low cladding temperature throughout the test. An attempt in this direction is shown in Figure 32, which presents data for high-burn-up PWR fuel rods that did not experience DNB and high cladding temperature under testing. One can therefore assume that the cladding deformation is caused by PCMI at low cladding temperature in these cases. The data are plotted with respect to peak fuel enthalpy *increase* under the test, rather than peak enthalpy, to account for the differences in pre-transient fuel enthalpy between CABRI and the NSRR.

Figure 32. Peak values of cladding hoop residual strain for high-burn-up PWR fuel rods that did not experience DNB and high cladding temperature under pulse irradiation tests in CABRI and the NSRR. The fuel burn-up was 54-76, 47-65 and 39-71 MWd(kgHM)⁻¹ for the considered CABRI UO₂, CABRI MOX and NSRR test rods, respectively.



The data from CABRI in Figure 32 show a linear relationship between hoop residual strain and fuel enthalpy increase, and no difference can be seen between UO₂ and MOX fuel. Moreover, the results from CABRI suggest that there is an apparent threshold enthalpy increase of roughly 265 Jg⁻¹ for onset of cladding plastic deformation: the threshold value is given by the intersection of the dashed line with the abscissa in Figure 32. Based on this observation, an empirical failure limit has been proposed for low-temperature PCMI-induced cladding failure of high-burn-up fuel rods under RIAs [207,220-221].

The NSRR test data in Figure 32 are more scattered than the data from CABRI, and the residual hoop strains are generally larger than for the CABRI rods at comparable fuel enthalpy increments. It has been suggested that this may be a result of insufficient pre-test rod conditioning in the NSRR [144]. During re-fabrication and handling of pre-irradiated test rods, chips and fragments of the cracked fuel pellets are stochastically displaced into the pellet-clad gap, which leads to a large variation in pre-test effective gap width. This process takes place in both NSRR and CABRI test rods, but in contrast to the NSRR specimens, the CABRI rods are held at a constant power and temperature, typical for PWR steady-state operation, for at least 24 hours before pulse irradiation. This preconditioning relocates displaced fuel fragments, which leads to a wider pre-test gap and also to a reduced variation in effective gap width. Hence, the rods tested in CABRI should have wider pre-test gaps than PWR rods tested in the NSRR, and this should lead to lower cladding deformations at comparable fuel enthalpy increments. In addition, the CABRI rods should have less variation in pre-test gap size, and therefore less scatter in cladding deformations. This is fully consistent with the results shown in Figure 32.

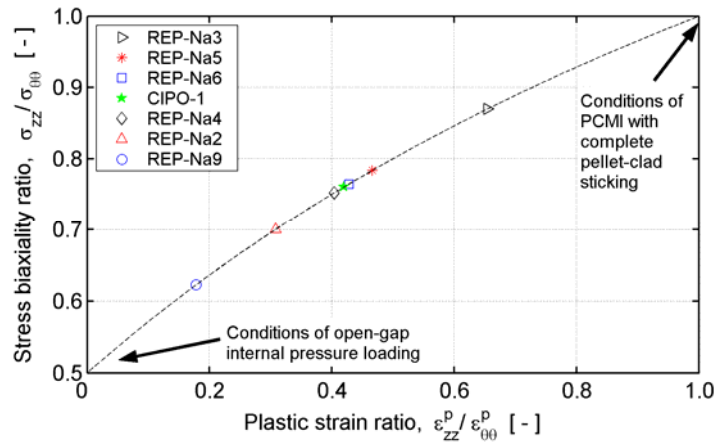
Post-test measurements of cladding residual strains can be used to estimate the stress state under which the deformation took place. By use of thin shell (membrane) theory for the cladding tube and

Levy-Mises theory [222] of plasticity in isotropic materials, one finds the following relation between the clad stress biaxiality ratio $\sigma_{zz}/\sigma_{\theta\theta}$ and the axial-to-hoop ratio of measured residual (plastic) strains:

$$\frac{\sigma_{zz}}{\sigma_{\theta\theta}} = \frac{1 + 2\varepsilon_{zz}^p/\varepsilon_{\theta\theta}^p}{2 + \varepsilon_{zz}^p/\varepsilon_{\theta\theta}^p}. \quad 13$$

By inserting average values of axial and hoop residual strains for non-failed fuel rods in CABRI into Equation 13, we find the results in Figure 33. Obviously, the estimated cladding stress biaxiality ratios, averaged over the rod active length, fall between 0.6 and 0.9 in these tests. This is just between the conditions of open-gap internal pressure loading¹⁵ ($\sigma_{zz}/\sigma_{\theta\theta}=0.5$) and PCMI-induced loading with complete pellet-clad sticking ($\sigma_{zz}/\sigma_{\theta\theta}=1.0$). As expected from the pellet-clad contact state, the stress biaxiality ratios are lowest for REP-Na2 and REP-Na9, which have significantly lower burn-ups than the other test rods included in Figure 33.

Figure 33. **Estimates of cladding stress biaxiality ratio under RIA, based on measured average ratios of axial-to-hoop plastic strains in CABRI tests [164]**



The axial-to-hoop ratio of measured residual strains can thus be used to quantify the degree of PCMI in relation to internal gas pressure loading. However, since measured *average* values are used for the axial and hoop residual strains, the data do not provide information on the axial variation in loading conditions and stress biaxiality along the fuel rod. It is known from simulations of RIA tests with transient fuel performance codes that the assumption of complete pellet-clad sticking in the closed gap regime generally leads to reasonable results for the calculated plastic deformation of the cladding, both in the axial and circumferential direction [86,223]. This indicates that the cladding stress biaxiality ratio $\sigma_{zz}/\sigma_{\theta\theta}$ is close to unity in part of the fuel rod, or alternatively, under parts of the loading history, but that internal gas pressure loading in other parts of the rod, or loading history, lowers the average biaxiality ratio.

So far, we have discussed experimental data from post-test measurements of cladding dimensional changes. These measurements provide information merely on the accumulated strains from plasticity and creep during the test, although the ratio of axial-to-hoop residual strains also gives some indication on the kind of loading responsible for the deformation, as illustrated in Figure 33. To determine the contribution of reversible deformation mechanisms, such as elasticity and thermal expansion, on-line measurements of cladding dimensional changes are needed. Such measurements are also needed to establish at what point of time the deformation occurs during the test.

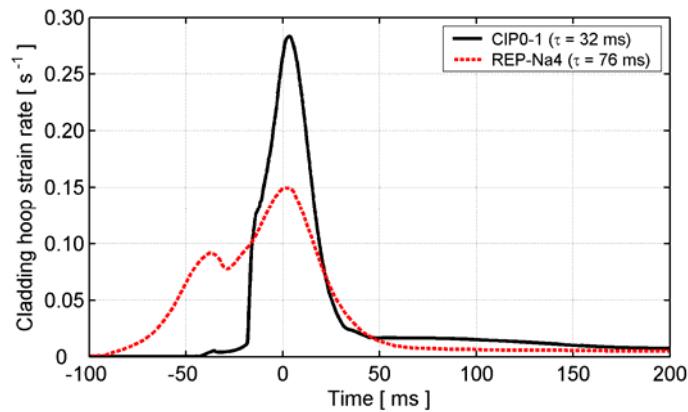
15. The stress biaxiality ratio for internal gas pressure loading (0.5) follows from the conditions of mechanical equilibrium in a closed-end tube.

Fuel rods tested in CABRI and the NSRR have for this purpose usually been instrumented with a linear variable differential transformer (LVDT) for on-line measurements of cladding elongation. Rods tested in the NSRR have usually been equipped also with an additional LVDT for simultaneous measurement of the pellet stack elongation, which makes it possible to determine the relative axial motion (slip) of fuel and cladding during the transient. Recently, also strain gauges attached to the cladding tube have been used for on-line measurements of cladding deformation under RIA simulation tests in the NSRR. Firstly, twelve PWR type test rods with fresh UO_2 fuel pellets and pre-hydrated cladding tubes were equipped with foil-type strain gauges to measure local cladding strains in both the axial and circumferential direction under pulse irradiation [91]. These tests are interesting, since the on-line measurements show that the local axial-to-hoop strain ratios are close to unity during the PCMI-induced loading. Secondly, a few tests on high-burn-up fuel rods have been conducted with strain gauges attached to the cladding, but in these cases, the deformation was measured only in the hoop direction [224-225]. Two of these tests, FK-10 and FK-12, were done on BWR fuel rods with a burn-up of $61 \text{ MWd}(\text{kgU})^{-1}$. The fuel enthalpies in these rods reached 430 and $373 \text{ J}(\text{gUO}_2)^{-1}$, and the pulse widths were 5.2 and 5.5 ms, respectively. The differences in peak fuel enthalpy and pulse width were reflected in the measured maximum hoop strain rate for the cladding, which was 1.2 s^{-1} for FK-10 and 0.9 s^{-1} for FK-12 [224].

The mechanical load on the cladding under an RIA is in high-burn-up fuel rods dominated by PCMI under the early stage of the accident. Since the pellets deform mainly by thermal expansion under this early heat-up stage, the PCMI-induced loading on the cladding closely follows the power pulse. This is illustrated in Figure 34, which shows the cladding hoop strain rate versus time, calculated with SCANAIR-3.2 for two tests in CABRI. The considered tests, REP-Na4 and CIP0-1, have similar peak fuel enthalpies, 364 and $389 \text{ J}(\text{gUO}_2)^{-1}$, respectively, but dissimilar pulse widths, 76 and 32 ms; see Section A.6 in Appendix A. The calculated deformation histories in Figure 34 are very close in shape to the power pulses, which shows that the load on the cladding tubes is dominated by the thrust from thermally expanding fuel pellets. As expected from the difference in pulse width, the calculated maximum strain rate in CIP0-1 is twice that in REP-Na4.

Figure 34. **Cladding hoop strain rate versus time**

Calculated for two tests in CABRI with similar peak fuel enthalpies but dissimilar pulse widths. The shapes of the calculated loading histories resemble the power pulses, since the loading is dominated by the thrust from thermally expanding fuel pellets.



6.2.3 Cladding high-temperature oxidation

In an early stage of an RIA, the cladding temperature is fairly low, i.e. close to the reactor system temperature, and cladding failure, if it occurs, would be due to PCMI caused by fuel expansion into the cladding. At a later stage of the accident, the heat transferred from the fuel can give rise to high cladding

temperatures ($> 1\,000\text{ K}$). As discussed in Section 6.2.1, pulse irradiation tests show that the cladding may remain at those temperatures for up to 15-20 s until rewetting takes place. In fact, in many early RIA tests made on fresh fuel rods of light water reactor, the rods experienced boiling crises, characterised by marked temperature rise of the cladding surface as a result of film boiling, accompanied by rapid steam oxidation of the cladding [111-226]. Ishikawa and Shiozawa [111] pointed out that during tests in the NSRR on fresh fuel rods, cladding failures were caused by cladding embrittlement, and usually occurred at the time of quenching. Therefore, an understanding of the mechanism of cladding embrittlement due to high temperature oxidation is imperative for the assessment of failure cause, in cases of fresh fuel rods and/or high energy deposits. High-temperature oxidation is also important with respect to hydrogen generation in the core under RIA [227]. In the following subsections, some basic past studies on oxidation and embrittlement of Zircaloy are reviewed and also model calculations are made to exemplify the time and temperature at which severe embrittlement and failure of cladding could occur.

Oxygen uptake, i.e. O_2 concentration and distribution in zirconium-base cladding, and zirconium phase transformations during temperature rise and fall, affect the microstructure of Zr alloys and thereby the mechanical properties of the cladding. Since temperature is the key variable controlling these phenomena, its accurate evaluation is important for a reliable assessment of failure under reactivity induced incidents. Experimentally, during RIA tests, the maximum cladding temperature can be estimated from the measured cladding surface thermocouple response, and after tests, from the observed cladding external ZrO_2 layer thickness and the ξ -layer thickness (layer of ZrO_2 + oxygen stabilised α -Zr; see below).

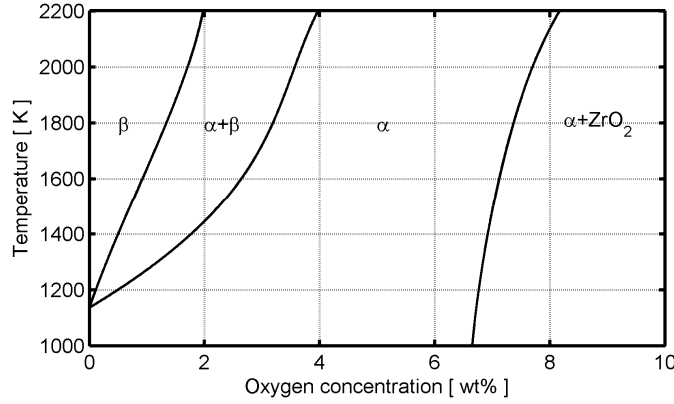
Isothermal oxidation

The oxidation reaction of Zr-base alloys with steam, ordinarily, may be described by $\text{Zr} + 2\text{H}_2\text{O} \rightarrow \text{ZrO}_2 + 2\text{H}_2$, with a released heat of reaction of $297\text{ kJ/mol H}_2\text{O}$, and besides, if the reaction product hydrogen is absorbed by the metal, additional heat of 138 kJ/mol H_2 is released [228]. This kind of oxidation at high temperatures, however, is generally known to involve not only the formation of the stable oxide film ZrO_2 on the free surfaces, but also an intermediate layer of oxygen stabilised metal layer. The extent of oxygen solubility in dilute zirconium alloys may be found through the phase diagram for the zirconium-oxygen system in Figure 35. Chung and Kassner [229] have studied an *isoplethal* (constant composition) section of the Zr-rich portion of Zircaloy-4/oxygen phase diagram by resistometry measurements and metallographic analyses of equilibrated and quenched specimens. Their study indicates that the β -phase boundary for Zircaloy-4/oxygen is virtually the same as that for the zirconium/oxygen system [230] and the Zircaloy-2/oxygen system [231]. The α -phase boundary for Zircaloy-4/oxygen solid solution is about 70 K lower than for the Zr/O system.

For oxidation at temperatures below the α to β phase transformation (hexagonal close-packed to body-centred cubic phase) of zirconium, the α -phase metal at the interface in contact with the growing oxide film will have about 7 wt% oxygen in solution, if a near-equilibrium condition is maintained at the moving-boundary [232]. Oxygen will diffuse into the α -Zr and its distribution at any time will depend on the diffusivity, the rate of oxide formation and the geometry of the sample. At temperatures above the α to β transition temperature, oxidation generally produces three phases: the outer oxide phase (ZrO_2) an interlayer of oxygen-stabilised α -Zr and an inner layer of remaining β -Zr. During cooling to room temperature, the β -Zr layer transforms back to α -Zr. But, the microstructure and hardness of this re-transformed α -Zr layer is much different from that of the oxygen-stabilised α -Zr layer, and hence the former β -Zr is easily distinguishable [232].

It is generally agreed that the mechanism governing the oxidation of zirconium alloys is the diffusion of oxygen anions through the anion deficient ZrO_2 lattice [100]. Oxygen therefore migrates through the ZrO_2 film to the metal and the film grows downward into the metal, rather than growing upwards at the outer surface.

Figure 35. **Portion of the zirconium-oxygen binary phase diagram**
based on the work of Abriata *et al.* [230]



The oxide film grows by a parabolic law, stemmed from oxygen flux balance. If we denote the oxide and oxygen-stabilised α -Zr layer by ξ , then the kinetics of growth is described by:

$$\frac{d\xi}{dt} = \frac{k}{\xi}, \quad 14$$

where k is a temperature dependent reaction rate coefficient, determined by measurements for a given alloy. A solution to Equation 14 for constant temperature conditions (constant k) is expressed as $\xi = \sqrt{2kt}$, hence the term parabolic growth law. The kinetics of phase growth in regard to the oxygen distribution in zirconium and its alloys has been examined extensively in a number of past studies, e.g. [232-236], which the interested reader can refer to. The oxygen gradient beneath the ZrO_2 layer in zirconium alloys has been measured and compared with model calculations [233-234].

High temperature oxidation of Zircalloys in steam has been a subject of many past investigations, e.g. see the brief review of the pre-1980 studies by Ocken [237] and Massih [238]. A noted study was the oxidation experiment made by Urbanic & Heidrick [239] on Zircaloy-2 and Zircaloy-4 specimens, whereupon reaction kinetics and the rate of growth of the combined ($\text{ZrO}_2 + \alpha\text{-Zr}$)-layer were measured over the temperature range 1 353-2 123 K. The investigators found that the reaction rates for both alloys were similar and followed parabolic kinetics. Urbanic and Heidrick also observed a discontinuous increase in the parabolic rate constant (k) above 1 853 K. At oxidation temperatures greater than 1 853 K, all specimens had a layer of ZrO_2 plus a layer of $\alpha\text{-Zr}$ overlaying a transformed $\beta\text{-Zr}$ matrix [239]. At oxidation temperatures less than 1 853 K, a similar structure was observed, but with an absence of transformed $\beta\text{-Zr}$ matrix.

According to the phase diagram of the Zr-O system [230,240-241], at temperatures above $\approx 1\,800$ K, $\beta\text{-Zr}$ reacts with oxygen to form a layer of cubic $\gamma\text{-ZrO}_2$ and a layer of $\alpha\text{-Zr}$, an interlayer of mixed-phase ($\alpha\text{-Zr} + \beta\text{-Zr}$) and an inner layer of $\beta\text{-Zr}$. When the material is cooled down through ≈ 1800 K the $\gamma\text{-ZrO}_2$ transforms to a tetragonal $\beta\text{-ZrO}_2$ (eutectic decomposition or transition) and a layer of $\alpha\text{-Zr}$. When it is further cooled below ≈ 1270 K, the $\beta\text{-ZrO}_2$ goes through yet another eutectic transition to a stable monoclinic $\alpha\text{-ZrO}_2$. Urbanic and Heidrick's observations of specimens' microstructure are consistent (roughly) with the phase diagram. Hence, the observed discontinuous increase in oxidation rate at high temperatures could be attributed to a change in oxide structure, namely $\gamma\text{-ZrO}_2 \rightarrow (\beta\text{-ZrO}_2 + \alpha\text{-ZrO}_2)$ transformation.

High-temperature oxidation of Zircaloy-4 tubing, over the temperature range 1 173-1 603 K, has been studied by Kawasaki *et al.* [242]. The main conclusions from their test were as follows. Above 1 273 K, the evolution of oxygen weight gain and growth of oxide layer and oxide + stabilised $\alpha\text{-Zr}$

layer followed a parabolic law, for which the temperature dependence of the rate constants, in terms of Arrhenius relations, was deduced from measurements. For temperatures from 1 173 to 1 223 K, the Zircaloy-steam reaction deviated from the parabolic law. In addition, it was found that the ductility of oxidized Zircaloy-4 tubing was primarily influenced by the distribution of oxygen in the metallic phase due to migration of absorbed oxygen in the cladding, which is temperature controlled, but not by oxide layer thickness. However, no quantitative relation between Zircaloy-4 ductility and the distribution of oxygen in the material was provided.

Zircaloy-4 cladding embrittlement caused by inner surface oxidation of the tube was examined by Uetsuka *et al.* [243]. These investigators heated a mock-up fuel rod (filled with Al_2O_3 pellets) in a flowing steam at temperatures between 1 153 and 1 440 K until cladding burst occurred. This exposed the inner surface of the cladding to steam, which caused severe oxidation and hydrogen absorption. Uetsuka and company found that the embrittlement of the specimen due to the *inner* surface oxidation was mainly influenced by the amount of hydrogen absorbed by the material. Post oxidation compression tests made on sliced segments of the cladding at 373 K in air indicated that 200-300 wppm of absorbed hydrogen made Zircaloy-4 brittle when it was oxidized above 1 273 K. Oxidation in the temperature range of 1 105-1 245 K did not cause brittleness below hydrogen contents of 500 to 750 wppm. The hydrogen absorbed by the Zircaloy-4 precipitated in the form of fine hydride crystals along former β -Zr grain boundaries [243].

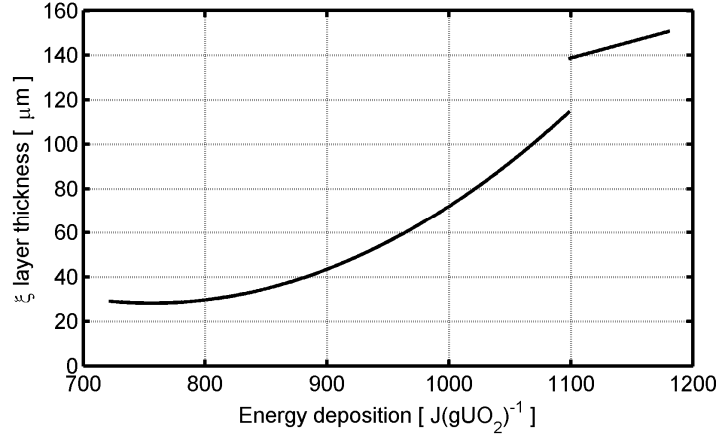
Recently, Nagase *et al.* [244] reported oxidation tests made in flowing steam on low-tin (1.3 wt%) Zircaloy-4 cladding tubes over the temperature range from 773 to 1 573 K. The oxidation kinetics generally followed a parabolic rate law for the examined periods up to 3 600 s at temperatures from 1 273 to 1 573 K, and for a restricted time range up to 900 s from 773 to 1 253 K. A cubic rate law, however, was found to be more suitable for describing the long-term oxidation at temperatures below 1 253 K. Nagase *et al.* measured the rate constants and fitted their data to Arrhenius-type relations to describe the temperature dependence [244]. They attributed the change in the oxidation kinetics, from cubic to parabolic rate, to the monoclinic/tetragonal phase transformation of ZrO_2 , which occurred somewhere between 1 173 and 1 273 K in the oxide layer. Furthermore, Nagase and co-workers concluded that the decrease in Sn content of Zircaloy-4 (from 1.5 to 1.3 wt%) has a negligible impact on the high-temperature oxidation kinetics. A more detailed review of high temperature oxidation of zirconium alloys, including Zr-Nb alloys, can be found in [238]. It is remarked that, in general, the high temperature oxygen uptake of the latter alloys are similar to that of Zircaloys. In the report [238], data on the effects of hydrogen uptake and pressure on cladding oxidation are also discussed.

In the aforementioned RIA tests on fresh fuel rods in the NSRR, Yanagihara and Shiozawa [245] made metallurgical examinations of cladding ring samples from fuel rods that were subjected to energy depositions over the range 750-1 170 $\text{J}(\text{gUO}_2)^{-1}$ (see also [226]). For the failed rods, they observed that Zircaloy-4 cladding (outer diameter 10.72 mm, wall thickness 0.62 mm) was heavily oxidized by $\text{Zr-H}_2\text{O}$ and Zr-UO_2 reactions at the outer and inner surfaces, respectively. The outer part of the tube wall was a layer of ZrO_2 with an adjacent layer of oxygen-stabilised α -Zr and the central layer of former β -Zr. The UO_2 -Zr reaction layers were observed along the entire cladding inner surface due to fuel-cladding interaction. In the inner part of the wall, layers of UZr , $\alpha\text{-Zr} + \text{O}_2$ and $\alpha\text{-Zr} + \text{U} + \text{O}_2$ were identified by electron microprobe analysis. The thickness ξ of oxidized layers ($\text{ZrO}_2 + \alpha\text{-Zr}$) was measured and correlated to the energy deposition (see Figure 36).

Yanagihara and Shiozawa [245] found that ξ increased monotonically with energy deposition up to around 1 100 $\text{J}(\text{gUO}_2)^{-1}$, upon which a discontinuous increase occurred due to fuel rod failure. They noted that the cladding specimens failed at the energy deposition threshold of about 1 100 $\text{J}(\text{gUO}_2)^{-1}$, with through-wall cladding cracks at regions with a large amount of oxidation. They estimated the local

temperature at the failed region of the cladding to be above the melting point of β -Zr. Nevertheless, they did not observe oxidation at any cracked surface of the cladding, suggesting that cracks were initiated during cooling as a consequence of embrittlement.

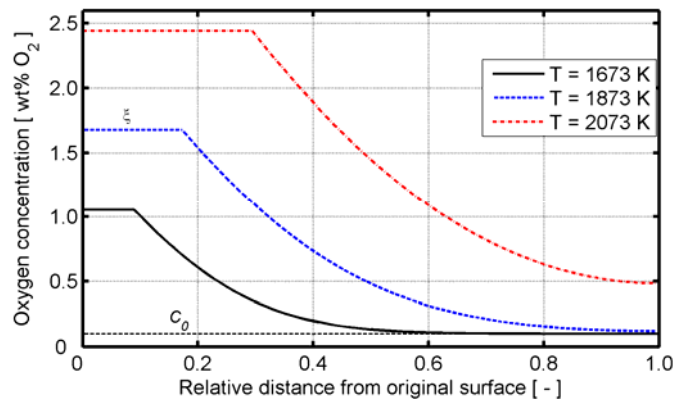
Figure 36. **Correlation between $(\text{ZrO}_2 + \alpha\text{-Zr})$ -layer thickness ξ and energy deposition** based on data obtained from NSRR RIA simulation tests on fresh fuel rods with Zircaloy-4 cladding [245]



Before discussing cladding embrittlement, let us evaluate the oxygen content of the former β -Zr layer produced during the NSRR standard RIA test conditions, i.e. during tests with stagnant water at room temperature and atmospheric pressure as coolant [245]. For this purpose, we have utilised an appropriate solution of the oxygen diffusion equation with moving-boundary in a finite slab [236]. In Figure 37, we illustrate the temperature dependence of oxygen concentration profiles after 10 s of reaction time in β -Zr, using this method and the correlations (Arrhenius-type) for the parabolic rate constant, oxygen diffusivity and equilibrium saturation of oxygen for Zircaloy [232]. The selected temperatures 1 673, 1 873 and 2 073 K correspond to the values used by Yanagihara and Shiozawa [245]. The flat shoulders of the curves were calculated using the terminal solubility of oxygen (equilibrium saturation of oxygen) in β -Zr by means of the Arrhenius-type relationship obtained by Pawel [232] for Zr and Zircaloy-2 materials. The slab thickness (clad wall thickness) is assumed to be 0.62 mm, and the oxidation is a single-sided reaction in this example.

Figure 37. **Oxygen concentration profiles across β -Zr layer with moving-boundary, $(\text{ZrO}_2 + \alpha\text{-Zr})$ -layer thickness ξ** , after 10 seconds of reaction time at several temperatures, calculated through an appropriate solution of the oxygen diffusion equation, and using the correlations given in [232]

Here, C_0 is the initial oxygen content of the specimen, and the oxidation is a single-sided reaction. The flat shoulders correspond to terminal solubility of oxygen in β -Zr.

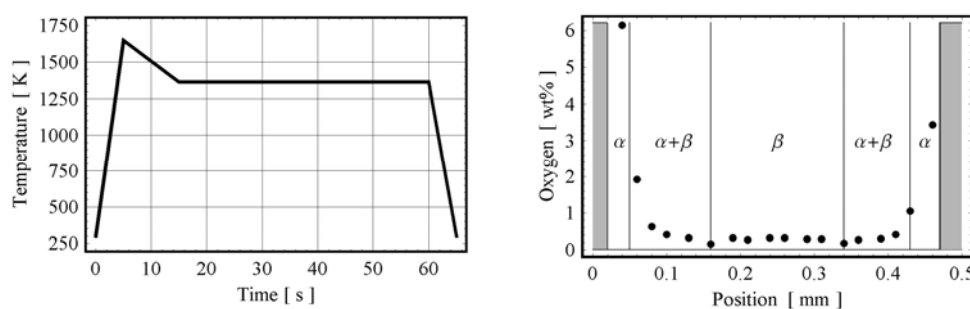


Non-isothermal oxidation

Non-isothermal oxidation of cladding under simulated loss-of-coolant temperature transients has been studied by many investigators, e.g. see a brief review by Massih [238]. In a classical experiment, Sawatzky *et al.* [246] studied the oxidation under rapid heating/cooling, by placing Zircaloy-4 tube specimens in an induction furnace and exposing them to steam under the temperature history shown in Figure 38. Figure 38 also shows the oxygen distribution in a specimen obtained from this test. The positions of the $\text{ZrO}_2/\alpha\text{-Zr}$ and $\alpha/(\alpha+\beta)\text{-Zr}$ boundaries were determined by metallographic examination. Sawatzky *et al.* found that, when Zircaloy-4 was cooled during oxidation from above the α/β transus, the $\alpha/(\alpha+\beta)$ interface moved more rapidly at the given temperature and interface position than it did under the same conditions during isothermal oxidation [246]. In the case when the specimen was cooled slowly (2 K/s) from above the α/β transus during oxidation, oxygen diffused back from the β phase to the β/α interface, resulting in a thicker β phase layer and depletion of the β phase region (see Figure 35). On the other hand, when the specimen was cooled rapidly (say 100 K/s) an $(\alpha+\beta)\text{-Zr}$ region was formed next to the $\alpha\text{-Zr}$ layer.

Figure 38. Sawatzky *et al.* [246] transient oxidation experiment of Zircaloy-4 tube specimen in steam

Left panel: temperature history. Right panel: oxygen distribution across the tube wall. Points are measurements and the shaded regions mark the ZrO_2 layers.



Pawel *et al.* [247] reported the results of a series of transient oxidation tests on Zircaloy-4 PWR cladding specimens in steam under several types of transient temperature histories. Their test series included two-peak temperature transients shown in Figure 39. The outcome was that the measured values for oxide layer thickness after these transients were 47.5 and 40.2 μm for path-1 and path-2, respectively. This, at first sight, was surprising, since path-2 after the first temperature excursion had the same temperature history as path-1. The explanation for this anomaly was provided by the structural phase transition behaviour (hysteresis) of ZrO_2 crystal [248]. It was noted that the oxide formed during heating to the first peak is largely tetragonal. On cooling to the first pit, if the temperature is lower than about 1 170 K, the oxide transforms from the tetragonal to a monoclinic structure. Then, during the second heating, because of the existence of the monoclinic oxide, oxidation proceeds more slowly than would have been predicted on the basis of the high temperature isothermal data. This condition will continue until the temperature reaches 1 470 K, when the monoclinic oxide is transformed back to the tetragonal phase.

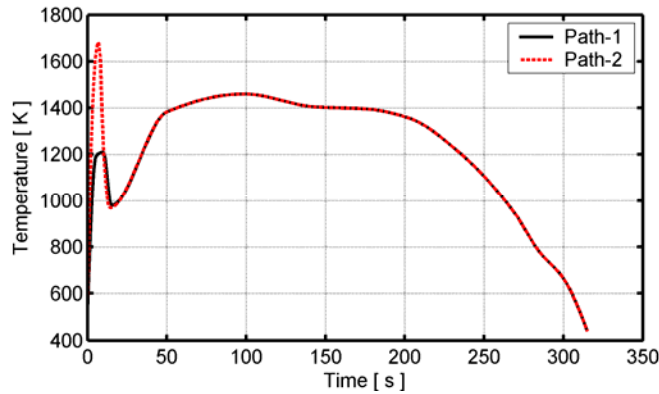
Moalem & Olander [228] studied as-received Zircaloy-4 oxidation rates in pure steam at 0.1 MPa and flow rates of 200-600 cc (STP)/min¹⁶ at up to temperatures greater than 1 873 K. At about 1 770 K, the stable oxide of zirconium converts from $\beta\text{-ZrO}_2$ (tetragonal) to $\gamma\text{-ZrO}_2$ (cubic). It was argued that oxygen diffusivity in $\gamma\text{-ZrO}_2$ is larger than in $\beta\text{-ZrO}_2$, resulting in a higher oxygen uptake at temperatures above 1 873 K. The transient oxidation test made by Moalem & Olander [228], by heating from 1 873 K

16. Cubic centimetre (cc) at standard temperature and pressure (STP), i.e. at 273.15 K and 1×10^5 Pa.

to a peak temperature of 2 075 K in 5 s, then cooling down slowly back to 1 873 K, indicated a linear oxygen mass gain followed by a weak parabolic solid-state diffusion-controlled mass gain. Moalem & Olander's conclusion was that above 1 773 K, a parabolic oxidation law cannot be observed; and thus the only reliable way of analysing oxygen uptake at high temperature is by an appropriate oxygen diffusion model, which accounts for the initial steam starvation and non-isothermal behaviour.

Figure 39. **Schematic temperature-time histories used in one of the steam oxidation tests on Zircaloy-4 PWR clad performed by Pawel *et al.* [247]**

The measured values for oxide layer thickness after these transients were 47.5 and 40.2 μm for path-1 and path-2, respectively.



Oxygen-induced cladding embrittlement

Oxygen-induced embrittlement of Zircaloy cladding has been assessed extensively by workers at Oak Ridge National Laboratory, based on original measurements reported in [249-250]. Ring specimens from Zircaloy-4 tubes that were previously steam-oxidized on both inner and outer surface at temperatures from 1 200 to 1 644 K for exposure times up to 1 h, were subjected to hoop compression (flattening) tests. The test temperatures varied from room temperature to either 422 K (slow strain rate tests) or 1 311 K (high strain rate tests). A nil ductility temperature (NDT) was defined using those specimens that fractured with no optically observable plastic deformation. Then they correlated the NDT to ξ , i.e., the thickness of oxide and oxygen stabilised α -Zr, or equivalently, the fraction of remaining β -Zr thickness $F_w = 1 - 2\xi_0 / h$, where ξ_0 is the penetration of the boundary from the original interface and h is the wall thickness and the factor 2 accounts for the two-sided reaction [232].

Generally, for a given thickness of (former) β -Zr layer in the specimen, the ductility would decrease with increasing oxygen concentration [250]. Moreover, for a given oxygen concentration, the ductility would be further decreased if material heterogeneities would be present. The α -Zr “incursions” (irregular finger-like growth of α -Zr) into the β -Zr layer, observed during high-temperature oxidation of Zircalloys, would introduce stress risers, augmenting the latent brittleness that might be present in the material [232]. Moreover, when incursions are present, it is difficult to define the effective thickness of the β -Zr layer. Hence, the mechanical response of isothermally oxidized specimen would depend on (i) the amount of β -Zr remaining, (ii) the oxygen concentration within β -Zr and (iii) the presence or absence of α -Zr incursions [232].

Pawel's evaluation of Hobson's data [232] indicated that the onset of room-temperature brittleness in Zircaloy-4 occurs when the average oxygen concentration in the transformed β -Zr reaches 0.7 wt%, or alternatively, when it reaches about 95% for the degree of saturation.¹⁷ Moreover, Pawel showed that this

17. Oxygen concentration divided by the oxygen solubility limit.

concentration could be reached during oxidation at around 1 589 K, which is above the loss-of-coolant accident design limit on peak cladding temperature (PCT) of 1 477 K (1 204°C). In addition, Pawel [232] points out that, at temperatures below about 1 570 K, the average concentration is limited to less than 0.7 wt% by solubility considerations. Hence, he concludes that at lower temperatures, the critical time for embrittlement is the time required for 95% saturation, while at higher temperatures, an average oxidation of 0.7 wt% or more is reached before 95% of saturation is attained. In fact, it may be argued that the 0.7 wt% average oxygen limit or the 95% degree of saturation, which can be calculated by a suitable model, may be more appropriate limits for cladding ductility than the PCT criterion used in LOCA analyses [232]. It should, however, be mentioned that the oxygen solubility in β -Zr is much affected by the presence of hydrogen, and this effect was not considered in Pawel's publication [232].

Yanagihara and Shiozawa [245] applied Pawel's embrittlement criteria to RIA conditions and found correlations between the average oxygen concentration, peak cladding temperature and cladding wall thickness. For example, their calculations show that the 0.7 wt% limit was reached when the wall thickness was reduced to about 0.4 mm in the case of PCT of 2 073 K. They point out that the wall thinning needs to be taken into account for the embrittlement of the cladding leading to failure. To illustrate the evolution of oxygen concentration in the β -Zr layer and the layer's thickness (F_w) during oxidation in the regime of interest, some computational results are presented. The same model and correlations used to produce Figure 37 were utilised for the two-sided oxidation of Zircaloy cladding with a wall thickness $h = 0.62$ mm. Figure 40 shows the average (total) oxygen concentration in the β -Zr layer versus time at three temperatures considered before (see Figure 37). It is seen that the oxygen concentration goes through a maximum during the oxidation. The decline and fall of the concentration is due to diminution of F_w with time, as shown in Figure 41. For the considered temperatures, 1 673, 1 873 and 2 073 K, the maximum concentrations occur at 52.6, 17.9 and 7.4 s, respectively, corresponding to the symmetric two-sided oxygen contents of 0.6, 0.86 and 1.14 wt%. It is seen that only at the two highest temperatures, the oxygen concentrations exceed the embrittlement limit of 0.7 wt% (see Figure 40). Hence, at lower temperatures, the embrittlement threshold based on 95% oxygen saturation should be used. In these computations, the initial oxygen content of the material was assumed to be zero. Nevertheless, we should emphasise that the temperatures utilised in the computations (after Yanagihara and Shiozawa [245]) are well above the values expected in LWRs under RIA conditions (see Figure 29).

Figure 40. Calculated total (average) oxygen concentration in β -Zr layer during two-sided oxidation of Zircaloy cladding in steam

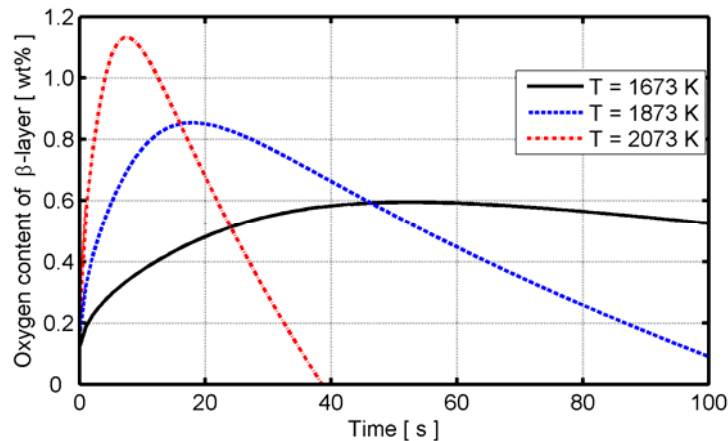
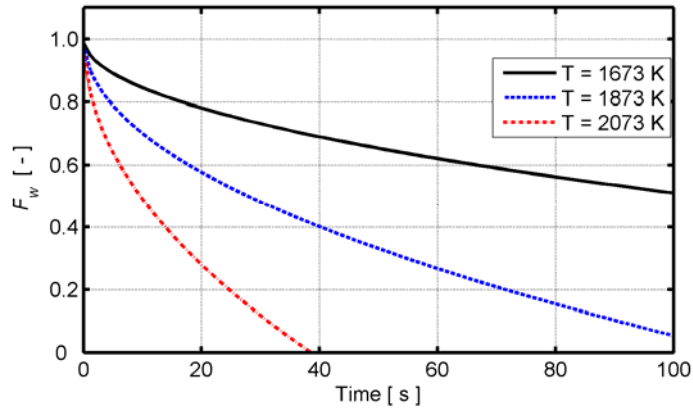


Figure 41. Calculated fraction of the β -Zr layer thickness (F_w) during oxidation of Zircaloy in steam

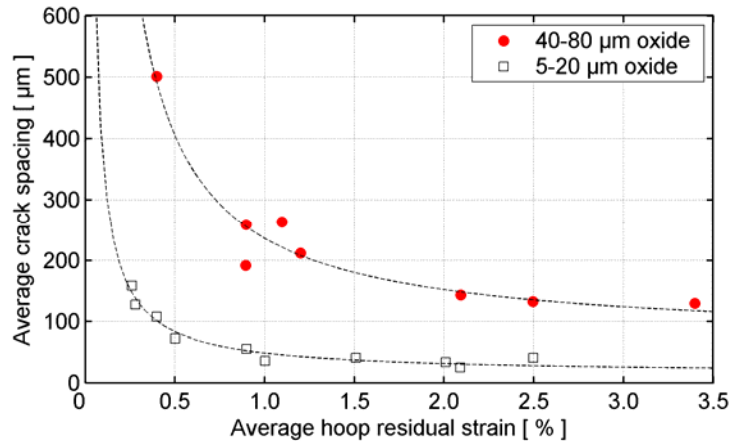


6.2.4 Oxide transient cracking and spallation

Metallographic examinations of cladding tubes after pulse irradiation tests generally reveal numerous radial cracks through the oxide layers at the cladding inner and outer surfaces (see Figure 12). The oxide cracks are usually uniformly spaced along the cladding circumference, and the crack spacing is correlated to oxide thickness and the inverse of cladding hoop residual strain [85], as shown in Figure 42. Obviously, cracks form easily in the brittle oxide layer, at only about 0.2-0.3% plastic strain of the underlying metal substrate. For hoop residual strains larger than 1-2%, the crack spacing seems to approach a limit value, which depends on the oxide layer thickness. The saturation in crack density is followed by transverse cracking, which ultimately leads to a grid of crossing cracks and a checkerboard appearance of the oxide surface [85]. It should be remarked that the behaviour shown in Figure 42 is not particular to RIA simulation tests, but can be observed also after power ramp tests and out-of-reactor burst tests on corroded cladding. The behaviour has been theoretically analysed and explained by treating the cladding oxide layer as a thin brittle coating on a ductile substrate [85,251].

The oxide cracking is important, since the cracks act as stress concentrators at the cladding surface; the thicker the oxide layer, the stronger is the stress concentration. Oxide cracking is therefore likely to play a role for initiation of radial cracks in severely corroded cladding under an RIA. This is further discussed in Section 6.2.5.1.

Figure 42. Relation between azimuthal spacing of oxide cracks, oxide layer thickness and cladding hoop residual strain, observed in post-test examinations of pre-irradiated fuel rods from the CABRI REP-Na test series [85]



Transient spallation of the external oxide layer has been observed in some RIA simulation tests on pre-irradiated and corroded PWR fuel rods [85]. It should be remarked that these observations are particular to tests conducted in the CABRI reactor: transient oxide spallation is not reported from tests in other pulse reactors. It is unclear why this difference exists, but suggested explanations [85] concern the differences in cooling conditions and pulse widths between the test reactors (see Table 7 in Section 5.1.1). At present, it is also unclear whether oxide spallation is likely to occur under RIAs in light water reactors.

The observations of oxide transient spallation in CABRI were made on fuel rods with oxide layers thicker than 40 μm . The oxide layer was peeled off in patches during the tests, and the spallation occurred preferentially along cladding azimuths with thin oxide layer [85]. This is somewhat surprising, since experience shows that thick oxide layers are generally more likely to spall under deformation than thin layers. However, the preferential spallation along azimuths with thin oxide layer could be an effect of crack density [85]. As shown in Figure 42, for a given cladding hoop strain, the density of oxide cracks depends on oxide layer thickness, and the higher density of cracks in areas with thin oxide could possibly promote spallation. Another explanation is that the azimuthal variation in oxide layer thickness leads to a non-uniform cladding temperature, which in turn leads to azimuthal variations in cladding mechanical properties. This phenomenon is important to the localisation of deformations, as indicated by the cladding ovalisation observed in post-test examinations of fuel rods with non-uniform oxide layer thickness [85].

A direct consequence of oxide transient spallation is that fine fragments ($\approx 50\text{--}100\ \mu\text{m}$) of zirconium dioxide are expelled into the coolant under a very short period of time. If the temperature of the spalling oxide layer is high, the transient spallation will provide a means for heat removal from the fuel rod. A supposedly more important consequence of the transient spallation is the change in cladding surface properties and its effect on clad-to-coolant heat transfer under the remaining part of the transient. As discussed in Sections 5.2.2 and 6.2.1, it is known from separate effect tests in the NSRR that heat transfer to the water coolant from bare zirconium metal is poorer than heat transfer from zirconium dioxide [191]. It has also been shown that a boiling crisis is more likely to occur with a bare metal surface than with an oxidized surface [94], which means that spalled regions of the cladding may experience much higher temperatures under the accident than regions with an adherent oxide layer. This would lead to large spatial variations in cladding mechanical properties and to localisation of cladding creep and plasticity to spalled regions with high temperature. However, none of these conjectured temperature effects of oxide transient spallation has to date been observed experimentally in pulse reactor tests. As already mentioned, oxide transient spallation has only been observed for tests in the sodium coolant loop of CABRI, where low cladding temperatures are maintained throughout the test.

6.2.5 Cladding failure

As already touched upon in Section 4.1, fuel rod failures under RIA simulation tests are usually divided into:

- Low temperature, PCMI-induced fuel rod failures, which occur under the early heat-up phase of the accident.
- High temperature failures, which occur at a later stage of the accident, as a result of film-boiling, degraded clad-to-coolant heat transfer and cladding overheating.

Low temperature failure is deemed to be the most restricting failure mode for high-burn-up fuel rods, due to the combined effects of aggravated PCMI and clad embrittlement at high burn-up. However, the occurrence of low or high temperature failures is not only related to the burn-up dependent state of the fuel rod, but also to the shape and duration of the power pulse, as well as to the pre-pulse power level and coolant conditions. For this reason, it can be assumed that low temperature

failures are most likely to occur in high-burn-up fuel under zero power reactivity accidents, such as HZP REAs or CZP RDAs, whereas the high temperature failure modes are the most likely in case the RIA occurs at full reactor power with the coolant close to saturation. We also note that only the high temperature failure modes are relevant to RIAs in CANDU reactors. The power surge in CANDU reactors is much slower than in LWRs, and the accidents occur over a time period that is sufficiently long to allow significant clad heating to take place concurrently with the PCMI-induced loading [21].

6.2.5.1 Low temperature PCMI-induced failures

Low temperature PCMI-induced clad failures under RIA may occur in high-burn-up fuel rods, but not in fresh fuel. The failure mode is more likely for accidents that initiate from conditions with low reactor power and/or significant subcooling than for accidents that occur at full reactor power.

Failure modes

Fractographic examinations of short-length fuel rods that have failed by PCMI in RIA simulation tests generally suggest that the failures occur by outside-in radial crack growth through the cladding. It is believed that this primary failure mechanism may be followed by axial growth of the through-wall cracks into long axial splits [101].

As for the radial growth of cladding cracks, it is generally observed that numerous radial cracks nucleate in the clad outer oxide layer under pulse reactor tests on high-burn-up fuel rods with corroded cladding (see Section 6.2.4). Some of these incipient oxide cracks also propagate through the oxygen- and hydrogen-rich material just beneath the oxide. This subjacent material is also brittle, at least at low temperature, and the radial crack path through the oxide layer and the outer part of the clad wall therefore appears characteristically brittle in fractographic examinations of high-burn-up fuel rods, which have failed in RIA simulation tests, e.g. see [44,156]. In contrast, the radial crack path through the innermost part of the clad wall generally indicates ductile failure, with the fracture surface typically inclined 45° to the main loading (hoop) direction. The ductile feature of the last part of the crack path is usually seen also in highly corroded and embrittled cladding, and it is believed that this inner ductile part of the clad wall offers significantly higher resistance to the radial crack propagation than the brittle outer part. A typical crack path, observed after a pulse reactor RIA test of a high-burn-up PWR fuel rod, is shown in Figure 12.

The transition from brittle fracture in the outer part to ductile failure in the inner part of the clad wall is governed by the radial gradient in both hydrogen concentration and temperature across the clad wall (see Sections 6.2.1 and 6.2.6 for further details on this matter). It seems that the gradient in hydrogen concentration is more important than that in temperature, since the same characteristic brittle/ductile fracture paths are observed in material property tests on hydrided cladding at isothermal conditions as in pulse reactor tests with sharp temperature gradients [252].

Of the numerous incipient radial cracks usually observed in the clad outer oxide layer, only one or a few usually develop into through-wall defects. These primary clad defects are believed to have limited axial extension, although it is difficult to draw definite conclusions on this matter for full-length LWR fuel rods: our understanding of RIA fuel rod failures is based on pulse reactor tests on short-length rodlets, whose failure behaviour may be different from that of full-length rods. However, axial propagation of the short primary defects into longer axial splits is usually considered to be a separate, second stage in the failure mechanism [101].

Figure 43 shows the post-test appearance of a high burn-up rodlet, VA-1, which was recently tested in the NSRR and failed through PCMI. The rodlet had an average burn-up of 71 MWd(kgU)⁻¹, and a

73 μm thick waterside oxide layer. It was re-fabricated from a full-length PWR fuel rod, which had been pre-irradiated in the Vandellós-2 PWR, Spain (see Section A.5, Appendix A). The rodlet failed at a fuel radial average enthalpy of $268 \text{ J(gUO}_2\text{)}^{-1}$, and the entire fuel inventory was dispersed into the coolant. Considering its importance with regard to fuel safety concerns about fuel dispersal, very little is known about the growth of primary defects into long axial splits [253]. It has been proposed that the primary defects grow axially through a fast and unstable propagation mechanism, which is driven by the mechanical thrust imposed by the expanding fuel pellets under the heat-up stage of the accident [254].

Figure 43. Post-test appearance of rodlet VA-1, which experienced PCMI-induced failure at a fuel enthalpy of $268 \text{ J(gUO}_2\text{)}^{-1}$ under an RIA simulation test in the NSRR [159,225]



Loading conditions

The loading conditions responsible for low temperature cladding failure under RIA is dominated by the mechanical thrust imposed by the rapidly expanding fuel pellets, and the contribution from rod internal gas pressure can generally be neglected. Moreover, as discussed in Section 6.1.2, the contribution to fuel expansion from fission gas swelling is insignificant under the early phase of RIA, and thermal expansion alone is responsible for the fuel pellet deformation under the heat-up phase.

Since the fuel is heated almost adiabatically during the early phase of an RIA, the rate of power increase directly controls the rate of fuel pellet thermal expansion. In high-burn-up fuel rods, where the pellet-clad gap is closed, the fuel thermal expansion is directly transferred to the cladding, and the rate of power increase thus also controls the loading rate on the cladding (see Section 6.2.2). Strain rates in the cladding hoop direction typically reach $0.1\text{--}1.0 \text{ s}^{-1}$ for fuel enthalpy injections up to 400 Jg^{-1} and pulse widths (FWHM) in the range of 5 to 75 ms (see Section 6.2.2). The loading rate is important, since clad ductility drops with increasing strain rate at low temperature (see Sections 5.2.1 and 6.2.6).

The rate of power increase controls not only the loading rate, but also the time lag between mechanical loading and heating of the clad tube. A fast power increase results in high PCMI-induced clad stresses at a time when the cladding has not yet been heated from its initial temperature. Since the ductility of oxidized and hydrided cladding is low at low temperature, fast power pulses are prone to cause clad failure. For slow power pulses, the clad temperature evolves concurrently with the mechanical loads, and the risk for brittle clad failure in the early part of the transient is therefore smaller [91]. This is illustrated in Figure 44, which shows the calculated cladding radial average temperature, plotted with respect to cladding radial average hoop strain, for two simulated pulse reactor tests in the CABRI REP-Na programme. In the first test, REP-Na1, the width (FWHM) of the power pulse was 9.5 ms, whereas in the second test, REP-Na4, it was 75 ms. The initial clad temperature was 553 K in both tests, and the total energy depositions in the two tests were similar; see section A.6 in Appendix A for details. The calculations were done with the SCANAIR computer code (see Section 8.2). The temperatures and strains presented in Figure 44 pertain to the peak power axial positions of the two rods, and the failure of REP-Na1 under the early part of the transient was not considered in the analyses.

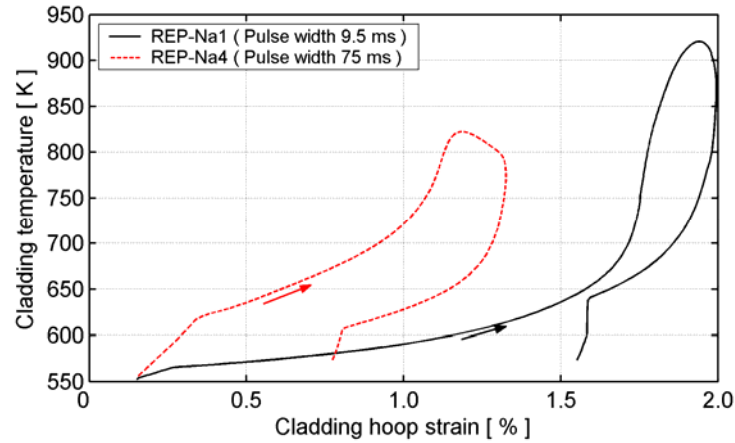
Clearly, in the fast power pulse test REP-Na1, most part of the cladding deformation takes place at temperatures below 600 K. On the other hand, in the REP-Na4 test, most of the clad deformation occurs at temperatures above 650 K, i.e. in a temperature range where the clad material is comparatively ductile.

It should be noticed that the effect of pulse width illustrated in Figure 44 is even more important if the transient starts from room temperature, such as in an RIA at BWR CZP conditions. This follows from the fact that the link between temperature and clad ductility is more pronounced at room temperature than at 550-600 K (see Section 6.2.6).

It should be pointed out that the mode of PCMI-induced loading is much different from that of gas overpressure loading in cladding tubes. The PCMI-induced loading is displacement controlled, which means that the loads are relaxed when the cladding expands and yields. This leads to a stable mode of deformation, which is completely opposite to the deformation behaviour under gas pressure loading, where yielding is usually followed by immediate cladding failure through localised plastic deformation (necking) [255]. This unstable mode of failure is promoted by biaxial loading and also by the loss of strain hardening in embrittled materials [256].

Figure 44. **Calculated evolution of clad temperature and deformation in the CABRI REP-Na1 and REP-Na4 pulse reactor test rods** (see Section A.6, Appendix A)

Calculated temperatures and strains are radial average values, pertaining to the peak power axial positions of the two rods.



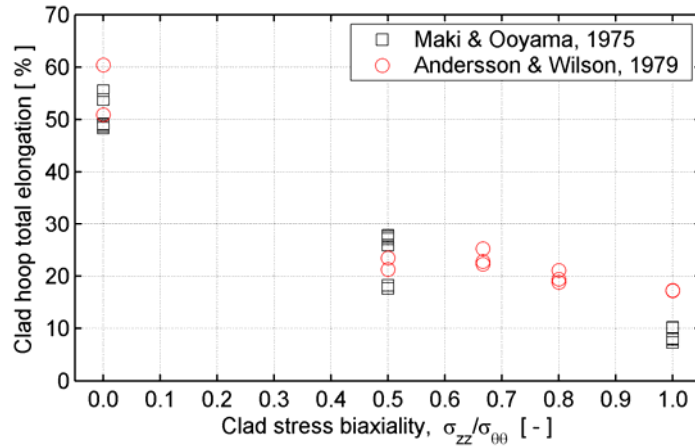
As mentioned in Section 3.3.2, friction and possible bonding between pellet and cladding are also important to the nature of PCMI loading. Prevention of *circumferential* sliding between pellet and cladding leads to localisation of hoop stresses and strains to small regions of the cladding, which are adjacent to mouths of radial cracks in the pellet [257]. Prevention of *axial* sliding, on the other hand, affects the overall axial loading of the clad tube. The axial contact forces imposed by the expanding fuel column result in significant clad axial stresses, from the bottom of the rod up to the point of pellet-clad contact. Hence, pellet clad bonding may lead to a change in load biaxiality for large parts of the clad tube. Measured ratios of axial-to-hoop cladding residual strains after RIA simulation tests on high-burn-up fuel rods indicate that the stress biaxiality ratio $\sigma_{zz}/\sigma_{\theta\theta}$ is 0.6-0.9 (see Figure 33 in Section 6.2.2). It should be remarked that these numbers are space-time average values, and that the biaxiality ratio may vary with axial position along the fuel rod and with time under the transient. Recent on-line measurements of cladding hoop and axial strains under RIA simulation tests in the NSRR, by use of strain gauges, show that the local stress biaxiality ratio is close to unity under PCMI-induced loading [91].

The stress biaxiality is important to fuel rod survivability, since it affects cladding ductility. More precisely, it is known from mechanical property tests that the hoop plastic strain to failure of zirconium alloy cladding has a minimum for equal axial-circumferential biaxial loading, i.e. for $\sigma_{zz}/\sigma_{\theta\theta}=1$. Figure 45 shows the results of two experiments, in which the influence of $\sigma_{zz}/\sigma_{\theta\theta}$ on the hoop total elongation of un-irradiated cladding tubes was studied at room temperature. The first study was on

RXA Zircaloy-2 material [258] and the second on RXA Zircaloy-4 [259]. From Figure 45, it is clear that the hoop total elongation drops markedly with increasing stress biaxiality in both materials, and it is therefore justified to assume that pellet-clad bonding increases the risk for clad tube failure under RIA. Another conclusion that can be drawn from Figure 45 is that any clad ductility test, intended to settle a strain-based criterion for PCMI-induced cladding failure under RIA, should be done with equal biaxial loading, i.e. with $\sigma_{zz}/\sigma_{\theta\theta}=1$. The bulk of clad ductility data in literature are for $\sigma_{zz}/\sigma_{\theta\theta}=0$ (uniaxial ring tensile tests) or $\sigma_{zz}/\sigma_{\theta\theta}=1/2$ (burst tests), and therefore cannot be used to formulate clad failure criteria for RIA, unless the differences in stress state are somehow compensated for. Various methods have been proposed for this purpose, and clad failure criteria have been formulated, based on compensated ductility data from out-of-pile mechanical tests [182,260-263].

Figure 45. Effect of clad stress biaxiality on hoop total elongation, i.e. the hoop plastic strain to failure

Data for un-irradiated RXA Zircaloy-2 [258] and Zircaloy-4 [259] cladding at room temperature.



In conclusion, cladding failure or survival under the early heat-up phase of an RIA is determined by the interplay between mechanical loading and heating, and the transient deformation behaviour of the cladding. The latter depends on the pre-accident state of the material, e.g. the initial temperature, degree of radiation damage and corrosion, but also on the rate of heating and loading, load biaxiality, etc. under the accident.

Figure 46 shows the results of pulse reactor tests on pre-irradiated UO_2 fuel rods, plotted with respect to fuel burn-up. Open symbols represent fuel rods that have survived the tests, whereas filled symbols are failed rods that bear evidence of low temperature PCMI-induced brittle failure. Hence, UO_2 fuel rods that have failed as a consequence of cladding high temperature ballooning and burst are not shown in the figure. Crosses indicate tests done on rods with hydride blisters in the cladding tube. The data in Figure 46 are plotted in terms of fuel *enthalpy increase* during the tests, rather than *total enthalpy*, because the former is more directly related to the PCMI-induced clad loading under RIA. For the failed rods, the presented fuel enthalpy increase is the increase up to the point of failure, provided that the point of failure is known. Otherwise, the *peak* fuel enthalpy increase under the test is used.

From Figure 46, it is clear that PCMI-induced cladding failures are rarely observed in pulse reactor tests, when the fuel burn-up is below $40\text{-}50 \text{ MWd}(\text{kgU})^{-1}$ and the fuel enthalpy increase is lower than $600 \text{ J}(\text{gUO}_2)^{-1}$. The two exceptions, PBF 802-3 and SPERT-CDC 859, failed due to severe cladding embrittlement by hydride blisters (see Appendix A, Sections A.1 and A.2). At fuel burn-ups beyond $40 \text{ MWd}(\text{kgU})^{-1}$, failed rods and survivals are interspersed in Figure 46). This is due to the large differences that exist between the tested rods (fuel rod design, clad corrosion) as well as between the

pulse reactor test facilities (power pulse width, cooling conditions). We also note that the failed high-burn-up rods seem to be concentrated to the *lower* part of the diagram, quite contrary to expectations. However, one should remember that Figure 46 shows the *peak* fuel enthalpy increase for the survivals, but the *enthalpy increase to failure* for the failed rods. A perhaps more consistent presentation of the data is given in Figure 55 of Section 7.2.1, where the data are plotted in terms of peak fuel enthalpy for both survivals and failed rods.

Figure 46. **Fuel enthalpy increase versus burn-up for pre-irradiated UO₂ fuel rods, tested in various pulse reactors**

Filled symbols represent low-temperature, PCMI-induced failures, whereas open symbols are survivals. Crosses indicate tests done on rods with hydride blisters in the cladding tube.

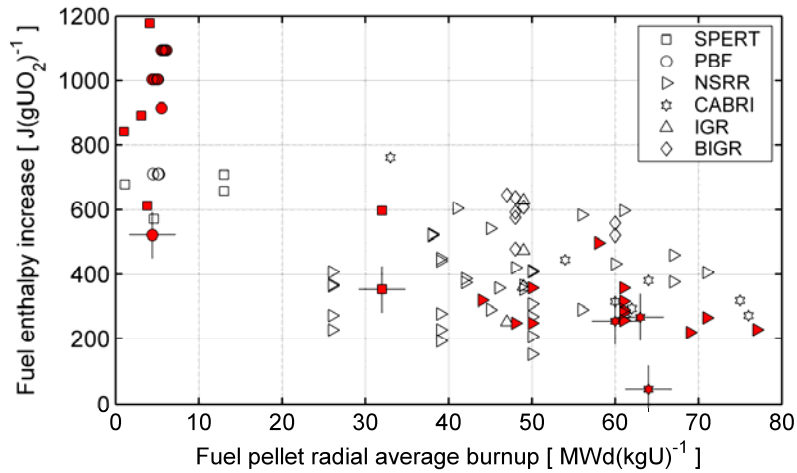
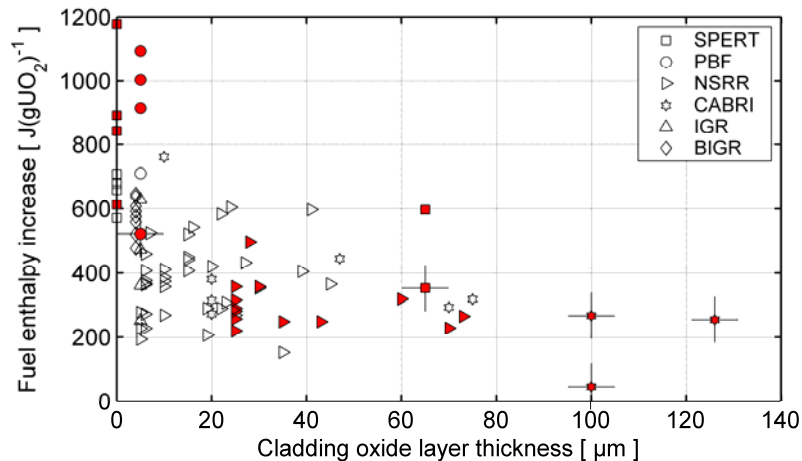


Figure 47. **Fuel enthalpy increase versus cladding oxide layer thickness for pre-irradiated UO₂ fuel rods, tested in various pulse reactors**

Filled symbols represent low-temperature, PCMI-induced failures, whereas open symbols are survivals. Crosses indicate tests done on rods with hydride blisters in the cladding tube.



It has been suggested that the propensity for PCMI-induced cladding failure under an RIA is more affected by cladding corrosion than by the fuel burn-up as such [144]. This hypothesis is tested in Figure 47, which shows the same data as in Figure 46, but plotted with respect to the cladding peak oxide layer thickness.

6.2.5.2 High-temperature failures

High-temperature clad failures under RIA may occur if normal cooling conditions are lost during the accident. This is always the case in the design basis RIA for CANDU reactors, which is assumed to be initiated by a loss of coolant accident (see Section 2.1.3). In CANDUs, off-normal cooling conditions and high cladding temperatures thus exist from the very beginning of the RIA. In light water reactors, high cladding temperatures can be reached only if the deposited energy is sufficient to induce a boiling crisis at the clad-to-coolant interface (see Section 6.2.1).

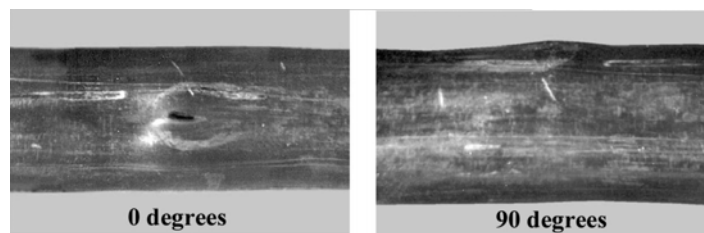
Failure modes

High-temperature fuel rod failures under RIA may occur by two different modes: clad ballooning and fuel rod disruption upon quenching. The latter failure mode resembles closely the kind of failures anticipated under loss of coolant accidents, and the reader is referred to the companion state-of-the-art report on LOCA for a detailed account of the phenomena involved [264]. In the following, we will place emphasis on the clad ballooning mode of failure under RIAs. Pulse reactor tests have shown that ballooning under RIAs is generally more limited than under LOCAs, especially for high-burn-up fuel rods, so this failure mode is not comparable between the two accident scenarios.

The high cladding temperatures reached after a boiling crisis may lead to significant cladding deformation by creep, if the temperature is maintained for a sufficiently long time and there is a pressure difference across the clad wall. The creep deformation can be either in the form of outward ballooning or inward collapse, depending on whether the rod internal gas pressure exceeds the coolant pressure or vice versa. Axial collapse of the cladding has been observed in fresh fuel rods with low internal gas pressure, tested in the NSRR [265-266] and in the PBF [148], and radial collapse into pellet-pellet axial gaps is also possible [267]. The tests show that the collapse does not lead to loss of cladding integrity, unless there are large axial gaps in the fuel pellet column.

Clad ballooning may cause more severe consequences. Figure 48 shows the post-test appearance of rodlet RT-9, which is a high-burn-up VVER fuel rod that failed by high temperature clad ballooning and burst under an RIA simulation test in the BGR. The rodlet had an average burn-up of $60 \text{ MWd}(\text{kgU})^{-1}$, and a clad waterside oxide layer thickness of about $5 \mu\text{m}$. It experienced a peak fuel enthalpy of $691 \text{ J}(\text{gUO}_2)^{-1}$ under the test, and failed without any fuel dispersal (see Section A.4 in Appendix A). As shown in Figure 48, the clad ballooning was moderate, and the failure took the form of several pin-hole cladding perforations, located in mid-pellet positions along the active length of the rodlet. The location to mid-pellet positions is due to the barrel-shape expansion of the pellets under the test and the fact that cladding temperatures are higher at mid-pellet positions than at pellet-pellet interfaces [151]. The pin-hole cladding perforations that result from clad high temperature ballooning and burst are much smaller than the PCMI-induced axial splits discussed in Section 6.2.5.1. Consequently, the fuel dispersed into the coolant from the failed rods is negligible, and in general, fuel-coolant interaction is not a concern for this kind of failure. Nevertheless, since the clad ballooning may be significant for fresh fuel rods, it could possibly impair core coolability [111].

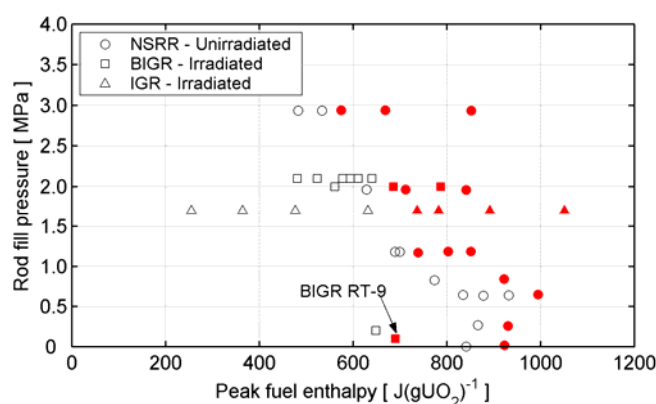
Figure 48. High-temperature ballooning and pin-hole cladding failure of rod RT-9 tested in the BGR [151]. See Section A.4, Appendix A for details.



Fuel rod failures caused by rupture of ballooned cladding have been frequently observed in pulse irradiation tests on fresh fuel rods in the NSRR [111-112], and also in tests on high burn-up VVER rods in the IGR and BIGH facilities [149,151]. Figure 49 shows a failure map of these rods, plotted with respect to peak fuel enthalpy and fuel rod fill pressure, i.e. the pre-test gas pressure within the rod. The peak fuel enthalpy to failure clearly drops with increasing fill pressure for the un-irradiated NSRR rods, but the irradiated rods seem to fail at about $650\text{--}700 \text{ J(gUO}_2\text{)}^{-1}$, irrespective of the initial gas pressure. Since the irradiated rods had burn-ups of $47\text{--}60 \text{ MWd(kgU)}^{-1}$, it is likely that transient fission gas release under the film-boiling phase made up the dominant part of the pressure loading in the low-pressure rods, and that the initial fill gas pressure was relatively unimportant for the high burn-up rods [151]. This is further discussed in Section A.4, Appendix A.

Figure 49. Uranium dioxide fuel rods that have failed by high temperature clad ballooning and burst under RIA simulation tests in the NSRR, IGR and BIGH [111-112, 149,151]

Filled symbols represent failed fuel rods; open symbols represent surviving sibling rods.



It is interesting to note that cladding failures by high temperature clad ballooning in high-burn-up fuel rods are seen for VVER type rods tested in the IGR and BIGH, but not for other fuel rod designs, tested in other facilities. A possible explanation to this difference is that the E110 cladding alloy (Zr-1.0Nb by wt%) is more resistant to waterside corrosion than Zircaloy-2 and Zircaloy-4, which are the cladding materials of most pulse-irradiated BWR and PWR fuel rods [268]. The outer surface oxide thickness was generally less than $5 \mu\text{m}$ for the high-burn-up fuel rods tested in the IGR and BIGH, and the cladding average hydrogen content was merely 60-80 wppm [149,151]. Hence, the cladding was not significantly embrittled by corrosion, and could therefore survive the early heat-up phase of the tests. Cladding failure instead occurred by high temperature ballooning and burst.

However, there is another difference in design between PWR and VVER fuel rods, which may also contribute to the observed difference in failure behaviour at high burn-up. In contrast to BWR and PWR rods, the VVER rods have annular fuel pellets, with a 1.2-2.4 mm diameter central hole. The central hole contains a significant amount of gas, which is rapidly heated to high temperature under an RIA. Experiments show that the expansion of this gas promotes cladding ballooning. More precisely, pulse irradiation tests were done on two types of PWR fuel rods in the NSRR - one type was charged with normal solid pellets, whereas the other type had annular pellets [269]. Except for the fuel pellets, the two types of rods were identical. The tests showed that, at comparable energy depositions, clad ballooning was larger for rods with annular pellets than for rods with solid pellets. It was also observed that rods with annular pellets failed by clad ballooning and burst under conditions that fuel rods with solid pellets survived [269].

It should also be remarked that the central hole provides a channel for axial gas flow, and a high gas pressure can therefore be maintained in regions where clad ballooning occurs. In contrast, axial gas flow

in BWR and PWR fuel rods is restricted to the pellet-clad gap. At high fuel burn-up, the gap is closed and axial flow of gas is negligible [270]. Consequently, clad ballooning will be driven only by the limited amount of gas that is available locally, and will not be supported by gas residing in regions outside the balloon. Hence, based on pulse irradiation tests of annular *vis-à-vis* solid fuel in the NSRR and experience from axial gas flow experiments, there is reason to believe that BWR and PWR fuel rods should be less prone for clad ballooning than VVER fuel rods with annular pellets, in particular at high burn-up.

The annular pellets may also affect the pellet-clad mechanical interaction, since some of the fuel expansion can be accommodated by the central hole. When the fuel is extensively fragmented, which is normally the case in RIA at high burn-up, it is likely that annular fuel pellets give a softer pellet-clad contact than solid pellets. This could, in addition to the low cladding corrosion, provide the remarkable resistance to PCMI-induced failures observed for high burn-up VVER fuel rods in RIA simulation tests.

As mentioned in the introduction, another possible high temperature failure mode is due to cladding embrittlement by high temperature oxidation under the film-boiling phase. As described in Section 6.2.3, at temperatures above 1 000 K, zirconium alloy cladding is rapidly oxidized from both the UO_2 -metal reaction on the inside surface and the water-metal reaction on the outside surface. Oxygen absorbed during the oxidation process embrittles the metal, and in severe cases, thermal stresses that arise under quenching (re-wetting) may be sufficient to disrupt the fuel rod. This failure mode was frequently observed in early pulse reactor tests on un-irradiated fuel rods, when the fuel enthalpy reached about $240 \text{ cal}(\text{gUO}_2)^{-1}$, i.e. about $1000 \text{ J}(\text{gUO}_2)^{-1}$ [111,113]. Early acceptance criteria for RIA in light water reactors were based largely on this threshold enthalpy. Tested fuel rods that failed upon quenching generally broke up into fragments that were centimetre-sized or larger. In cases where the fuel enthalpy was near the failure threshold, the rods failed by guillotine breaks, creating decimetre-long segments of the fuel rod. Only weak pressure pulses were recorded in the coolant, and the lack of violent fuel-coolant interaction was explained by the fairly low temperature of both fuel and cladding at time of rupture. In the experiments, the coolant was at ambient conditions, and quenching occurred when the cladding surface temperature was about 800-1 000 K [111,113]; see the discussion on quench temperature in Section 6.2.1. Cladding disruption upon quenching from high temperature is largely controlled by two factors:

- The brittleness of the oxidized material. As discussed in Section 6.2.3, the degree of embrittlement depends principally on the oxygen concentration in the transformed β -phase zirconium.
- The magnitude of thermal stress in the cladding. The thermal stress is caused by temperature gradients in the material, and the magnitude of these gradients depends on the quench temperature (see Section 6.2.1).

The magnitude of hoop thermal stress under quenching can be estimated by assuming a logarithmic temperature distribution across the cladding wall. With this assumption, it follows from theory of thermo-elasticity that the hoop thermal stress at the cold cladding outer surface is:

$$\sigma_{\theta\theta} = \frac{\alpha E \Delta T}{2(1-\nu)} \left[\frac{1}{\ln(x)} - \frac{2}{x^2 - 1} \right], \quad 15$$

where α , E and ν are the coefficients of thermal expansion, Young's modulus and Poisson's ratio of the cladding material, x is the ratio of the cladding outer radius to the inner radius, and ΔT is the temperature difference between the cladding inner and outer surfaces. To apply Equation 15, the cladding inner surface temperature can be assumed equal to the quenching temperature, as defined in Section 6.2.1, and the outer surface temperature can be set equal to the coolant saturation temperature.

Hence, by setting $\Delta T = 900 - 300 = 600$ K and using typical values for the material properties and dimensions of a PWR fuel rod with Zircaloy-4 cladding in Equation 15, it follows that the thermal hoop stress at the cladding outer surface is about 290 MPa. Equation 15 suggests that the hoop thermal stress increases linearly with the quenching temperature, and the stress also increases as the cladding wall becomes thinner, e.g. as a result of ballooning or oxidation.

Finally, it should be remarked that out-of-pile tests on high-temperature oxidation of cladding materials, summarised in Section 6.2.3, suggest that temperatures close to the melting point are needed to severely oxidize and embrittle the material during the film-boiling phase of an RIA, since pulse reactor tests show that this phase lasts for only 2-15 s. However, since it cannot be ruled out that the film-boiling phase in some scenarios for RIA in light water reactors may have longer duration, and that embrittlement-induced clad failure thus is possible at lower cladding temperatures and at lower fuel enthalpies than the typical pulse reactor threshold value of $1\,050\text{ J(gUO}_2\text{)}^{-1}$, acceptance criteria usually postulate that fuel rod failure should be assumed when film-boiling is predicted to occur under the reactivity-initiated accident. Hence, fuel rods that are deemed to experience departure from nucleate boiling in PWRs and dryouts in BWRs are assumed to fail.

6.2.6 Hydrogen-induced embrittlement

As already touched upon in Section 3.2.2, part of the hydrogen produced in the metal-water corrosion process at the cladding outer surface enters the cladding material under normal reactor operation. The hydrogen picked up by the metal migrates by thermo-diffusion (Soret effect) towards colder regions, and will therefore accumulate close to the comparatively cold outer surface of the cladding tube [98]. When the local hydrogen concentration exceeds the terminal solid solubility, precipitates of zirconium hydride are formed. Zirconium hydride can have three different crystallographic structures (phases) [271], but here, we will restrict the discussion to the face-centred cubic δ -phase, which is the commonly observed hydride phase in cladding tubes. The δ -hydride is non-stoichiometric, with a chemical composition in the range of $\text{ZrH}_{1.5}$ to $\text{ZrH}_{1.67}$ [99]. It precipitates in the form of platelets, approximately 0.1-0.4 μm thick and 0.5-2 μm wide [272]. However, these primary hydrides are stacked together into platelets with much larger size, which form the hydride structure that is usually observed in microscopy. In engineering literature, the word “hydride” usually refers to these plate-shaped clusters.

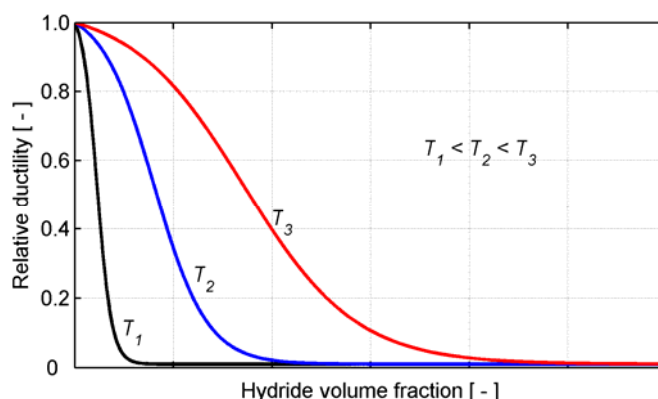
Since zirconium δ -hydride is brittle [273], it embrittles the cladding as it precipitates in the metal. For a given temperature, the degree of embrittlement depends on the concentration, size, orientation and distribution of the hydride precipitates. In terms of cladding mechanical properties, hydrides affect primarily the fracture toughness and the total elongation, i.e. the plastic strain to failure in tension. If the material contains hydride platelets with their normals parallel to the loading direction, also the yield strength and ultimate tensile strength (UTS) are degraded. If not, the yield strength and UTS are known to be unaffected or even increase slightly with hydride content, up to at least 2 000 wppm hydrogen [252,274-276]. This is in glaring contrast to the fracture toughness and total elongation, which drop significantly over the same range of hydrogen concentrations.

Temperature has a strong impact on the ductility of hydrided zirconium alloys, and the relation between temperature, hydride content and ductility is schematically illustrated in Figure 50. The relative ductility on the ordinate is defined as the ductility of the hydrided material in relation to that of hydride-free material, in terms of either total elongation [277] or fracture toughness [278]. Figure 50 shows that the material is less ductile (more brittle) at low temperature, and also that the relative ductility changes more dramatically with respect to hydride volume fraction at low temperature.

In the following subsections, we discuss the mechanisms for hydrogen-induced embrittlement and how they are influenced by temperature, hydride distribution and hydride orientation. The presentation

is focused on experimental data, and models for the embrittlement are, with a few exceptions, not discussed. However, it should be mentioned that micro-mechanical models for hydrogen-induced embrittlement of zirconium alloy cladding are available in literature [279-280], and also that various empirical models, intended for application as cladding failure criteria in analyses of RIA, have been proposed [182,196,262,281]. The latter models are based on data from mechanical testing of hydrided cladding, and they correlate the cladding ductility to temperature, hydrogen content and other parameters of relevance.

Figure 50. **Schematic relation between relative ductility, temperature (T) and hydride volume fraction in zirconium alloys [277-278]**



6.2.6.1 Embrittling mechanisms

Several mechanisms contribute to hydride-induced embrittlement of zirconium alloys [96]. At low temperature and high hydride concentration, the embrittlement is mainly due to hydride fracture, i.e. a crack propagates through a network of more or less interconnected hydrides, which provide a brittle crack path through the material. Hydrides precipitate preferentially, but not exclusively, on grain boundaries, which means that the hydride network morphology is affected by the grain structure of the cladding material. Consequently, the hydrogen concentration required to form a continuous network of hydrides, through which brittle fracture can take place, depends on the thermo-mechanical manufacturing route for the cladding. It has been shown that manufacturing routes leading to finer grain structures generally give materials that can accommodate larger concentrations of hydrogen without loss of ductility [282-283].

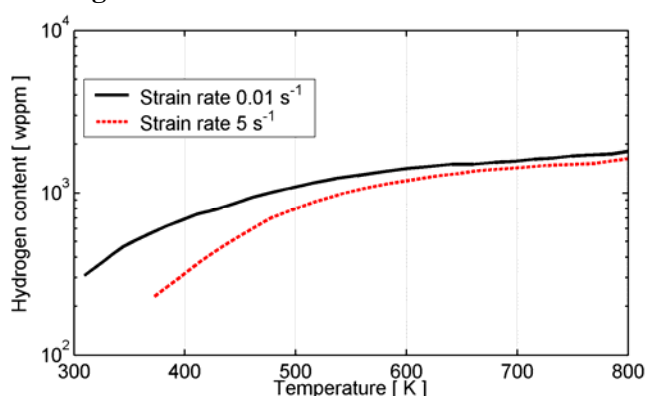
The threshold hydrogen concentration for formation of a continuous hydride network is in the range of 250-600 wppm, depending on the material's grain structure. However, continuous brittle crack paths through hydrides can be formed at even lower hydrogen concentrations, since the hydrides are preferentially oriented. The direction of loading in relation to the hydride orientation is important for formation of these cracks (see Section 6.2.6.4). At temperatures above approximately 400-450 K, the metal matrix generally yields before the hydrides fracture [284], which means that brittle fracture through the hydride network is unlikely. Hence, at low hydrogen concentration and/or elevated temperature, the hydride-induced embrittlement is generally not caused by hydride fracture. The embrittlement is instead attributed to either of two effects, pertaining to irradiated and un-irradiated materials, respectively. In irradiated zirconium alloys, plastic deformation takes place in dislocation channels with limited extension, and may therefore be hindered even by a moderate concentration of hydride precipitates [80]. In an un-irradiated material, plastic deformation takes place more uniformly, and it is therefore not so easily hindered by sparsely located hydrides. In this case, the embrittlement is likely due to the fact that hydrides promote initiation and link-up of voids in the material [285]. Nucleation and growth of voids reduce the macroscopic ductility of the material, even though the solid material between the voids possesses significant ductility.

The fact that different embrittling mechanisms come into play, depending on the hydride concentration, temperature, irradiation dose and stress state in the material, makes it difficult to interpret experimental data. In addition, there are also differences between tested materials, e.g. in alloy composition and heat treatment, which further complicates the picture. To this end, it should be noticed that the majority of published studies on “hydrided cladding” have been performed on un-irradiated materials, which are charged with hydrogen under elevated temperature in a laboratory environment. Although the hydride distribution and morphology in these materials usually seem similar to those in clad tubes subjected to in-reactor irradiation and oxidation, one should bear in mind that the behaviour observed for the laboratory-type materials is not necessarily representative for in-pile cladding materials. In particular, the effects of irradiation, oxygen uptake and the presence of an external oxide layer are overlooked in tests on laboratory-type materials.

6.2.6.2 Influence of temperature

Temperature is a key parameter for the behaviour of hydrogen in zirconium alloys. Firstly, the temperature field controls the distribution of hydride precipitates in the material, due to the thermo-diffusion of solute hydrogen downhill temperature gradients and the strong influence of temperature on hydrogen solid solubility (see Figure 13 in Section 3.2.2.2). Secondly, hydrided zirconium alloys undergo a ductile-to-brittle transition at a certain temperature, i.e. the ductility changes dramatically over a narrow temperature interval. From experiments, it is well known that hydride embrittlement is more pronounced at room temperature compared to typical in-reactor clad temperatures, and studies have been performed to determine the ductile-to-brittle transition temperature (DBT) for hydrided clad materials. An estimate of the DBT for highly irradiated Zircaloy-4 is shown in Figure 51. It seems that, for hydrogen concentrations up to 1 000 wppm, the ductile to-brittle transition occurs between room temperature and typical cladding in-reactor operating temperatures (570-620 K). This conclusion is corroborated by experiments on other cladding materials, e.g. [274,276], as well as by tests on the Zr-2.5%Nb material used in CANDU reactors [286]. From Figure 51, it is also clear that the ductile-to-brittle transition temperature for a given hydrogen content increases with increasing strain rate, at least for temperatures below 500-600 K. This effect of strain rate has been observed also in earlier studies [287]. It has also been reported that irradiation increases the DBT [288].

Figure 51. **Ductile-to-brittle transition temperature for irradiated Zircaloy-4 cladding, estimated through axial tensile tests at two different strain rates [168]**



It should be remarked that a ductile-to-brittle transition is difficult to define unambiguously. It can be defined either from a change in macroscopic material properties, such as total elongation or reduction of specimen cross-sectional area in tensile tests, or from a change in visual appearance of fracture surfaces, examined locally by microscopy. Since it has been observed that a change in macroscopic behaviour from ductile to brittle need not be reflected in a corresponding change of fractographical appearance, the definition of a ductile-to-brittle transition is somewhat arbitrary [168,278].

A change in temperature changes the hydrogen solid solubility, and thus the partitioning of hydrogen between solid solution and hydride phase. Heating leads to dissolution of hydrides, whereas cooling leads to hydride precipitation. The phase transformation is diffusion controlled, which means that some time is needed for phase equilibrium to be reached upon a change in temperature. Ham [289] studied the kinetics of diffusion controlled precipitation on a periodic array of nucleation sites theoretically, and found that the rate of change for the precipitate volume fraction, κ , could be written:

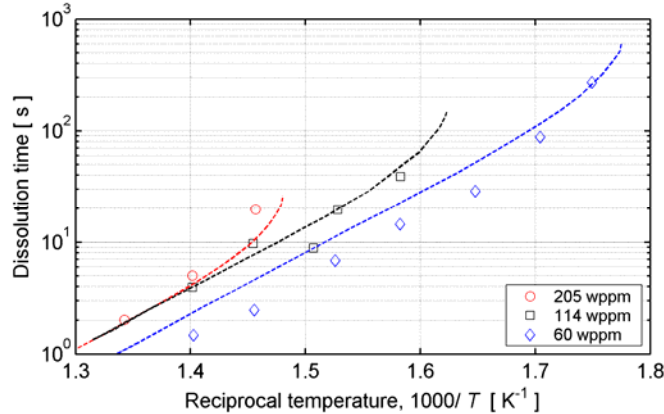
$$\frac{\partial \kappa}{\partial t} + \frac{1}{t_c}(\kappa - \kappa_e) = 0, \quad 16$$

where t_c is a characteristic time, and κ_e is the precipitate volume fraction under equilibrium conditions, i.e. the volume fraction that would be reached after infinite time, if the current temperature were held constant. Ham's results can be applied to the problem of hydride precipitation and dissolution, if κ_e is interpreted as the equilibrium volume fraction of hydride phase in the material. This property can be calculated from the hydrogen concentration of the material and the current solubility limit.

Kearns [290] reported that a phase kinetics model similar to that in Equation 16 fitted his hydride dissolution data for un-irradiated Zircaloy-4 well, when combined with the relation $t_c \propto l_h^2/D$, where D is the hydrogen diffusivity in α -phase zirconium and l_h is the distance between hydrides. This distance is inversely proportional to the hydrogen concentration [290]. Figure 52 shows the hydride dissolution data for un-irradiated Zircaloy-4 from the work of Kearns. The measured time for complete hydride dissolution is plotted versus inverse temperature for three different concentrations of hydrogen in the material. The dissolution time calculated on the basis of Kearns diffusion controlled phase kinetics model is shown with a dashed line for each hydrogen concentration.

Figure 52. Measured (symbols) and calculated (dashed lines) time needed for complete dissolution of zirconium δ -hydride precipitates in un-irradiated Zircaloy-4 [290]

The dissolution time was measured for samples with three different concentrations of hydrogen, as indicated in the legend.



It is clear from Figure 52 that the hydride dissolution rate depends strongly on temperature, but that there is also an effect of hydrogen concentration, through the size and number density of hydrides. It is interesting to note that the time needed for complete dissolution of hydrides at a temperature of 700 K is 2-10 s, depending on hydrogen concentration. It can therefore be concluded that hydride dissolution is too slow to occur under the early heat-up stage of an RIA, and unless a boiling crisis occurs, hydrides will hardly dissolve at all as a result of the cladding temperature excursion (confer Section 6.2.1).

6.2.6.3 Influence of hydride distribution

In experimental studies on hydride-induced embrittlement of cladding tubes, the distribution of hydrides in the material has been found equally important as the average hydride content. Most reported studies, e.g. those of Nagase *et al.* [291], Fuketa *et al.* [44] and Daum *et al.* [178] have been done on un-irradiated materials, which have been artificially hydrided in laboratory environment to obtain desired distributions of hydrides. These investigations have generally shown that, for the same average hydride content, materials with uniformly distributed hydrides are more ductile than those having local concentrations of hydrides in certain regions.

This result has bearing upon the formation of hydride rim structures in highly oxidized and hydrided cladding tubes, which arise from the radial temperature gradient and its effects on migration and precipitation of hydrogen (see Section 3.2.2.2). Irradiated and oxidized PWR clad tubes often have significant radial concentration gradients, whereas BWR clad tubes usually have fairly uniform hydride distributions. The tendency for the concentration gradients to turn into layered structures, with a densely hydrided rim at the clad outer surface, as shown in Figure 12, increases with clad surface heat flux, average hydrogen content and also with the strength of the radial temperature gradient. A few quantitative analyses of the hydrogen distribution across the cladding wall in high-burn-up PWR fuel rods are available in open literature [80,292].

A common finding in experiments on laboratory-hydrided un-irradiated material, such as those by Daum *et al.* [178], Fuketa *et al.* [44] and Pierron *et al.* [92], is that the ductility decreases rapidly with increasing thickness of the hydride rim at the clad outer surface. The ductility decreases up to a rim thickness of about 100 μm , after which the embrittlement seems to saturate, and for rims thicker than 100 μm , the ductility is fairly constant. Daum *et al.* [178] and Pierron *et al.* [92] have suggested that this results from the fact that the brittle hydride rim cracks at low plastic strain, and that the cracks act as nucleation sites for further crack propagation through the ductile material beneath the rim. Hence, in laboratory-hydrided materials, the hydride rim seems to play the same role as the external oxide layer plays for in-pile oxidized clad tubes (see Section 6.2.4). At present, it is not clear whether the localisation effects from the oxide layer and the subjacent hydride rim are additive. If they are, one could suspect that there is a threshold of about 100 μm for the combined oxide + hydride rim thickness, above which the embrittlement saturates.

For irradiated cladding materials, there are only a few reported experiments that focus on the influence of a radial gradient in hydride concentration. Garde *et al.* [80] tested highly irradiated and corroded Zircaloy-4 cladding, and concluded that the important parameter affecting clad ductility is the *local* hydride concentration, rather than the *average* concentration. Their findings thus corroborate the conclusions drawn in aforementioned tests on un-irradiated materials, that presence of a hydride rim at the clad outer surface has a detrimental effect on clad ductility. This conclusion is also indirectly supported by tests performed on irradiated Zircaloy-2 by Wisner and Adamson [274]. They tested material taken from water rod tubes, which operate without a temperature gradient, and consequently have an almost uniform hydride distribution. This material was found to have superior ductility in comparison to materials with similar average hydride content, but with the hydrides concentrated to a rim at the cladding outer surface.

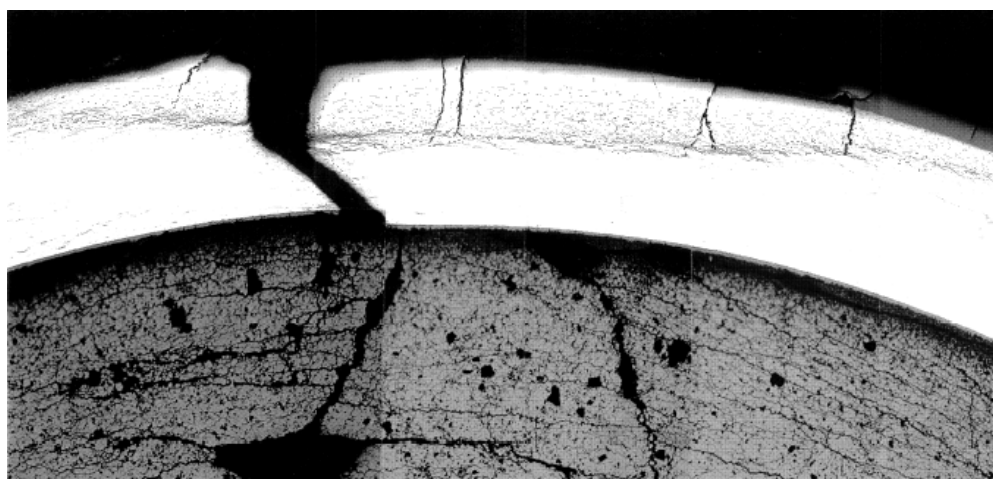
The detrimental effects of a hydride rim on cladding ductility can be understood and successfully modelled by use of fracture mechanics [174-175]. However, this is only true as long as crack propagation in the inward radial direction of the clad tube is concerned. When it comes to crack propagation in the tube axial direction, Fuketa *et al.* [44] found no detrimental effect of a hydride rim in burst tests on un-irradiated Zircaloy-4 cladding. On the contrary, axial cracks were found to be shorter in samples with hydride rims than in uniformly hydrided samples with similar average hydride

content. A possible explanation to this observation is that the inner part of the cladding, with low hydride content, had a beneficial effect on fracture toughness in the axial direction, which outweighed the detrimental effect of the hydride-rich outer rim.

The non-uniform distribution of hydrides in the clad tube radial direction has received much attention, since it is a consequence of the unavoidable radial temperature gradient under reactor operation. However, gradients in temperature and hydride concentration may under certain conditions appear also in the axial and circumferential directions of the clad tube. Regions with high concentrations of hydrogen and clad hydride content are often found at pellet-pellet interfaces, since the clad temperature is somewhat lower at these locations. If inter-pellet axial gaps occur in the fuel column, massive hydriding may appear at the resulting cold rings of the clad tube [293].

Severe local hydriding can also result from spallation of the oxide layer, creating cold spots at which hydride blisters may form. As shown in Figure 53, these blisters are lens-shaped, typically a few millimetres in diameter, and contain a very high hydride concentration or even massive hydride.

Figure 53. **Cladding failure initiated at a hydride blister in the CABRI REP-Na8 test** [204]



The influence of hydride blisters on clad ductility has recently been both experimentally and theoretically studied by Pierron *et al.* [92]. From tensile tests on small-scale un-irradiated Zircaloy-4 specimens with artificially induced hydride blisters, they found that the loss of local ductility correlated well with blister depth. The observed behaviour was successfully explained by an analysis based on non-linear fracture mechanics, in which it was assumed that the blisters provide initiation sites for radial cracks. Hence, it seems that local hydride blisters play a similar role as a hydride rim or external oxide layer for initiating radial cracks, thereby degrading the macroscopic ductility of the cladding.

Post-irradiation examinations of BWR cladding with an inner liner of zirconium, sampled from high-burn-up fuel rods that have undergone RIA simulation tests in the NSRR, indicate that the liner may affect the cladding failure behaviour [156]. Local concentrations of hydrides were observed not only at the clad outer surface, but also within the liner material at the clad inner surface. Moreover, the crack path through the liner appeared to be caused by brittle fracture. Hence, it seems that the liner material, due to its slightly lower solubility for hydrogen [294], is more sensitive to hydride-induced embrittlement than the Zircaloy-2 base material. If so, liner cladding of high-burn-up fuel rods may suffer from double-sided hydride-induced embrittlement.

Influence of hydride orientation

The orientation of zirconium hydride platelets with respect to residual or applied tensile stresses strongly influences the embrittlement. The orientation of hydrides in cladding tubes is affected by the thermo-mechanical treatment of the tubes under manufacturing, and by the stress state prevailing under hydride precipitation. In general, hydride platelets are oriented with their surface normals preferentially aligned to the clad tube radial direction, and the width of the platelets along the tube axial direction is significantly larger than in the circumferential direction. These hydrides, usually termed “circumferential” hydrides, have only a moderate embrittling effect, since there is no tensile stress in the clad tube radial direction, i.e. in the direction perpendicular to the hydride platelets [99].

However, there are also hydride platelets oriented with their surface normals more or less aligned to the cladding circumferential direction. These hydrides, which are usually termed ‘radial’ hydrides, are much more deleterious, since they are perpendicular to the dominating tensile stress in cladding tubes of high-burn-up fuel rods. These detrimental radial hydrides are more common in recrystallization annealed clad materials than in materials subjected to milder heat treatments, such as stress relieved annealed cladding [99]. The former heat treatment results in a larger fraction of grain boundaries in the radial direction, and since hydrides tend to precipitate along grain boundaries, this could to some extent explain the differences in hydride orientation between RXA and SRA materials. However, there are also other causes to these differences, such as material texture. Nakamura *et al.* [158] have reported a more brittle fracture behaviour for typical RXA BWR cladding than for SRA PWR materials, when tested under similar conditions in the NSRR.

In addition to the thermo-mechanical treatment of the cladding material under fabrication, the hydride orientation is also affected by the stress state prevailing under hydride precipitation, or more precisely, under the nucleation phase of the precipitation process. Under stress-free conditions, hydrides nucleate in the direction and on the plane that gives the minimal hydride-metal interface energy, thereby minimizing the free energy of formation. If the material is stressed, the free energy of formation includes a strain energy term, which depends on both the stress state and the orientation of the hydride nucleus [295]. Hence, the presence of stress under hydride nucleation, either externally applied or residual in the material, may affect hydride orientation. The hydride platelets have a tendency to precipitate perpendicularly to the direction of the major principal stress, provided that this stress is tensile and has sufficient magnitude. The external stress required for hydride re-orientation depends on material strength, texture, grain structure and residual stresses in the material; see e.g. [99,296] and the references therein. Although stress-directed orientation of zirconium hydrides has been thoroughly investigated in the past, systematic measurements of the threshold stress for hydride re-orientation have usually been done on sheets or thick-walled tubing, and not on cladding tubes. Moreover, measurements on irradiated material are, to the authors’ knowledge, unavailable in open literature.

Studies on the threshold stress for hydride re-orientation in un-irradiated, recrystallised Zircaloy sheets [297-298] indicate that a tensile stress of about 100 MPa is required to perturb the hydride orientation in these materials, and complete re-orientation requires a stress of about 200 MPa. These results are consistent with those from hydride re-orientation tests on un-irradiated Zircaloy-2 cladding by Nagase and Fuketa [299], who obtained partial re-orientation of hydrides, from the usual circumferential direction to the radial direction, for hoop cladding stresses in the range of 90 to 150 MPa. Available data thus indicate that a tensile hoop stress of about 100 MPa is sufficient to increase the fraction of radial hydrides that precipitate in cladding tubes. As a consequence, the fraction of radial hydrides in the cladding may start to increase after a certain in-reactor operating time, when the PCMI-induced tensile hoop stress reaches the threshold needed to affect the orientation of precipitating hydrides. However, radial hydrides may also form as a result of power cycling or overpower transients: existing circumferential hydrides may dissolve by the temperature excursion under high power, and then re-precipitate as radial hydrides, if the tensile hoop stress is large enough [300].

Attempts have been made to quantify the effect of hydride orientation on the hydride-induced embrittlement of zirconium alloys. From uniaxial tensile tests on un-irradiated Zircaloy-2, carried out at room temperature, Marshall and Louthan [301] found that the presence of perpendicular hydrides, i.e. hydride platelets oriented with their surface normals along the direction of tensile loading, completely dominated the embrittlement. They therefore introduced an equivalent, or effective, hydrogen concentration:

$$C_{Heff} = C_H f_{\perp}, \quad 17$$

where C_{Heff} and C_H are the effective and actual hydrogen concentrations, respectively, and f_{\perp} is the fraction of hydrides oriented perpendicular to the tensile stress. Marshall and Louthan found that their measured data for total elongation and reduction of test specimen area correlated well with C_{Heff} , and that both these ductility parameters approached zero for C_{Heff} in the range of 40-50 wppm [301]. The concept of effective hydrogen concentration from Equation 17 has also been successfully applied to describe hydrogen-induced embrittlement of un-irradiated Zircaloy-4 cladding, tested in uniaxial tension at room temperature [300].

The results from the uniaxial tensile tests mentioned above suggest that radial hydrides alone would govern cladding hoop ductility, at least at low temperature. However, this picture is contradicted by results from recent burst tests on un-irradiated Zircaloy-2 cladding, which were performed to gain better understanding of PCMI-induced failures observed under RIA tests on high-burn-up BWR fuel rods in the NSRR [299]. The cladding samples were gaseously hydrided to 200-650 wppm hydrogen, and some of the samples were then subjected to hydride re-orientation treatment by heat-up and cooling under controlled hoop stress. By varying the hoop stress from 90 to 150 MPa, fractions of radial hydrides in the range of 0.23 to 0.30 were produced. These fractions were significantly larger than the fraction found before hydride re-orientation treatment (0.12), and somewhat larger than normally found in high-burn-up BWR fuel cladding (≈ 0.20). Burst tests were performed at room temperature, 373 and 553 K. For these temperatures, the cladding ductility and rupture stress were only weakly affected by the fraction of radial hydrides in the investigated range (0.12-0.30). The most notable effect of hydride orientation was that axial crack propagation was much more extensive in samples with large fractions of radial hydrides, when tested at room temperature. However, at 553 K, there were no differences in behaviour between the samples [299]. Based on these results, the investigators concluded that radial hydrides alone cannot explain the loss of ductility observed in high-burn-up BWR cladding [299]. It should be remarked that the employed burst test samples had lower, and more representative, fractions of radial hydrides than samples used in the uniaxial tensile tests mentioned above [300-301]. Secondly, the cladding stress state differed between the burst tests and the uniaxial tests, with the burst test conditions being closer to the in-service loading for a cladding tube. Thirdly, the cladding material in the burst tests had a zirconium liner that contained a high local concentration of hydride. These differences could explain the seemingly conflicting results on the importance of hydride orientation from the referred burst and uniaxial tensile tests.

7. SUMMARY OF RESULTS FROM INTEGRAL RIA TESTING PROGRAMMES

7.1 Tests on fresh fuel rods

A large number of RIA simulation tests have been conducted on fresh (un-irradiated) fuel rods of various designs. The tests can be largely divided into two groups:

- Tests done to establish thresholds, in terms of peak fuel enthalpy, for cladding failure, fuel dispersal, melting, etc. Since these tests are generally aimed at establishing acceptance criteria for RIAs in power reactors, the tests are done on fuel rods of prevalent commercial design and under conditions that, as closely as possible, resemble those expected for power reactor RIAs.
- Parametric studies, intended to shed light on the fuel behaviour and mechanisms of fuel failure under RIAs, and to generate data needed for verification and calibration of computer codes. The effects of selected parameters are studied by performing series of tests, in which a single parameter of interest is varied at a time. The impact of fuel rod design parameters as well as power pulse characteristics and reactor coolant conditions has been studied in this manner.

In the following, we will treat mainly the first group of tests; the results of parametric studies have been discussed at some length in Section 6 of the report. Reviews of RIA simulation tests on fresh fuel rods are available in literature, e.g. [111,113,142-143,152].

Table 10. Overview of pulse reactor facilities used for RIA simulation tests on fresh fuel rods

	SPERT US	PBF US	IGR KZ	BIGR RU	HYDRA* RU	NSRR JP	PITESTI RO
Test conditions							
Coolant temperature [K]	293	538	293	293	293	293 – 578	293
Coolant pressure [MPa]	0.1	6.45	0.1 – 16	0.1	0.1	0.1 – 16	0.1
Coolant flow [ms ⁻¹]	0	0.5	0	0	0	0 – 1.8	0
Pulse width [ms]	13 – 31	11 – 16	100 – 1000	2 – 3	4 – 8	4 – 7	4 – 7
Test rods							
Rod type	BWR	PWR	VVER	VVER	VVER	BWR PWR	CANDU
Active length [mm]	≈ 130	≈ 1000	≈ 150	≈ 150	≈ 150	≈ 130	≈ 130

* The full name for the Russian HYDRA reactor is IIN-3M GIDRA.

Table 10 summarises the characteristics of seven pulse reactors, which have been used for RIA simulation tests of fresh fuel rods. Except for SPERT and PBF, the reactors are still in operation [302]. The type of fuel tested in each reactor is also indicated in Table 10. A few fresh fuel rods with MOX [202], ROX [49] and BA [41] fuels have been tested, but apart from these exceptions, the tests have been done on rods charged with UO₂ fuel. To this, end it should be remarked that the test rods are often, but not always, charged with fuel pellets enriched to higher fractions of ²³⁵U than typically used in commercial fuel rod designs. This is necessary in some of the pulse reactor facilities in order to increase the energy deposition to levels where fuel rod fragmentation and melting occur. As shown in

Section 3.1.1, enrichment affects the radial distribution of power and temperature in the fuel pellet, and parametric studies in the NSRR have shown that increased enrichment lowers the enthalpy threshold for failure of fresh fuel rods [111].

7.1.1 Cladding failure

The results of pulse irradiation tests on fresh fuel rods suggest that there are two limiting failure mechanisms at low fuel burn-up:

Fracture of oxygen-embrittled cladding upon quenching, following a sustained period of film boiling, high cladding temperature and severe cladding oxidation. This failure mode is limiting for fresh fuel rods, unless there is a substantial gas overpressure in the rod. Table 11 summarises reported fuel enthalpy thresholds for this failure mode. The failure threshold reported for VVER fuel rods, tested in the IGR, is clearly higher than the thresholds reported for PWR and BWR rods. It is unclear whether this is due to the particular VVER fuel rod design, or to the exceptionally wide power pulses in the IGR. The failed VVER rods bear witness to fuel and cladding melting.

Clad ballooning and burst at high temperature. This is the limiting failure mode, when there is a substantial gas overpressure, ΔP , in the fuel rod. Experimentally determined enthalpy thresholds for this failure mode are also summarised in Table 11. The enthalpy threshold falls off with increasing overpressure (see Section 6.2.5.2) and the works by Horhoianu *et al.* [143] and Saito *et al.* [112]. From a series of tests in the NSRR, the latter investigators reported that the effect of overpressure was observable only for $\Delta P \geq 0.8$ MPa; for lower values, the fresh fuel rods failed by oxygen embrittlement rather than ballooning.

Table 11. Enthalpy thresholds reported for limiting failure modes of fresh UO_2 fuel rods. The thresholds are given in terms of fuel pellet peak radial average enthalpy ($\text{J}(\text{gUO}_2)^{-1}$) during the tests. ΔP denotes the difference between the rod internal fill gas pressure and the coolant pressure (MPa).

	SPERT US	PBF US	IGR KZ	HYDRA RU	NSRR JP
Fuel type	BWR	PWR	VVER	VVER	PWR, BWR
Clad failure upon quenching	860 - 940	940 – 1050	1130	–	920
Clad ballooning and burst	–	–	670 ($\Delta P=2.4$)	670 ($\Delta P=2.4$)	900 – 590 ($\Delta P=0.25\text{-}3.0$)

We should also mention that cladding collapse has been observed in pulse irradiation tests on fresh fuel rods, carried out in the PBF, IGR, BGR and the NSRR [142,148,266-267]. The collapse occurs when the coolant pressure exceeds the rod internal gas pressure; the aforementioned tests have been done with ΔP in the range from -15.9 to -6.4 MPa, i.e. for typical PWR/VVER and BWR coolant overpressures. The tests suggest that the collapse per se does not lead to loss of cladding integrity, and it seems therefore inappropriate to classify cladding collapse as a separate failure mode for RIA. In the aforementioned tests, the cladding actually failed by oxygen-induced embrittlement, sometimes in combination with melting, and the observed failure threshold in terms of fuel enthalpy was in the range $960\text{-}1\,050 \text{ J}(\text{gUO}_2)^{-1}$.

Extensive parametric studies have been carried out in the NSRR to examine the effects of fuel rod design and cooling conditions on the failure behaviour of fresh fuel rods. Studies carried out up to the late eighties are reviewed in [111,152]. Among various fuel rod design parameters, the fuel rod internal fill gas pressure was found to have the most evident effect, manifested by the aforementioned change of failure mode. Moreover, the enthalpy threshold for clad failure upon quenching was found to depend on cladding thickness. Thin cladding has less heat capacity, reaches higher temperatures,

and is more rapidly penetrated by diffusing oxygen than thick cladding. Due to the difference in clad wall thickness, clad failure upon quenching occurred at slightly lower fuel enthalpies for PWR than for BWR rods in tests on fresh fuel [111].

The parametric studies on cooling conditions in the NSRR showed that cooling by forced convection increased the failure threshold relative to the standard tests with stagnant water [190]. Moreover, tests conducted at elevated coolant pressure and temperature, corresponding to hot operating conditions of BWRs and PWRs, indicated that the failure thresholds under these conditions were not different from those in standard tests, conducted at atmospheric pressure and room temperature [266]. The NSRR tests on clustered fuel rods should also be mentioned. These tests were done on bundles with five fresh PWR fuel rods, and showed that the central rod in the bundles failed at lower enthalpy than its neighbours, because of impaired cooling [111,303]. This is an interesting result, since RIA simulation tests are usually performed on single fuel rods.

Finally, it should be mentioned that the NSRR tests on rods with fresh (U,Pu)O₂ mixed oxide fuel and Gd₂O₃-bearing burnable absorber fuel showed that the failure behaviour of these fuel rods was not different from that of fresh UO₂-charged rods [41,200]. Also, the threshold enthalpies for cladding failure were consistent with that of uranium dioxide fuel.

7.1.2 Fuel dispersal and fuel-coolant interaction

An important experience gained from pulse irradiation tests on fresh fuel rods is that cladding failure does not necessarily lead to fuel rod fragmentation and dispersal of the fuel inventory into the coolant. This is particularly true for ballooning-type cladding failures, which occur with no or very limited fuel dispersal [111,142].

Pulse irradiation tests on fresh PWR and BWR rods in the SPERT, PBF and NSRR show that rod fragmentation occurs at fuel enthalpies that are somewhat higher than the threshold for fuel rod failure through quenching of oxygen-embrittled cladding [111,113]. Tests on fresh VVER rods in the IGR, however, show that cladding failure and fuel rod fragmentation occur at the same fuel enthalpy [142,149]. As mentioned in Section 7.1.1, the reason to this difference is unclear. Reported enthalpy thresholds for fuel rod fragmentation are summarised in Table 12. Also included in Table 12 are the reported thresholds for cladding quench-type failure (confer Table 11). Obviously, the reported enthalpy thresholds for fuel rod fragmentation are up to 145 J(gUO₂)⁻¹ higher than the thresholds for quench-type cladding failure.

Table 12. Enthalpy thresholds reported for fuel rod fragmentation, in comparison with those for cladding failure by quenching. The thresholds are given in terms of fuel pellet peak radial average enthalpy (J(gUO₂)⁻¹) during the tests. All data are from tests on fresh UO₂ fuel rods.

	SPERT US	PBF US	IGR KZ	NSRR JP
Fuel type	BWR	PWR	VVER	PWR, BWR
Fuel rod fragmentation	1 005	1 045	1 130	1 045
Clad failure upon quenching	860 – 940	940 – 1 050	1 130	920

The fuel rod fragmentation thresholds reported in Table 12 define the peak fuel enthalpies that fresh test rods can sustain without losing their rod-like geometry. At higher enthalpies, the test rods are broken into several pieces by circumferential (guillotine) cladding cracks. This fragmentation mode leads to partial dispersal of the fuel inventory; the more numerous the guillotine breaks, the more extensive is the fuel loss. The guillotine break fragmentation mode changes to a more severe fragmentation mechanism, caused by fuel pellet melting, if the deposited energy is increased to very

high values. From tests on fresh fuel rods in the NSRR, it was reported that the transition occurred at a total energy deposition of $340\text{--}380 \text{ cal}(\text{gUO}_2)^{-1}$, corresponding to a peak fuel enthalpy of about $1\,190\text{--}1\,360 \text{ J}(\text{gUO}_2)^{-1}$ [111,152]. At energies above this threshold, particles of molten UO_2 were expelled into the coolant, causing violent fuel-coolant interaction and coolant pressure pulses. It was also found that the fuel rod internal fill gas pressure had a strong effect on both the fuel dispersal and the mixing of dispersed particles with the coolant; the higher the pressure, the more violent was the fuel-coolant interaction [102]. Thermal-to-mechanical energy conversion ratios for dispersed fuel, molten and non-molten, are discussed in Section 4.3.1.

7.2 Tests on pre-irradiated fuel rods

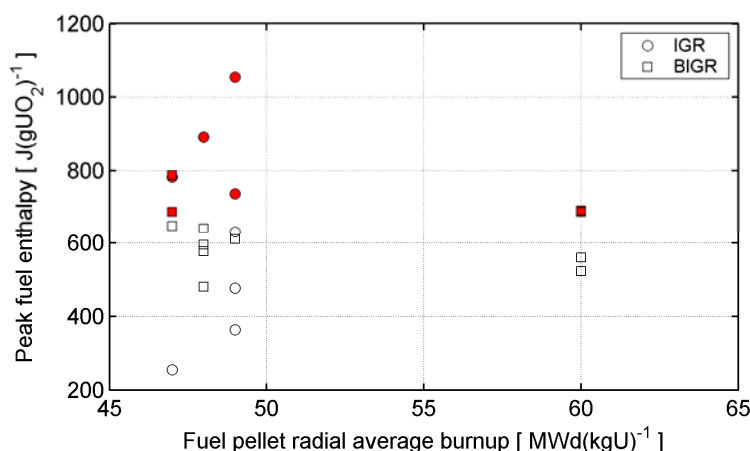
About 140 RIA simulation tests have to date been carried out on pre-irradiated LWR fuel rods. The major part of these tests was done on UO_2 fuel rods, but 13 of the tests pertain to $(\text{U,Pu})\text{O}_2$ mixed oxide fuel. The tests, as well as the six pulse reactors in which they were carried out, are briefly reviewed in Section 5.1, and a more detailed presentation is given in Appendix A. Here, we will summarise the most important results, with emphasis placed on the failure- and post-failure behaviour.

7.2.1 Cladding failure

When identifying the dominant failure mode for pre-irradiated fuel rods under RIA, the pulse test data at hand suggest, correctly or not, that a distinction should be made between VVER and PWR or BWR fuels. In the following, we will present experimental data for these fuel designs separately.

All reported pulse test failures of pre-irradiated VVER fuel rods are due to clad ballooning and burst, caused by high temperature deformation (see Sections A.3 and A.4 of Appendix A). This failure mode is observed for tests on high burn-up VVER fuel rods in both the IGR and BGR, notwithstanding the difference in pulse width (750-950 and 2.5-3.1 ms, respectively) between these facilities. The failures occur at fairly high fuel enthalpies, as shown in Figure 54; the lowest peak fuel enthalpy for which a pre-irradiated VVER fuel rod has failed in IGR or BGR is $687 \text{ J}(\text{gUO}_2)^{-1}$. The data in Figure 54 suggest a failure/no-failure demarcation line at approximately $650 \text{ J}(\text{gUO}_2)^{-1}$. No burn-up-dependence of this failure threshold can be discerned over the fairly narrow range of burn-up covered by the data. Moreover, there are no obvious differences between test results from the IGR and BGR facilities.

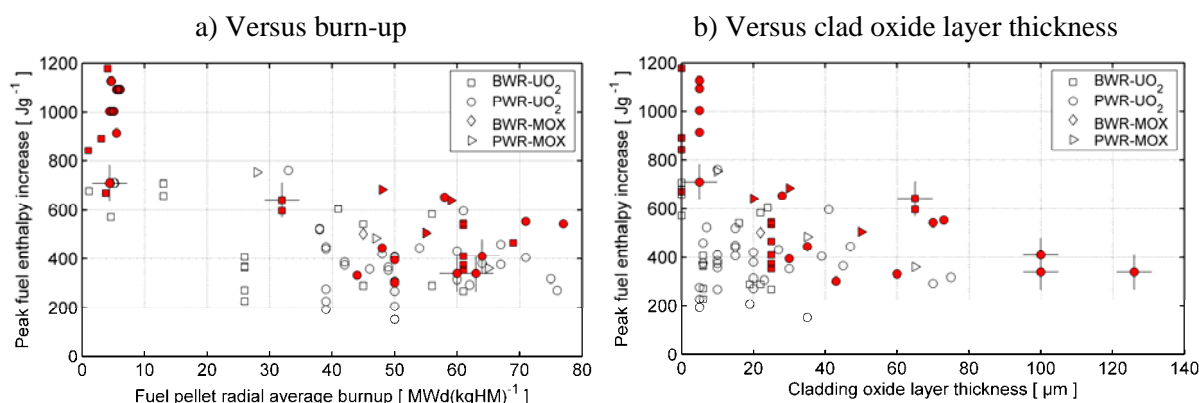
Figure 54. Peak fuel enthalpy versus burn-up for pre-irradiated VVER fuel rods tested in the IGR and BGR



(see Sections A.3 and A.4 of Appendix A). Filled symbols represent fuel rods that failed the tests through clad ballooning and burst, whereas open symbols are survivals.

In contrast to the VVER rods, most pulse test failures of pre-irradiated PWR and BWR fuel rods are due to partially brittle fracture of the cladding, caused by pellet-clad mechanical interaction under the early stage of the power pulse.¹⁸ Moreover, for high-burn-up fuel rods with severely corroded cladding, these PCMI-induced failures occur at fairly low fuel enthalpies, as shown in Figure 55.

Figure 55. **Peak fuel enthalpy increase versus a) burn-up and b) clad oxide layer thickness for pre-irradiated PWR and BWR fuel rods, tested in RIA simulation experiments. Crosses indicate tests done on rods with hydride blisters in the cladding tube.**



The data in Figure 55 are plotted in terms of fuel *enthalpy increase* during the test, rather than total enthalpy, since the former is more directly related to the PCMI-induced clad loading under an RIA (confer Section 6.2.5.1). Also note that the *peak* fuel enthalpy increase is plotted for both failed rods and survivals in Figure 55, in contrast to Figures 46 and 47 in Section 6.2.5.1.

The apparent difference in failure behaviour between high-burn-up VVER fuel rods and PWR or BWR rods in pulse irradiation tests deserves attention. As noted in Section 6.2.5.2, proposed explanations are related to the differences in design between VVER and PWR/BWR fuel rods. Firstly, the E110 (Zr-1.0Nb by wt%) cladding alloy used for the VVER rods is more resistant to corrosion than Zircaloy-2 and Zircaloy-4, which are the cladding materials of most pulse irradiated PWR and BWR fuel rods [268]. The cladding outer surface oxide thickness was generally less than 5 μm for the high-burn-up VVER fuel rods tested in the IGR and BIGR, and the cladding average hydrogen content was merely 60-80 wppm [149,151]. The E110 cladding of the VVER test rods was therefore not significantly embrittled by corrosion, and could therefore survive the PCMI-induced loading during the early heat-up phase of the tests. The importance of cladding corrosion to the propensity for PCMI-induced failure is underlined by recent tests on PWR fuel rods with M5 cladding, which has a corrosion behaviour similar to that of E110. Four high-burn-up PWR fuel rods with M5 cladding have been tested to date; rods RH-1 and RH-2 in the NSRR and rods REP-Na11 and CIP0-2 in CABRI. All rods survived, notwithstanding their high burn-up, 60-76 $\text{MWd}(\text{kgU})^{-1}$, and peak fuel enthalpy, 345-533 $\text{J}(\text{gUO}_2)^{-1}$.

Secondly, VVER fuel rods are charged with annular fuel pellets. Experiments on fresh fuel rods with annular *vis-à-vis* solid pellets have shown that thermal expansion of gas in the pellet annulus promotes cladding ballooning under RIAs [269]. Following our discussion in Section 6.2.5.2, it is likely that this phenomenon becomes even more prominent in high-burn-up fuel. The pellet annulus may also have a mitigating effect on pellet-clad mechanical interaction, since expansion of the fragmented UO_2 material in high-burn-up fuel rods could be partly accommodated by the central hole. This could, in addition to the low cladding corrosion, provide the remarkable resistance to PCMI-induced failures observed for high burn-up VVER fuel rods in RIA simulation tests.

18. The only exceptions are the PBF tests 801-1 through 801-4 (see Section A.2 of Appendix A).

We note from Figure 55 that the peak fuel enthalpy increase at which PCMI-induced cladding failure occurs seems to be similar for PWR and BWR fuel rods. A difference may very well exist, but it cannot be discerned from the scattered data in Figure 55. A difference in failure thresholds can be expected, not so much from the fuel rod designs, but from the difference in coolant pressure between PWRs and BWRs under normal operation, which leads to slower creepdown of the cladding tube, and hence, to slower closure of the pellet-clad gap for the BWR fuel rods. Consequently, for the same degree of pellet expansion under an RIA, the PCMI-induced loading on the clad tube will be milder in a BWR than in a PWR fuel rod, given a certain burn-up.¹⁹ The comparison of measured cladding residual strains in Figure 31, Section 6.2.2, also indicates that the PCMI is generally milder for BWR than for PWR fuel rods.

Possible differences between pre-irradiated MOX and UO₂ fuel with respect to PCMI loading under the early heat-up phase of an RIA have been studied on the basis of results from the CABRI REP-Na test series by Vitanza and Conde-Lopez [207]. The investigators found no significant difference in PCMI behaviour between MOX and UO₂ fuel, at least not for transient fuel enthalpy increments lower than 500 Jg⁻¹. To this end, it should be remarked that fuel rods in the CABRI REP-Na test series were efficiently cooled by sodium, and the fuel did not reside at high temperature for more than a few seconds. Fission gas induced transient swelling of the fuel was therefore not observed, except for rods REP-Na2 (UO₂) and REP-Na9 (MOX) [86].

In contrast, the pre-irradiated ATR MOX fuel rods tested in the NSRR were subjected to more challenging temperature histories (see Appendix A, Section A.5.3.1). The rods with highest fuel enthalpy, i.e. ATR-3 to ATR-5, experienced boiling crises and subsequent film boiling during the tests. These rods showed significant transient fission gas release and about 1.5% gas-induced volumetric swelling under the test, probably as a result of the dwell time at high temperature (confer Figure 24 in Section 6.1.2). Sasajima and co-workers [45] compared the behaviour of these ATR MOX fuel rods with that of BWR UO₂ rods. They concluded that cladding deformations and fission gas release in ATR-3 and ATR-4 were much more significant than in BWR UO₂ fuel rods with similar burn-up and peak fuel enthalpy [45]. In conclusion, the tests performed on pre-irradiated MOX fuel in the NSRR and CABRI suggest that the potential for transient fission gas induced swelling is more substantial in MOX than in UO₂ fuel, but that the phenomenon becomes significant to PCMI-loading under RIAs only in case the fuel rod experiences a boiling crisis and prolonged dwell time at high temperature.

7.2.2 Fuel dispersal and fuel-coolant interaction

In Section 7.1.2, we showed that RIA simulation tests on fresh fuel rods in various pulse reactors result in fuel rod fragmentation and dispersal of fuel into the coolant, when the peak fuel enthalpy exceeds roughly 1 000 Jg⁻¹. Pulse reactor tests on pre-irradiated fuel rods show that fuel may be dispersed into the coolant at significantly lower fuel enthalpy, when the fuel burn-up exceeds approximately 40 MWd(kgU)⁻¹. The fuel dispersal occurs in connection with PCMI-type cladding failure; the ballooning and burst type of failure does not lead to significant fuel dispersal.

Figure 56 shows the measured fuel dispersal from 25 pre-irradiated UO₂ fuel rods that have failed through PCMI under RIA simulation tests in the SPERT, CABRI and the NSRR. Filled symbols represent specimens, for which more than 10% of the UO₂ fuel inventory was dispersed into the coolant under the tests, whereas open symbols are samples with no or marginal fuel loss. The data behind Figure 56 are presented in Appendix A.

19. This is true at least for moderate burn-up; at high burn-up, the pellet-clad gap closes for both kinds of fuel rods, and this difference between BWR and PWR rods vanishes.

From Figure 56, it is clear that significant fuel dispersal was observed in only two out of nine fuel rods within the low- to intermediate burn-up range, which is here defined by the SPERT and JMTR test rods, ranging in burn-up from 21 to 38 MWd(kgU)⁻¹. Moreover, the peak radial average fuel enthalpies for the two rods that failed with significant fuel dispersal were very high, 850 and 910 J(gUO₂)⁻¹, respectively. Hence, according to these tests, the potential for dispersion of non-molten fuel fragments from failed fuel rods is low at low- and intermediate fuel burn-up.

The situation is much different at high burn-up. In the upper burn-up range of Figure 56, i.e. in the range of 44 to 77 MWd(kgU)⁻¹, we find that significant (>10%) fuel dispersal was reported in eleven of the sixteen tests. These eleven rods were all tested in the NSRR, and most of them failed by a combination of cladding axial splits and circumferential (guillotine) breaks. It should be remarked that the large fuel dispersal for three of the rods, HBO-1, FK-9 and OI-11, resulted from atypical clad tube failure. In these specimens, the fuel column was dispersed through a circumferential break along the weld to the bottom end fitting, which was completely separated from the upper part of the rod. The fuel dispersal behaviour for this failure mode is not transferable to full length fuel rods, for which only a minor part of the fuel column could possibly be expelled through a break at the bottom end plug.

There are several reasons to why the fuel dispersal is more extensive for high-burn-up than for low-burn-up fuel. Firstly, for a given fuel energy deposition, the cladding cracks are generally larger and wider for the high-burn-up fuel. This is most likely a result of hard PCMI and/or a more embrittled cladding in the high-burn-up fuel rods. The larger crack opening area eases the escape and dispersal of fuel particles. Secondly, as discussed in Section 6.1.2, high-burn-up oxide fuel turns into fine fragments when subjected to an RIA, as a result of fission gas induced grain boundary decohesion. This fragmentation mechanism promotes fuel dispersal, since the fine (<50 µm) fragments are easily expelled through cladding cracks under the power pulse [84].

Figure 56. Fuel dispersal observed for 25 pre-irradiated UO₂ fuel rods, all of which failed by PCMI under pulse reactor tests. Filled symbols represent specimens, for which more than 10% of the fuel inventory was dispersed into the coolant under the test, whereas open symbols are samples with no or marginal (<10%) fuel loss.

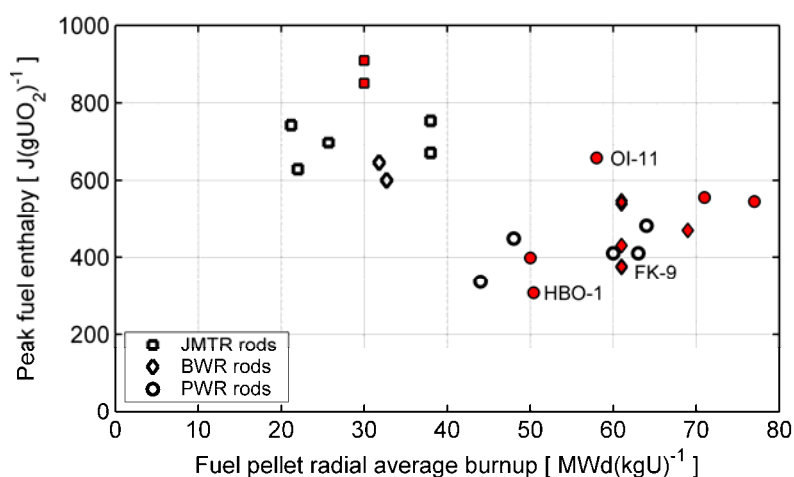
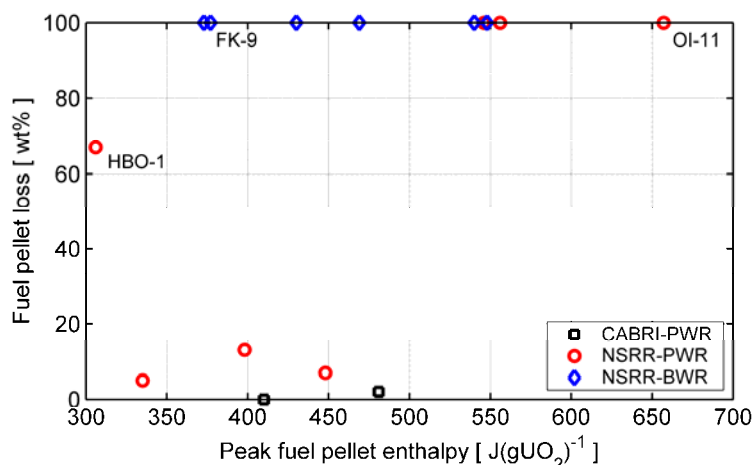


Figure 57 shows the measured fuel loss for the sixteen aforementioned high-burn-up UO₂ fuel rods that have failed through PCMI. The fuel loss is plotted with respect to peak fuel enthalpy under the test, and data for BWR and PWR fuel rods are shown separately. The results suggest that fuel dispersal is more significant from failed BWR rods than from PWR rods in the considered range of burn-up, i.e. from 44 to 77 MWd(kgU)⁻¹. For the failed BWR rods, there is no correlation between peak fuel enthalpy

and fuel loss, since all failures resulted in complete dispersal of the fuel inventory. For the failed PWR rods, fuel dispersal was moderate at peak fuel enthalpies below approximately $500 \text{ J(gUO}_2\text{)}^{-1}$. The exception is rod HBO-1, which failed by a cladding circumferential break along the weld to the bottom end fitting.

Figure 57. Measured fuel loss in failed BWR and PWR high-burn-up UO_2 fuel rods. The fuel burn-up of the rods ranges from 44 to 77 MWd(kgU)^{-1} . The test rods HBO-1, FK-9 and OI-11 failed in the weld to the bottom end fitting, a failure mode that leads to large fractional fuel loss in short-length test rods.



The difference in BWR and PWR fuel dispersal behaviour suggested by Figure 57 should be discussed in light of observed differences in ductility and hydride morphology between BWR and PWR cladding of high burn-up fuel rods. Firstly, in-reactor oxidized and hydrided BWR cladding usually has a more uniform radial distribution of hydrides than PWR cladding. As discussed in Section 6.2.6.3, the radial hydride distribution affects the cladding ductility and failure behaviour. Secondly, as mentioned in Section 6.2.6.4, typical BWR cladding materials are recrystallization annealed (RXA) in the final step of the manufacturing process, which results in a microstructure with equiaxed grains. Stress relieved annealed (SRA) PWR cladding materials, on the other hand, have grains that are elongated in the circumferential direction. Due to this difference in grain structure, radially oriented hydrides are more likely in RXA than in SRA materials, and for the same hydride concentration, RXA is generally more brittle than SRA cladding, when loaded in the circumferential direction [304].

It should also be remarked that there were large differences in failure behaviour between pre-irradiated rods tested in the NSRR and the CABRI pulse reactor, respectively. In the NSRR, the rods failed primarily by axial or spiral splits in the clad tube. These splits had wide openings, and they usually extended over the entire active length of the rod, i.e. $\approx 125 \text{ mm}$. Some of the rods were also broken apart by circumferential cracks, resulting in large loss of fuel. All the failed rods in CABRI had multiple axial splits in the clad tube. The splits were typically 50-100 mm long, with narrow openings, and they were concentrated to the central region of the test rods, which experienced higher power and energy deposition than the end regions. Marginal fuel loss, about 2% of the inventory, was observed for rod REP-Na1, but no fuel was dispersed in other CABRI tests on pre-irradiated UO_2 fuel rods. However, 6% of the fuel inventory was dispersed from the MOX fuel rod REP-Na7, which was tested in CABRI (see Section A.6 in Appendix A).

The reasons to the observed differences in failure behaviour between the NSRR and the CABRI test rods are not clear, but they are most likely related to the differences in pulse width, test rod length,

axial power distribution and coolant conditions between the reactors (see Table 7 in Section 5.1.1). The dissimilar failure behaviour underlines the importance of prototypical test conditions in studies of fuel rod failure and post-failure behaviour.

Although the database is limited to only ten tests, the data at hand for failed PWR UO_2 fuel rods with burn-up beyond $40 \text{ MWd}(\text{kgU})^{-1}$ suggest that a peak fuel enthalpy of at least $500 \text{ J}(\text{gUO}_2)^{-1}$ is required to expel a significant part ($>15\%$) of the fuel inventory into the coolant (see Figure 57). However, it must be questioned whether this empirical enthalpy threshold for fuel dispersal from high-burn-up PWR fuel rods can be applied to PWR conditions, considering that the power pulse widths and cooling conditions used in the pulse tests differ notably from those expected in a PWR reactivity-initiated accident that initiates from hot zero power conditions. In addition, the internal gas pressure of the failed PWR fuel rods included in Figure 57 was 0.1-0.3 MPa at room temperature (see Appendix A). The internal gas pressure of high burn-up PWR fuel rods may be higher. As mentioned in Section 7.1.2, experiments on fresh fuel rods have shown that the internal gas pressure affects fuel dispersal.

Finally, it should be recalled that fuel coolant interaction is less energetic for dispersed high-burn-up, solid fuel than for molten fuel particles. As discussed in Section 4.3.1, measurements of thermal-to-mechanical energy conversion ratios for fuel dispersed under pulse-irradiation tests in the NSRR show that the conversion ratio for solid high-burn-up fuel is about an order of magnitude lower than for molten fuel, given a particular size of the dispersed fuel fragments. This is, however, to some extent counterbalanced by the fact that solid fuel fragments, dispersed from high-burn-up fuel rods, are much smaller than molten fuel fragments (see Section 4.3.1) and the references therein for further discussions on this topic.

8. PREDICTIVE COMPUTER CODES

Modelling of reactivity-initiated accidents involves the simultaneous solution of equations for neutron transport, heat transport within the fuel rods and across the clad-to-coolant interface, and coolant thermal-hydraulics. These equations are strongly interconnected and dependent on both space and time. Since they are difficult to solve in full detail in core-wide analyses on the computers available today, various simplifications are usually employed in engineering analyses.

The neutron transport problem is normally simplified by applying a two-step procedure, where different computer codes are used for each step. The first step involves detailed preparatory calculations at the level of the fuel assemblies, whereas the second step involves core-wide calculations with more approximate methods. In the first step, nuclear cross-sections and neutron kinetics data are calculated for each fuel assembly design by use of lattice physics codes, and then transformed (homogenised) into a form that can be used in the second step. This is achieved by solving Boltzmann's transport equation for each fuel assembly by recourse to multi-group neutron transport theory and detailed modelling of the assembly design. The results from these preparatory calculations comprise homogenised few-group (usually two energy groups) cross-sections and neutron kinetics data, which are then used for the second step of the calculations. The second step calculations involve the solution to the transient three-dimensional diffusion equation, which provides the space-time variation of neutron flux and core power across the complete reactor core. These analyses are typically done with nodal diffusion codes, which are integrated with models for heat transfer and thermal-hydraulic calculations.

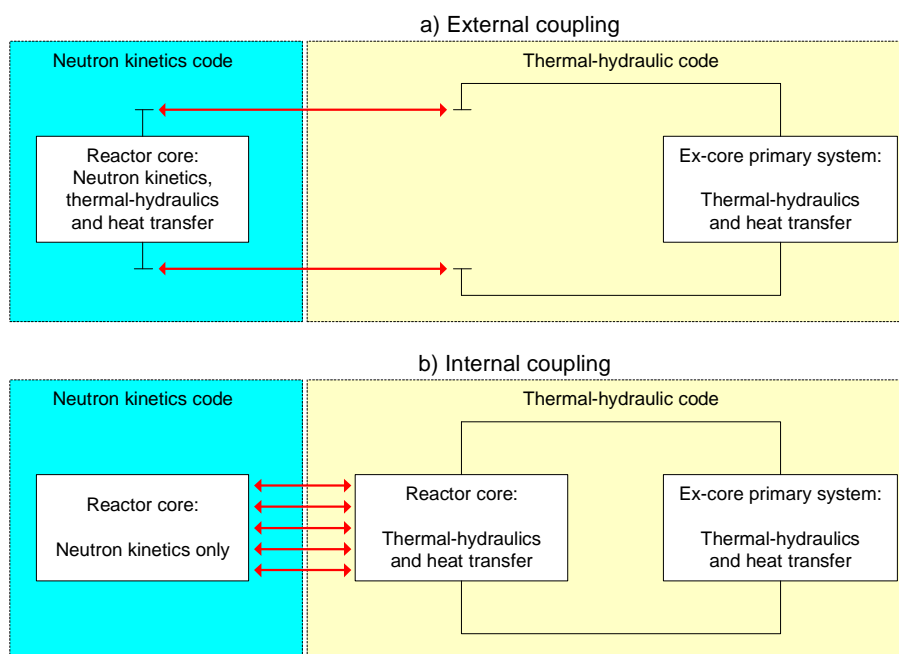
The core-wide thermal-hydraulic calculations are typically done by considering each fuel assembly as a vertical flowchannel. In analyses of BWRs, each fuel assembly can be treated by a one-dimensional model, since the assemblies are enclosed by fuel channels (boxes). Three-dimensional thermal-hydraulic models are on the other hand often needed in analyses of PWRs, due to lateral cross flow between assemblies. Calculations of heat generation and heat transport within fuel rods are needed to determine the rate of heat transfer to the coolant, and to provide fuel temperature feedback for calculations of cross-sections in the neutron transport problem. The fuel rod models used for this purpose are fairly simple, and they are normally applied to a single, average-power, fuel rod in each thermal-hydraulic flowchannel. Hence, all fuel rods in the flowchannel are lumped to a single rod, and the behaviour of individual rods is not analysed at this stage. A specifically designated fuel rod performance code is needed for this purpose, and rod-level analyses are normally done as a post-processing step to the core-wide neutronics/thermal-hydraulic calculations.

The coupling between core-wide neutron kinetics and thermal-hydraulic calculations can be handled in two different ways, as illustrated in Figure 58 [305]. External coupling implies that the neutron kinetics code uses built-in models for thermal-hydraulics and heat transfer within the core. If needed, a separate thermal-hydraulic code can be used to model feedback from the ex-core primary system. The codes are coupled to each other by passing a limited amount of data, which define the coolant conditions at the top and bottom of the core. Internal coupling, on the other hand, implies that the external thermal-hydraulic code handles heat transfer also within the core, and if needed, in the rest of the primary system. Internal coupling requires exchange of large amounts of data, but the benefit is improved accuracy and consistency in thermal-hydraulic calculations.

Hence, the typical procedure for analysis of reactivity-initiated accidents in LWRs is to solve a simplified set of coupled equations on a spatial mesh, which is made up of the fuel assemblies in the horizontal plane. In the axial direction, the core is typically divided into 20-25 nodes. This discretization results in calculational nodes (discrete volumes) with approximately cubic shape. The primary output from the core-wide analysis is the space-time variation of coolant properties and fuel assembly power. The power histories of individual fuel rods are then calculated from these fuel assembly data by neutron flux reconstruction, and the pin power is integrated to obtain an estimate of fuel pellet enthalpy, which is the parameter of primary concern in RIAs. The core-wide analyses are preceded by a preparatory step, in which nuclear cross-sections and neutron kinetics data are generated at the level of fuel assemblies by use of lattice physics codes. Following the core-wide analyses, specifically designated codes can be used to analyse the thermo-mechanical behaviour of particular fuel rods in detail, and to assess the risk for fuel rod failure.

An overview of methods and computer codes for analysis of reactivity-initiated accidents is given in the following subsections. Codes for neutron kinetic and thermal-hydraulic analyses, both core-wide and at the level of fuel assemblies, are briefly reviewed in Section 8.1, whereas Section 8.2 is devoted to fuel rod codes. Since the emphasis in this report is on fuel behaviour, the main thrust of the presentation is directed towards fuel rod codes. The list of codes is by no means exhaustive, since the purpose of this section is merely to provide an overview of state-of-the-art computational methods and tools for analyses of RIA. Precedence is given to modern and internationally known codes that have a wide user community.

Figure 58. **External (a) and internal (b) coupling of computer codes for neutron kinetics and thermal-hydraulics in core-wide transient analyses. Red arrows denote exchange of data.**



8.1 Core and fuel assembly codes

8.1.1 Codes for generation of homogenised cross-sections

The probabilities (cross-sections) for various neutron reactions, such as absorption, fission or scattering, depend on the neutron energy and the isotopic composition of the material in which the reaction takes place. The first step of a core-wide analysis of the neutron distribution, whether it is a

steady-state or a transient analysis, is to condense the cross-sections with respect to neutron energy and to homogenise them with respect to space. This is done by use of lattice physics codes, in which the two-dimensional neutron transport equation is solved within individual fuel assemblies, utilizing multi-group transport theory and databases for microscopic cross-sections, such as ENDF or JEFF [306-307]. User-defined input to the calculations consists of the fuel assembly design, fuel isotopic composition and coolant/moderator properties. Output comprise homogenised cross-sections for the fuel assembly, usually condensed into two neutron energy groups, delayed neutron data and fuel assembly discontinuity factors. The latter are needed to account for the heterogeneity of the fuel assembly. They improve the accuracy of subsequent core-wide analyses, and are also used to reconstruct the neutron flux and power for individual fuel rods within the homogenised assembly.

For application in core-wide neutron kinetics analyses, the homogenised cross-sections must be calculated and tabulated as functions of fuel burn-up, spectral history and a number of feedback variables, such as fuel and coolant temperature, coolant density, steam content and boron concentration, and the presence of control rods. The cross-section's dependence on these variables can be defined either through fitted polynomials, or by use of multidimensional look-up tables [308]. Some widely used lattice physics codes used for generation of homogenised cross-sections are listed in Table 13. It should be remarked that these codes are fairly general, and some of them have interfaces for convenient transfer of the calculated cross-sections to several neutron kinetics codes. The codes in Table 13 differ with respect to applied solution methods for the neutron transport equations, libraries used for microscopic cross-section data, the capability to handle various fuel assembly designs, and their applicability to three-dimensional neutron transport problems.

Table 13. **Examples of lattice physics codes that can be used for generation of homogenised cross-sections.** The codes are briefly described in Appendix B, Section B.1.

Code		Maintaining organisation
APOLLO2	[309]	Commissariat à l'Énergie Atomique, France
CASMO-4	[310]	Studsvik Scandpower, Sweden
HELIOS	[311]	Studsvik Scandpower, Sweden
TransLAT	[312]	TransWare Enterprises Inc, USA
WIMS9	[313]	Serco Assurance, England

The procedures for generating the homogenised cross-sections are similar for the codes: starting at the level of a single fuel rod with its surrounding coolant volume, the neutron flux distribution is computed for this unit cell in detail energetically, but only in one dimension spatially – the rod is assumed axisymmetric with infinite axial extension. The cross-sections for the unit cell is then condensed into a smaller number of energy groups, typically 10 to 20, and these are then used to compute the two-dimensional distribution of neutron flux at the fuel assembly level. Next, a new condensation is made in order to get the final set of two-group cross-sections for the assembly, which is to be used in the subsequent core-wide analyses.

8.1.2 Codes for core-wide neutron kinetics calculations

The state-of-the-art approach for calculating the space-time variation of neutron flux and power over the entire core in light water reactors is to solve the three-dimensional neutron diffusion equation for two neutron energy groups,²⁰ considering six groups of delayed neutron precursors [314]. The restriction to two energy groups is linked to the coarse discretization applied in core-wide analyses. As already mentioned, the neutron diffusion equation is usually solved on a mesh, in which each node is

20. For LWRs, it is often assumed that the two energy groups join at a neutron energy of 0.625eV.

typically made up of a fuel assembly in the horizontal plane. Since the neutron energy spectrum in a given fuel assembly (node) is little affected by the spectra in adjacent assemblies, the use of only two energy groups in core-wide analyses is justified.

The governing equations for the time-dependent neutron diffusion problem can be solved by various methods [315]. The space dependence of the equations is often tackled by use of nodal methods, which may be regarded as extensions to the finite difference method. The nuclear properties as well as the coolant properties are thereby assumed to be uniform within each node, which requires that lattice physics codes are used in a preparatory step to generate homogenised nuclear cross-sections and kinetic data for each node (see Section 8.1.1). Likewise, the primary results from the calculations are nodal average values, which means that methods for de-homogenisation are needed to extract results for individual fuel rods, such as the fuel enthalpy.

As mentioned already in Section 2, the neutron kinetics depends on a number of feedback variables, such as fuel temperature and coolant properties, which affect the neutron cross-sections. Neutron kinetics codes therefore comprise ancillary models for fuel-to-coolant heat transfer and coolant thermal-hydraulics, by which these feedback variables can be calculated. The thermal-hydraulic models are essentially one-dimensional, and they are typically applied to vertical flow-channels, each of which is made up of an axial stack of discrete nodes in the neutron kinetics problem. Consequently, thermal-hydraulic boundary conditions must be supplied for the coolant conditions at the top and bottom of the core. In analyses of transients with strong feedback effects from the ex-core primary system, these boundary conditions cannot be given a priori. They must instead be generated by a thermal-hydraulic model for the ex-core primary system, executed concurrently with the neutron kinetics code. This is illustrated in Figure 58a. Some state-of-the-art codes for neutron kinetics calculations can be linked more tightly to thermal-hydraulic codes, as shown in Figure 58b. In this case, the thermal-hydraulic code handles heat transfer and thermal hydraulics in the entire primary system, including the core. In practice, the neutron kinetics code is integrated as a part of the thermal-hydraulic system analysis code. A state-of-the-art report on coupled neutron kinetics calculations and thermal-hydraulic system analyses in light water reactors can be found elsewhere [305]. Some widely used computer codes for three-dimensional neutron kinetics calculations are listed in Table 14.

Table 14. Examples of codes for three-dimensional neutron kinetics calculations

Brief summaries of these codes are given in Appendix B, Section B.2.

Code	Maintaining organisation
BARS [316]	Kurchatov Institute, Russia
CRONOS2 [317]	Commissariat à l'Énergie Atomique, France
DYN3D [318]	Forschungszentrum Rossendorf, Germany
PARCS [319]	Purdue University, USA
SIMULATE-3K [320]	Studsvik Scandpower, Sweden

8.1.3 Codes for thermal-hydraulic analyses

The codes for three-dimensional core-wide neutron kinetics calculations described above comprise ancillary models for core thermal-hydraulics and heat transfer, which makes it possible to run the codes in stand-alone mode. These models are usually based on simplified hydrodynamic descriptions of the two-phase coolant. For instance, it is customary to assume one-dimensional homogeneous flow, with thermodynamic equilibrium between the two phases. However, there is a current trend to replace these simplified models with more sophisticated methods. This is usually done by integrating the neutron kinetics code with a thermo-hydraulic system analysis code, as illustrated in Figure 58b (internal coupling). The aim is to improve the thermal-hydraulic modelling of the core, but also to gain better modelling consistency between the core and ex-core components of the primary system.

Current state-of-the-art thermal-hydraulic system analysis codes for LWRs are based on hydrodynamic models with six conservation equations for mass, energy and momentum of the two phases – liquid and vapour [321]. These first-principle equations are supplemented by empirical constitutive relations for the fluid, which are needed to describe wall friction, wall heat transfer, and also the transfer of mass, energy and momentum between the two phases of the fluid. With few exceptions, the equations are formulated for one-dimensional flow, but multidimensional flow can be simulated, in an approximate way, by prescribing cross-junctions between parallel flow channels. In the hydrodynamic models, provision is usually made for soluble components in the liquid phase, and non-condensable components in the vapour phase. This functionality is often combined with algorithms for tracking the transport of boron or escaped gaseous fission products with the coolant.

The numerical techniques for solving the system of conservation equations are usually based on finite difference donor cell schemes with staggered mesh, meaning that computational cells (volumes) for the momentum equations are displaced half a cell-length relative to the mass and energy cells. Integration with respect to time is usually done with implicit or semi-implicit time stepping schemes, which maintain numerical stability also for long time steps. The drawback with implicit schemes is that they have a diffusive influence on the solution, i.e. they have a tendency to smooth gradients in the field variables. This is often an undesirable effect, which may become significant in cases where a fine mesh with short nodes is used. Some internationally known computer codes for three-dimensional neutron kinetics calculations are listed in Table 15. The reader can find additional information on these codes in Appendix B, Section B.3.

Table 15. Examples of codes for core thermal-hydraulic calculations.

Brief summaries of these codes are given in Appendix B, Section B.3.

Code		Maintaining organisation
ATHLET	[324]	Gesellschaft für Anlagen- und Reaktorsicherheit, Germany
FLICA4	[325]	Commissariat à l'Énergie Atomique, France
RELAP5	[326]	Idaho National Laboratory, USA
TRACE	[327]	US Nuclear Regulatory Commission, USA

It should be remarked that the empirical constitutive relations used in thermal-hydraulic codes are based on experiments carried out largely under static or quasi-static conditions, and their applicability to fast transients, such as RIAs, must therefore be questioned. As shown in Section 6.2.1, the phenomena leading to a boiling crisis at the cladding surface differ between fast transients and quasi-static conditions, and the same is true also for the clad-to-coolant heat transfer under film boiling. Hence, particular models for clad-to-coolant heat transfer should be used in core kinetics analyses of RIA, in order to accurately calculate the fuel temperature and thermal-hydraulic feedback parameters. Such models have recently been developed [94], but they are not yet available in codes for thermal-hydraulic or neutron kinetics analyses. A related issue is the dynamics of vapour (void) generation under an RIA: Under the RIA, the amount of vapour generated at the hot cladding surface is determined by several factors, such as the surface characteristics and the temperature and flow velocity gradients across the boundary layer at the surface [322]. In the two-phase fluid models used in thermal-hydraulic codes, these dependencies are accounted for by empirical relations, which are based on experiments done under quasi-static conditions. When they are applied to RIA conditions, they seem to overestimate the vapour generation and its associated reactivity feedback [323]. As mentioned in Section 5.2.2.2, a series of out-of-pile experiments on transient vapour generation under RIAs is currently conducted by the JAEA. The first results of these tests are available in literature [193].

8.2 Fuel rod codes

Detailed analyses of the thermo-mechanical behaviour of individual fuel rods are needed for evaluation and interpretation of RIA simulation tests, which are performed on single fuel rods under

well-controlled test reactor conditions. Detailed thermo-mechanical analyses of selected fuel rods are also common as a post-processing step to core-wide analyses of postulated RIAs in power reactors. The purpose of these analyses is to calculate key fuel rod properties with a higher degree of accuracy than achieved in the core-wide analyses: as already mentioned, core-wide analyses are usually done at the fuel assembly level, with all fuel rods in the assembly/flowchannel lumped into an average-power rod. In addition, the fuel rod models used in core-wide analyses must by necessity be kept simple. Changes to the fuel rod state during the RIA, resulting e.g. from transient fission gas release, cladding oxidation or deformation, are therefore not considered in core-wide analyses.

Properties of particular interest in the detailed fuel rod analyses are fuel pellet temperatures and enthalpies, clad tube deformations and temperatures, and assessments of the risk for cladding failure. The detailed analyses of the fuel rod behaviour must be done with software designed to handle rapid power transients, and several computer codes of this kind exist. Some of the codes, such as RANNS [215] and RAPTA-5 [267] are used in-house by national research organizations, but a few transient fuel rod codes have wider user communities. The latter group includes FALCON, FRAPTRAN, SCANAIR and TRANSURANUS. A review of fuel rod analysis codes with applicability to RIA is given in Appendix B, Section B.4. A brief description of the codes is also given in Table 16, where some modelling differences with importance to analyses of RIAs are summarised.

Table 16. Comparison of transient fuel rod analysis codes, applicable to analyses of reactivity-initiated accidents. The codes are described in Appendix B, Section B.4.

	FALCON MOD-01	FRAPTRAN Version 1.3	SCANAIR Version 3.2	TRANSURANUS V1M1Y96	RANNS Version 1
Maintaining organisation	EPRI, USA	PNNL, USA	IRSN, France	ITU, Germany	JAEA, Japan
Range of application	Transients, steady-state	Transients only	Transients only	Transients, steady- state	Transients only
Geometrical representation	2D	1D	1½D	1½D	1½D (2D)*
Clad tube representation	Thick wall	Thin shell	Thick wall	Thick wall	Thick wall
Pellet-clad contact modelling	Frictional sliding	Axial sticking	Axial sticking	Frictional sliding	Frictional sliding
Fission gas release model	NRO-MT	None	RIA	NRO-MT	NRO-MT and RIA
Fuel gaseous swelling model	Steady-state only	No	Transient only	Steady-state only	Steady-state only
Cladding failure criterion for RIA	Strain energy density	Hoop strain	Nonlinear fracture mechanics	No	Linear fracture mechanics

NRO-MT: Model for normal reactor operation and mild transients.

RIA: Specific model for reactivity-initiated accidents.

* In RANNS, an optional 2D local model for detailed PCMI analyses can be applied to an axial segment that corresponds to the length of half a pellet [328].

Readers unfamiliar with the general modelling concepts used in fuel rod performance codes are referred to the reviews in [329-330]. All the codes listed in Table 16 follow the common modelling approach of using an axisymmetric representation of the fuel rod geometry, where the fuel pellet stack is treated as a continuum. With the exception of FALCON, the analyses are done by one-dimensional (1D) or quasi two-dimensional (1½D) modelling, which means that the fuel rod is represented by a stack of axial segments. The heat transfer and deformations in each segment are calculated by solving one-dimensional (radial) equations, which are connected axially merely by coolant heat transfer and a common internal fuel rod gas pressure. In some codes, the segments are axially connected also by transfer of axial forces from pellet-clad mechanical interaction. In those codes, which are referred to as 1½-dimensional, the axial contact forces are usually calculated iteratively from the axial deformations of fuel and cladding. The calculations for all fuel rod segments must then be embedded in an axial iteration

loop, which increases the computational cost. To avoid the axial iterations, FRAPTRAN applies a local contact model to each axial segment independently. The local contact modelling is fast, but it can give unphysical results for cases where the pellet-clad gap conditions vary significantly along the rod [329].

All the codes listed in Table 16 are equipped with one-dimensional models for axial heat transport in the coolant. In these models, the fuel rod is assumed to be surrounded by a steam/water coolant, the properties of which depend on the axial coordinate only. Hence, radial and azimuthal variations in coolant temperature and/or steam content at the cladding surface are not explicitly modelled, and the water and steam phases are assumed to be in thermodynamic equilibrium (homogeneous equilibrium model). These fairly simple coolant channel models are used to calculate the thermal boundary conditions for each axial segment of the fuel rod, i.e. the coolant temperature and the clad-to-coolant heat transfer coefficient, based on prescribed time histories of fuel rod power, coolant inlet enthalpy, inlet mass flow and pressure. The clad-to-coolant heat transfer models used in these codes are generally designed for analyses of steady-state operation and mild transients, and their applicability to RIAs and other extremely fast overpower transients must be questioned. Clad-to-coolant heat transfer models intended specifically for RIA conditions have recently been proposed by Bessiron and co-workers [94,192]. These models are based on the results from the PATRICIA experimental program (see Section 5.2.2.1), and RIA simulation tests in the NSRR.

The codes listed in Table 16 model PCMI with various degrees of sophistication. In the simplest models, relative axial motion between pellet and cladding is completely suppressed, once the gap is closed. These models work fairly well for high-burn-up fuel, where pellet-clad bonding prevents slip between the objects (see Section 3.3.2). However, for fuel rods with low or moderate burn-up, pellet-clad mechanical contact is better represented by models based on frictional sliding.

Other important differences among the codes in Table 16 concern the modelling of transient fission gas release and fuel deformation (swelling and/or burst) induced by rapid expansion of the accumulated gas under heating. FRAPTRAN lacks this kind of models, and it also differs from the other codes by having a thin shell model for the cladding tube. The thin shell model is based on the assumption that temperature, material properties, stresses and strains are uniform across the cladding thickness, which is hardly the case in reactivity-initiated accidents.

An important part of the fuel rod analysis is to predict cladding failure. The codes are therefore equipped with cladding failure criteria, which are formulated on the basis of out-of-reactor mechanical tests on cladding tubes. As shown in Table 16, strain energy density, hoop strain and concepts from linear or non-linear fracture mechanics are employed in the formulation of these failure criteria. Further details are given in Appendix B, Section B.4.

Except for TRANSURANUS, the fuel rod codes in Table 16. have been verified and calibrated against experimental data from RIA simulation tests in the NSRR and/or CABRI, e.g. see [215,223,262,328,331-332]. A general conclusion from these efforts is that the codes are quite successful in reproducing measured fuel rod temperatures and deformations for cases in which the cladding tube remains at low temperature throughout the test. Also cladding failures are captured with fair accuracy for these cases, provided that the degree of cladding corrosion is known and can be used as input to the analysis. However, for tests under which a boiling crisis occurs, neither temperatures nor deformations are accurately reproduced by the codes. It is likely that the aforementioned clad-to-coolant heat transfer models for RIA will improve the accuracy [94,192]. Yet, these models still await validation against a more substantial database.

The stand-alone fuel rod codes generally fail to accurately reproduce transient fission gas release under RIA simulation tests on pre-irradiated fuel rods. This is not surprising, considering that fuel fission gas release is difficult to model with exactitude even under normal reactor operation. Model

improvements are needed, since transient release of gaseous fission products and helium from high-burn-up fuel has potential to increase the fuel rod internal gas pressure, with possible consequences to cladding integrity.

The FALCON and TRANSURANUS codes are applicable not only to transients, but also to analyses of fuel rod behaviour under normal reactor operation. These codes can therefore be used to model the entire in-reactor life of a fuel rod, starting with long-term steady-state operation and ending with a postulated RIA. Transient codes without capacity to model long-term steady-state operation must be used in combination with a separate program, by which the burn-up-dependent pre-transient state of the fuel rod can be calculated.

Finally, it should be remarked that all fuel rod codes available today lack capacity for modelling post-failure phenomena, such as gap gas ejection, fuel dispersal, fuel-coolant interaction and loss of axisymmetric geometry.

9. RESULTS OF ENERGY AND FAILURE DISTRIBUTION CALCULATIONS

In Section 2.2 of this Report, we discussed power pulses generated under severe reactivity-initiated accidents, such as control rod ejection accidents in PWRs and control rod drop accidents in BWRs. We concluded that the pulse width is a core-wide parameter, which for large reactivity insertions ($\Delta\rho > \beta$) is approximately proportional to the inverse of the prompt reactivity insertion $\Delta\rho/\beta$. The pulse amplitude, however, is a local property that falls off with increasing distance from the failed control rod, and it also depends on fuel burn-up (see Section 2.2.2).

To assess the consequences of an RIA, i.e. to estimate the number of failed fuel rods, it is necessary to first calculate the pulse amplitude and the resulting peak fuel enthalpy for each fuel rod.²¹ The peak fuel enthalpy of each rod is then compared with relevant failure criteria, in which the state (burn-up, internal gas overpressure, clad corrosion, etc.) of the fuel rod is considered. A few studies of this kind are available in open literature. More precisely, state-of-the-art computational methods have been used to analyse postulated REAs and RDAs, and the distribution of energy and failed fuel rods have been calculated across the reactor core for these accident scenarios. An overview of reported studies on postulated REAs is given in Section 9.1, whereas Section 9.2 summarises analyses of RDAs. All studies covered in these subsections were done with three-dimensional neutron kinetics codes, but large differences exist as to the postulated accident scenarios and reactivity additions. Moreover, the applied fuel rod failure criteria varied significantly between the reported studies.

9.1 Control rod ejection accidents in PWRs

Table 17 summarises computational studies of postulated REAs, in which calculated results on the distribution of energy and failed fuel rods across the reactor core are presented. All studies in Table 17 were done for end-of-cycle core conditions, and with one exception, they all pertain to REAs that initiate from hot zero power reactor conditions.

Table 17. Summary of computational studies of postulated control rod ejection accidents in which calculated distributions of energy and failed fuel rods are reported.

Core initial conditions	Reactivity insertion ($\Delta\rho/\beta$)	Peak enthalpy increase [$\text{J}(\text{gUO}_2)^{-1}$]	Fraction of failed rods [-]	Investigator [reference]
EOC HZP	1.89	247	0	Nakajima [30]
EOC HZP	0.88	30	0	Dias <i>et al.</i> [17]
EOC HZP	1.30	71	0	Dias <i>et al.</i> [17]
EOC HZP	1.58	143	3.6×10^{-2}	Lee <i>et al.</i> [25]
EOC HFP	0.15	83	9.0×10^{-3}	Lee <i>et al.</i> [25]

For illustration, we will consider the study by Nakajima [30]. This study was done for a typical four-loop PWR, in which the core consisted of 193 fuel assemblies of 17×17 design. The ejection of a fully inserted control rod was postulated at the end of a reactor operating cycle, while the core was held

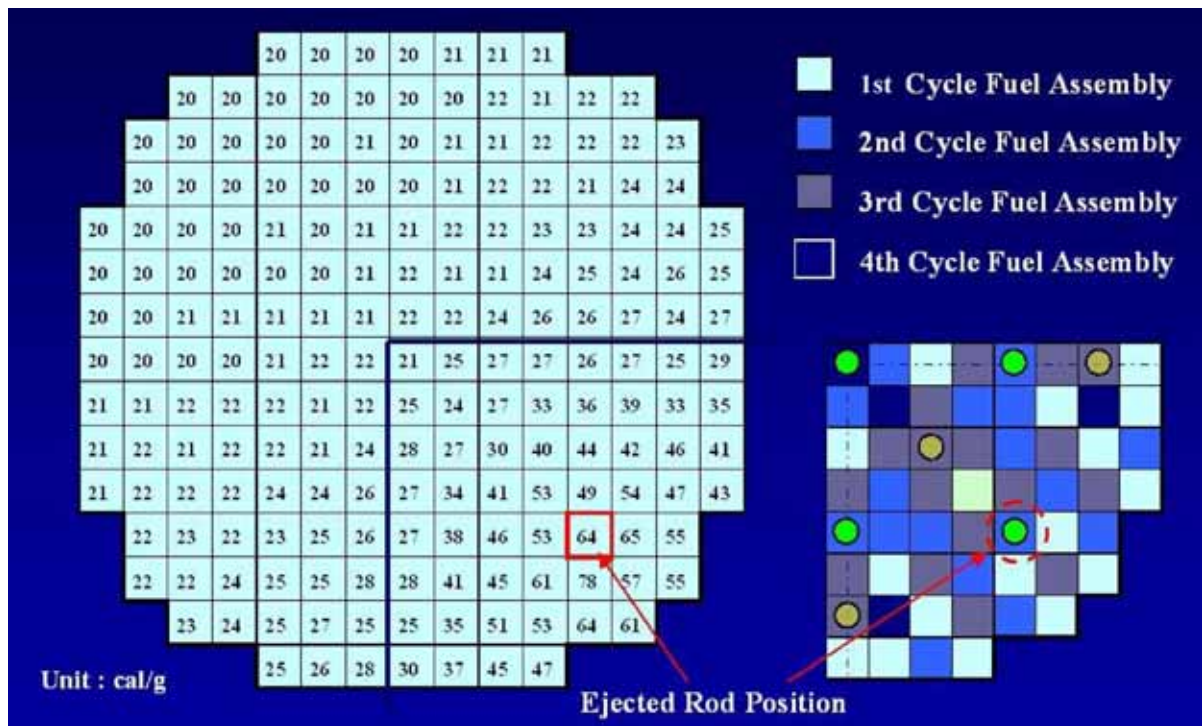
21. Here, the peak fuel enthalpy refers to the peak value, with respect to time and axial position, of the radial average fuel enthalpy under the accident.

at hot zero power conditions. The reactivity worth of the ejected control rod, $\Delta\rho$, was increased from 6.0×10^{-3} to 8.7×10^{-3} , and penalizing assumptions were also made regarding reactivity feedback effects, in order to increase the energy deposition to the fuel. The calculations were made with the EUREKA-JINS/S three-dimensional neutron kinetics code [30].

Figure 59 shows the position of the ejected control rod, together with the calculated distribution of energy in terms of peak fuel enthalpy. The highest enthalpy, $78 \text{ cal(gUO}_2\text{)}^{-1}$ or $327 \text{ J(gUO}_2\text{)}^{-1}$, is reached in a first cycle fuel assembly, neighbouring to the assembly from which the control rod is ejected. The fuel assembly loading pattern in the reactor core is shown to the right in Figure 59. The calculations show that first cycle fuel assemblies close to the ejected control rod position reach the highest fuel enthalpies, as a consequence of the comparatively high reactivity of low-burn-up fuel. It is clear from Figure 59 that the calculated peak fuel enthalpy around the ejected control rod decreases rapidly, as the distance from the ejected rod increases. The enthalpy increases by more than $10 \text{ cal(gUO}_2\text{)}^{-1}$ in only 39 of the 193 fuel assemblies; the initial, pre-transient, fuel enthalpy was $19 \text{ cal(gUO}_2\text{)}^{-1}$ throughout the core.

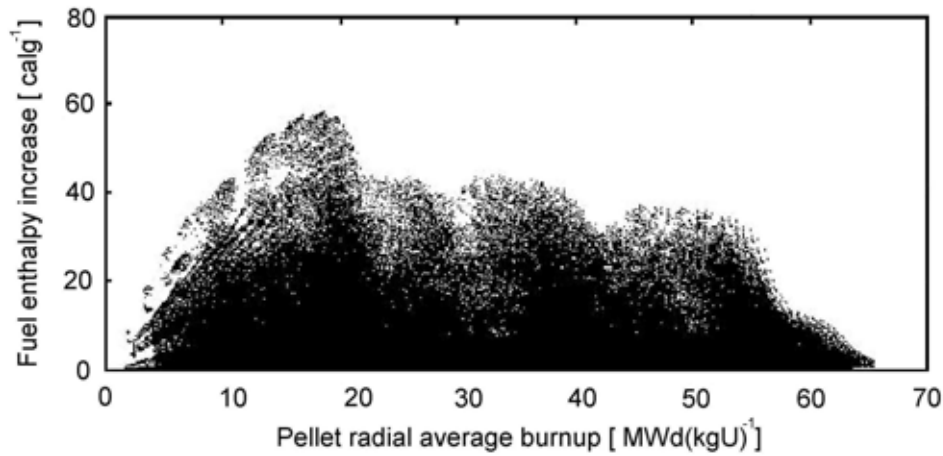
The calculated peak fuel enthalpy increase of individual fuel rods is shown in Figure 60. The highest enthalpy increase is experienced by fuel rods in first cycle fuel assemblies, which have a fuel pellet average burn-up below 20 MWd(kgU)^{-1} .

Figure 59. Calculated distribution of peak fuel pellet enthalpy, in units of $\text{cal(gUO}_2\text{)}^{-1}$, resulting from the postulated HZP REA considered by Nakajima [30]



For rods with higher burn-up, the fuel enthalpy increase is typically below $45 \text{ cal(gUO}_2\text{)}^{-1}$, or $190 \text{ J(gUO}_2\text{)}^{-1}$. Since the calculated peak fuel enthalpies were well below all conceivable failure thresholds determined in pulse reactor tests, Nakajima concluded that all fuel rods in the core would survive the postulated accident [30].

Figure 60. Scatter plot of calculated peak fuel enthalpy increase versus fuel pellet average burn-up under the postulated HZP REA considered by Nakajima [30]



9.2 Control rod drop accidents in BWRs

Table 18 summarises computational studies of postulated RDAs, in which calculated results on the distribution of energy and failed fuel rods across the reactor core are presented. With one exception, the analyses in Table 18 were done for end-of-cycle core conditions. The studies pertain to RDAs that initiate from either cold or hot zero power reactor conditions. For illustration, we will consider the analyses of CZP RDAs by Nakajima [30] and Heck *et al.* [18].

Nakajima analysed a General Electric design BWR (BWR-5), in which the core comprised 764 fuel assemblies of 9×9 design. The postulated control rod drop occurred at the end of a reactor operating cycle under CZP conditions, meaning that the coolant was close to room temperature and atmospheric pressure, and the core power was negligible. The reactivity worth of the dropped control rod, $\Delta\rho$, was 1.3×10^{-2} , which is a conservative postulation and not a realistic value. The calculations were made with the EUREKA-JINS/S three-dimensional neutron kinetics code [30].

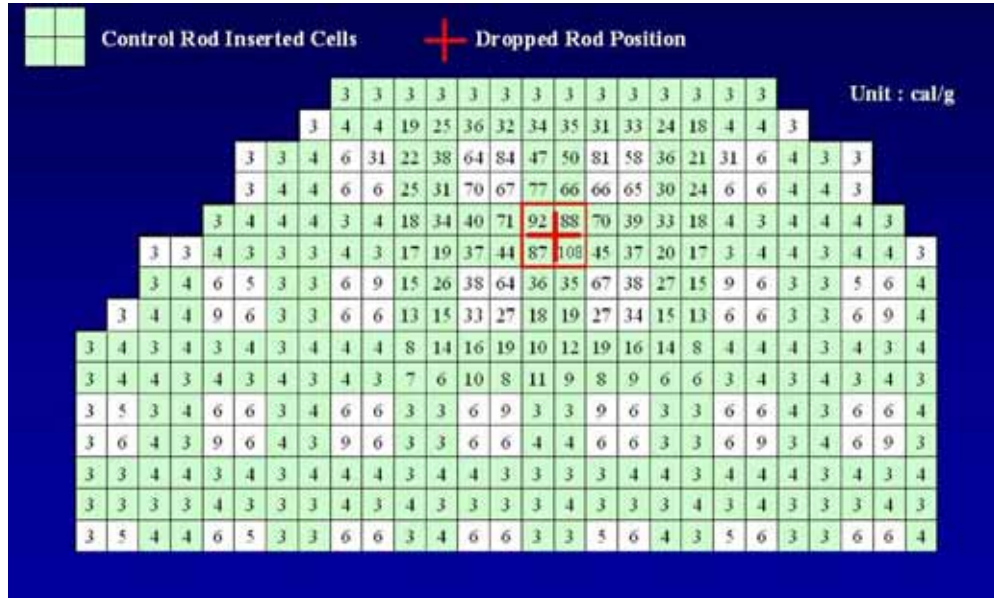
Figure 61 shows the position of the failed control rod, together with the calculated peak fuel enthalpy across the reactor core. The calculations show that the highest fuel enthalpy, $108 \text{ cal}(\text{gUO}_2)^{-1}$ or $452 \text{ J}(\text{gUO}_2)^{-1}$, is reached for a fuel rod in one of the four fuel assemblies that are adjacent to the dropped control rod. High enthalpies are reached also in the other three assemblies within this control cell. Outside the cell, however, the peak enthalpies are significantly lower.

Table 18. Summary of computational studies of postulated control rod drop accidents, in which calculated distributions of energy and failed fuel rods are reported.

Core initial conditions	Reactivity insertion ($\Delta\rho/\beta$)	Peak enthalpy increase [$\text{J}(\text{gUO}_2)^{-1}$]	Fraction of failed rods [–]	Investigator [reference]
EOC CZP	2.24	450	2.4×10^{-3}	Nakajima [30]
EOC HZP	2.32	322	1.4×10^{-3}	Nakajima [30]
EOC CZP	1.40	146	0	Heck <i>et al.</i> [18]
EOC CZP	1.30	134	0	Dias <i>et al.</i> [17]
EOC HZP	1.50	95	0	Dias <i>et al.</i> [17]
BOC CZP	2.65	461	8.2×10^{-3}	Ohta <i>et al.</i> [35]
BOC HZP	2.65	264	4.1×10^{-3}	Ohta <i>et al.</i> [35]
EOC CZP	2.65	448	1.4×10^{-2}	Ohta <i>et al.</i> [35]
EOC HZP	2.65	297	1.0×10^{-2}	Ohta <i>et al.</i> [35]

Figure 61. Calculated distribution of peak fuel enthalpy, in units of $\text{cal}(\text{gUO}_2)^{-1}$, under the postulated CZP RDA considered by Nakajima [30]

Cells shaded with green have inserted control rods.



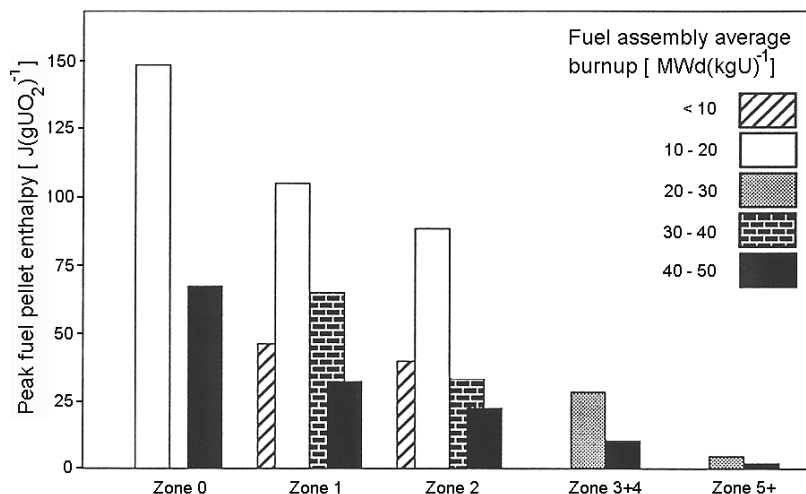
According to the calculations, the fuel enthalpy increased by more than $10 \text{ cal}(\text{gUO}_2)^{-1}$ in only 78 of the 764 fuel assemblies; the pre-transient fuel enthalpy was $2 \text{ cal}(\text{gUO}_2)^{-1}$ throughout the core. Nakajima also found that 110 fuel rods transgressed a burn-up dependent enthalpy limit for PCMI-induced cladding failure, which was used in the analyses [30]. In addition, 36 rods transgressed an enthalpy limit for high temperature rupture. Hence, the calculated fraction of failed fuel rods in the core was 2.4×10^{-3} . It should be remarked that these results were calculated with consideration of negative reactivity feedback from vapour generation in the coolant. Since prevalent models for vapour generation are believed to overestimate the amount of vapour and the associated reactivity feedback under fast power transients (cf. Section 8.1.3), Nakajima repeated the calculations with the vapour reactivity feedback set to zero. As a consequence, the number of high-temperature failures increased by an order of magnitude [30].

Heck and co-workers [18] analysed a similar control rod drop accident as Nakajima, using the TRACG three-dimensional neutron kinetics code. More precisely, they considered an RDA at EOC CZP conditions in a BWR of the same General Electric design as in the study by Nakajima, and also the 9×9 fuel assembly design (GE11) was the same. However, the reactivity worth of the dropped control rod was much lower than in Nakajima's analyses, since Heck *et al.* used realistic rather than penalizing modelling assumptions in their study [18].

The highest calculated fuel enthalpy in the study by Heck and co-workers, $35 \text{ cal}(\text{gUO}_2)^{-1}$ or $147 \text{ J}(\text{gUO}_2)^{-1}$, was reached for a fuel rod within a first cycle fuel assembly, neighbouring to the dropped control rod. Figure 62 illustrates the dependence of calculated peak fuel enthalpy on fuel assembly burn-up and distance from the failed control rod. The calculated peak fuel enthalpy is plotted by zones, where zone 0 corresponds to the four fuel assemblies in the control cell around the dropped control rod, zone 1 includes the twelve assemblies that are one assembly away from the dropped rod, and so forth. Figure 62 shows that the calculated peak fuel enthalpy falls to less than 20 % of its core-wide maximum value already in zone 3, i.e. only three fuel assemblies away from the dropped control rod. This is consistent with the results of Nakajima's analysis, shown in Figure 61.

Figure 62. Calculated dependence of peak fuel enthalpy on fuel assembly burn-up and distance from the dropped control rod under the CZP RDA considered by Heck *et al.* [18].

The zone number alludes to the distance from the dropped control rod, in units of intermediate fuel assemblies.



Moreover, within a particular zone, the calculations show that the peak fuel enthalpy is correlated to the fuel assembly average burn-up. The calculated peak enthalpy in fuel assemblies with average exposures below 10 MWd(kgU)⁻¹ is fairly low, because the fuel is still poisoned with the burnable absorber gadolinium (see Section 3.1.1). Fuel assemblies with a burn-up of 10 to 20 MWd(kgU)⁻¹ yield the highest peak fuel enthalpies, since most, or all, of the pertinent gadolinium isotopes have been consumed, while substantial amounts of ²³⁵U still remain. As the fuel assembly burn-up increases beyond 20 MWd(kgU)⁻¹, the peak fuel enthalpies in the assembly progressively decrease, as the ²³⁵U content is consumed. Figure 62 shows that in fuel assemblies with average burn-ups beyond 40 MWd(kgU)⁻¹, the calculated peak fuel enthalpies are 25-50% of those reached in the most reactive fuel assemblies at comparable distance to the dropped control rod. Heck and co-workers concluded that the trend for peak fuel enthalpy versus burn-up is similar to the burn-up trend for the infinite lattice multiplication factor, k_{∞} , of the fuel assembly [18].

9.3 Summary remarks on energy and failure distribution calculations

Results of three-dimensional core kinetics analyses of postulated REAs and RDAs, which were briefly summarised in Sections 9.1 and 9.2, show that only 10-20 % of the fuel within a typical reactor core experiences a significant energy deposition under these accidents. The energy falls off rapidly with increasing distance from the failed control rod, and except for a 6×6 to 8×8 array of fuel assemblies around the rod, the calculated results suggest that the energy deposition is too low to cause fuel rod failure, even under very severe postulated accidents.

However, in the considered calculations of the distribution of fuel rod failure across the core, rod failure is predicted based on comparisons of the calculated fuel pellet enthalpy with a set of failure thresholds on a rod-to-rod basis. Hence, the predicted failure or survival of each rod is unaffected by the state of surrounding rods. The possibility of “domino effects” on fuel rod failure, caused e.g. by the build-up and propagation of coolant pressure pulses through energetic fuel-coolant interaction, is thus not considered in the calculations. Presently, such effects would be very difficult to treat with physically based computational models, since it would require modelling of the fuel post-failure behaviour in core-wide analyses. Yet, as discussed in Section 4.3.2, the very few multi-rod pulse irradiation tests performed to date provide no direct experimental evidence that fuel rod failure by propagation of coolant pressure pulses would occur under reactivity-initiated accidents.

10. SUMMARY AND CONCLUSIONS

Our current knowledge of reactivity-initiated accidents in light water reactors and their consequences is based largely on two sources of information:

- Pulse irradiation tests of instrumented fuel rodlets, carried out in research reactors.
- Best-estimate computer analyses of the reactor response to postulated accident scenarios, by use of coupled neutron kinetics, thermal-hydraulics and heat transfer calculations on a core-wide level.

Since the tests and the computer analyses are performed on very different scales, it is difficult to bridge the gap between them. For example, very little of the knowledge gained from pulse irradiation tests has so far been used to improve the fuel rod modelling in core-wide computer analyses of RIAs. Experiments and modelling on an intermediate scale, i.e. at the level of fuel assemblies, would probably help to bridge the gap, but RIA simulation tests with fuel assemblies are difficult to conduct for safety reasons. It is interesting to make a comparison with loss-of-coolant accidents, for which numerous tests have been done on fuel assemblies, and computer codes are available for accident analyses on the fuel assembly level [333]. This is not the case for reactivity-initiated accidents.

10.1 Experimental data

The current database on RIA simulation tests comprises more than a thousand tests on fresh (un-irradiated) LWR fuel rods and about 140 tests on pre-irradiated samples. Most of the data pertain to PWR type of rods, and the great majority of tests have been done on UO_2 fuel. However, some data are also available for other kinds of fuel material, such as $(\text{U,Pu})\text{O}_2$ mixed oxide fuel, gadolinium-bearing UO_2 and inert matrix fuel.

The tests on fresh fuel rods show that the extent of damage inflicted to the fuel rod correlates well with the peak value of fuel pellet radial average specific enthalpy under the test. The observed failures are related to cladding overheating as a result of film-boiling and impaired clad-to-coolant heat transfer. There are two limiting failure modes for the fresh rods: fracture of the overheated and oxygen-embrittled cladding upon quenching, or clad ballooning and burst. The latter failure mode is restricting when there is a substantial gas overpressure in the fuel rod.

The tests on pre-irradiated fuel rods show that irradiated rods are more susceptible to cladding failure than fresh rods, i.e. they fail at lower fuel enthalpy. The tests also suggest that high-burnup fuel rods fail either by cladding high-temperature ballooning and burst, or at low temperature, by pellet-clad mechanical interaction during the early heat-up stage of the accident. The high-temperature failure mode is observed for pre-irradiated VVER fuel rods, whereas pre-irradiated PWR and BWR rods fail almost exclusively by PCMI in the tests. Moreover, the high-temperature failures correlate well with peak fuel specific enthalpy, in contrast to the PCMI-induced failures. The latter show a significant scatter for the failure enthalpy, which could have several possible explanations. Firstly, it is clear from the tests that the pre-test state of the fuel rod, e.g. the pellet-clad gap width and the degree of cladding corrosion, affects the susceptibility to PCMI-induced failure. Secondly, the pre-irradiated

test rods, which are re-fabricated from full-length fuel rods, may not be sufficiently pre-conditioned to reach an equilibrium pellet-clad contact state before testing. In some pulse test facilities, it is not possible to operate the test rods at pre-conditioning power to reach this state. Thirdly, peak fuel enthalpy is related to the thermal load imposed on the fuel rod, and may not be an expedient parameter in criteria for the low-temperature, PCMI-induced failures.

There are several reasons to question whether the aforementioned tests reproduce the true fuel behaviour under reactivity-initiated accidents foreseen in light water reactors:

- Many of the un-irradiated test rods were designed with high (≥ 10 wt%) enrichments of ^{235}U . Parametric studies show that enrichment has an observable effect on the behaviour of fresh fuel rods under RIAs.
- Most tests, both on un- and pre-irradiated fuel rods, were done with cooling by stagnant water at room temperature and atmospheric pressure. While these cooling conditions are fairly close to those at cold zero power in BWRs, they are very different to those associated with rod ejection accidents in PWRs. We also note that data for fuel rod post-failure behaviour, i.e. for fuel-coolant interaction and thermal-to-mechanical energy conversion ratios, originate almost exclusively from tests with stagnant water at ambient conditions.
- About thirty of the pre-irradiated test rods, namely those in the SPERT and NSRR/JMTR tests, had atypical design and/or were pre-irradiated under atypical reactor conditions. Unfortunately, these rods make up most of the available test data for the burnup range of 10 to 40 MWd(kgU)⁻¹.
- Pulse widths in the NSRR (4-7 ms FWHM) and the BGR (2-3 ms) are much smaller than those expected for control rod ejection/drop accidents. The pulse width affects the PCMI failure mode, most importantly because it controls the time lag between mechanical loading and heating of the cladding tube; a narrow power pulse leads to mechanical loading at a time when the cladding is insignificantly heated from its initial temperature and therefore potentially brittle. This effect is illustrated by Figure 44 in Section 6.2.5.1.

It should also be remarked that all tests, except for those in the PBF and CABRI, were done on rodlets with very short (120-150 mm) active length. Data are therefore unavailable as to what typical axial extent can be expected for the cladding damage in full-length (3.6-4.0 m) fuel rods under RIAs. It is tacitly assumed that results from short-length rodlets can be extrapolated to full-length fuel rods, based on the local values for fuel specific enthalpy.

Notwithstanding the above objections, we believe that the failure behaviour of LWR fuel rods under reactivity-initiated accidents is fairly well investigated experimentally, and that the failure mechanisms are largely understood. Yet, additional RIA simulation tests are warranted at cooling conditions and with power pulses that reproduce light water reactor conditions with higher fidelity. More attention should also be paid to the role of pre-conditioning in tests on pre-irradiated fuel rods. Finally, significant knowledge gaps currently exist as to the post-failure behaviour of failed rods, and measurements of thermal-to-mechanical energy conversion ratios at other coolant conditions than room temperature and atmospheric pressure are needed. Not only tests on individual rodlets, but also fuel rod bundle tests should be used in these experiments, if possible.

10.2 Computational methods

The consistency of calculated results in reported state-of-the-art analyses of postulated control rod ejection/drop accidents suggest that current computational methods used to analyse these accidents are well established and reliable. The calculated results reviewed in this report show that a control rod

ejection/drop accident leads to a significant power increase in about 10-20% of the reactor core, and that the power pulse width and the core-wide maximum of fuel specific enthalpy increase are well correlated to the prompt reactivity insertion under the accident.

The core-wide calculations are made with three-dimensional neutron kinetics codes, in which ancillary models for fuel rod heat transfer and coolant thermal-hydraulics are used to account for reactivity feedback effects. The fuel rod models used for this purpose are fairly simple, and they are normally applied to a lumped, average-powered, fuel rod in each fuel assembly. There are no models for the fuel rod post-failure behaviour, which in a strict sense means that the calculated results for the reactor core behaviour are valid only up to the point of first fuel rod failure. Moreover, the applied models for clad-to-coolant heat transfer in these codes are generally designed for analyses of steady-state reactor operation and mild transients, and they are known to be inaccurate for modelling RIAs. More appropriate models for transient clad-to-coolant heat transfer have recently been formulated on the basis of results from both in- and out-of-reactor RIA experiments [94,192]. These models seem promising, and should be considered for implementation in existing code systems for analyses of RIAs. Another modelling issue is the dynamics of coolant vapour generation under reactivity-initiated accidents. Current models for vapour generation are empirically based and rely on experimental data obtained under quasi-static test conditions. When these models are used in simulations of RIAs, they seem to overestimate the vapour generation and its associated reactivity feedback.

The models used in computer codes for stand-alone analyses of fuel rod thermo-mechanical behaviour under RIAs are considerably more sophisticated than those used for fuel rod thermal analyses in large code systems for core-wide analyses. The stand-alone codes are generally quite successful in reproducing the results of RIA simulation tests when it comes to temperatures and fuel rod deformations, provided that the cladding temperature remains low throughout the tests. Also cladding failures are captured with fair accuracy for the low temperature tests, if the degree of pre-test cladding corrosion is known and can be used as input to the analysis. However, due to the lack of appropriate clad-to-coolant heat transfer models for reactivity accidents, the codes fail to accurately reproduce temperatures and deformations in cases where a boiling crisis occurs. The new heat transfer models mentioned above could hopefully improve the situation.

The stand-alone fuel rod codes generally fail to accurately reproduce transient fission gas release under RIA simulation tests on pre-irradiated fuel rods. Model improvements are needed, since transient release of gaseous fission products and helium from high-burnup fuel has potential to increase the fuel rod internal gas pressure, with possible consequences to cladding integrity. Finally, it should be remarked that all fuel rod codes available today lack capacity for modelling post-failure phenomena, such as gap gas ejection, fuel dispersal, fuel-coolant interaction and loss of axisymmetric geometry.

11. NOMENCLATURE

The symbols and abbreviations used in this report are listed below, together with a brief explanation to the notation. The ambition to conform to prevalent nomenclature in international literature has unfortunately led to inevitable conflicts. However, in case a symbol is used in different contexts with different meanings, this is clearly indicated in the list. Throughout the text, all mathematical symbols are printed in italic. The international system of units (SI) is applied, except for the use of Curie (Ci) instead of Becquerel (Bq) for radiation: $1\text{Bq} = 1$ disintegration or nuclear transformation per second $[\text{s}^{-1}]$, and $1\text{Ci} = 3.7 \times 10^{10}\text{Bq}$.

For country names, we use the two-letter codes defined in the international ISO 3166-1 alpha-2 standard. These are the codes used in the internet as country code top-level domain identifiers.

11.1 Fundamental definitions

Cladding refers to the thin-walled tube that encapsulates the fuel pellets and separates the radioactive material from the primary coolant. Zirconium base alloys are used for the cladding tubes in light water reactors, due to their high resistance to corrosion by water and their small cross-section for capture of neutrons. Typical compositions of the cladding alloys treated in the report are summarised in Table 19. Besides the composition, also the final heat treatment is important to the cladding properties. A distinction is usually made between stress relieved annealed (SRA) and recrystallisation annealed (RXA) materials [82].

Table 19. Typical composition of zirconium alloys used as cladding materials in LWRs. The composition is given in wt%, and the balance is zirconium and impurities.

Cladding alloy	Elements					
	Sn	Fe	Cr	Ni	O	Nb
Zircaloy-2	1.5	0.1	0.1	0.06	0.12	0
Zircaloy-4	1.5	0.2	0.1	0	0.12	0
E110	0	0	0	0	0.12	1.0
HANA-4	0.4	0.2	0.1	0	0.12	1.5
MDA	0.8	0.32	0.1	0	0.12	0.5
M5	0	0	0	0	0.13	1.0
NDA	1.0	0.27	0.16	0.01	0.12	0.1
ZIRLO	1.0	0.1	0	0	0.12	1.0

Fuel burn-up refers to the amount of energy generated per unit of initial mass of heavy nuclides. The unit used for burn-up in this report is $\text{MWd}(\text{kgU})^{-1}$ for fuel of UO_2 , or $\text{MWd}(\text{kgHM})^{-1}$ for fuel that contains several fissionable heavy metals (HM). This is the most common measure for fuel burn-up in engineering literature, although atomic% and $\text{MWd}(\text{kgUO}_2)^{-1}$ are sometimes used. Burn-ups beyond about $60\text{MWd}(\text{kgHM})^{-1}$ are today considered as “high” burn-ups, but this threshold is continually moving upwards.

Fuel specific enthalpy, sometimes referred to as fuel energy density, is the enthalpy per unit mass of the fuel pellet material. The unit used for specific enthalpy in this report is Jg^{-1} . For clarity, we write

the unit as $\text{J}(\text{gUO}_2)^{-1}$, when referring to UO_2 fuel. As long as the fuel is in solid state, its specific enthalpy, h_f , is simply calculated from the fuel temperature, T_f , through:

$$h_f(T_f) = \int_{T_0}^{T_f} c_f(T) dT \quad 18$$

where c_f is the specific heat capacity of the solid fuel and T_0 is a reference temperature at which $h_f=0$. In this report, we use $T_0=273$ K. Terminology in engineering literature is a bit slack, and the word “specific” in specific fuel enthalpy is mostly left out for brevity. In this report, we adhere to this standard.

11.2 Latin symbols

A_o	Test specimen cross-sectional area	$[\text{m}^2]$
c_f	Fuel specific heat capacity	$[\text{J}(\text{gK})^{-1}]$
C_H	Hydrogen concentration	$[\text{molm}^{-3}]$
C_{Heff}	Effective hydrogen concentration	$[\text{molm}^{-3}]$
C_O	Oxygen concentration	$[\text{wt}\%]$
D	Hydrogen diffusivity	$[\text{m}^2\text{s}^{-1}]$
d_{32}	Mean diameter (volume-to-surface diameter)	$[\text{m}]$
E	Yong modulus	$[\text{Pa}]$
E_n	Neutron energy	$[\text{eV}]$
E_{tot}	Total energy deposited to the fuel	$[\text{J}(\text{gUO}_2)^{-1}]$
f	Fraction of radionuclide inventory released in accidents	$[-]$
f_{\perp}	Fraction of hydride platelets perpendicular to the loading direction	$[-]$
F_w	Fractional thickness of cladding beta-Zr layer	$[-]$
h	Cladding wall thickness	$[\text{m}]$
h_f	Radially averaged fuel specific enthalpy	$[\text{Jg}^{-1}]$
I	Reactor core radionuclide inventory	$[\text{Ci}]$
k	Effective neutron multiplication factor	$[-]$
k_{∞}	Infinite lattice multiplication factor	$[-]$
l_h	Hydride spacing	$[\text{m}]$
L_o	Test specimen gauge length	$[\text{m}]$
P_{max}	Power pulse amplitude	$[\text{W}(\text{gUO}_2)^{-1}]$
Q	Radiological source term	$[\text{Ci}]$
R	Universal gas constant ($R=8.3143$)	$[\text{J}(\text{molK})^{-1}]$
t	Time	$[\text{s}]$
$t_{1/2}$	Half life	$[\text{s}]$
t_c	Characteristic time for hydride dissolution/precipitation	$[\text{s}]$
T	Temperature	$[\text{K}]$
T_0	Reference temperature, at which $h_f=0$. Here, $T_0=273$ K	$[\text{K}]$
T_f	Fuel temperature	$[\text{K}]$
T_m	Moderator temperature	$[\text{K}]$
T_s	Solidus (melting) temperature	$[\text{K}]$
W_o	Test specimen gauge section with	$[\text{m}]$
w_{Ox}	Clad oxide layer thickness	$[\text{m}]$
x	Ratio of cladding outer-to-inner radius	$[-]$
y	Mole fraction of PuO_2 in $(\text{U,Pu})\text{O}_2$ MOX fuel	$[-]$

11.3 Greek symbols

α	Coefficient of linear thermal expansion	[K ⁻¹]
α_m	Moderator void volume fraction	[-]
β	Effective delayed neutron fraction	[-]
δ	Extension of test sample due to local deformation (necking)	[m]
ΔP	Fuel rod internal gas overpressure	[Pa]
$\varepsilon_{\theta\theta}$	Hoop (circumferential) strain	[-]
ε_{zz}	Axial (longitudinal) strain	[-]
ε_{te}	Total elongation (measured plastic strain to failure)	[-]
ε_{ue}	Uniform elongation (measured plastic strain to instability)	[-]
Φ	Clad fast neutron fluence ($E_n > 1\text{MeV}$)	[m ⁻²]
κ	Hydride volume fraction	[-]
Λ	Effective neutron lifetime	[s]
ν	Poisson ratio	[-]
ρ	Reactivity	[-]
σ	Uniaxial or effective stress	[Pa]
$\sigma_{\theta\theta}$	Hoop (circumferential) stress	[Pa]
σ_{zz}	Axial (longitudinal) stress	[Pa]
σ_y	Clad yield stress	[Pa]
τ	Pulse width (Full width at half maximum - FWHM)	[s]
μ	Coefficient of friction	[-]
ξ	Thickness of cladding oxide + oxygen stabilised alpha-Zr layer	[m]

11.4 List of abbreviations

ACPR	Annular Core Pulse Reactor
AESJ	Atomic Energy Society of Japan
ANL	Argonne National Laboratory (USA)
ATR	Advanced Thermal Reactor
AUC	Ammonium uranocarbonate
BA	Burnable Absorber
BIGR	Fast Impulse Graphite Reactor (Russia)
BOC	Beginning of Cycle
BR3	Belgian Reactor 3 (Belgium)
BWR	Boiling Water Reactor
CANDU	Canadian Deuterium Uranium (Canadian type pressure tube heavy water reactor)
CEA	Commissariat à l'Energie Atomique (French atomic energy commission)
CIEMAT	Centro de Investigaciones Energeticas, Medioambientales y Tecnologicas (Spain)
CIP	CABRI International Program
CSED	Critical Strain Energy Density
CSNI	Committee on the Safety of Nuclear Installations
CVCS	Chemical and Volume Control System
CZP	Cold Zero Power
DBA	Design Basis Accident
DBT	Ductile-to-Brittle Transition
DNB	Departure from Nucleate Boiling
dpa	Displacement Per Atom
EDC	Expansion Due to Compression
EDF	Electricité de France
EOC	End of Cycle

EPRI	Electric Power Research Institute (USA)
ETR	Engineering Test Reactor (USA)
E110	Cladding material used in VVER fuel rods (Zr-1.0Nb by wt%)
FCI	Fuel-Coolant Interaction
FGR	Fission gas Release
FWHM	Full Width at Half Maximum
HANA-4	Clad alloy developed by KAERI (Zr-1.5Nb-0.4Sn-0.2Fe-0.1Cr by wt%)
HFP	Hot Full Power
HM	Heavy Metal
HSE	Health and Safety Executive (UK)
HTR	High Temperature Reactor
HZP	Hot Zero Power
IAEA	International Atomic Energy Agency (Austria)
IGR	Impulse Graphite Reactor (Kazakhstan)
IMF	Inert Matrix Fuel
INL	Idaho National Laboratory (USA)
IPSN	Institut de Protection et de Sûreté Nucléaire (now IRSN, France)
IRSN	Institut de Radioprotection et de Sûreté Nucléaire (formerly IPSN, France)
ITU	Institute for Transuranium Elements (Germany)
JAEA	Japan Atomic Energy Agency (formerly JAERI)
JAERI	Japan Atomic Energy Research Institute (now JAEA)
JMTR	Japanese Material Test Reactor
KAERI	Korean Atomic Energy Research Institute
LHGR	Linear Heat Generation Rate
LMFBR	Liquid Metal Fast Breeder Reactor
LOCA	Loss of Coolant Accident
LVDT	Linear Variable Differential Transformer
LWR	Light Water Reactor
MDA	Mitsubishi Developed Alloy (Zr-0.8Sn-0.5Nb-0.32Fe-0.1Cr by wt%)
M5	Cladding trademark of Framatome ANP (Zr-1.0Nb-0.13O by wt%)
MIMAS	MIcronised MAsterblend
MOX	Mixed Oxide (UO ₂ /PuO ₂)
NDA	New Developed Alloy (Zr-1.0Sn-0.27Fe-0.16Cr-0.1Nb-0.01Ni by wt%)
NDT	Nil Ductility Temperature
NEA	Nuclear Energy Agency
NFD	Nippon Nuclear Fuel Development
NFIR	Nuclear Fuel Industry Research
NRC	Nuclear Regulatory Commission (USA)
NRX	Test reactor (Canada)
NSRR	Nuclear Safety Research Reactor (Japan)
OECD	Organisation for Economic Co-operation and Development
PBF	Power Burst Facility (USA)
PCMI	Pellet-Clad Mechanical Interaction
PCT	Peak Cladding Temperature
PNNL	Pacific Northwest National Laboratory (USA)
PSU	Pennsylvania State University (USA)
PWR	Pressurised Water Reactor
RBMK	Russian type, graphite moderated, pressure tube light water reactor
RCS	Reactor Coolant System
RDA	Control Rod Drop Accident
REA	Rod Ejection Accident

REP	Réacteurs à Eau Pressurisée (Pressurised water reactor)
RI	Organic iodides
RIA	Reactivity-initiated Accident
RIL	Rod Insertion Limit
RISA	Radiation Induced Surface Activation
ROX	Rock-like Oxide
RST	Ring Stretch Test
RXA	Recrystallisation Annealed
SBR	Short Binderless Route
SED	Strain Energy Density
SKI	Statens Kärnkraftinspektion (Swedish Nuclear Power Inspectorate)
SI	Le Système Internationale d'unités (The international system of units)
SIMS	Secondary Ion Mass Spectrometry
SL-1	Stationary Low Power Plant No. 1 (USA)
SOAR	State-of-the-art report
SPERT	Special Power Excursion Reactor (USA)
SRA	Stress Relieved Annealed
SSM	Strålsäkerhetsmyndigheten (Swedish Radiation Safety Authority)
STP	Standard Temperature and Pressure (273.15 K and 1×10^5 Pa)
TD	Theoretical Density
TCO	Cladding outer surface temperature
TMI-2	Three Mile Island, Unit 2
TRIGA	Training, Research, Isotopes General Atomics
UTS	Ultimate Tensile Strength
VVER	Russian type pressurised water reactor
WGFS	Working Group on Fuel Safety
wppm	Weight Parts Per Million
XRF	X-ray Fluorescence
ZIRLO	Cladding trademark of Westinghouse, (Zr-1.0Nb-1.0Sn-0.1Fe by wt%)

Appendix A

SUMMARY OF PULSE REACTOR TESTS ON PRE-IRRADIATED LWR FUEL RODS

In the following, a summary is made of pulse reactor RIA simulation tests that have been done on pre-irradiated LWR fuel rods and reported in literature up to March 2009. Readers interested in RIA simulation tests on un-irradiated UO_2 fuel rods are referred to the reviews by MacDonald *et al.* [113] Ishikawa and Shiozawa [111], and Ishikawa *et al.* [152] Tests on un-irradiated MOX fuel have been reported by Abe *et al.* [200] and similar work on un-irradiated ROX fuel can be found in [48-49].

The data presented below are taken from open-literature sources. When compiling the data, it was found that data reported for a particular test could vary slightly from one source to another. For instance, it is not unusual that preliminary data are presented at conferences, and later adjusted as the experiments are more carefully evaluated. Precedence has therefore been given to the latest published data, in those cases where we have found conflicting values reported in literature.

All reported fuel enthalpies are axial peak, radial average values for the fuel pellets, and they are calculated with respect to a reference temperature of 273 K. Since all power pulses in the summary are initiated from zero or near zero power, the initial fuel temperature is very close to the coolant temperature. Hence, the fuel enthalpy *increase* under the pulse test can be calculated by subtracting the reported peak fuel enthalpy with the initial fuel enthalpy, under the assumption that the initial fuel and coolant temperatures are equal.

Finally, it should be mentioned that tests have been done also with power pulses that simulate the conditions of RIAs at full reactor power [343]. These tests, carried out on un-irradiated UO_2 fuel rods, are not considered here.

A.1 SPERT-CDC tests

The SPERT-CDC tests simulated the conditions of a BWR during cold start-up. More specifically, the thermo-mechanical behaviour of BWR-type UO_2 test rodlets was investigated. The coolant was stagnant water at atmospheric pressure and 298 K. The pulse widths were in the range of 13 to 31 ms [113]. Each test rod contained a short, 132 mm fuel length, clad tube of 10% cold-worked Zircaloy-2. The UO_2 fuel pellets had a density of 0.94 TD (theoretical density) with the enrichment of 7 wt% ^{235}U . Two different fuel rod designs were used: GEX-type with a cladding outer diameter of 7.94 mm and GEP-type with a diameter of 14.29 mm. The small-diameter GEX-rods were designed to increase the attainable energy deposition in the RIA simulation facility, and their clad wall thickness and fuel-cladding gap were reduced proportionally to the clad diameter.

The total deposited energies for the pre-irradiated test rods in SPERT-CDC, along with their respective burn-ups, are presented in Table A.1. The energy deposition was determined by measuring the activity of a cobalt wire located in the vicinity of the test capsule. The technique provides the total energy deposition during the transient and has an accuracy of $\pm 12\%$. Around 10 to 20% of the energy deposition occurs after the power pulse, i.e. during low powers prior to reactor scram. This delayed energy deposition does not contribute to the peak fuel enthalpy. The radially averaged peak fuel enthalpy was therefore estimated using a correction of 17% to account for the delayed energy deposition [113].

Table A.1. SPERT-CDC tests on pre-irradiated fuel rods

Data compiled from [113,144]

Test ID	Fuel burn-up [MWd(kgU) ⁻¹]	Clad oxide thickness [μm]	Pulse width [ms]	Peak fuel enthalpy [J(gUO ₂) ⁻¹]	Failure enthalpy [J(gUO ₂) ⁻¹]	Fuel loss [%]
567	3.1	0	18	896	896	NA
568	3.8	0	24	674	615	NA
569	4.1	0	14	1 181	1 181	NA
571	4.6	0	31	574	Survived	–
684	13	0	20	712	Survived	–
685	13	0	23	662	Survived	–
703	1.1	0	15	682	Survived	–
709	1.0	0	13	846	846	NA
756	32	65	17	600	600	0
859	32	65	16	645	356	>0

NA: Data are not available.

Several of the low-burn-up rods failed during or following the power pulse. Also, both of the failed high-burn-up rods (rods 756 and 859) exhibited brittle-type clad fracture. Rod 756 failed for a peak fuel enthalpy of 600 J(gUO₂)⁻¹, whereas rod 859 failed at 356 J(gUO₂)⁻¹. A large hydride blister was found in rod 859. The cause of failure for these two rods was attributed to heavy accumulations of zirconium hydride. Moreover, the non-prototypical test conditions could also have contributed to the cladding failure. The low initial cladding temperatures in combination with the narrow power pulses, which were utilised in the SPERT-CDC tests, resulted in relatively low cladding temperatures at the time of maximum cladding stresses. The effect of pulse width on the cladding thermo-mechanical loading path is illustrated in Figure 44 (p. 108).

The direct applicability of the SPERT-CDC test results to LWR RIA conditions must be questioned, since the design of the test rods is different from that of today's light water reactor fuel. In addition, the test rods were pre-irradiated in the ETR facility at very high linear heat generation rate, 46-67 kWm⁻¹, resulting in fuel restructuring and central hole formation. Hence, these tests are not typical of fuel rods in commercial light water reactors.

A.2 PBF tests

Three series of tests were performed in the Power Burst Facility on pre-irradiated rodlets of PWR design. The rodlets were about 900 mm long, and were fuelled with UO₂ pellets. The ²³⁵U fuel enrichment was 5.7-5.8 wt%, i.e. slightly higher than in commercial PWR fuel rods. The rodlets were pre-irradiated in the Saxton PWR to a burn-up of about 5 MWd(kgU)⁻¹. The cladding oxide thickness of the pre-irradiated test rods was roughly 5 μm, and the average hydrogen content was about 40 wppm.

The main objective of the RIA 1-1 tests was to provide a comparison of irradiated and un-irradiated fuel behaviour at the US NRC licensing fuel enthalpy limit of 280 cal(gUO₂)⁻¹ (1 172 J(gUO₂)⁻¹). Two of the four rodlets in the RIA 1-1 test were pre-irradiated in the Saxton reactor to a burn-up of 4.6 MWd(kgU)⁻¹. All test rods failed by rod fragmentation and fuel dispersal for a peak fuel enthalpy of 1 193 J(gUO₂)⁻¹ (see Table A.2). The RIA 1-2 tests were conducted using four individually shrouded rodlets, which had been irradiated to a burn-up of 5.2 MWd(kgU)⁻¹ in the Saxton reactor. Two of the rodlets were opened and back-filled with helium to about 2.4 MPa to simulate end-of-life rod internal pressure. One rodlet was opened, instrumented, and back-filled to a rod internal pressure of 0.105 MPa. The four fuel rodlets used in tests RIA 1-2 were subjected to a radially averaged peak fuel enthalpy of 775 J(gUO₂)⁻¹.

Only one rodlet failed in the RIA 1-2 experiment. The failure was caused by 22 small (<1 cm long) longitudinal cracks, starting at about 14.5 cm and extending to about 68.1 cm from the bottom of

the 91 cm long fuel stack. The radial average fuel enthalpy at the 14.5 and 68.1 cm locations was about $586 \text{ J(gUO}_2\text{)}^{-1}$. This failed rod had a burn-up of $4.4 \text{ MWd(kgU)}^{-1}$, and was not opened for re-pressurisation and instrumentation. It should be emphasized that this rod was not pre-pressurised with helium, but was air filled at atmospheric pressure before pre-irradiation. This fact, in combination with the large number of cladding perforations observed in post-test examinations, makes it reasonable to believe that the cladding contained hydride blisters, induced by air humidity. However, since the rod experienced film boiling and high ($>1000\text{K}$) cladding temperature under 10-15 s, which is sufficient to dissolve zirconium hydride, no blisters could be seen in post-test examinations [148].

Table A.2. Summary of PBF tests. Data compiled from [113-114]

Test ID	Rod ID	Fuel burn-up [MWd(kgU) ⁻¹]	Clad oxide thickness [μm]	Fill gas pressure [MPa]	Pulse width [ms]	Peak fuel enthalpy [J(gUO ₂) ⁻¹]	Failure enthalpy [J(gUO ₂) ⁻¹]	Fuel Loss [%]
RIA 1-1	801-1	4.6	5	NA	13	1 193	1 193	65
	801-2	4.7	5	NA	13	1 193	1 193	65
	801-3	0.0	0	NA	13	1 193	1 193	35
	801-4	0.0	0	NA	13	1 193	1 193	35
RIA 1-2	802-1	5.2	5	0.1	16	775	Survived	—
	802-2	5.1	5	2.4	16	775	Survived	—
	802-3	4.4	5	NA	16	775	586	0
	802-4	4.5	5	2.4	16	775	Survived	—
RIA 1-4	804-1	6.1	5	NA	11	1 160	<1 160	0
	804-3	5.5	5	NA	11	1 160	<1 160	0
	804-4	5.0	5	NA	11	1 068	<1 068	0
	804-5	5.5	5	NA	11	980	980	0
	804-6	5.1	5	NA	11	1 068	<1 068	0
	804-7	5.9	5	NA	11	1 160	<1 160	0
	804-8	4.7	5	NA	11	1 068	<1 068	0
	804-9	5.7	5	NA	11	1 160	<1 160	0
	804-10	4.4	5	NA	11	1 068	<1 068	0

NA: Data are not available.

Significant differences were observed between the two intact rods with high internal pressure and the intact low-pressure rod. The maximum hoop plastic strain for the high-pressure rods was twice that of low-pressure rods; the maximum cladding hoop plastic strain measured in the two high-pressure rods was about 6% whereas for the low-pressure rod, it was around 3%. It should be remarked that these post-test strains were determined with reference to the as-fabricated diameter of the test rods, and they therefore represent the accumulated cladding deformation not only under the RIA simulation test, but also under pre-irradiation. More pronounced clad ridging was observed for the high-pressure rods, at intervals equal to the length of fuel pellets.

The nine rods in test RIA 1-4 were ramped to radially averaged peak fuel enthalpies of $980\text{--}1\,160 \text{ J(gUO}_2\text{)}^{-1}$ and all of them failed by PCMI-induced cracks.

A.3 IGR tests

Thirteen tests on pre-irradiated VVER fuel rods were carried out in the IGR from 1990 to 1992. All test rodlets were sampled from two full-length mother rods, taken from a fuel assembly that had been operated in a VVER-1000 reactor, more precisely in Unit 5 of the Novovoronezh nuclear power plant, Russia [149]. Eight of the rodlets were sampled directly from the mother rods, and contained UO₂ fuel pellets with a burn-up of 47 to 49 MWd(kgU)⁻¹. In the remaining rodlets, the original fuel pellets were replaced with fresh fuel. The outer and inner diameters of the annular fuel pellets were 7.56 and 2.20-2.40 mm, respectively. The length of the fuel stack in the rodlets was 141-167 mm.

All re-fabricated rodlets were back-filled with pure helium to a pressure of 1.7 MPa. The E110 cladding had an outer diameter of 9.10 mm and a wall thickness of 0.69 mm. The pre-test oxide layer thickness was about 5 μm . The rodlets were not instrumented, but extensively characterised before and after the tests. All tests were done with stagnant water as coolant. The water was at atmospheric pressure and the initial temperature was 293 K.

The test results are summarised in Table A.3. Five of the rodlets failed at high fuel enthalpy as a consequence of cladding high temperature ballooning and burst. Some of the rodlets also showed signs of high temperature oxidation of the cladding, with oxide layers reaching up to 18 μm in thickness [149]. Fuel dispersal into the coolant did not take place, in spite of the high fuel enthalpies.

Table A.3. Summary of IGR tests on VVER fuel rods [149]

Test ID	Fuel burn-up [MWd(kgU) ⁻¹]	Clad oxide thickness [μm]	Fill gas pressure [MPa]	Pulse width [ms]	Peak fuel enthalpy [J(gUO ₂) ⁻¹]	Failure or survival	Clad mean hoop strain [%]	Clad max hoop strain [%]	Fuel loss [%]
H1T	49	5	1.7	750	632	Survived	1.4	–	–
H2T	48	5	1.7	800	892	Failed	7.9	12.6	0
H3T	49	5	1.7	800	1055	Failed	8.6	NA	0
H4T	49	5	1.7	800	477	Survived	0.0	–	–
H5T	49	5	1.7	800	737	Failed	3.1	6.5	0
H6T	49	5	1.7	800	364	Survived	0.0	–	–
H7T	47	5	1.7	600	783	Failed	3.4	22.8	0
H8T	47	5	1.7	850	255	Survived	0.0	–	–
H14T	0	5	1.7	900	255	Survived	0.5	–	–
H15T	0	5	1.7	900	816	Failed	NA	9.6	0
H16T	0	5	1.7	850	509	Survived	0.0	–	–
H17T	0	5	1.7	950	380	Survived	1.5	–	–
H18T	0	5	1.7	850	355	Survived	2.4	–	–

Test rodlets H1T-H8T comprised high burn-up UO₂ fuel pellets, whereas rodlets H14T-H18T were re-charged with fresh UO₂ pellets. All rodlets had irradiated E110 cladding (Zr-1.0Nb by wt%) with comparable exposure. In the table, residual clad hoop strains are reported for the ballooned region at the failure position (max) and for non-ballooned region (mean).

NA: Data are not available. Indicated hoop strains are residual (non-elastic) strains.

A.4 BGR tests

Twelve tests on pre-irradiated VVER fuel rods were done in the BGR from 1997 to 2000 [151]. These tests were intentionally very similar to those carried out earlier in the IGR, but the pulse widths differed significantly (see Table A.4). The main purpose of the BGR tests was to study the impact of narrow pulses. The test rodlets were sampled from six full-length mother rods, which had been operated to high burn-up in three different power reactors. Eight of the rodlets were sampled from VVER-1000 fuel rods operated in Unit 5 of the Novovoronezh nuclear power plant, Russia. These rodlets had burn-ups ranging between 47 and 49 MWd(kgU)⁻¹. The remaining four rodlets had a burn-up of 60 MWd(kgU)⁻¹, and were re-fabricated from VVER-440 fuel rods that had been irradiated in two different reactors.

The mother rods had comparable designs, with the exception of the fuel pellet geometry [151]. The fuel pellets had an outer diameter of 7.54-7.60 mm, and the fuel stack length of the re-fabricated rodlets ranged between 149 and 155 mm. The rodlets were back-filled with pure helium to pressures

between 0.1 and 2.1 MPa. In conformity with earlier tests in the IGR, all tests were done in stagnant water at atmospheric pressure and room temperature. The rodlets were not instrumented.

Table A.4. Summary of BIGR tests on VVER fuel rods [151]

Test ID	Fuel design VVER	Fuel burn-up [MWd(kgU)-1]	Clad oxide thickness [μm]	Fill gas pressure [MPa]	Pulse width [ms]	Peak fuel enthalpy [J(gUO ₂)-1]	Failure or survival	Clad mean hoop strain [%]	Clad max hoop strain [%]	Transient FGR [%]	Post-test gas pressure [MPa]	Fuel loss [%]
RT-1	1000	48	3-5	2.1	2.6	595	Survived	2.2	4.1	22.8	2.19	–
RT-2	1000	48	3-5	2.1	3.1	481	Survived	0.6	0.9	16.1	2.22	–
RT-3	1000	48	3-5	2.1	2.5	578	Survived	2	3.4	21.3	2.35	–
RT-4	440	60	3-5	2.1	2.5	523	Survived	3.7	5.5	NA	NA	–
RT-5	1000	49	3-5	2.1	2.5	611	Survived	2.7	4.2	26	2.24	–
RT-6	1000	48	3-5	2.1	2.6	641	Survived	3.2	6	26.5	2.29	–
RT-7	440	60	3-5	2	2.6	561	Survived	2.1	3.5	26.8	2.7	–
RT-8	440	60	5-7	2	2.6	687	Failed	NA	11.1	–	–	0
RT-9	440	60	5	0.1	2.7	691	Failed	NA	9.6	–	–	0
RT-10	1000	47	4-7	2	2.6	687	Failed	NA	18.9	–	–	0
RT-11	1000	47	4	2	2.6	787	Failed	NA	8.2	–	–	0
RT-12	1000	47	3-5	0.2	2.8	649	Survived	4.4	5.8	22.7	0.5	–

The test rods were sampled from irradiated fuel rods of both VVER-440 and VVER-1000 design. The reported post-test gas pressure refers to cold state (293 K).

NA: Data are not available. Indicated hoop strains are residual (non-elastic) strains.

Four of the rods failed. The failure mode, cladding high temperature ballooning and burst, was common to all failed rods. Two rods, both with a burn-up of 47 MWd(kgU)⁻¹, failed by a single pinhole perforation of the cladding. The other two failed rods, which had a burn-up of 60 MWd(kgU)⁻¹, failed by two and four perforations, respectively. All perforations were located at mid-pellet positions along the fuelled length of the rodlet. This preferential failure position was attributed to the barrel-shape expansion of the fuel pellets and the fact that cladding temperatures are higher at mid-pellet positions than at pellet-pellet interfaces [151]. The failure mode is illustrated in Figure 48 (p. 111).

It is interesting to note that the initial fill gas pressure did not notably affect the fuel rod failures. From Table A.4, it is clear that the transient fission gas release was 16-27% for the intact rodlets, and that the rod internal gas pressure in cold state increased by 0.1-0.7 MPa due to the transient gas release. Although this increase in rod pressure is moderate, the fission gas release contributed significantly to the gas pressure loading in rodlets RT-9 and RT-12, i.e. the samples with low initial fill gas pressure. No fuel loss was observed from the failed fuel rodlets, i.e. no fuel was dispersed into the coolant.

A.5 NSRR tests

The following subsections summarise tests performed in the Nuclear Safety Research Reactor on UO₂ fuel rods that have been pre-irradiated in PWRs and BWRs. Tests on pre-irradiated MOX fuel rods are also summarised. Most of the data are compiled from open-literature sources, but some data provided in reference [335] have not been published at the time of writing (April 2009). Reference [335] also contains recent revisions to previously published data.

A.5.1 Tests on PWR fuel rods

The tests done on pre-irradiated PWR fuel rods in the NSRR consist of nine different tests series, with fuel rods pre-irradiated in nine different power reactors. Six of these reactors are located in Japan, the others in Spain, Sweden and the USA. Two of the test series used rods from 14×14 fuel assemblies, but the remaining test series were carried out on rodlets sampled from mother rods of 17×17 design. The 14×14 rods were pre-irradiated in the Mihama (MH) reactor and the Genkai (GK) reactor to a rod

average burn-up of 39 and 42 MWd(kgU)⁻¹, respectively. Concurrently, rods from Ohi 1 (HBO) and Ohi 2 (OI) were pre-irradiated to rod average burn-ups of 50 MWd(kgU)⁻¹ and 39 MWd(kgU)⁻¹, respectively. In a separate series, 17×17 fuel rods irradiated in Takahama 3 reactor (TK series) with low-tin Zircaloy-4 clad material (1.3 wt% Sn) were subjected to RIA simulation tests.

Tests on 17×17 PWR fuel with other cladding materials than Zircaloy-4 have also been done: Three test rods, named OI-10, OI-11 and OI-12, were pre-irradiated in Ohi 4 to 58-61 MWd(kgU)⁻¹. In addition, two tests were done on rods that were pre-irradiated to a burn-up of 71-77 MWd(kgU)⁻¹ in Vandellós 2, Spain. The most recent tests were done on two high-burn-up rods from Ringhals, Sweden, and one rod from McGuire, USA. The eight rods had different Zr-Nb type cladding materials.

A.5.1.1 MH and GK rods

The MH and GK test series comprised altogether five PWR 14×14-test rods. The rods were subjected to power pulses, yielding radial average peak fuel enthalpies from 196 to 389 J(gUO₂)⁻¹, as shown in Table A.5. All the rods survived the tests. During the power pulse, a prompt cladding axial displacement was observed, indicating the occurrence of PCMI. The maximum axial displacement was reached 5 to 10 ms after the peak power, and then decreased after 5 s to its equilibrium position. The cladding surface temperature increased to saturation temperature (373 K), and nucleate boiling, but not film boiling, occurred for a few seconds.

Table A.5. Summary of the NSRR Test Series MH, GK, OI Unit 2 and HBO on pre-irradiated PWR rods

Test ID	Fuel design	Fuel burn-up [MWd(kgU) ⁻¹]	Clad oxide Thickness [μm]	Fill gas pressure [MPa]	Pulse width [ms]	Peak fuel enthalpy [J(gUO ₂) ⁻¹]	Failure enthalpy [J(gUO ₂) ⁻¹]	Clad max hoop strain [%]	Transient FGR [%]	Fuel loss [%]	Peak TCO [K]
MH-1	14×14	39	5	4.6	5.6	196	Survived	0.0	3.5	—	380
MH-2	14×14	39	5	4.6	5.5	230	Survived	0.1	NA	—	370
MH-3	14×14	39	5	4.6	4.4	280	Survived	1.6	4.0	—	475
GK-1	14×14	42	10	4.3	4.6	389	Survived	2.2	12.8	—	580
GK-2	14×14	42	10	0.1	4.6	377	Survived	1.1	7	—	570
OI-1	17×17	39	15	0.1	4.4	444	Survived	1.3	NA	—	725
OI-2	17×17	39	15	0.1	4.4	452	Survived	4.8	10.5	—	660
HBO-1	17×17	50	43	0.1	4.4	306	251	NA	(5.1)	67	(325)
HBO-2	17×17	50	35	5.1	6.9	155	Survived	0.4	17.7	—	395
HBO-3	17×17	50	23	0.1	4.4	310	Survived	1.5	22.7	—	670
HBO-4	17×17	50	19	0.1	5.3	209	Survived	0.2	21.1	—	385
HBO-5	17×17	44	60	0.1	4.4	335	322	NA	(2.8)	5	(335)
HBO-6	17×17	49	30	0.1	4.4	356	Survived	1.1	10.4	—	430
HBO-7	17×17	49	45	0.1	4.4	368	Survived	2.2	8.5	—	NA

All rods have standard Zircaloy-4 cladding (Zr-1.5Sn-0.2Fe-0.1Cr by wt%).

Data compiled from [84,109,153,335,338].

NA: Data are not available. **TCO:** Cladding outer surface temperature. Indicated hoop strains are residual (non-elastic) strains. For failed rods, fission gas release was evaluated from test capsule gas analyses with low accuracy. These results are given in brackets. For failed rods, the peak TCO (in brackets) pertains to the temperature at time of cladding failure.

Cladding dimensional changes were measured after testing. Plastic hoop strains were found in rods where the peak fuel enthalpy exceeded 230 J(gUO₂)⁻¹, with the maximum value of 2.2% for rod GK-1, which had experienced a peak fuel enthalpy of 389 J(gUO₂)⁻¹. The peak residual hoop strains are listed for these rods in Table A.5. All the test rods experienced considerable fission gas release,

which contributed to a transient 4 to 8 MPa pressure increase in the rods. The fission gas release, determined by rod puncturing, ranged between 3.5 and 12.8% during the transient, as shown in Table A.5. Destructive examination of fuel pellet material revealed cracks extending through a 1 mm thick rim at the pellet surface [336].

A.5.1.2 First series of OI tests and HBO rods

Two rods in the first OI test series, pre-irradiated in Ohi 2, and 7 rods in the HBO series (all of 17×17 design) were subjected to power pulses with peak fuel enthalpies ranging from 155 to 452 J(gUO₂)⁻¹, as shown in Table A.5. Two of the rods, HBO-1 and HBO-5, failed. The failure enthalpies for these rods were 251 and 322 J(gUO₂)⁻¹, respectively.

Rod dimensional measurements carried out after testing showed cladding residual deformation. The peak residual hoop cladding strains for the OI-1 and OI-2 rods were 1.3 and 4.8%, respectively. For the surviving HBO rods, the peak residual strains varied from 0.2 to 2.2% (see Table A.5). Fission gas release during the transient was determined by rod puncturing. The transient release for the HBO rods varied from 8.5 to 22.7%. It is noteworthy that HBO-2, HBO-3 and HBO-4 had remarkably high release fractions, considering the fairly moderate fuel enthalpies in these tests. The transient fission gas release fraction for OI-2 was 10.5%, as shown in Table A.5.

Cladding failure modes for the HBO-1 and HBO-5 rods have been discussed in some detail by Fuketa *et al.* [84] and Ishijima *et al.* [337]. In these two rods, axial cracks in the cladding were over the entire active length of the rod and the fracture was attributed to hydride-induced embrittlement. Significant hydride deposition below the oxide film on the cladding outer surface and many small cracks, perpendicular to the surface, were observed (see Figure 12). In both HBO-1 and HBO-5, the main crack emanated from one of these small cracks and then propagated through the hydride layer and the remaining part of the clad wall. According to Fuketa *et al.* [84], failure occurred predominantly for test fuel rodlets taken from the uppermost sections of the parent rod. Significant fuel dispersion occurred only in HBO-1 [84]. After testing, fuel material was found as fine fragments, half of them with sizes smaller than 50 µm. In HBO-5, only a small amount of fuel powder was released to the coolant water.

A.5.1.3 TK rods

All rods in the TK test series were of 17×17 design, and had low-tin Zircaloy-4 cladding. Among the ten test rods, two rods, TK-2 and TK-7, failed at fuel enthalpies of 251 and 360 J(gUO₂)⁻¹, respectively [44,339]. Dimensional measurements of the cladding after testing showed residual deformations. The peak residual hoop strains for the intact rods varied from 0.2 to 25%, as shown in Table A.6. Transient fission gas release, determined by rod puncturing, was between 5.9 and 20%. Cladding cracks in the failed rods TK-2 and TK-7 started at the clad outer surface, in the oxide layer and the heavily hydrided region, and propagated through the clad wall. Axial cracking occurred over the fuel active length and had a zigzag appearance. Moderate fuel dispersal occurred in both TK-2 and TK-7.

A.5.1.4 Second series of OI tests, VA, RH and MR rods

The tests OI-10 and OI-11 were carried out in July 2003, whereas OI-12 was done in March 2005. These test rods were all of 17×17 design, but they had three different Zr-Nb type alloy claddings: OI-10 had Mitsubishi Developed Alloy (MDA), OI-11 had ZIRLO cladding, and OI-12 had NDA cladding (New Developed Alloy). The results from these tests, survival of OI-10 and OI-12, and very high failure enthalpy for OI-11, reflect the better performance of these cladding materials in terms of higher corrosion resistance and lower hydrogen uptake under in-reactor irradiation.

It should be remarked that rod OI-10 showed exceptionally low fission gas release and cladding residual deformation. From the peak fuel enthalpy in this test, it is expected that film-boiling occurred during the transient [225]. Yet, the cladding peak residual hoop strain is merely 0.7%, and the transient fission gas release is only 2.6%. These unusually low values are probably a consequence of the large grain ($\approx 28 \mu\text{m}$) UO_2 fuel that was used in the OI-10 test rod. Due to the large grain size, there is less fission gas accumulated in grain boundary bubbles, and the transient fission gas release is lower than from fuel pellets with normal grain size ($\approx 10 \mu\text{m}$).

The VA-1 and VA-2 rodlets were sampled from two mother rods of 17×17 design, which were irradiated to very high burn-up in the Vandellós-2 reactor, Spain. The cladding was severely corroded for both rods, but the oxide layers were uniform; see Table A.6. Both VA-1 and VA-2 failed by PCMI at fairly low fuel enthalpy. A crack propagated all over the active length in both rodlets, and the entire fuel inventory was lost from the rods and dispersed into the coolant [159] (see Figure 43) in Section 6.2.5.1. It is interesting to note that the failure enthalpies of VA-1 and VA-2 are comparable to those of HBO-1 and TK-2, both of which had a burn-up of about $50 \text{ MWd}(\text{kgU})^{-1}$ and a clad oxide thickness around $40 \mu\text{m}$. This suggests that high burn-up effects, such as the re-structuring of UO_2 at the pellet rim, have very little impact on the propensity for PCMI-induced fuel rod failure [225].

Table A.6. Summary of the NSRR Test Series TK, OI unit 4, VA, RH and MR on Pre-irradiated PWR Rods

Test ID	Clad tube material	Fuel burn-up $[\text{MWd}(\text{kgU})^{-1}]$	Clad oxide thickness $[\mu\text{m}]$	Fill gas pressure $[\text{MPa}]$	Pulse width $[\text{ms}]$	Peak fuel enthalpy $[\text{J}(\text{gUO}_2)^{-1}]$	Failure enthalpy $[\text{J}(\text{gUO}_2)^{-1}]$	Clad max hoop strain $[\%]$	Transient FGR $[\%]$	Fuel loss $[\%]$	Peak TCO $[\text{K}]$
TK-1	Low-Sn Zr-4	38	7	0.1	4.4	527	Survived	25	20.0	-	860
TK-2	Low-Sn Zr-4	48	35	0.1	4.4	448	251	NA	(6.9)	7	NA
TK-3	Low-Sn Zr-4	50	10	0.1	4.4	414	Survived	5.6	10.9	-	980
TK-4	Low-Sn Zr-4	50	15	0.1	4.4	410	Survived	4.2	8.3	-	NA
TK-5	Low-Sn Zr-4	48	20	0.1	4.4	423	Survived	4.2	11.1	-	NA
TK-6	Low-Sn Zr-4	38	15	0.1	4.4	523	Survived	15.5	16.2	-	NA
TK-7	Low-Sn Zr-4	50	30	0.1	4.3	398	360	NA	(4.6)	13	NA
TK-8	Low-Sn Zr-4	50	10	0.1	7.0	272	Survived	0.3	5.9	-	NA
TK-9	Low-Sn Zr-4	50	<10	3.0	4.4	414	Survived	14.6	6.2	-	NA
TK-10	Low-Sn Zr-4	46	<10	0.1	4.4	360	Survived	0.2	NA	-	NA
OI-10	MDA	60	27	0.1	5.6	435	Survived	0.7	2.6	-	NA
OI-11	ZIRLO	58	28	0.1	4.4	657	500	NA	(13)	100	(300)
OI-12	NDA	61	41	0.1	4.4	600	Survived	2.9	22.4	-	NA
VA-1	ZIRLO	71	73	0.1	4.4	556	268	NA	(21.4)	100	NA
VA-2	MDA	77	70	0.1	4.4	546	231	NA	(27.7)	100	NA
RH-1	M5	67	6	0.1	4.4	462	Survived	1.0	21.4	-	390
RH-2	M5	67	6	0.1	4.5	447	Survived	1.1	26	-	870
MR-1	NDA	71	39	0.1	NA	408	Survived	0.4	8.7	-	373

All rods are of 17×17 design. Data compiled from [107,109,159,225,335,340-341]. The coolant initial temperature and pressure were 293 K and 0.1 MPa in all tests except for RH-2, which was performed at 551 K and 6.4 MPa.

NA: Data are not available. **TCO:** Cladding outer surface temperature. **Low-Sn Zr-4:** Low-tin Zircaloy-4, Zr-1.3Sn-0.2Fe-0.1Cr by wt%. **MDA:** Mitsubishi Developed Alloy, Mitsubishi Heavy Industries, Zr-0.8Sn-0.5Nb-0.32Fe-0.1Cr by wt%. **NDA:** New Developed Alloy, Nuclear Fuel Industries, Zr-1.0Sn-0.27Fe-0.16Cr-0.1Nb-0.01Ni by wt%. **ZIRLO:** Trademark of the Westinghouse Electric Company, Zr-1.0Nb-1.0Sn-0.1Fe by wt%. **M5:** Trademark of Framatome ANP, Zr-1.0Nb-0.13O by wt%.

The RH-1 and RH-2 rodlets were sampled from a mother rod of 17×17 design that had been operated in Ringhals, Sweden, to a rod average burn-up of $67 \text{ MWd}(\text{kgU})^{-1}$. The rodlets had a cladding oxide thickness of 5-6 μm . The exceptionally low corrosion is due to the M5 cladding material, and to the fact that the rodlets were sampled from the lower part of the mother rod [159,340]. RH-1 was tested at standard NSRR coolant conditions (289 K, 0.1 MPa), whereas RH-2 was tested in a capsule

with high coolant temperature and pressure (551 K, 6.4 MPa). Both rodlets survived the test, reaching a peak fuel enthalpy of 462 and 447 J(gUO₂)⁻¹, respectively [335,340].

For RH-1, transient records from thermocouples welded to the cladding showed no occurrence of film-boiling, and cladding temperatures remained low throughout the test. The cladding residual hoop strain was below 1%. This is the cladding residual deformation expected from PCMI, if the pellets are assumed to deform only by solid thermal expansion [159].

Finally, the MR-1 test rod was sampled from a mother rod of 17×17 design, which had been irradiated in the McGuire PWR, USA, and then accumulated further irradiation in the R2 research reactor, Sweden. The average burn-up of the test rodlet was 71 MWd(kgU)⁻¹, and the cladding oxide layer was 39 µm [159]. The rod had NDA cladding, and pellets with unusually large (40 µm) grains. The initial fuel enrichment was fairly low (3.75 wt% ²³⁵U), which resulted in a moderate peak fuel enthalpy of 408 J(gUO₂)⁻¹ during the test, although the rodlet was subjected to the maximum pulse achievable in the NSRR. The rod survived the test, and cladding residual hoop strains were < 0.4%.

It should be noted that a straightforward comparison between MR-1 and other tests cannot be made, since the irradiation conditions in the R2 reactor differ from those in PWRs. For example, the rod power was appreciably higher during the irradiation in R2 than in the McGuire reactor [159].

A.5.2 Tests on BWR fuel rods

Two series of BWR rods, TS and FK, have been tested in the NSRR. In the TS series, parent fuel rods of 7×7 assembly design, with non-liner Zircaloy-2 cladding, were base irradiated in Tsuruga Unit 1. The burn-up of the re-fabricated TS rodlets is about 26 MWd(kgU)⁻¹. In the FK series, parent rods of 8×8 design with liner Zircaloy-2 cladding were base irradiated in the Fukushima Daiichi unit 3 (FK-1 to FK-3) or in the Fukushima Daini unit 2 (FK-4 to FK-12) to different levels of burn-up. In the FK-1 to FK-3 rodlets, the fuel burn-up ranged from 41 to 45 MWd(kgU)⁻¹, and in the FK-4 to FK-12 test rods, the burn-ups were either 56 or 61 MWd(kgU)⁻¹.

In addition to the TS and FK test series, a single rod of 10×10 assembly design, which was pre-irradiated to 69 MWd(kgU)⁻¹ in the Leibstadt BWR, Switzerland, has been tested in the NSRR. The rod is designated LS-1. A summary of test conditions and results for all tests on pre-irradiated BWR fuel rods in the NSRR is given below.

A.5.2.1 TS rods

In the TS series, five BWR test rods with non-liner Zircaloy-2 cladding were subjected to peak fuel enthalpies between 230 and 410 J(gUO₂)⁻¹, as shown in Table A.7. The data presented here are taken mainly from [155]. All the rods survived the transient testing. A summary of clad residual strain and fission gas release data is also presented in Table A.7. Two of the rods, TS-4 and TS-5, experienced limited PCMI with small residual deformation of the cladding. Finally, rod puncturing indicated that the fission gas release during the transients ranged from 8 to 15%.

Destructive examination of the TS-4 fuel pellets revealed the presence of numerous small radial cracks in the outer periphery, which extended inward to about 3/4 of the pellet radius. In addition to radial cracks, a thin layer (≈100 µm), which showed extensive grain boundary separation, was identified by scanning electron microscopy of the surface layer [155]. It was judged that these effects were due to a large temperature gradient, occurring during the transient.

Table A.7. Summary of NSRR tests on pre-irradiated BWR rods

Test ID	Fuel design	Fuel burn-up [MWd(kgU) ⁻¹]	Clad oxide thickness [μm]	Fill gas pressure [MPa]	Pulse width [ms]	Peak fuel enthalpy [J(gUO ₂) ⁻¹]	Failure enthalpy [J(gUO ₂) ⁻¹]	Clad max hoop strain [%]	Transient FGR [%]	Fuel loss [%]	Peak TCO [K]
TS-1	7×7	26	6	1.1	6.0	230	Survived	0	NA	-	385
TS-2	7×7	26	6	1.1	5.3	275	Survived	0	12	-	385
TS-3	7×7	26	6	1.1	4.8	366	Survived	0	10	-	395
TS-4	7×7	26	6	1.1	4.6	370	Survived	0	15	-	425
TS-5	7×7	26	6	1.1	4.4	410	Survived	0	8	-	445
FK-1	8×8	45	16	0.3	4.4	544	Survived	0.8	8.2	-	625
FK-2	8×8	45	19	0.3	6.5	293	Survived	0	3.1	-	NA
FK-3	8×8	41	24	0.3	4.4	607	Survived	1.5	4.7	-	895
FK-4	8×8	56	22	0.5	4.3	586	Survived	1.2	15.7	-	900
FK-5	8×8	56	22	0.5	7.3	293	Survived	0.0	9.6	-	375
FK-6	8×8	61	20-30	0.1	4.3	548	293	< 0.1	(16.9)	100	NA
FK-7	8×8	61	20-30	1.5	4.3	540	260	< 0.1	(17)	100	NA
FK-8	8×8	61	20-30	1.5	7.3	272	Survived	< 0.1	11.3	-	370
FK-9	8×8	61	20-30	1.5	5.7	377	360	NA	(16.6)	100	(315)
FK-10	8×8	61	20-30	1.4	5.1	430	335	NA	(16.1)	100	NA
FK-12	8×8	61	20-30	1.4	5.8	373	301	NA	(17.8)	100	NA
LS-1	10×10	69	25	0.1	4.4	469	222	NA	(23.1)	100	(320)

Data compiled from [44,109,155-156,213,224,304,335,342]. The coolant initial temperature was 353 K for FK-10 and 358 K for FK-12. All other tests were initiated from room temperature.

NA: Data are not available. **TCO:** Cladding outer surface temperature. Indicated hoop strains are residual (non-elastic) strains. For failed rods, fission gas release was evaluated from test capsule gas analyses with low accuracy. These results are given in brackets. For failed rods, the peak TCO (in brackets) pertains to the temperature at time of cladding failure.

A.5.2.2 FK rods

As shown in Table A.7, a total of eleven BWR rods in the FK series have been subjected to RIA simulation tests in the NSRR (FK-11 was not an RIA test). For these rods, the peak fuel enthalpies ranged from 293 to 607 J(gUO₂)⁻¹ and the average oxide layer thickness were below 30 μm [109]. The Zircaloy-2 cladding tubes had a 90 μm thick zirconium liner at the cladding inner surface. Upon re-fabrication, the test rods were back-filled to pressures ranging between 0.1 and 1.5 MPa. Rods FK-1 to FK-4 were back-filled with pure helium, whereas the other rods in the FK test series were filled with a mixture of He and Ar, to simulate end-of-life gap gas composition. It should also be remarked that FK-10 and FK-12 were tested at higher initial coolant temperature than normally used in the NSRR: the initial temperature was 353 K for FK-10 and 358 K for FK-12. All other tests in the FK series were initiated from room temperature, which is the standard procedure in the NSRR RIA simulation tests. The rods FK-10 and FK-12 also differed from other rods by having strain gauges attached to the cladding surface, which allowed on-line measurements of cladding hoop strain under the tests [224].

Five rods, FK-6, FK-7, FK-9 FK-10 and FK-12, failed during the power excursion at fuel enthalpies between 260 and 360 J(gUO₂)⁻¹ (see Table A.7). No differences in failure mode between rods tested at high coolant temperature (FK-10, FK-12) and those tested at room temperature were observed. A summary of clad strain and fission gas release data is presented in Table A.7. Clad residual deformation was observed in three of the rods, for which the measured peak residual hoop strain ranged from 0.8 to 1.5%. Transient fission gas release, determined by rod puncturing for non-failed rods and capsule gas analyses for failed rods, varied between 3.1 and 17.8%.

Destructive examination of the fuel pellets in rod FK-4, as in the TS series, showed the occurrence of numerous small radial cracks in the outer periphery, which extended inward to about 3/4 of the pellet radius [154,312]. Moreover, circumferential cracks were observed in the FK-4 pellets. All the failed rods in the FK test series had large crack openings or breaks in the cladding, and all of the fuel pellets were finely fragmented and dispersed into the capsule water.

According to Nakamura *et al.* [156], in the test rods FK-6 through FK-9 with a burn-up of $61 \text{ MWd}(\text{kgU})^{-1}$, extensive bonding between the Zr-liner and the fuel pellets had occurred, and the pellet-to-clad gap was completely closed before the pulse irradiation. The results of these tests indicate intense PCMI loading of the cladding due to the bonding.

A.5.2.3 LS-1 test rod

The LS-1 test rod was sampled from a parent rod of 10×10 assembly design, which had been pre-irradiated in the Leibstadt BWR, Switzerland. The rod had Zircaloy-2 cladding with Zr liner, and the fuel pellets were enriched to 4.5 wt% ^{235}U . The sampled rodlet had a fuel burn-up of $69 \text{ MWd}(\text{kgU})^{-1}$, and a cladding oxide thickness and hydrogen content of 25 μm and 300 wppm, respectively [304,342].

LS-1 was pulse irradiated to a peak fuel enthalpy of $469 \text{ J}(\text{gUO}_2)^{-1}$. The test was conducted with the coolant initially at ambient conditions (290 K, 0.1 MPa). The rod failed by an axial split along the entire fuelled section of the rodlet, at a fuel pellet radial average enthalpy of $222 \text{ J}(\text{gUO}_2)^{-1}$. The failure generated mechanical energy in the surrounding coolant, and when the test capsule was opened after the test, all pellets were fragmented and found in the coolant [304,335,342].

A.5.3 Tests on MOX fuel rods

Nine RIA simulation tests on pre-irradiated MOX fuel rods have to date been carried out in the NSRR, and seven of the rods have survived the tests (see Table A.8). The rods were of ATR, PWR and BWR design.

A.5.3.1 ATR rods

Six of the MOX test rods were re-fabricated from mother fuel rods, which had been irradiated in the prototype Advanced Thermal Reactor (ATR) in Fugen, Japan, to burn-ups in the range of 20 to $30 \text{ MWd}(\text{kgHM})^{-1}$. The fuel rods to this reactor had larger diameter (14.5 mm) than standard LWR fuel, and they were charged with fuel pellets that contained 2.98 wt% fissile plutonium (^{239}Pu and ^{241}Pu) [45]. The cladding material was Zircaloy-2, without inner surface liner.

Very little data have been published in open literature on ATR-5 and ATR-6, but the other ATR tests have been reported in detail by Sasajima *et al.* [45]. Data from the rod in-pile instrumentation indicated that pellet-clad mechanical interaction and subsequent boiling crisis occurred in ATR-3 and ATR-4, whereas ATR-1 and ATR-2 showed no signs of PCMI or film boiling under the tests. This explains the large difference in clad hoop residual strain and transient fission gas release between these two groups of rods (see Table A.8). Sasajima and co-workers also compared the MOX fuel rod behaviour under RIA tests with the behaviour of UO_2 fuel rods, more precisely the BWR fuel rods in the FK test series. They concluded that cladding deformations and fission gas release in ATR-3 and ATR-4 were much more significant than in FK test rods with comparable peak fuel enthalpy.

A.5.3.2 BZ rods

The rodlets for the BZ-1 and BZ-2 tests were re-fabricated from PWR MOX fuel rods of 14×14 assembly design, which had been irradiated in the Beznau PWR, Switzerland [304]. Both rods had

Zircaloy-4 cladding, and were charged with MOX fuels of comparable chemical compositions [343]. However, the burn-up and the manufacturing process of the fuel pellets differed between the rods. The BZ-1 test rod was charged with fuel produced with the short binderless route (SBR) process. The local burn-up was 48 MWd(kgHM)⁻¹, and the cladding oxide thickness and hydrogen content were about 30 µm and 340 wppm, respectively. The BZ-2 rod was fuelled with MOX pellets produced in the Micronised masterblend (MIMAS) process. The local burn-up was 59 MWd(kgHM)⁻¹, and the cladding oxide thickness and hydrogen content were about 20 µm and 160 wppm, respectively.

Both rods were pulse irradiated in the NSRR with the coolant initially at room temperature and atmospheric pressure. Rod BZ-1 reached higher fuel enthalpy than BZ-2 during the test, since it had lower burn-up and thus carried more residual fissile material. The rods failed by PCMI at radial average fuel enthalpies of 318 and 545 Jg⁻¹, respectively; see Table A.8. For both rods, the entire fuel inventory was dispersed into the coolant through long axial cracks in the cladding tube [304,343].

A.5.3.3 DW-1 test rod

The DW-1 test rod was sampled from a BWR mother rod of 8×8 design, which had been irradiated in the Dodewaard BWR, the Netherlands. The MOX fuel pellets were produced with the MIMAS manufacturing process, and the cladding tube was made of Zircaloy-2 with liner [343]. The fuel in the DW-1 test rod was operated to a burn-up of approximately 45 MWd(kgHM)⁻¹, and the cladding tube had an oxide thickness of 4-40 µm.

Table A.8. Summary of NSRR tests on pre-irradiated MOX fuel rods

Test ID	Fuel design	Fuel burn-up [MWd(kgHM) ⁻¹]	Clad oxide thickness [µm]	Fill gas pressure [MPa]	Pulse width [ms]	Peak fuel enthalpy [Jg ⁻¹]	Failure enthalpy [Jg ⁻¹]	Clad max hoop strain [%]	Transient FGR [%]	Fuel loss [%]	Peak TCO [K]
ATR-1	ATR	20	7-15	0.3	6.5	335	Survived	0	1.0	–	355
ATR-2	ATR	20	7-15	0.3	5.2	461	Survived	0	8.8	–	380
ATR-3	ATR	20	7-15	0.3	4.7	502	Survived	1.9	17.7	–	965
ATR-4	ATR	20	7-15	0.3	4.5	586	Survived	3.2	19.9	–	NA
ATR-5	ATR	20	15	0.3	4.4	586	Survived	NA	20.5	–	NA
ATR-6	ATR	30	NA	0.3	4.4	356	Survived	NA	NA	–	NA
BZ-1	PWR	48	30	0.1	4.4	688	318	NA	(14)	100	(300)
BZ-2	PWR	59	20	0.1	4.4	644	545	NA	(26.7)	100	(335)
DW-1	BWR	45	4-40	0.1	4.4	505	Survived	0.55	12.9	–	740

Data compiled from [45,144,335,342-343]

NA: Data are not available. **TCO:** Cladding outer surface temperature. Indicated hoop strains are residual (non-elastic) strains. For failed rods, fission gas release was evaluated from test capsule gas analyses with low accuracy. These results are given in brackets. For failed rods, the peak TCO (in brackets) pertains to the temperature at time of cladding failure.

The DW-1 test rod was pulse irradiated to a peak radial average fuel enthalpy of 505 Jg⁻¹, with the coolant initially at room temperature and atmospheric pressure. The rod survived the test [343]. Although the cladding reached a fairly high temperature during the test, the cladding deformation was moderate; see Table A.8.

A.5.4 Tests on JMTR fuel rods

A total of 22 rodlets have been pre-irradiated in the Japanese Material Test Reactor to rod average burn-ups ranging from 13 to 38 MWd(kgU)⁻¹ and then subjected to RIA simulation tests in the

NSRR. All test rods were short 14×14 PWR type rods, designed for testing in the NSRR. The rodlets were sheathed with standard Zircaloy-4 cladding, and filled with helium to an initial pressure of 0.1 MPa. Results of the NSRR tests on JMTR rods are summarised in Table A.9 below.

Table A.9: Summary of NSRR tests on JMTR rods.

Test ID	Fuel burn-up [MWd(kgU) ⁻¹]	Pulse width [ms]	Peak fuel enthalpy [J(gUO ₂) ⁻¹]	Failure enthalpy [J(gUO ₂) ⁻¹]	Clad max hoop strain [%]	Fuel loss [%]
JM-1	22	9.0	385	Survived	0.1	-
JM-2	27	9.0	352	Survived	0.0	-
JM-3	20	7.8	553	Survived	0.4	-
JM-4	21	5.5	743	743	6.3	0
JM-5	26	5.6	697	682	2.7	0
JM-6	15	7.1	653	Survived	1.0	-
JM-7	13	7.8	611	Survived	0.4	-
JM-8	20	7.2	674	Survived	1.6	-
JM-9	25	6.8	628	Survived	0.7	-
JM-10	21	5.6	837	Survived	7.7	-
JM-11	31	6.3	670	Survived	0.9	-
JM-12	38	5.3	754	653	3.2	0
JM-13	38	6.3	628	Survived	0.7	-
JM-14	38	6.0	670	515	NA	>0
JM-15	31	6.5	586	Survived	3.5	-
JM-16	38	6.4	544	Survived	3.2	-
JMH-1	22	8.3	628	Survived	1.7	-
JMH-2	22	6.8	795	Survived	9.5	-
JMH-3	30	6.2	850	858	NA	>0
JMH-4	30	7.9	628	Survived	3.6	-
JMH-5	30	6.2	910	790	NA	20
JMN-1	22	7.1	628	486	NA	0

All rods were of 14×14 PWR design. Pre-irradiation in the JMTR took place in an un-pressurised, non-oxidizing helium environment, leading to clad oxide layers less than 2 µm thick. Indicated hoop strains are residual (non-elastic) strains. Data compiled from [144,153,335,344].

The JMTR tests can be divided into three subgroups: JM series have standard 14×14 rod dimensions with UO₂ fuel of 10 wt% ²³⁵U enrichment, JMH series have 20 wt% ²³⁵U enrichment, and the JMN test rod has 10 wt% ²³⁵U enrichment with a narrow pellet-clad gap. Higher ²³⁵U pellet enrichments in JMTR rods compared to the concentrations used in PWRs allow for higher energy depositions during the tests.

Due to the high enrichment and the fact that pre-irradiation took place in an un-pressurised, non-oxidizing helium environment, the JMTR test rods are not representative for LWR fuel [84]. Moreover, due to moist residual air in the pre-irradiation capsule, zirconium hydride blisters were formed in the cladding. As discussed by Fuketa *et al.* [84], the appearance of the cladding cracks in the failed JMTR test rods suggests a strong influence of the hydride blisters on the failure mode. In some tests, a large number of small cladding perforations could be seen in post-test examinations. For instance, 12 perforations were found for JM-4 and 23 cladding perforations were found for JM-5. Each perforation was caused by fracture of a hydride blister. In tests with higher fuel enthalpies, such as JM-14 and JMH-3, the local perforations were connected into long axial splits of the cladding tube.

A.6 CABRI tests

Fourteen pre-irradiated PWR fuel rods have to date been subjected to RIA simulation tests in the CABRI facility. These tests were carried out in the sodium coolant loop, which is currently being replaced with a pressurised water loop. Four of the tests were done on MOX fuel rods (see Table A.10). A recent summary and interpretation of the twelve tests carried out within the REP-Na program can be found in [86], whereas details of the CIP0-1 and CIP0-2 tests are given in [345]. The tests are summarised in the following, with emphasis placed on the four rods that failed.

A.6.1 Tests on UO_2 fuel rods

All CABRI test rods charged with UO_2 fuel had a ^{235}U enrichment of 4.5 wt%, except for REP-Na2, which had an enrichment of 6.85 wt%. The REP-Na2 rodlet was exceptional not only in its design, but also since it was pre-irradiated in the BR3 test reactor. Rodlet REP-Na3 was pre-irradiated in a commercial PWR as part of a segmented fuel rod. All other rodlets were re-fabricated from full-length PWR fuel rods that had been operated in commercial PWRs.

The UO_2 rodlets tested in CABRI experienced radial average peak fuel enthalpies ranging from 343 to 832 $\text{J}(\text{gUO}_2)^{-1}$ during the RIA simulations. Three of the ten UO_2 rodlets failed the tests, and the failure enthalpies varied between 117 and 338 $\text{J}(\text{gUO}_2)^{-1}$. Test rod REP-Na1, with a burn-up of 64 $\text{MWd}(\text{kgU})^{-1}$, failed in the range of 117 to 150 $\text{J}(\text{gUO}_2)^{-1}$. Since this failure enthalpy is significantly lower than recorded in other RIA simulation tests, the validity of the test is a matter of discussion. An international team of experts that was recently formed to settle the discussion failed to reach a consensus [86,346]. The cladding of rodlet REP-Na1 had spalled oxide and a strongly non-uniform hydride distribution prior to the RIA simulation tests in CABRI.

Table A.10. Summary of CABRI tests on PWR fuel rods. Data compiled from [86,204,345,347]

Test ID	Fuel type	Clad tube material	Fuel burn-up $[\text{MWd}(\text{kgHM})^{-1}]$	Clad oxide thickness $[\mu\text{m}]$	Fill gas pressure $[\text{MPa}]$	Pulse width $[\text{ms}]$	Peak fuel enthalpy $[\text{Jg}^{-1}]$	Failure enthalpy $[\text{Jg}^{-1}]$	Clad max hoop strain $[\%]$	Transient FGR $[\%]$	Fuel loss $[\%]$
REP-Na1	UO_2	Zr-4	64	100, spalled	0.1	9.5	481	117-150	-	-	2
REP-Na2	UO_2	BR3	33	10	0.1	9.6	832	Survived	3.5	5.5	-
REP-Na3	UO_2	Low-Sn Zr-4	54	35-60	0.3	9.5	516	Survived	2.2	13.7	-
REP-Na4	UO_2	Zr-4	62	60-80	0.3	76	364	Survived	0.4	8.3	-
REP-Na5	UO_2	Zr-4	64	15-25	0.3	8.8	451	Survived	1.1	15.1	-
REP-Na6	MOX	Zr-4	47	35	0.3	32	556	Survived	2.6	21.3	-
REP-Na7	MOX	Zr-4	55	50	0.3	40	577	473	-	-	6
REP-Na8	UO_2	Zr-4	60	126, spalled	0.3	75	410	184-326	-	-	0
REP-Na9	MOX	Low-Sn Zr-4	28	10	0.3	33	824	Survived	7.2	33.0	-
REP-Na10	UO_2	Zr-4	63	100, spalled	0.3	31	410	338	-	-	0
REP-Na11	UO_2	M5	60	15-25	0.3	31	385	Survived	0.4	6.8	-
REP-Na12	MOX	Zr-4	65	60-70	0.3	63	431	Survived	1.1	20.5	-
CIP0-1	UO_2	ZIRLO	75	50-100	0.3	32	389	Survived	0.5	15.0	-
CIP0-2	UO_2	M5	76	15-25	0.3	28	343	Survived	0.3	NA	-

NA: Data are not available. **Zr-4**: Standard Zircaloy-4, Zr-1.5Sn-0.2Fe-0.1Cr by wt%.

BR3: Cladding used for BR3 test reactor fuel rods (standard Zircaloy-4 manufactured by Mannesmann, Germany)

Low-Sn Zr-4: Low-tin Zircaloy-4, Zr-1.3Sn-0.2Fe-0.1Cr by wt%. **M5**: Trademark of Framatome ANP, Zr-1.0Nb-0.13O by wt%.

ZIRLO: Trademark of the Westinghouse Electric Company, Zr-1.0Nb-1.0Sn-0.1Fe by wt%.

The REP-Na8 test was performed on a rodlet with standard Zircaloy-4 cladding and a burn-up of 60 $\text{MWd}(\text{kgU})^{-1}$. The cladding was severely oxidized (locally spalled) and hydrided. The power pulse applied in the RIA test was 75 ms wide, and loss of cladding integrity was detected at a fuel enthalpy of 326 $\text{J}(\text{gUO}_2)^{-1}$. However, acoustic emissions from the rodlet indicated possible initiation of failure

in a hydride blister, without loss of cladding integrity, already at an enthalpy of $184 \text{ J(gUO}_2\text{)}^{-1}$. The blister is shown in Figure 53 (p. 119). Post-test examination of REP-Na8 revealed long axial cracks, which initiated in the heavily hydrided region of the clad outer rim and then propagated radially through the cladding wall. According to Waeckel *et al.* [348], the cracks had propagated axially and opened during the cool-down phase of the test, due to residual thermal stresses in the cladding. Later studies suggest that the post-test crack propagation observed for failed rodlets in CABRI is due to sodium ingress rather than residual thermal stresses [86]. Sodium oxidation leads to fuel swelling under post-test storage of the failed rodlets, which results in further axial crack growth and tangential crack opening after the tests.

Test REP-Na10 was done on a rodlet with a burn-up of 63 MWd(kgU)^{-1} . The rod was taken from the same fuel assembly as rod REP-Na1, and consequently, it had the same pre-irradiation power history. The state of the cladding was similar to that of REP-Na1, i.e. it had spalled oxide and a strongly non-uniform hydride distribution. The REP-Na10 rodlet was subjected to a 31 ms power pulse, and reached a peak fuel enthalpy of $410 \text{ J(gUO}_2\text{)}^{-1}$. The cladding failed at $338 \text{ J(gUO}_2\text{)}^{-1}$ with no fuel dispersal. Examination of the rod directly after the test showed only one small crack, about 70 mm long, located in the peak power region of the rod. This crack grew by about 150 mm during 20 months of post-test storage [86].

In summary, the UO_2 rodlets that have failed the tests in CABRI are distinguished by their severely corroded cladding with spalled oxide layer. Because of the spalled oxide and the non-uniform temperature distribution that results from it, the cladding tubes comprised densely hydrided regions and hydride blisters, which reduced the strength and ductility of the material. Large hydride blisters were found in all test rods with spalled oxide layers [86]. The detrimental effect of oxide spallation on cladding ductility is evident in the CABRI tests, since all rodlets with uniform cladding oxide survived.

While there is disagreement among experts as to the validity of test REP-Na1, the validity of other tests in the REP-Na series seems widely accepted. A technical advisory group of the international CABRI project has recently summarised the main conclusions from the REP-Na tests on UO_2 fuel rods, excluding the controversial REP-Na1 test. These conclusions, which are here reproduced in exact wording from reference [349], represent a consensus position of the CABRI project members:

RIA criteria

- The failures at low enthalpy level ($\leq 80 \text{ cal/g}$) obtained with REP Na UO_2 rods having hydride concentrations (“blisters”) in the cladding due to in-reactor oxide spalling, together with other evidence, revealed the need for evolution of the current safety criteria.

Physical understanding

- The cladding corrosion and associated hydrogen absorption, aggravated by oxide spalling and hydride concentrations (with their specific distribution and orientation), are the main parameters leading to loss of ductility of the cladding and to increased risk of rod failure. However, in the REP Na UO_2 tests, the fuel rods having a corrosion thickness up to $80 \mu\text{m}$ without initial oxide spalling, exhibited ductility enough to prevent cladding failure under pellet-clad mechanical interaction (PCMI) loading for energy injections up to 100 cal/g , in the investigated burn-up range (up to 64 GWd/t).
- PCMI loading occurs during the phase of fast energy injection and is mainly due to fuel thermal expansion (below 100 cal/g radially averaged fuel enthalpy) in the investigated burn-up range (up to 64 GWd/t).

- The failure mechanism of all the REP Na UO₂ test rods was the cladding embrittlement due to in-reactor oxide spalling and hydride blister formation. The embrittled cladding was not able to sustain the increasing PCMI mechanical loading (for instance, in test REP Na8, microphone signals started at an average fuel enthalpy of 44 cal/g at the peak power node in the zone where a very deep hydride blister was located, and loss of rod tightness occurred at 78 cal/g).
- Due to fast power transients, the fuel micro-structure undergoes significant changes linked to fission gas inventory (and thus to burn-up level) and to temperature gradient: fuel fragmentation and grain boundary separation as a result of high overpressure developed in inter-granular bubbles and large pores in high burn-up fuel; grain boundary gas expansion is however limited during PCMI with sodium cooling (high clad strength linked to limited temperature increase).
- Fission gas release due to RIA transient is significant and increases with burn-up and enthalpy level.
- The major part of the fission gas release comes from the grain boundary gases (due to fuel fragmentation, grain boundary opening and fuel permeability evolution) and is correlated to free volume evolution and cladding strain (higher strain, higher fission gas release); however, fission gas release timing and kinetics are not yet precisely known.
- Under high energy injection (maximum radially averaged enthalpy above 110 cal/g), intra-granular fission gas contributes to cladding straining, depending on cladding temperature and swelling kinetics.
- Helium release up to 30% of the total fission gas release has been measured and needs to be better understood.
- Transient oxide spalling has been observed in some of the REP Na UO₂ tests, for cladding corrosion thicknesses exceeding 30-40 µm. The detailed mechanism of such a phenomenon is not well understood.
- In the REP Na UO₂ test series, due to the limited number of failed rods, it is not possible to clearly assess the conditions leading to fuel ejection after failure; however, other results suggest that fuel ejection is promoted when significant energy is injected after loss of rod tightness. Such conclusion is supported by the REP Na UO₂ failed rods.

Analyses about pulse width effects indicate the following:

- Under fast pulses (10 ms), higher fuel temperatures are reached in the periphery, in relation with the radial power profile of irradiated fuel and due to nearly adiabatic heat-up; PCMI is thus stronger and applies to a cladding, which is still at low temperature, with increased risk of rod failure if the cladding is brittle.
- Under fast pulses the extension of the fuel fragmented zone is greater (linked to higher fuel temperature) and the driving force (gas pressure) for post-failure ejection of fine fuel particles is more likely.
- Further data will be obtained to confirm those points.

Considerations for rods behaviour under pressurised water conditions:

- If transient oxide spalling is to occur under pressurised water conditions, it may affect the cladding to coolant heat transfer and thus lead to early boiling crisis.

- Due to higher cladding temperature than in the REP Na tests, especially if boiling crisis is reached, fission gas induced fuel swelling linked to grain boundary gas expansion is expected to contribute to cladding loading.
- Helium release is to be considered when pressure clad loading is at work (after boiling crisis, MOX fuel).

Recommendations

- The mechanism of transient oxide spalling should be clarified.
- The impact of pulse width, the rod behaviour after boiling crisis (in particular fuel swelling), and the post-failure events need to be investigated; some specific tests in the CIP program will address these points

Finally, a comment should be made on the CIP0-1 and CIP0-2 tests [345]. As shown in Table A.10, these are the rods with highest fuel burn-up that have hitherto been tested in CABRI. Notwithstanding their high burn-up, the rods survived fairly high energy depositions. This suggests that high burn-up effects, such as the re-structuring of UO_2 at the pellet rim, would have very little impact on the propensity for PCMI-induced fuel rod failure. The same conclusion was drawn from the VA-1 and VA-2 tests in the NSRR (see Section A.5.1).

A.6.2 Tests on MOX fuel rods

The MOX fuel rods tested in CABRI had fuel pellets of MIMAS AUC (ammonium uranocarbonate) type. This fuel is produced by blending plutonium-rich particles, formed by a mixture of 25-30% PuO_2 and 70-75% UO_2 powders, into a matrix of depleted UO_2 . The fuel pellet average enrichment of Pu was 5.89-6.56 wt% in the tested rodlets.

The failure at a fuel enthalpy of 473 J(gMOX)^{-1} of the REP-Na7 MOX rodlet, which had a burn-up of $55 \text{ MWd(kgHM)}^{-1}$, cannot be attributed to clad oxide layer spallation and/or excessive hydriding. The oxide layer thickness was around $50 \mu\text{m}$, with no sign of spallation prior to the pulse reactor test. It has therefore been suggested that the failure of REP-Na7 was caused by additional loading from transient gaseous swelling of the MOX fuel [95] or by rapid fission gas release [86]. Gaseous swelling would aggravate the PCMI, and fission gas release would lead to a combined loading by PCMI and gas overpressure. In either case, the additional loading would be specific to MOX fuel [86].

Appendix B

OVERVIEW OF COMPUTER CODES

This appendix provides a brief overview of state-of-the-art computer codes used for analysis of light water reactor fuel behaviour under reactivity-initiated accidents. The overview covers codes for lattice physics calculations, three-dimensional core-wide neutron kinetics and thermal-hydraulic analyses, and thermo-mechanical analyses of individual fuel rods. The list of codes is not exhaustive. Precedence is given to modern and internationally known codes that have a wide user community.

B.1 Lattice physics codes

B.1.1 APOLLO2

APOLLO2 is a French lattice physics code, which is developed and maintained by the Commissariat à l'Énergie Atomique [309]. The first version of the code, presented in 1987, was developed by the CEA alone. Later, the French utility *Électricité de France* and the reactor constructor Areva-Framatome have joined the CEA in financial support for the code development. These organisations use APOLLO2 for a wide range of applications [350]. The code is two-dimensional in nature, and applicable to fuel assemblies of all kinds of thermal reactors (PWR, BWR, VVER, HTR, CANDU, RBMK). APOLLO2 is part of the SAPHYR code system for reactor transient analyses, together with CRONOS2 and FLICA4 for core-wide neutron kinetics and thermal-hydraulic calculations (see Sections B.2.2 and B.3.2, respectively).

B.1.2 CASMO-4

CASMO-4 is a widely used two-dimensional neutron transport code, which is developed and maintained by Studsvik [310]. The code is applicable to BWR and PWR fuel assemblies with fuel rods arranged in a square pitch. It solves the multi-group neutron transport equations either for a single fuel assembly or for a set of 2×2 assemblies. CASMO-4 is tightly linked to the Studsvik SIMULATE-3K neutron kinetics code (see Section B.2.5).

B.1.3 HELIOS

HELIOS is another two-dimensional multi-group neutron transport code developed by Studsvik. In comparison with CASMO-4, HELIOS provides more flexibility in the geometrical modelling, and the code can be applied to geometries ranging from single fuel rods up to multiple fuel assemblies and even small reactor cores [311]. It is applicable to fuel assemblies of all kinds of thermal reactors (PWR, BWR, VVER, HTR, CANDU, RBMK).

B.1.4 TransLAT

The TransLAT lattice physics code is part of the TransFX software system for three-dimensional particle transport calculations, developed and maintained by Transware Enterprises Inc. [312]. The code offers a flexible and fully arbitrary one-, two- and three-dimensional geometry modelling capability.

B.1.5 WIMS9

The WIMS9 code is a three-dimensional lattice physics code provided by Serco Assurance (earlier AEA Technology) [313]. The code is applicable to all thermal reactor types, since it can treat a variety of coolants, moderators and fuel assemblies with fuel rods arranged in either square or triangular pitch. Single or multiple fuel assemblies, or even full reactor cores, can be analysed. WIMS has a very long history, and the code is used in different versions by organisations worldwide.

B.2 Codes for core-wide three-dimensional neutron kinetics calculations

B.2.1 BARS

The three-dimensional neutron kinetics code BARS is developed at the Russian Research Centre – Kurchatov Institute [316]. In contrast to most other codes for core-wide neutron kinetics analyses, BARS uses a heterogeneous representation of the fuel assemblies. Each fuel rod in an assembly is thereby explicitly represented in the horizontal plane by use of a Green's function approach. The Green's functions are based on diffusion theory, and the calculation of the neutron flux is typically performed with four or five energy groups. In the axial direction, a harmonic expansion is used to represent the flux. Although each fuel rod is represented explicitly in the neutronics calculations, the fuel temperature for each rod is based on an assembly-average calculation.

B.2.2 CRONOS2

CRONOS2 is a modular three-dimensional neutronics code, which solves the equations for time dependent or static diffusion or transport of neutrons, in two or three dimensions, in a reactor core. Several methods are available for diffusion calculations: the finite element method, finite differences with acceleration by coarse mesh, and nodal methods. The transport calculations are either done by use of the Sn method (integral differential equation) with even parity flux or with the simplified Pn (SPn) method [317]. The code can either use homogenized fuel assemblies or represent every fuel rod in the assembly explicitly. Thermal-hydraulic feedback effects can be accounted for either by use of a one-dimensional internal model, or by coupling with the tree-dimensional code FLICA4 (see Section B.3.2). The thermal-hydraulic calculations are usually done with assembly-wide flowchannels, although the code allows the use of several subchannels per fuel assembly.

B.2.3 DYN3D

DYN3D is a neutron diffusion code for three-dimensional simulations of steady-state operation and transients in LWR cores with quadratic or hexagonal fuel assemblies [318], which means that it is applicable to PWR, BWR and VVER cores. For hexagonal fuel assemblies, each assembly constitutes a node in the horizontal plane, but quadratic assemblies can, if needed, be subdivided into finer nodes. The neutron diffusion equation is solved with two energy groups, utilising the nodal expansion method. The thermal-hydraulic model in DYN3D is one-dimensional and considers four equations for the two-phase flow, representing the balance of mass, momentum and energy of the two-phase mixture, and the mass balance of the vapour phase. DYN3D is developed and maintained by Forschungszentrum Rossendorf, Germany, and it can be linked to the German thermal-hydraulic code ATHLET, either by external or internal coupling (see Figure 58). Internal coupling with RELAP5 is also possible (see Section B.3).

B.2.4 PARCS

The Purdue Advanced Reactor Core Simulator – PARCS – is a three-dimensional reactor core neutronics simulator for both steady-state conditions and transients, maintained by Purdue University,

USA [319]. The code is applicable to PWR and BWR cores loaded with either square or hexagonal fuel assemblies. Several methods are available for solution of the neutron transport equation or the SP3 neutron transport equations; the solution method and the number of considered neutron energy groups depend on the geometry under study [351]. The development of PARCS is supported by the US NRC, which uses the code for best-estimate core neutronics calculations. PARCS can be run in stand-alone mode or coupled to either of the US NRC thermal-hydraulic codes TRACE and RELAP [352] (see Section B.3).

B.2.5 SIMULATE-3K

SIMULATE-3K, also known as S3K, is a three-dimensional two-group neutron diffusion code for core-wide transient analyses of PWRs and BWRs [320]. The last letter (K) of the name alludes to “kinetic”, and the code has a sibling for steady-state analyses, named SIMULATE-3. Both codes are provided by Studsvik. SIMULATE-3K solves the time-dependent two-group neutron diffusion equation by use of the nodal expansion methods. The code has a built-in one-dimensional thermal-hydraulic model, which uses one flow channel per fuel assembly. Simulation of ex-core primary system components is also possible in the thermo-hydraulic model, but if needed, the code can be coupled to the thermal-hydraulic codes RELAP5 and RETRAN.

B.3 Codes for thermal-hydraulic calculations

B.3.1 ATHLET

ATHLET – Analysis of Thermal-Hydraulics of LEaks and Transients – is a code for thermal-hydraulic system analysis, developed and maintained by *Gesellschaft für Anlagen- und Reaktorsicherheit* (GRS) in Germany [324], and used by numerous European institutions. The code is intended for thermal-hydraulic analyses of a wide spectrum of events in LWRs, from anticipated operational transients to design basis accidents. It has a modular structure, and can be coupled to the DYN3D neutron kinetics code, either externally or internally. ATHLET offers the possibility to choose between various hydrodynamic models for the two-phase fluid. The standard option in the current version of the code is a five-equation model, with separate balance equations for liquid and vapour mass and energy, and a common equation for the momentum.

B.3.2 FLICA4

FLICA4 is a modular three-dimensional thermal-hydraulics code for compressible two-phase flow, developed by the CEA, France [325]. The code is intended specifically for steady-state and transient reactor core thermal-hydraulics. The two-phase fluid is described by four balance equations: mass, energy and momentum for the two-phase mixture, and a separate balance equation for the vapour phase mass. FLICA4 has a “zooming” feature, which allows refinement of the spatial discretization in parts of the computational domain. This is achieved by coupling two calculations, one on the full domain with a coarse mesh, and one in the area of interest with a finer mesh. Results from the coarse mesh calculation are thereby used as boundary conditions to the fine mesh domain.

B.3.3 RELAP5

The RELAP – Reactor Excursion and Leak Analysis Program – is probably the most widely used computer code for LWR transient thermal-hydraulic system analyses [326]. The code is developed and maintained by the Idaho National Laboratory (INL) under the auspices of the US NRC. However, active maintenance will be gradually phased out, as RELAP5 will be succeeded by the TRACE code; see the following subsection. The hydrodynamic model in RELAP5 considers one-dimensional flow of a two-

phase fluid by solving six balance equations for mass, energy and momentum of the two phases. Fictitious three-dimensional modelling is possible by prescribing cross-junctions between parallel flowchannels.

B.3.4 TRACE

TRACE is an acronym for TRAC/RELAP Advanced Computational Engine. TRACE has recently been developed on the initiative of the US NRC [327], with the aim to consolidate and extend the capabilities of four different thermal-hydraulic system codes at the US NRC: TRAC-P, TRAC-B, RAMONA and RELAP5. These codes will be gradually phased out and replaced by TRACE, when the latter has been sufficiently validated. To conserve the investments in input models, and also to ease the code transition, TRACE will accept input formats for RELAP, TRAC-P and TRAC-B. As mentioned in Section B.2.4, TRACE has a three-dimensional thermal-hydraulic model for the reactor core, which can be linked to the PARCS three-dimensional neutron kinetics code by internal coupling [352]. Moreover, the code is intended for system analyses of future (Generation IV) nuclear reactors with other coolants than water, such as helium, carbon dioxide or liquid metals.

B.4 Codes for fuel rod analysis

B.4.1 FALCON

FALCON is a light water reactor fuel rod analysis program, developed under the auspices of the Electric Power Research Institute in the United States [353]. Outside EPRI, the program is currently in use by three research organisations worldwide, a few nuclear power utilities, and the ANATECH Corporation, who developed the code for EPRI. The program originates from the ESCORE and FREY codes, which were earlier used by EPRI for modelling fuel rod performance under steady-state operation and transients, respectively. These two codes have been merged into FALCON, which is applicable to a wide range of fuel operating regimes, from normal steady-state operation to severe transients [354].

FALCON comprises best-estimate models for the involved physical phenomena, and uses a two-dimensional finite element method to solve the coupled equations of heat conduction and mechanical equilibrium. The fuel rod can be modelled in either axisymmetric or cross-sectional ($r\theta$ -plane) geometry. Pellet-clad mechanical interaction can in both geometries be modelled with the Amontons-Coulomb law of friction for the tangential contact forces; most other fuel performance codes are restricted to either complete slipping ($\mu=0$) or complete sticking ($\mu=\infty$) between fuel and cladding.

The deformation mechanisms considered for the cladding are thermoelasticity, plasticity, creep and irradiation growth, whereas the fuel pellets are assumed to deform by thermal expansion, elastoplasticity, cracking and creep. Fuel swelling induced by solid and gaseous fission products is also considered. To the authors' knowledge, the gaseous swelling model is not applicable to fast transients, such as RIAs, and it does not consider the high-burn-up re-structured fuel material at the pellet rim. A semi-empirical model for burst release of fission product gases, caused by grain boundary decohesion, is also available in FALCON. This model is intended particularly for analyses of MOX fuel under RIAs.

The cladding failure criterion for RIA in FALCON is based on the concept of a critical strain energy density, meaning that failure is assumed as soon as the strain energy density (SED) in the material reaches a critical value [182]. The critical strain energy density (CSED) is a measure of clad ductility. In FALCON, the CSED is correlated to cladding oxide thickness and pre-transient temperature, and the correlation is based on mechanical property tests performed on irradiated Zircaloy-4 cladding [182]. It should be remarked that the CSED is not a true material property. In similarity with total elongation, i.e. the plastic strain to failure, the CSED depends on the stress state

and loading path up to failure. The CSED applied in clad tube failure criteria should therefore be determined from tests performed with similar biaxial stress state as expected under RIA (see Section 6.2.5.1, p. 106). The correlation for CSED used in FALCON has been determined from clad tube burst tests, ring tension tests and uniaxial tensile tests, using penalty factors to compensate for the non-prototypical stress states in the tests. A critical review of FALCON's criterion for cladding failure under RIAs can be found elsewhere [355].

B.4.2 FRAPTRAN

FRAPTRAN is a computer code for analysing the thermomechanical behaviour of LWR fuel rods under transients and accidents, such as LOCAs and RIAs [356]. The code originates from FRAP-T6, a fuel rod code for transient thermomechanical analysis from the 1970s. In comparison with its ancestor, FRAPTRAN has extended capability for modelling high-burn-up fuel rods. The code is based on best-estimate models, but comprises some conservative optional models, intended for licensing analyses.

FRAPTRAN is closely linked to FRAPCON-3, which is a fuel performance code for analysis of steady-state operating conditions [357]. The necessary initial conditions for a transient analysis with FRAPTRAN can be generated with FRAPCON-3, whereby data for a selected burn-up step are streamlined from the output deck of FRAPCON-3 to the input deck of FRAPTRAN. Both codes have been developed for the US NRC, and they are maintained by the Pacific Northwest National Laboratory (PNNL) in the United States. The codes are used worldwide, and the user community contributes to the development and testing of new models.

FRAPTRAN uses an axisymmetric representation of the fuel rod geometry, but a model accounting for local non-axisymmetric cladding deformation (ballooning) can be used in analyses of LOCA. The code is one-dimensional in nature, and governing equations are solved with respect to the radial coordinate direction in a number of disjointed axial segments. Interaction between the axial segments of the rod is confined to calculations of coolant axial flow and rod internal gas pressure.

In contrast to the other fuel rod analysis codes in our review, FRAPTRAN uses a thin shell model for the cladding. The temperature, material properties, stresses and strains are thus assumed to be uniform across the cladding thickness. This is a definite drawback in analyses of RIAs, in which large radial gradients in temperature and stress arise in the cladding [215].

The pellets are assumed to deform only by thermal expansion under the transient [262], whereas the cladding is assumed to deform by thermoelasticity, plasticity and creep. Pellet-clad mechanical interaction is treated in each axial segment separately. This local approach is somewhat simplistic, since axial contact forces induced in the cladding are not transferred to axial segments below the region of pellet-clad contact. Moreover, complete sticking is assumed, i.e. axial slip between the contacting pellet and cladding is precluded. FRAPTRAN has no model for transient fission gas release, but it comprises a model for axial flow of gas in the pellet-clad gap. This model is of importance to clad ballooning.

Cladding failure under RIA is predicted by use of a strain-based failure criterion. The calculated plastic strain in the hoop direction is in each time step compared with a threshold value, which is correlated to temperature and hydride content of the cladding material [262]. The failure strain correlation is based on uniform elongation data from burst tests and uniaxial ring tensile tests on irradiated Zircaloy-2 and Zircaloy-4 cladding. This makes the failure criterion conservative, since observed failure strains under RIA fall somewhere between data for uniform elongation and total elongation. The advantage of using uniform elongation as a basis for the failure criterion is that uniform elongation is not much affected by stress state and loading path. It can therefore be viewed as a material property, in contrast to the total elongation.

B.4.3 SCANAIR

The French *Institut de Radioprotection et de Sûreté Nucléaire* initiated the development of the SCANAIR computer code in parallel with the CABRI REP-Na test program on RIA (see Section 5.1.8, p. 69). The code is used by the IRSN and by organisations participating in the CABRI REP-Na and the CABRI International Programs. Hence, in contrast to other fuel rod codes reviewed in this appendix, SCANAIR is specifically designed for analyses of RIAs. It distinguishes itself by having models that link the fission gas behaviour to the fuel pellet deformation [194,358].

SCANAIR uses an axisymmetric representation of the fuel rod geometry, and the code is 1½-dimensional in makeup. All fundamental equations are solved with respect to the radial coordinate direction, treating each axial segment of the rod separately. However, the segments are collectively treated in calculations of coolant axial flow, rod internal gas pressure and transfer of axial forces from pellet-clad mechanical interaction. The axial contact forces are calculated by assuming perfect sticking of the two objects: when pellet and cladding come into contact anywhere along the rod, the code postulates zero relative axial motion between fuel and cladding, not only in the segment where contact occurs, but also in the segments below the contact point.

The fuel pellets are assumed to deform by thermoelasticity, plasticity, transient expansion of gaseous fission products and fuel cracking. Deformations due to fuel densification, creep and solid fission product swelling are not modelled in SCANAIR, since the code is intended for analysis of short-term transients. Yet, a model for transient fuel creep is underway, since experiments indicate that fuel creep is in fact important under RIAs [86]. The cladding tube is assumed to deform by thermoelasticity and plasticity, but transient creep is neglected. The equations of mechanical equilibrium are discretized in the radial direction and solved by use of a finite element method, both for the fuel pellet and the cladding tube. Hence, the cladding tube can be divided into several annuli, and the variation of temperature, hydrogen concentration and material properties across the cladding thickness can be considered in analyses.

SCANAIR has a model for transient fission gas release, but no model for axial flow and mixing of gas in the pellet-clad gap. The fission gas release model does not account for the migration of individual gas atoms in the fuel, since all fission product gases are assumed to be collected in pores and bubbles. Hence, the slow diffusion of gas atoms in the fuel is not modelled, but the transport of intragranular gas bubbles into the grain boundaries and the formation of inter-granular bubbles are modelled. Also the release of inter-granular bubble gas into large pores, through which it can be conveyed to the rod free volume, is considered. Release of fission gas takes place by rupture (overpressurisation) of grain boundaries and/or pores.

A cladding failure criterion to be used in analyses of RIA with SCANAIR has recently been proposed by IRSN [359]. The details of this failure criterion are yet unknown to us, but it seems that elastoplastic fracture mechanics is applied to calculate a critical initial crack length for cladding failure under the considered RIA. Cladding failure is assumed to occur, if there are pre-transient defects or flaws at the cladding outer surface, which are deeper than the calculated critical crack length. Moreover, for corroded cladding tubes, it is assumed that the depth of the surface defects is equal to the thickness of the densely hydrided rim at the cladding outer surface [359].

Other failure criteria for SCANAIR have been proposed by users of the code. The staff of *Centro de Investigaciones Energeticas, Medioambientales y Tecnológicas* (CIEMAT) in Spain formulated a cladding failure criterion based on strain energy density, by making use of mechanical property data for Zircaloy-4 from the PROMETRA program [281]. Moreover, a strain-based failure criterion was formulated and implemented in SCANAIR within the framework of a Swedish assessment of fuel failure

limits for RIA [196,260]. This criterion is based on the results of more than 200 out-of-pile mechanical tests on Zircaloy-2 and Zircaloy-4 cladding.

B.4.4 TRANSURANUS

The TRANSURANUS computer program is intended for thermal and mechanical analyses of LWR fuel rods under normal reactor operation as well as transients [360-361]. In this respect, it is similar to the FALCON code described above. The history of TRANSURANUS and its ancestor URANUS goes back to the early 1970s. Today, the code is developed and maintained by scientists at the European Institute for Transuranium Elements (ITU), Karlsruhe, Germany. It is used by research organisations, industry and nuclear safety authorities in about a dozen European countries [361].

TRANSURANUS uses an axisymmetric representation of the fuel rod geometry, and the discretization of both fuel pellets and cladding is flexible. The cladding tube can be divided into several annuli, and the variation of temperature, hydrogen concentration and material properties across the cladding thickness can be considered in analyses. The governing equations for heat transfer and deformations are solved with respect to the radial co-ordinate in a number of axial segments of the rod. Interaction between the axial segments is confined to calculations of coolant axial flow, rod internal gas pressure and transfer of axial forces from pellet-clad mechanical interaction. The latter are calculated through a fairly advanced model for frictional contact, which makes the handling of fuel rod deformations in TRANSURANUS similar to that in full-fledged two-dimensional codes [329].

Since the time scale of the problems treated by TRANSURANUS may range from milliseconds to years, the code comprises models for both long and short-term deformation mechanisms. Hence, it considers cladding deformations caused by thermoelasticity, plasticity, creep and irradiation-induced growth. Likewise, thermoelasticity, plasticity, creep, densification, cracking, swelling induced by solid and gaseous fission products, and radial relocation of pellet fragments, are considered in calculations of pellet deformations. To the best of our knowledge, the gaseous swelling model is not applicable to very fast power transients, such as RIAs. The code considers the re-structuring of the fuel at high burnup. The increase of porosity at the pellet rim is accounted for in calculations of fuel thermal conductivity and fission gas release, but not in calculations of fuel swelling.

TRANSURANUS has been used for analysis of fuel rod behaviour under reactivity-initiated accidents in BWRs [36], PWRs [362] and VVERs [363], although the code lacks models for phenomena that are specific to RIA. For example, cladding failure criteria for RIA are currently unavailable in TRANSURANUS. However, specific models for analyses of design basis accidents, such as LOCA and RIA, are currently under development [364].

B.4.5 RANNS

RANNS is a computer code for analysing the thermomechanical behaviour of LWR fuel rods under transients and accidents, such as LOCAs and RIAs [215,328,332]. The code has been developed by the Japan Atomic Energy Agency, particularly for analyses of data from RIA tests in the NSRR. Its basic structure is common to that of FEMAXI-6, which has been developed by the JAEA for many years as a fuel performance code for analysis of steady-state operating conditions [365]. The two codes are closely linked; the necessary initial conditions for a transient analysis with RANNS can be generated with FEMAXI-6 and fed to RANNS.

In similarity with other codes of this kind, RANNS uses an axisymmetric representation of the fuel rod geometry. The code is one-dimensional in nature, and governing equations are solved with respect to the radial coordinate direction in a number of disjointed axial segments. However, the segments are

collectively treated in calculations of coolant axial flow, rod internal gas pressure and transfer of axial forces from pellet-clad mechanical interaction. The axial contact forces are calculated by assuming frictional sliding of the two objects, with perfect bonding as a special case. Optionally, detailed analyses of local PCMI can be carried out on a single axial segment, corresponding to half a pellet. In this geometry, an axisymmetric two-dimensional finite element model is used for solving the governing equations.

In RANNS, the pellet stack and clad tube consist of several ring elements (annuli), the number of which can be varied by input settings. Consequently, the large radial gradients in temperature and stress that arise in both the pellet and cladding under an RIA can be spatially resolved [215,328,332]. The fuel pellets as well as the clad tube are assumed to deform by thermoelasticity, plasticity and creep under the transient. A model for transient fission gas release due to grain separation is currently under development for analysis of post-DNB fuel behaviour. Cladding failure under RIA is predicted by use of a criterion based on linear elastic fracture mechanics. The criterion, which considers the hoop stress at the tip of an incipient cladding crack, needs verification and extension to failures associated with cladding plastic deformation. Also, RANNS has capability of predicting the cladding behaviour anticipated in LOCAs, such as high temperature steam oxidation and thermal stress generation. Axial stresses induced by quench of the overheated cladding can be evaluated and compared with experimental data.

Appendix C

REFERENCES

1. NEA (2009), *Nuclear Fuel Behaviour in Loss-of-Coolant Accident Conditions*, Report NEA No. 6846, ISBN 978-92-64-99091-3, Nuclear Energy Agency, OECD, Paris, France.
2. McLaughlin, T.P., *et al.*, *A Review of Criticality Accidents – 2000 Revision*, 2000, Report LA-13638, Los Alamos National Laboratory, Los Alamos, NM, USA.
3. Hatfield, G.W., *A Reactor Emergency with Resulting Improvements*, Mechanical Engineering, 1955. 77(2): pp. 124-126.
4. McKeown, W., *Idaho Falls: The Untold Story of America's First Nuclear Accident*. 2003, ECW Press.
5. Glasstone, S. and A. Sesonske, *Nuclear Reactor Engineering*, 3rd Edition (1991), Malabar, FL, USA: Krieger Publishing Company.
6. Bodansky, D., *Nuclear Energy: Principles, Practices and Prospects*. 2nd Edition 2004, New York: Springer AIP Press.
7. *INSAG-7: The Chernobyl Accident – Updating of INSAG-1*, 1992, IAEA Safety Series Report 75-INSAG-7, International Atomic Energy Agency, Austria, Vienna.
8. Vitanza, C. and M. Hrehor, *Review of High Burn-up RIA and LOCA Database and Criteria*, 2006, Report NEA/CSNI/R(2006)5, OECD Nuclear Energy Agency, Committee on the Safety of Nuclear Installations, Paris, France.
9. Nakajima, T. *RIA Criteria in Japan* (2002), *NEA CSNI Topical Meeting on RIA Fuel Safety Criteria*, May 13-15, 2002, Aix-en-Provence, France, NEA/CSNI/R(2003)8/Vol 2, pp. 9-20, OECD Nuclear Energy Agency, Paris, France.
10. Maeder, C. and H. Wand, *Sicherheitskriterien für Reaktivitätsstörfälle in Schweizerischen Kernkraftwerken*, 2004, Report HSK-AN-5208, Swiss Federal Nuclear Safety Inspectorate (HSK), Villigen, Switzerland.
11. US NRC (2007), *Technical and Regulatory Basis for the Reactivity-initiated Accident Interim Acceptance Criteria and Guidance*, ADAMS accession number ML070220400, US Nuclear Regulatory Commission, Washington DC, USA.
12. Clifford, P.M. (2007), *The U.S. Nuclear Regulatory Commission's Strategy for Revising the RIA Acceptance Criteria*, 2007 International LWR Fuel Performance Meeting, San Francisco, CA, USA: American Nuclear Society, pp. 543-545.
13. Hetrick, D.L. (1993), *Dynamics of Nuclear Reactors*, American Nuclear Society.

14. Stacey, W.M. (2001), *Nuclear Reactor Physics*, John Wiley & Sons, Inc., New York, USA.
15. IAEA (1993), *Reactivity Accidents*, Technical Report Series, Report 354, International Atomic Energy Agency, Vienna, Austria.
16. Diamond, D.J., B.P. Bromley, and A.L. Aronson (2002), *Studies of the Rod Ejection Accident in a PWR*, Technical report W-6382, Brookhaven National Laboratory, Upton, NY, USA.
17. Dias, A.F., *et al.*, Realistic Scoping Study of Reactivity Insertion Accidents for Typical PWR and BWR Cores, Nuclear Technology, 1998. 121: pp. 346-358.
18. Heck, C.L., *et al.* (1995), Realistic Evaluation of Reactivity Insertion Accidents in Boiling Water Reactors, CSNI Specialist Meeting on Transient Behaviour of High Burnup Fuel, September 12-14, 1995, Cadarache, France, Nuclear Energy Agency, NEA/CSNI/R(95)22, pp. 377-399.
19. Gomez, A.J., *et al.* (2005), Analysis of a reactivity-initiated accident (RIA) in Confrontes NPP, cold and hot conditions with RETRAN-3D, 2005 Water Reactor Fuel Performance Meeting, October 2-6, 2005, Kyoto, Japan, pp. 767-781.
20. Snell, V.G., *et al.* (1990), *CANDU Safety under Severe Accidents: An Overview*, Nuclear Safety, 31(1): pp. 20-36.
21. Luxat, J.C. and B.W. Spencer (1998), *Insights to the Phenomenology and Energetics of Reactivity-initiated Accidents*, International ENS/ANS Conference on Thermal Reactor Safety (NUCSAFE 88), October 2-7, 1988, Avignon, France, 6, pp. 2241-2250.
22. Jeong, C.J. and H.C. Suk (2006), *The Core Characteristics of a LOCA Power Pulse in a CANDU-6 Reactor with the CANFLEX-RU Fuel*, Nuclear Technology, 154: pp. 215-223.
23. Riverola, J., T. Nunez, and J. Vicente (2004), *RIA Analysis for PWR at both HZP and HFP Operation and All Cycle Fuel Exposure with 3D Techniques*, International Meeting on LWR Fuel Performance, September 19-22, 2004, American Nuclear Society, pp. 640-649, Orlando, FL, USA.
24. In de Betou, J., *et al.* (2004), Assessment of Burn-up-Dependent Fuel Rod Failure Threshold under Reactivity-Initiated Accidents in Light Water Reactors, International Meeting on Light Water Reactor Fuel Performance, September 19-22, 2004, American Nuclear Society, Orlando, FL, USA.
25. Lee, C.B., *et al.* (1995), *Analysis of the Fuel Behaviour under Rod Ejection Accident in the Pressurized Water Reactor*, CSNI Specialist Meeting on Transient Behaviour of High Burn-up Fuel, September 12-14, 1995, Cadarache, France, Nuclear Energy Agency, NEA/CSNI/R(95)22, pp. 279-290.
26. Stelletta, S. and N. Waeckel (1997), *Fuel Failure Risk Assessment under Rod Ejection Accident in PWRs Using the RIA Simulation Tests Database – the French Utility Position*, American Nuclear Society, pp. 721-728, ANS Topical Meeting on Light Water Reactor Fuel Performance, March 2-6, 1997, Portland, OR, USA.
27. Risher, D.H., *et al.* (1997), *Advanced Methods for Analysis of the Reactivity Insertion Accident for Pressurized Water Reactors*, 5th International Conference on Nuclear Engineering (ICONE5), ASME, May 26-30, 1997, Nice, France.
28. Bender, D., *et al.* (1995), *Methodology and Results of RIA Studies at Siemens*, CSNI Specialist Meeting on Transient Behaviour of High Burn-up Fuel, September 12-14, 1995, Cadarache, France, Nuclear Energy Agency, NEA/CSNI/R(95)22, pp. 305-314.

29. Kim, Y.H., C.K. Sung, and C.K. Yang (2008), *Development of System Response Analysis Method for Rod Ejection Accident of OPR1000 and APRI400 Using RETRAN Code*, Journal of Nuclear Science and Technology, 45(1): pp. 52-59.
30. Nakajima, T. (2002), *Realistic analysis of RIA in PWR and BWR*, CSNI Topical Meeting on RIA Fuel Safety Criteria, May 13-15, 2002, Aix-en-Provence, France, Nuclear Energy Agency, NEA/CSNI/R(2003)8/Vol1, pp. 15-32.
31. Cuadra, A. and D.J. Diamond (2005), *BWR Rod Drop Accident Analysis*, Transactions of the American Nuclear Society, 93: pp. 376-377.
32. Nakajima, T., I. Komatsu, and R. Yoshiki (2002), *Three Dimensional Analysis of RIA in PWR and BWR with High Burnup Fuel*, Fuel Safety Research Specialist's Meeting, March 4-5, 2002, Tokai, Japan, Japan Atomic Energy Research Institute, JAERI Conf 2002-009, pp. 163-181.
33. Massih, A.R., S. Persson, and Z. Weiss (1992), *Modelling of (U,Gd)O₂ Fuel Behaviour in Boiling Water Reactors*, Journal of Nuclear Materials, 188: pp. 323-330.
34. Ray, S., *et al.* (1995), *A Best-Estimate Assessment of Rod Ejection Fuel Duty in PWRs*, CSNI Specialist Meeting on Transient Behaviour of High Burnup Fuel, September 12-14, 1995, Cadarache, France, Nuclear Energy Agency, NEA/CSNI/R(95)22, pp. 245-250.
35. Ohta, T., *et al.* (1995), *Analyses of Rod Drop Accidents Using a Three Dimensional Transient Code for Reactivity-Initiated Events of Boiling Water Reactors*, CSNI Specialist Meeting on Transient Behaviour of High Burn-up Fuel, September 12-14, 1995, Cadarache, France, Nuclear Energy Agency, NEA/CSNI/R(95)22, pp. 353-376.
36. Sengstag, T. (2001), *On the Modeling of Reactivity-initiated Accidents in Light Water Reactor Cores Containing High-Burn-up Fuel*, in Thesis No. 2355, Department of Physics, École Polytechnique Fédérale de Lausanne: Lausanne, Switzerland.
37. Lassmann, K., *et al.* (1994), *The Radial Distribution of Plutonium in High Burn-up UO₂ fuels*, Journal of Nuclear Materials, 208: pp. 223-231.
38. Yanagisawa, K., *et al.* (1990), *Behaviour of PCI-Resistant Additive Fuel for BWR under Reactivity-initiated Accident Conditions*, Journal of Nuclear Science and Technology, 27(1): pp. 56-67.
39. Minato, K., *et al.* (2001), *Thermal Conductivity of Irradiated UO₂ and (U,Gd)O₂*. Journal of Nuclear Materials, 288(1): pp. 57-65.
40. Yamanouchi, S., *et al.* (1998), *Melting Temperature of Irradiated UO₂ and UO₂-2wt%Gd₂O₃ Fuel Pellets up to Burn-up of about 30 GWd/tU*, Journal of Nuclear Science and Technology, 25(6): pp. 528-533.
41. Shiozawa, S., *et al.* (1998), *Study on the Behaviour of Gd₂O₃ Fuel Rod Failure under a Reactivity-initiated Accident*, Report JAERI-M-88-084, Japan Atomic Energy Research Institute (JAERI), Tokyo, Japan.
42. IAEA (2003), *Status and advances in MOX fuel technology*, IAEA Technical report series 415, International Atomic Energy Agency, Vienna, Austria.
43. Massih, A.R., *Models for MOX fuel behaviour – A selective review*, 2006, SKI Technical Report 2006:10, Swedish Nuclear Power Inspectorate, Stockholm, Sweden.

44. Fuketa, T., *et al.* (2000), *Behaviour of PWR and BWR fuels during reactivity-initiated accident conditions*, American Nuclear Society, ANS Topical Meeting on Light-Water Reactor Fuel Performance, April 10-13, 2000, Park City, Utah, USA.
45. Sasajima, H., *et al.* (2000), *Behaviour of Irradiated ATR/MOX Fuel under Reactivity-initiated Accidents Conditions*, Journal of Nuclear Science and Technology, 37(5): pp. 455-464.
46. Carmack, W.J., *et al.* (2006), *Inert Matrix Fuel Neutronic, Thermal-Hydraulic, and Transient Behaviour in a Light-Water Reactor*, Journal of Nuclear Materials, 352(1-3): pp. 276-284.
47. Hellwig, C., *et al.* (2006), *Inert Matrix Fuel Behaviour in Test Irradiations*, Journal of Nuclear Materials, 352: pp. 291-299.
48. Nakamura, T., *et al.* (2003), *Morphology Change of Rock-Like Oxide Fuels in Reactivity-Initiated-Accident Simulation Tests*, Journal of Nuclear Materials, 319: pp. 95-101.
49. Nakamura, T., *et al.* (2003), *Behaviour of YSZ Based Rock-Like Oxide Fuels under Simulated RIA Conditions*, Journal of Nuclear Science and Technology, 40(1): pp. 30-38.
50. Matzke, H.(1995), *The Rim-Effect in High Burnup UO₂ Nuclear Fuel*, Ceramics: Charting the Future, World Ceramics Congress, June 28 – July 4, 1995, Florence, Italy, P. Vincenzini, Editor, pp. 2913-2920.
51. Spino, J., K. Vennix, and M. Coquerelle (1996), *Detailed Characterization of the Rim Microstructure in PWR Fuels in the Burn-up Range 40-67 GWd/tM*. Journal of Nuclear Materials, 231: pp. 179-190.
52. Lassmann, K., *et al.* (1995), *Modelling the high burnup UO₂ structure in LWR fuel*, Journal of Nuclear Materials, 226: pp. 1-8.
53. Walker, C.T. (1999), *Assessment of the Radial Extent and Completion of Recrystallization in High Burn-up UO₂ Nuclear Fuel by EPMA*, Journal of Nuclear Materials, 275: pp. 56-62.
54. Une, K., *et al.* (2000), *Effects of grain size and PCI restraint on the rim structure formation of UO₂ fuels*, American Nuclear Society's (ANS) Topical Meeting on Light Water Reactor Fuel Performance, April 10-13, 2000, Park City, Utah, USA.
55. Romano, A., M.I. Horvath, and R. Restani, *Evolution of porosity in the high-burnup fuel structure*. Journal of Nuclear Materials, 2007. 361: pp. 62-68.
56. Une, K., *et al.* (2001), *Rim Structure Formation of Isothermally Irradiated UO₂ Fuel Discs*, Journal of Nuclear Materials, 288: pp. 20-28.
57. Manzel, R. and C.T. Walker (2000), *High burnup fuel microstructure and its effect on fuel rod performance*, ANS Topical Meeting on Light Water Reactor Fuel Performance, April 10-13, 2000, Park City, UT, USA.
58. Tsukuda, Y., *et al.* Performance of advanced fuel materials for high burnup, 2003. In: ENS TopFuel 2003/ANS LWR Fuel Performance Meeting, Marc 16-19, 2003, Wurzburg, Germany: European Nuclear Society.
59. Fink, J.K., *Melting Point Of Uranium Dioxide*, INSC material properties database, International Nuclear Safety Center (INSC), Argonne National Laboratory, USA: Available via internet at www.insc.anl.gov/matprop.

60. Christensen, J.A., R.J. Allio, and A. Biancheria, *Melting Point of Irradiated Uranium Dioxide*. Transactions of the American Nuclear Society, 1964. 7(2): pp. 390-391.
61. Adamson, M.G., E.A. Aitken, and R.W. Caputi, *Experimental and Thermodynamic Evaluation of the Melting Behavior of Irradiated Oxide Fuels*. Journal of Nuclear Materials, 1985. 130: pp. 349-365.
62. Popov, S.G., *et al.*, *Thermophysical Properties of MOX and UO₂ Fuels Including the Effects of Irradiation*, 2000, Report ORNL/TM-2000/351, Oak Ridge National Laboratory, Oak Ridge, TN, USA.
63. Carbajo, J.J., *et al.*, *A Review of the Thermophysical Properties of MOX and UO₂ fuels*. Journal of Nuclear Materials, 2001. 299: pp. 181-198.
64. Komatsu, J., T. Tachibana, and K. Konashi, *The Melting Temperature of Irradiated Oxide Fuel*. Journal of Nuclear Materials, 1988. 154: pp. 38-44.
65. Lucuta, P.G., H. Matzke, and I.J. Hastings, *A Pragmatic Approach to Modelling Thermal Conductivity of Irradiated UO₂ Fuel: Review and Recommendations*. Journal of Nuclear Materials, 1996. 232: pp. 166-180.
66. Jernkvist, L.O. and A.R. Massih, *Analysis of the Effect of UO₂ High Burnup Microstructure on Fission Gas Release*, 2002, Research report 02:56, Swedish Nuclear Power Inspectorate, Stockholm, Sweden.
67. Kinoshita, M., *et al.* High Burnup Rim Project (III): Properties of rim-structured fuel,, 2004. In: 2004 international meeting on light water reactor fuel performance, September 19-22, 2004, Orlando, Florida, USA: American Nuclear Society.
68. Nakamura, T., *et al.*, *Boiling Water Reactor Fuel Behavior under Reactivity-Initiated-Accident Conditions at Burnup of 41 to 45 GWd/tonneU*. Nuclear Technology, 2000. 129: pp. 141-151.
69. Carey, V.P., *Liquid-Vapor Phase-Change Phenomena: An Introduction to the Thermophysics of Vaporization and Condensation Processes in Heat Transfer Equipment*. 2 ed. 2007, Washington, USA: Taylor & Francis.
70. IAEA (2001), *Thermohydraulic Relationships for Advanced Water Cooled Reactors*, IAEA TECDOC-1203, International Atomic Energy Agency, Vienna, Austria.
71. Olander, D.R., *Fundamental Aspects of Nuclear Reactor Fuel Elements*, 1976, TID-26711-P1, National Technical Services, US Department of Commerce, Springfield, VA, USA.
72. Sontheimer, F. and H. Landskron (2000), *Puzzling features of EPMA radial fission gas release profiles: The key to realistic modeling of fission gas release up to ultra high burnup of 100 MWd/kgM with CARO-E*, IAEA Technical Committee Meeting on Nuclear Fuel Behaviour Modeling at High Burnup and its Experimental Support, June 19-23, 2000, Windermere, UK: International Atomic Energy Agency, IAEA-TECDOC-1233.
73. Mogensen, M., J.H. Pearce, and C.T. Walker, *Behaviour of Fission Gas in the Rim Region of High Burn-up UO₂ Fuel Pellets with Particular Reference to Results from an XRF Investigation*. Journal of Nuclear Materials, 1999. 264: pp. 99-112.

74. Noirot, J., *et al.* Fission Gas Inventory in PWR High Burnup Fuel: Experimental Characterization and Modelling, 2004. In: 2004 International Meeting on LWR Fuel Performance, September 19-22, 2004, Orlando, FL, USA: American Nuclear Society.
75. Bernard, L.C., J.L. Jacoud, and P. Vesco, *An Efficient Model for the analysis of Fission Gas Release*. Journal of Nuclear Materials, 2002. 302: pp. 125-134.
76. Une, K., *et al.* (1997), *Effect of irradiation-induced microstructural evolution on high burnup fuel behaviour*, ANS Topical Meeting on Light Water Reactor Fuel Performance, March 2-6, 1997, Portland, OR, USA, pp. 478-489.
77. Lassmann, K., *et al.* (2000), Recent Developments of the TRANSURANUS Code with Emphasis on High Burn-up Phenomena, IAEA-TECDOC-1233, IAEA Technical Committee Meeting on Nuclear Fuel Behaviour Modeling at High Burn-up and its Experimental Support, June 19-23, 2000, Windermere, United Kingdom, International Atomic Energy Agency, Vienna, Austria.
78. Robinson, M.T. (1994), *Basic Physics of Radiation Damage Production*, Journal of Nuclear Materials, 216: pp. 1-28.
79. Schilling, W. and H. Ullmaier (1994), Physics of Radiation Damage in Metals, in Materials Science and Technology – A Comprehensive Treatment, Vol. 10B: Nuclear Materials, B.R.T. Frost, Editor, VCH: Weinheim, Germany.
80. Garde, A.M., G.P. Smith, and R.C. Pirek (1996), *Effects of Hydride Precipitate Localization and Neutron Fluence on the Ductility of Irradiated Zircaloy-4*, Zirconium in the nuclear industry; 11th International Symposium, E.R. Bradley and G.P. Sabol, Editors, American Society for Testing and Materials, ASTM STP-1295, pp. 407-430.
81. Torimaru, T., T. Yasuda, and M. Nakatsuka (1996), *Changes in Mechanical Properties of Irradiated Zircaloy-2 Fuel Cladding due to Short-term Annealing*, Journal of Nuclear Materials, 238: pp. 169-174.
82. Lemaignan, C. and A.T. Motta (1994), Zirconium Alloys in Nuclear Applications, in Materials Science and Technology – A Comprehensive Treatment, Vol 10B: Nuclear Materials, B.R.T. Frost, Editor, VCH: Weinheim, Germany.
83. IAEA (1998), *Waterside corrosion of zirconium alloys in nuclear power plants*, IAEA TECDOC-996, International Atomic Energy Agency, Vienna, Austria.
84. Fuketa, T., *et al.* (1997), Fuel Failure and Fission Gas Release in High Burn-up PWR Fuels under RIA Conditions. Journal of Nuclear Materials, 248: pp. 249-256.
85. Georgenthum, V., J. Desquines, and V. Besson, Influence of outer zirconia transient cracking and spalling on thermomechanical behaviour of high burnup fuel rod submitted to RIA. Journal of Nuclear Science and Technology, 2006. 43(9): pp. 1089-1096.
86. Papin, J., *et al.*, *Summary and interpretation of the CABRI REP-Na program*. Nuclear Technology, 2007. 157: pp. 230-250.
87. Bai, J.B., *Influence of an oxide layer on the hydride embrittlement in Zircaloy-4*. Scripta Metallurgica et Materialia, 1993. 29: pp. 617-622.

88. Berat-Robert, L., *et al.* Influence of a zirconia layer on the mechanical behavior of Zircaloy-4 cladding and thimble tubes, 2000. In: ANS topical meeting on light water reactor fuel performance, April 10-13, 2000, Park City, Utah, USA: American Nuclear Society.
89. Grange, M., *et al.* Combined effects of oxide and hydride on the mechanical behavior of Zircaloy-4, 1997. In: Eight international symposium on environmental degradation of materials in nuclear power systems – water reactors, Amelai Island, FL, USA: American Nuclear Society, 2, pp. 990-996.
90. Kim, J.H., *et al.*, Effects of oxide and hydrogen on the circumferential mechanical properties of Zircaloy-4 cladding. Nuclear Engineering and Design, 2006. 236: pp. 1867-1873.
91. Tomiyasu, K., T. Sugiyama, and T. Fuketa, *Influence of cladding-peripheral hydride on mechanical fuel failure under reactivity-initiated accident conditions*. Journal of Nuclear Science and Technology, 2007. 44(5): pp. 733-742.
92. Pierron, O.N., *et al.*, *The influence of hydride blisters on the fracture of Zircaloy-4*. Journal of Nuclear Materials, 2003. 322: pp. 21-35.
93. Glendening, A., *et al.*, Failure of hydrided Zircaloy-4 under equal-biaxial and plane-strain tensile deformation. Journal of ASTM International, 2005. 2(5).
94. Bessiron, V., *Modelling of clad to coolant heat transfer for RIA applications*. Journal of Nuclear Science and Technology, 2007. 44(2): pp. 211-221.
95. Schmitz, F. and J. Papin, High burnup effects on fuel behaviour under accident conditions: the tests CABRI REP-Na. Journal of Nuclear Materials, 1999. 270: pp. 55-64.
96. Coleman, C.E., *Cracking of hydride-forming metals and alloys*, in *Environmentally assisted failure*, J. Petit and P.M. Scott, Editors. 2003, Elsevier Pergamon: Amsterdam.
97. Une, K. and S. Ishimoto, Dissolution and precipitation behavior of hydrides in Zircaloy-2 and high Fe Zircaloy. Journal of Nuclear Materials, 2003. 322: pp. 66-72.
98. Sawatzky, A., *Hydrogen in Zircaloy-2: Its distribution and heat of transport*. Journal of Nuclear Materials, 1960. 2(4): pp. 321-328.
99. Northwood, D.D. and U. Kosasih, *Hydrides and delayed hydrogen cracking in zirconium and its alloys*. International Metals Reviews, 1983. 28: pp. 92-121.
100. Douglass, D.L., *The metallurgy of zirconium*, 1971, International Atomic Energy Agency, Vienna, Austria.
101. Chung, H.M. and T.F. Kassner, Cladding metallurgy and fracture behavior during reactivity-initiated accidents at high burnup. Nuclear Engineering and Design, 1998. 186: pp. 411-427.
102. Fuketa, T. and T. Fujishiro, Generation of destructive forces during fuel/coolant interactions under severe reactivity-initiated accident conditions. Nuclear Engineering and Design, 1994. 146: pp. 181-194.
103. Bozhko, Y.V., *et al.*, Coefficient of static friction of the uranium dioxide-zirconium alloy pair under irradiation. Atomic Energy, 1991. 71(5): pp. 945-948.

104. Nogita, K. and K. Une, *Formation of pellet-cladding bonding layer in high burnup BWR fuels*. Journal of Nuclear Science and Technology, 1997. 34(7): pp. 679-686.
105. Wesley, D.A., K. Mori, and S. Inoue. *Mark-BEB ramp testing program*, 1994. In: *1994 ANS/ENS international topical meeting on light water reactor fuel performance*, April 17-21, 1994, West Palm Beach, FL, USA: American Nuclear Society, pp. 343-351.
106. Cox, B., Pellet-clad interaction (PCI) failures of zirconium alloy fuel cladding – a review. Journal of Nuclear Materials, 1990. 172: pp. 249-292.
107. Fuketa, T., H. Sasajima, and T. Sugiyama, Behavior of high-burnup PWR fuels with low-tin Zircaloy-4 cladding under reactivity-initiated-accident conditions. Nuclear Technology, 2001. 133: pp. 50-62.
108. Boyack, B.E., *et al.*, Phenomenon identification and ranking tables (PIRTs) for rod ejection accidents in pressurized water reactors containing high burnup fuel, 2001, NUREG/CR-6742, US Nuclear Regulatory Commission, Washington DC, USA.
109. Fuketa, T., F. Nagase, and T. Sugiyama. RIA- and LOCA-simulating experiments on high burnup LWR fuels, 2005. In: IAEA technical meeting on fuel behaviour modelling under normal, transient and accident conditions and high burnups, September 5-8, 2005, Kendal, United Kingdom, International Atomic Energy Agency.
110. Luxat, J.C. and D.R. Novog. A generalized failure map for fuel elements subject to a power pulse, 2007. In: 19th international conference on structural mechanics in reactor technology (SMiRT-19), August 12-17, 2007, Toronto, Canada.
111. Ishikawa, M. and S. Shiozawa, *A study of fuel behaviour under reactivity-initiated accident condition*. Journal of Nuclear Materials, 1980. 95: pp. 1-30.
112. Saito, S., *et al.*, Effects of rod pre-pressurization on light water reactor fuel behavior during reactivity-initiated accident conditions. Journal of Nuclear Science and Technology, 1982. 19(4): pp. 289-306.
113. MacDonald, P., *et al.*, Assessment of light-water reactor fuel damage during a reactivity-initiated accident. Nuclear Safety, 1980. 21(5): pp. 582-602.
114. Berthoud, G., *Vapor explosions*. Annular Review of Fluid Mechanics, 2000. 32: pp. 573-611.
115. Corradini, M.L., B.J. Kim, and M.D. Oh, *Vapor explosions in light water reactors: A review of theory and modelling*. Progress in Nuclear Energy, 1988. 22(1): pp. 1-117.
116. Tsuruta, T., M. Ochiai, and S. Saito, *Fuel fragmentation and mechanical energy conversion ratio at rapid deposition of high energy in LWR fuels*. Journal of Nuclear Science and Technology, 1985. 22(9): pp. 742-754.
117. El-Genk, M.S., R.R. Hobbins, and P.E. MacDonald, *Molten fuel-coolant interaction during a reactivity-initiated accident experiment*. Nuclear Engineering and Design, 1981. 66: pp. 247-267.
118. Sugiyama, T. and T. Fuketa, Mechanical energy generation during high burnup fuel failure under reactivity-initiated accident conditions. Journal of Nuclear Science and Technology, 2000. 37(10): pp. 877-886.

119. Cook, B.A. and Z.R. Martinson, *Reactivity-initiated accident test series, test RIA 1-4 fuel behavior report*, 1984, Report NUREG/CR-3938, US Nuclear Regulatory Commission, Washington DC, USA.
120. Tanzawa, S. and T. Fujishiro, *Effects of waterlogged fuel rod rupture on adjacent fuel rods and channel box under RIA conditions*. Journal of Nuclear Science and Technology, 1987. 24(1): pp. 23-32.
121. Azuma, M., *et al.*, Assessment on integrity of BWR internals against impact load by water hammer under conditions of reactivity-initiated accidents. Nuclear Technology, 2005. 149: pp. 243-252.
122. Cronenberg, A.W., Recent developments in the understanding of the energetic molten fuel-coolant interactions. Nuclear Safety, 1980. 21(3): pp. 319-337.
123. Wilson, R., *et al.*, Report to the American Physical Society of the study group on radionuclide release from severe accidents at nuclear power plants. Reviews of Modern Physics, 1985. 57(3): pp. S1-S144.
124. Soffer, L., *et al.*, *Accident source terms for light-water nuclear power plants*, 1995, Report NUREG-1465, US Nuclear Regulatory Commission, Washington DC, USA.
125. *Sources and effects of ionizing radiation*, 2000, Report UNSCEAR 2000, Vol. 2 Annex J, United Nations Scientific Committee on the Effects of Atomic Radiation (UNSCEAR), New York, USA.
126. Anspaugh, L.R., R.J. Catlin, and M. Goldman, *The global impact of the Chernobyl reactor accident*. Science, 1988. 242: pp. 1513-1519.
127. Takano, M., *et al.*, *Reactivity accident of nuclear submarine near Vladivostok*. Journal of Nuclear Science and Technology, 2001. 38(2): pp. 143-157.
128. Lorenz, R.A. and M.F. Osborne, *A summary of ORNL fission product release tests with recommended release rates and diffusion coefficients*, 1995, Report ORNL/TM-12801, also NUREG/CR-6261, Oak Ridge National Laboratory, Oak Ridge, TN, USA.
129. Iglesias, F.C., *et al.*, *Fission product release mechanisms during reactor accident conditions*. Journal of Nuclear Materials, 1999. 270: pp. 21-38.
130. Kudo, T., *et al.*, Influence of pressure on cesium release from irradiated fuel at temperatures up to 2773 K. Journal of Nuclear Science and Technology, 2001. 38: pp. 910-911.
131. Kudo, T., *et al.*, Effects of fuel oxidation and dissolution on volatile fission product release under severe accident conditions. Journal of Nuclear Science and Technology, 2007. 44(11): pp. 1428-1435.
132. Leveque, J.P., *et al.*, *The HEVA experimental program*. Nuclear Technology, 1994. 108: pp. 33-44.
133. Pontillon, Y., *et al.*, Lessons learnt from VERCORS tests. Study of the active role played by UO₂-ZrO₂-FP interactions on irradiated fuel collapse temperature. Journal of Nuclear Materials, 2005. 344: pp. 265-273.
134. Schwarz, M., B. Clement, and A.V. Jones, *Applicability of PHEBUS FP results to severe accident safety evaluations and management measures*. Nuclear Engineering and Design, 2001. 209: pp. 173-181.

135. Clement, C., *et al.*, LWR severe accident simulation: synthesis of the results and interpretation of the first PHEBUS FP experiment FPT0. Nuclear Engineering and Design, 2003. 226: pp. 5-82.
136. Wren, J.C., J.M. Ball, and G.A. Glowa, *The chemistry of iodine in containment*. Nuclear Technology, 2000. 129: pp. 297-324.
137. Wren, J.C. Radioiodine chemistry: the unfinished story, 2005. In: First European review meeting on severe accident research (ERMSAR-2005), November 14-16, 2005, Aix-en-Provence, France.
138. Beahm, E.C., *et al.*, *Iodine chemical forms in LWR severe accidents*, 1992, Report ORNL/TM-11861, also NUREG/CR-5732, Oak Ridge National Laboratory, Oak Ridge, TN, USA.
139. Krausmann, E., A state-of-the-art report on iodine chemistry and related mitigation mechanisms in the containment, 2001, Report EUR 19752/EN, European Commission.
140. Clement, B., *et al.*, *State of the art report on iodine chemistry*, 2007, Report NEA/CSNI/R(2007)1, OECD Nuclear Energy Agency, Paris, France.
141. Guntay, S., *et al.*, On the radiolytic decomposition of colloidal silver iodide in aqueous suspension. Nuclear Technology, 2005. 150: pp. 303-314.
142. Asmolov, V. and L. Yegorova, The Russian RIA research program: Motivation, definition, execution and results. Nuclear Safety, 1996. 37(4): pp. 343-371.
143. Horhoianu, G., *et al.*, *CANDU type fuel behavior during rapid overpower transients*. Nuclear Engineering and Design, 1998. 179: pp. 267-274.
144. Meyer, R.O., An assessment of fuel damage in postulated reactivity-initiated accidents. Nuclear Technology, 2006. 155: pp. 293-311.
145. Garde, A.M. Influence of cladding microstructure on the low enthalpy failures in RIA simulation tests, 2000. In: Zirconium in the nuclear industry; 12th international symposium: G.P. Sabol and G.D. Moan, Editors, American Society for Testing and Materials, ASTM STP-1354, pp. 234-255.
146. Semken, R.S., *et al.*, *Reactivity-initiated accident test series, RIA scoping tests fuel behavior report*, 1980, Report NUREG/CR-1360, US Nuclear Regulatory Commission, Washington DC, USA.
147. Seiffert, S.L., Z.R. Martinson, and S.K. Fukuda, *Reactivity-initiated accident test series, Test RIA 1-1 (radial average fuel enthalpy of 285 cal/g) fuel behavior report*, 1980, Report NUREG/CR-1465, US Nuclear Regulatory Commission, Washington DC, USA.
148. Cook, B.A., *et al.*, *Reactivity-initiated accident test series, Test RIA 1-2 fuel behavior report*, 1981, Report NUREG/CR-1842, US Nuclear Regulatory Commission, Washington DC, USA.
149. Yegorova, L., Data base on the behavior of high burnup fuel rods with Zr-1%Nb cladding and UO₂ fuel (VVER type) under reactivity accident conditions, 1999, NUREG/IA-0156, US Nuclear Regulatory Commission, Washington DC, USA.
150. Bogdanov, V.N., *et al.* Irradiating complex on BIGH reactor for simulation accidents of RIA type, 2003. In: Seventh international conference on nuclear criticality and safety, October 20-24, 2003, Tokai, Japan: Japan Atomic Energy Research Institute, pp. 770-772.

151. Yegorova, L., *et al.*, Experimental study of narrow pulse effects on the behavior of high burnup fuel rods with Zr-1%Nb cladding and UO₂ fuel (VVER type) under reactivity-initiated accident conditions: Program approach and analysis results, 2006, NUREG/IA-0213, US Nuclear Regulatory Commission, Washington DC, USA.
152. Ishikawa, M., T. Fujishiro, and S. Kawasaki, *LWR fuel safety research with particular emphasis on RIA/LOCA and other conditions*. Journal of Nuclear Science and Engineering, 1989. 26: pp. 118-125.
153. Fujishiro, T., *et al.*, Transient fuel behaviour of preirradiated PWR fuels under reactivity-initiated accidents. Journal of Nuclear Materials, 1992. 188: pp. 162-167.
154. Nakamura, T. FK test series with high burnup BWR fuel and analytical test program, 1999. In: 23rd NSRR technical review meeting, November 11-12, 1999, Tokyo, Japan.
155. Nakamura, T., *et al.*, Boiling water reactor fuel behaviour at burnup of 26 MWd/kgU under reactivity-initiated accident conditions. Nuclear Technology, 1994. 108: pp. 45-59.
156. Nakamura, T., K. Kusagaya, and T. Fuketa, *High-burnup BWR fuel behavior under simulated reactivity-initiated accident conditions*. Nuclear Technology, 2002. 138: pp. 246-259.
157. Fuketa, T. High burnup BWR fuel response to reactivity transients and a comparison with PWR fuel response, 2000. In: 24th NSRR technical review meeting, November 13-14, 2000, Tokyo, Japan.
158. Nakamura, T., *et al.* NSRR RIA tests on PWR, BWR and MOX fuel, 2002. In: *Fuel safety research specialist's meeting*, March 4-5, 2002, Tokai, Japan: Japan Atomic Energy Research Institute, JAERI Conf 2002-009, pp. 71-83.
159. Fuketa, T., *et al.* Behaviour of high burnup PWR fuels during simulated reactivity-initiated accident conditions, 2006. In: *TopFuel-2006*, October 22-26, Salamanca, Spain: European Nuclear Society, pp. 279-283.
160. Marquie, C., *et al.* SURF: A test facility to investigate the safety of LMFBR and PWR fuels, 1999. In: International symposium on research reactor utilization, safety and management, September 6-10, 1999, Lisbon, Portugal: International Atomic Energy Agency, IAEA-SM-360, pp. 132-133.
161. Bates, D.W., D.A. Koss, and A.T. Motta. Influence of specimen design on the deformation and failure of Zircaloy cladding, 2000. In: ANS topical meeting on light water reactor fuel performance, April 10-13, 2000, Park City, Utah, USA: American Nuclear Society, pp. 296-305.
162. Barba, M.J., *Resistance a la traction et allongements des metaux apres rupture*. Memoires de la Societe des ingenieurs civils de France, Part I, 1880: p. 682.
163. *Standard test method for tension testing of metallic materials*, 2003, ASTM E8-04, American Society for Testing and Materials,
164. Cazalis, B., *et al.*, The PROMETRA program: Fuel cladding mechanical behavior under high strain rate. Nuclear Technology, 2007. 157: pp. 215-229.
165. Yvon, P., *et al.* Development of new techniques to assess the mechanical behaviour of Zircaloy-4 during an RIA, 2001. In: IAEA technical committee meeting on fuel behaviour under transient and LOCA conditions, September 10-14, 2001, Halden, Norway: International Atomic Energy Agency, IAEA-TECDOC-1320, pp. 111-122.

166. Cazalis, B., *et al.* The PROMETRA program: A reliable material database for highly irradiated Zircaloy-4, ZIRLO and M5 fuel claddings, 2005. In: 18th international conference on structural mechanics in reactor technology (SMiRT-18), August 7-12, 2005, Beijing, China, pp. 383-393.
167. Desquines, J., *et al.*, Mechanical properties of Zircaloy-4 PWR fuel cladding with burnup 54-64 MWd/kgU and implications for RIA behavior. Journal of ASTM International, 2005. 2(6).
168. Balourdet, M., *et al.* The PROMETRA programme: Assessment of mechanical properties of Zircaloy-4 fuel cladding during an RIA, 1999. In: 15th international conference on structural mechanics in reactor technology (SMiRT-15), August 15-20, 1999, Seoul, Korea, Volume II, pp. 485-492.
169. Balourdet, M. and C. Bernaudat. Tensile properties of Zircaloy-4 cladding submitted to fast transient loading, 1995. In: CSNI specialist meeting on transient behaviour of high burnup fuel September 12-14, 1995, Cadarache, France, OECD Nuclear Energy Agency, NEA/CSNI/R(95)22, pp. 417-431.
170. Le Saux, M., *et al.*, A model to describe the anisotropic viscoplastic mechanical behavior of fresh and irradiated Zircaloy-4 fuel claddings under RIA loading conditions. Journal of Nuclear Materials, 2008. 378: pp. 60-69.
171. Nakatsuka, M., *et al.* (2004), *Mechanical properties of high burnup BWR fuel cladding tubes under simulated RIA conditions*, 2004 International Meeting on Light-water Reactor Fuel Performance, September 19-22, 2004, American Nuclear Society, Orlando, FL, USA.
172. Electric Power Research Institute (2004), *Cladding transient response: Rapid burst tests on unirradiated and irradiated Zircaloy samples*, TR-1003405, Palo Alto, CA, USA.
173. Nagase, F. and T. Fuketa, *Investigation of hydride rim effect on failure of Zircaloy-4 cladding with tube burst test*, Journal of Nuclear Science and Technology, 2005. 42(1): pp. 58-65.
174. Kuroda, M., *et al.*, Analysis of the fracture behavior of hydrided fuel cladding by fracture mechanics, Nuclear Engineering and Design, 2001. 203: pp. 185-194.
175. Kuroda, M. and S. Yamanaka, Assessment of the combined effects of irradiation and hydrogenation on the fracture behavior of Zircaloy fuel claddings by fracture mechanics, Journal of Nuclear Science and Technology, 2002. 39(3): pp. 234-240.
176. Daum, R.S., *et al.* (2002), Mechanical property testing of irradiated Zircaloy cladding under reactor transient conditions, Small specimen test techniques: Fourth volume: M.A. Sokolov, J.D. Landes, and G.E. Lucas, Editors, American Society for Testing and Materials, ASTM STP-1418.
177. Link, T.M., D.A. Koss, and A.T. Motta, *Failure of Zircaloy cladding under transverse plane-strain deformation*. Nuclear Engineering and Design, 1998. 186: pp. 379-394.
178. Daum, R.S., *et al.* *On the embrittlement of Zircaloy-4 under RIA-relevant conditions*, 2002. In: *Zirconium in the Nuclear Industry; 13th International Symposium*: G.P. Moan and P. Rudling, Editors, American Society for Testing and Materials, ASTM STP-1423, pp. 702-719.
179. Kim, J.H., *et al.*, *Behavior of zirconium fuel cladding under fast pressurization rates*. Nuclear Engineering and Design, 2008. 238: pp. 1441-1447.
180. Grigoriev, V., *et al.* Mechanical testing of high burnup PWR cladding to simulate RIA, 2000. In: *Jahrestagung Kerntechnik*, May 23-25, 2000, Bonn, Germany.

181. Grigoriev, V., R. Jakobsson, and D. Schrire, *Experimental evaluation of critical strain energy density for irradiated cladding under simulated RIA conditions*, 2001. In: *ENS TopFuel*, May 27-30, 2001, European Nuclear Society, Stockholm, Sweden.
182. Rashid, Y.R., *et al.* A cladding failure model for fuel rods subjected to operational and accident transients, 2000. In: IAEA technical committee meeting on nuclear fuel behaviour modeling at high burn-up and its experimental support, June 19-23, 2000, Windermere, United Kingdom, International Atomic Energy Agency, IAEA-TECDOC-1233.
183. Le Saux, M., *et al.* (2007), High Temperature Expansion due to Compression Test for the Determination of a Cladding Material Failure Criterion under RIA Loading Conditions, International LWR Fuel Performance Meeting, September 30 – October 3, 2007, San Francisco, CA, USA: American Nuclear Society, pp. 526-535.
184. Grigoriev, V., *et al.*, *Impact of corrosion on rapid deformation capabilities of ZIRLO cladding*, 2002. In: *NEA topical meeting on RIA fuel safety criteria*, May 13-15, 2002, Aix-en-Provence, France, OECD Nuclear Energy Agency, NEA/CSNI/R(2003)8/Vol2, pp. 132-140.
185. Kaplar, E., *et al.* (2001), *Mechanical properties of unirradiated and irradiated Zr-1%Nb cladding: Procedures and results of low temperature biaxial burst tests and axial tensile tests*, Report NUREG/IA-0199, U.S. Nuclear Regulatory Commission, Washington DC, USA.
186. Bessiron, V. (2003), *The PATRICIA Program on Clad to Coolant Heat Transfer during Reactivity-initiated Accidents*, 10th International Topical Meeting on Nuclear Reactor Thermal Hydraulics (NURETH-10), October 5-9, 2003, Seoul, Korea.
187. Bessiron, V. (2004), *Clad-to-Coolant Heat Transfer during a RIA Transient: Analysis of the PATRICIA Experiments, Modelling and Applications*, Fuel safety research meeting, March 1-2, 2004, Tokyo, Japan.
188. Sibamoto, Y., *et al.* (2007), *In-pile experiment in JMTR on the radiation induced surface activation (RISA) effect on flow-boiling heat transfer*, Journal of Nuclear Science and Technology, 44(2): pp. 183-193.
189. Mori, M., *et al.*, *Transient cooling process of fuel rod in reactivity-initiated accident*, Journal of Nuclear Science and Technology, 1980. 17(6): pp. 413-424.
190. Fujishiro, T., *et al.*, Effects of coolant flow on light water reactor fuel behaviors during reactivity-initiated accident. Journal of Nuclear Science and Technology, 1981. 18(3): pp. 196-205.
191. Sugiyama, T. and T. Fuketa (2004), *Effect of cladding pre-oxidation on rod coolability under reactivity-initiated accident conditions*. Journal of Nuclear Science and Technology, 41(11): pp. 1083-1090.
192. Bessiron, V., T. Sugiyama, and T. Fuketa (2007), *Clad-to-coolant heat transfer in NSRR experiments*, Journal of Nuclear Science and Technology, 44(5): pp. 723-732.
193. Maruyama, Y., *et al.* (2006), *Single Rod Experiments on Transient Void Behaviour during Low-Pressure Reactivity-Initiated Accidents in Light Water Reactors*, Nuclear Engineering and Design, 236: pp. 1693-1700.

194. Federici, E., *et al.* (2000), *Status of the development of the SCANAIR code for the description of fuel behavior under reactivity-initiated accidents*, ANS Topical Meeting on Light Water Reactor Fuel Performance, April 10-13, 2000, American Nuclear Society, Park City, UT, USA.
195. Fink, J.K., *Enthalpy and heat capacity of solid uranium dioxide*, INSC material properties database, International Nuclear Safety Center (INSC), Argonne National Laboratory, USA: Available via internet at www.insc.anl.gov/matprop.
196. Jernkvist, L.O. (2006), *Computational Assessment of burn-up-Dependent Fuel Failure Thresholds for Reactivity-initiated Accidents*, Journal of Nuclear Science and Technology, 43(5): pp. 546-561.
197. Jernkvist, L.O. and A.R. Massih (2005), *Assessment of core failure limits for light water reactor fuel under reactivity-initiated accidents*, Research report 2005:16, Swedish Nuclear Power Inspectorate (SKI), Stockholm, Sweden.
198. Montgomery, R.O. (2002), *Topical report on reactivity-initiated accident: Bases for RIA fuel and core coolability criteria*, Report TR-1002865, Electric Power Research Institute, Palo Alto, CA, USA.
199. Fink, J.K., *Solidus/liquidus of uranium-plutonium dioxide*, INSC material properties database, International Nuclear Safety Center (INSC), Argonne National Laboratory, USA: Available via internet at www.insc.anl.gov/matprop.
200. Abe, T., *et al.* (1992), Failure behaviour of plutonium-uranium mixed oxide fuel under reactivity-initiated accident condition. Journal of Nuclear Materials, 188: pp. 154-161.
201. Freshley, M.D., *et al.* (1972), *Behaviour of Discrete Plutonium-Dioxide Particles in Mixed-Oxide Fuel during Rapid Power Transients*, Nuclear Technology, 1972(15): pp. 239-248.
202. Lespiaux, D., J. Noirot, and P. Menut (1997), *Post-test Examinations of High burn-up PWR Fuels Submitted to RIA Transients in the CABRI Facility*, ANS topical meeting on light water reactor fuel performance, March 2-6, 1997, American Nuclear Society, pp. 650-658, Portland, OR, USA.
203. Lemoine, F. (1997), *High Burn-up Fuel Behaviour Related to Fission Gas Effects under Reactivity-initiated Accidents (RIA) Conditions*, Journal of Nuclear Materials, 1997(248): pp. 238-248.
204. Papin, J., F. Lemoine, and E. Federici (2002), *Main Outcomes from the CABRI Test Results*, NEA CSNI topical meeting on RIA fuel safety criteria, May 13-15, 2002, Aix-en-Provence, France, OECD Nuclear Energy Agency, NEA/CSNI/R(2003)8/Vol 2, pp. 61-81.
205. Lemoine, F. (2006), *Estimation of the Grain Boundary Gas Inventory in MIMAS/AUC MOX Fuel and Consistency with REP-Na Test Results*, Journal of Nuclear Science and Technology, 43(9): pp. 1105-1113.
206. Nakamura, T., *et al.*, *Fission Gas Induced Cladding Deformation of LWR Fuel Rods Under Reactivity-initiated Accident Conditions*, Journal of Nuclear Science and Technology, 1996. 33(12): pp. 924-935.
207. Vitanza, C. and J.M. Conde Lopez (2004), *PCMI implications for high burn-up light-water reactor fuel in reactivity-initiated accidents*, International seminar on pellet-clad interaction in water reactor fuels (PCI-2004), March 9-11, 2004, Aix-en-Provence, France, OECD Nuclear Energy Agency, Paris, France.

208. Lemoine, F., *et al.* (2002), *The role of grain boundary fission gases in high burn-up fuel under reactivity-initiated accident conditions*, NEA Seminar on Fission Gas Behaviour in Water Reactor Fuels, September 26-29, 2002, Cadarache, France, OECD Nuclear Energy Agency, Paris, France.
209. Guerin, Y. (2002), *In-pile and Out-of-Pile Burst Release of Fission Gases*, Enlarged Halden Programme Group Meeting, September 8-13, 2002, Halden Reactor Project, Gol, Norway.
210. Noirot, J., L. Desgranges, and P. Marimbeau (2000), *Contribution of the rim to the overall fission gas release: What do isotopic analyses reveal?*, NEA Seminar on Fission Gas Behaviour in Water Reactor Fuels, September 26-29, 2000, Cadarache, France, OECD Nuclear Energy Agency, Paris, France.
211. White, R.J. (2000), *Fission gas release*, Halden Reactor Project Report HWR-632, Halden, Norway.
212. Sasajima, H., *et al.*, *Fission gas release behaviour of high burn-up UO_2 fuel under reactivity-initiated accident conditions*, Journal of Nuclear Science and Technology, 1999. 36(11): pp. 1101-1104.
213. Amaya, M., *et al.*, *Fission Gas Release in BWR Fuel with a Burn-up of 56 GWd/t During Simulated Reactivity-initiated Accident (RIA) Condition*, Journal of Nuclear Science and Technology (2008), 45(5): pp. 423-431.
214. Fuketa, T., *et al.* (2003), *Effects of Pellet Expansion and Cladding Hydrides on PCMI failure of High Burnup LWR Fuel during Reactivity Transients*, Nuclear safety research conference, US Nuclear Regulatory Commission, Washington DC, USA.
215. Suzuki, M., H. Saitou, and T. Fuketa, Analysis on split failure of cladding of high burnup BWR rods in reactivity-initiated accident conditions by RANNS code. Nuclear Engineering and Design, 2006. 236: pp. 128-139.
216. Fink, J.K., *Zircaloy-4(O) Solidus Temperature*, INSC Material Properties Database, International Nuclear Safety Center (INSC), Argonne National Laboratory, USA, Available via internet at www.insc.anl.gov/matprop.
217. Saito, S., *et al.* (1981), *Development of in-reactor fuel behavior observation system*, Journal of Nuclear Science and Technology, 18(6): pp. 427-439.
218. Gomez, A., *et al.* (2006), *Analysis of CRDA in a High Burn-up Fuel Core for Confrontes NPP with RETRAN-3D*, pp. 456-460, TopFuel-2006, October 22-26, Salamanca, Spain, European Nuclear Society.
219. Carbajo, J.J. and A.D. Siegel (1980), *Review and Comparison Among the Different Models for Rewetting in LWRs*, Nuclear Engineering and Design, 58: pp. 33-44.
220. Vitanza, C. (2002), *An Analysis of the CABRI REP Na Tests*, NEA CSNI Topical Meeting on RIA Fuel Safety Criteria, May 13-15, 2002, Aix-en-Provence, France, OECD Nuclear Energy Agency, Report NEA/CSNI/R(2003)8/Vol 2, pp. 39-50.
221. Vitanza, C. (2006), *RIA failure threshold and LOCA limit at high burn-up*, Journal of Nuclear Science and Technology, 43(9): pp. 1074-1079.
222. Hill, R. (1950), *The mathematical theory of plasticity*, Oxford, United Kingdom, Oxford Classic Texts in Physical Sciences, Clarendon Press, 1998.

223. Sunderland, D., R. Montgomery, and O. Ozer (2004), *Evaluation of recent RIA-simulation experiments with the FALCON fuel performance code*, pp. 551-564, 2004 International Meeting on Light Water Reactor Fuel Performance, September 19-22, 2004, Orlando, FL, USA, American Nuclear Society,.
224. Nakamura, T., *et al.* (2004), *Failure Thresholds of High Burn-up BWR Fuel Rods under RIA Conditions*, Journal of Nuclear Science and Technology, 41(1): pp. 37-43.
225. Fuketa, T., T. Sugiyama, and F. Nagase (2006), *Behaviour of 60 to 78 MWd/kgU PWR Fuels under Reactivity-Initiated-Accident Conditions*, Journal of Nuclear Science and Technology, 43(9): pp. 1080-1088.
226. Shiozawa, S., S. Saito, and S. Yanagihara (1982), *Zircaloy-UO₂ and -Water Reactions and Cladding Temperature Estimation for Rapidly Heated Fuel Rods under an RIA Condition*, Journal of Nuclear Science and Technology, 19(5): pp. 368-383.
227. Fuketa, T., K. Ishijima, and T. Fujishiro (1996), *Hydrogen Generation during Cladding/Coolant Interactions under Reactivity-initiated Accidents*. Journal of Nuclear Science and Technology, 33(1): pp. 43-51.
228. Moalem, M. and D.R. Olander (1991), *Oxidation of Zircaloy by Steam*, Journal of Nuclear Materials, 182: pp. 170-194.
229. Chung, H.M. and T.F. Kassner (1979), *Pseudobinary Zircaloy-oxygen Phase Diagram*, Journal of Nuclear Materials, 84: pp. 327-339.
230. Abriata, J.P., J. Garces, and R. Versaci (1986), *The O-Zr (oxygen-zirconium) System*, Bulletin of Alloy Phase Diagrams, 7: pp. 116-124.
231. Mallet, M.W., W.M. Albrecht, and P.R. Wilson (1959), *The Diffusion of Oxygen in Alpha and Beta Zircaloy-2 and Zircaloy-3 at High Temperatures*. Journal of the Electrochemical Society, 106: pp. 181-184.
232. Pawel, R.E. (1974), *Oxygen Diffusion in Beta Zircaloy during Steam Oxidation*, Journal of Nuclear Materials, 50: pp. 247-258.
233. Pemsler, J.P. (1962), *Studies on the Oxygen Gradients in Corroding Zirconium Alloys*, Journal of Nuclear Materials, 7: pp. 16-25.
234. Pemsler, J.P. (1965), *Studies on the Oxygen Gradients in Corroding Zirconium Alloys: III Kinetics of the Oxidation of Zirconium at High Temperatures*, Journal of the Electrochemical Society, 112: pp. 477-484.
235. Rosa, C.J., *Oxidation of Zirconium: a Critical Review of Literature*. Journal of Less Common Metals, 1968. 16: pp. 173-201.
236. Pawel, R.E., *Diffusion in Finite System with a Moving Boundary*. Journal of Nuclear Materials, 1973. 49: pp. 281-290.
237. Ocken, H., *An Improved Evaluation Model for Zircaloy Oxidation*. Nuclear Technology, 1980. 47: pp. 343-357.

238. Massih, A.R., Review of Experimental Data for Modelling LWR Fuel Cladding Behaviour under Loss of Coolant Accident Conditions, 2007, Research report Swedish Nuclear Power Inspectorate (SKI), Stockholm, Sweden.
239. Urbanic, V.F. and T.R. Heidrick, *High-temperature Oxidation of Zircaloy-2 and Zircaloy-4 in Steam*. Journal of Nuclear Materials, 1978. 75: pp. 251-261.
240. Liang, P., *et al.*, *Thermodynamic Assessment of the Zr-O Binary System*. Zeitschrift fuer Metallkunde, 2001. 92: pp. 747-756.
241. Perez, R.J. and A.R. Massih, *Thermodynamic Evaluation of the Nb-O-Zr system*. Journal of Nuclear Materials, 2007. 360: pp. 242-254.
242. Kawasaki, S., T. Furuta, and M. Suzuki, *Oxidation of Zircaloy-4 under high temperature steam atmosphere and its effect on ductility of cladding*. Journal of Nuclear Science and Technology, 1978. 15(8): pp. 589-596.
243. Uetsuka, H., T. Furuta, and S. Kawasaki, *Zircaloy-4 cladding embrittlement due to inner surface oxidation under simulated loss-of-coolant condition*. Journal of Nuclear Science and Technology, 1981. 18: pp. 705-717.
244. Nagase, F., T. Otomo, and H. Uetsuka, *Oxidation kinetics of low-Sn Zircaloy-4 at the temperature range from 773 to 1573 K*. Journal of Nuclear Science and Technology, 2003. 40: pp. 213-219.
245. Yanagihara, S. and S. Shiozawa, *Cladding embrittlement and fuel rod failure threshold under reactivity-initiated accident condition*. Journal of Nuclear Science and Technology, 1987. 24(11): pp. 897-905.
246. Sawatzky, A., G.A. Ledoux, and S. Jones. *Oxidation of zirconium during a high-temperature transient*, 1977. In: *Zirconium in the nuclear industry: third international symposium*: A.L. Lowe Jr and G.W. Parry, Editors, American Society for Testing and Materials, ASTM STP-633, pp. 134-149.
247. Pawel, R.E., J.V. Cathcart, and R.A. McKee, *Anomalous oxide growth during transient-temperature oxidation of Zircaloy-4*. Oxidation of Metals, 1980. 14: pp. 1-13.
248. Baun, W.L., Phase transformations at high temperature in hafnia and zirconia. Science, 1963. 140: pp. 1330-1331.
249. Hobson, D.O. and P.L. Rittenhouse, *Embrittlement of Zircaloy clad fuel rods by steam during LOCA transients*, 1972, Technical report Oak Ridge National Laboratory, Oak Ridge, TN, USA.
250. Hobson, D.O. *Ductile-brittle behavior of Zircaloy fuel cladding*, 1973. In: *ANS topical meeting on reactor safety*, March 26 1973, Salt Lake City, UT, USA: American Nuclear Society.
251. Desquines, J., *et al.* The fracture and spallation of zirconia layers in high burnup PWR fuel claddings submitted to RIA transients, 2005. In: 18th international conference on structural mechanics in reactor technology (SMiRT-18), August 7-12, 2005, Beijing, China, pp. 444-453.
252. Yagnik, S.K., A. Hermann, and R.-C. Kuo, *Ductility of Zircaloy-4 fuel cladding and guide tubes at high fluences*. Journal of ASTM International, 2005. 2(5).

253. Rashid, Y.R., C. Lemaignan, and A. Strasser. *Evaluation of fracture initiation and extension in fuel cladding*, 2000. In: *ANS topical meeting on light water reactor fuel performance*, April 10-13, 2000, Park City, Utah, USA: American Nuclear Society, pp. 151-161.
254. Chung, H.M. Fundamental metallurgical aspects of axial splitting in zircaloy cladding, 2000. In: *ANS topical meeting on light water reactor fuel performance*, April 10-13, 2000, Park City, Utah, USA: American Nuclear Society.
255. Montgomery, R., *et al.* The mechanical response of cladding with a hydride lens under PCMI loading conditions, 2004. In: *International seminar on pellet-clad interaction in water reactor fuels (PCI-2004)*, March 9-11, 2004, Aix-en-Provence, France: OECD Nuclear Energy Agency.
256. Jernkvist, L.O. Prediction of failure of highly irradiated Zircaloy clad tubes under reactivity-initiated accidents, 2003. In: *17th international conference on structural mechanics in reactor technology (SMiRT-17)*, August 17-22, 2003, Prague, Czech Republic.
257. Walker, S.P., A. Yu, and R.T. Fenner, *Pellet-clad mechanical interaction: pellet-clad bond failure and strain relief*. Nuclear Engineering and Design, 1992. 138: pp. 403-408.
258. Maki, H. and M. Ooyama, *Plastic deformation and fracture behavior of Zircaloy-2 fuel cladding tubes under biaxial stress*. Journal of Nuclear Science and Technology, 1975. 12(7): pp. 423-435.
259. Andersson, T. and A. Wilson. Ductility of Zircaloy canning tubes in relation to stress ratio in biaxial testing, 1979. In: *Zirconium in the nuclear industry; 4th international symposium*: J.H. Schemel and T.P. Papazoglou, Editors, American Society for Testing and Materials, ASTM STP-681, pp. 60-71.
260. Jernkvist, L.O., A.R. Massih, and P. Rudling, *A strain-based clad failure criterion for reactivity-initiated accidents in light water reactors*, 2004, Research report 2004:32, Swedish Nuclear Power Inspectorate (SKI), Stockholm, Sweden.
261. Leclercq, S., G. Rousselier, and A. Parrot. Rupture of the fuel rod cladding under RIA conditions: A scheme to make the experimental mechanical data base representative of standard in-pile thermomechanical conditions, 2005. In: *2005 Water reactor fuel performance meeting*, October 2-6, 2005, Kyoto, Japan, pp. 751-766.
262. Geelhood, K.J., C.E. Beyer, and M.E. Cunningham. Modifications to FRAPTRAN to predict fuel rod failures due to PCMI during RIA-type accidents, 2004. In: *2004 International Meeting on LWR Fuel Performance*, September 19-22, 2004, Orlando, FL, USA: American Nuclear Society, pp. 585-595.
263. Leclercq, S., A. Parrot, and M. Leroy, *Failure characteristics of cladding tubes under RIA conditions*. Nuclear Engineering and Design, 2008. 238: pp. 2206-2218.
264. Pettersson, K., *Fuel behaviour under LOCA conditions*, 2006, (In preparation), OECD Nuclear Energy Agency, Paris, France.
265. Ishijima, K. and T. Nakamura, *Transient elongation of a fresh fuel rod under reactivity-initiated accident conditions*. Journal of Nuclear Science and Technology, 1996. 33(3): pp. 229-238.
266. Tanzawa, S., S. Kobayashi, and T. Fujishiro, *Fuel behaviour in simulated RIA under high pressure and temperature coolant conditions*. Journal of Nuclear Science and Technology, 1993. 30(4): pp. 281-290.

267. Fedotov, P.V., *et al.* Estimation of water-water energy reactor fuel rod failure in design basis accidents, 2005. In: 2005 Water reactor fuel performance meeting, October 2-6, 2005, Kyoto, Japan, pp. 835-847.
268. Nikulina, A.V., *Structural materials for elements of nuclear-reactor active zones*. Metal Science and Heat Treatment, 2004. 46(11-12): pp. 458-462.
269. Yanagisawa, K., A study on the behavior of pressurized hollow UO₂ fuel under reactivity-initiated accident conditions. Nuclear Engineering and Design, 1989. 116: pp. 171-180.
270. Dagbjartsson, S.J., *et al.*, *Axial gas flow in irradiated PWR fuel rods*, 1977, TREE-NUREG-1158, US Nuclear Regulatory Commission, Washington DC, USA.
271. Lanzani, L. and M. Ruch, *Comments on the stability of zirconium hydride phases in Zircaloy*. Journal of Nuclear Materials, 2004. 324: pp. 165-176.
272. Veleva, M., *et al.*, Hydride embrittlement and irradiation effects on the hoop mechanical properties of pressurized water reactor (PWR) and boiling water reactor (BWR) Zircaloy cladding tubes: Part II. Morphology of hydrides investigated at different magnifications and their interaction with the process of plastic deformation. Metallurgical and Materials Transactions A, 2003. 34A: pp. 567-578.
273. Barraclough, K.G. and C.J. Beevers, Some observations on the deformation characteristics of bulk polycrystalline zirconium hydrides: Part I. The deformation and fracture of hydrides based on the delta-phase. Journal of Materials Science, 1969. 4: pp. 518-525.
274. Wisner, S.B. and R.B. Adamson, *Combined effects of radiation damage and hydrides on the ductility of Zircaloy-2*. Nuclear Engineering and Design, 1998. 185: pp. 33-49.
275. Garde, A.M. Effects of irradiation and hydriding on the mechanical properties of Zircaloy-4 at high fluence, 1989. In: Zirconium in the nuclear industry; 8th international symposium: L.F.P. van Swam and C.M. Eucken, Editors, American Society for Testing and Materials, ASTM STP-1023, pp. 548-569.
276. Arsene, S., J.B. Bai, and P. Bompard, Hydride embrittlement and irradiation effects on the hoop mechanical properties of pressurized water reactor (PWR) and boiling water reactor (BWR) Zircaloy cladding tubes: Part I. Hydride embrittlement in stress-relieved, annealed, and recrystallized Zircalloys at 20C and 300C. Metallurgical and Materials Transactions A, 2003. 34A: pp. 553-566.
277. Bai, J.B., Effect of hydriding temperature and strain rate on the ductile-brittle transition in beta-treated Zircaloy-4. Journal of Nuclear Science and Technology, 1996. 33(2): pp. 141-146.
278. Bertolino, G., G. Meyer, and J. Perez Ipina, *Effects of hydrogen content and temperature on fracture toughness of Zircaloy-4*. Journal of Nuclear Materials, 2003. 320: pp. 272-279.
279. Chan, K.S., *A fracture model for hydride-induced embrittlement*. Acta Metallurgica et Materialia, 1995. 43(12): pp. 4325-4335.
280. Chan, K.S., A micromechanical model for predicting hydride embrittlement in nuclear fuel cladding material. Journal of Nuclear Materials, 1996. 227: pp. 220-236.

281. Del Barrio, M.T. and L.E. Herranz. Predictive methodology of a cladding failure criterion based on PROMETRA database: Application to CABRI CIP0-1 experiment, 2002. In: Enlarged Halden Programme Group Meeting, September 8-13, 2002, Gol, Norway: Halden Reactor Project.
282. Bai, J.B., C. Prioul, and D. Francois, Hydride embrittlement in Zircaloy-4 plate: Part I. Influence of microstructure on the hydride embrittlement in Zircaloy-4 at 20 C and 350 C. Metallurgical and Materials Transactions A, 1994. 25A: pp. 1185-1197.
283. Gill, B.J., J.E. Bailey, and P. Cotterill, *The effects of hydride precipitates on the mechanical properties of zirconium-hydrogen alloys*. Journal of Less Common Metals, 1975. 40: pp. 129-138.
284. Shi, S.-Q. and M.P. Puls, *Fracture strength of hydride precipitates in Zr-2.5Nb alloys*. Journal of Nuclear Materials, 1999. 275: pp. 312-137.
285. Yunchang, F. and D.A. Koss, The influence of multiaxial states of stress on the hydrogen embrittlement of zirconium alloy sheet. Metallurgical Transactions A, 1985. 16A: pp. 675-681.
286. Wallace, A.C., G.K. Shek, and O.E. Lepik. *Effects of hydride morphology on Zr-2.5Nb fracture toughness*, 1989. In: *Zirconium in the nuclear industry; 8th international symposium*: L.F.P. van Swam and C.M. Eucken, Editors, American Society for Testing and Materials, ASTM STP-1023, pp. 66-88.
287. Coleman, C.E. and D. Hardie, *The hydrogen embrittlement of zirconium in slow-bend tests*. Journal of Nuclear Materials, 1966. 19: pp. 1-8.
288. Wood, D.S., J. Winton, and B. Watkins, *Effect of irradiation on the impact properties of hydrided Zircaloy-2 and zirconium-niobium alloy*. Journal of Electrochemical Technology, 1966. 4: pp. 250-258.
289. Ham, F.S., *Stress-assisted precipitation on dislocations*. Journal of Applied Physics, 1959. 30(6): pp. 915-926.
290. Kearns, J.J., *Dissolution kinetics of hydride platelets in Zircaloy-4*. Journal of Nuclear Materials, 1968. 27: pp. 64-72.
291. Nagase, F., K. Ishijima, and T. Furuta. Influence of locally concentrated hydrides on ductility of Zircaloy-4, 1995. In: CSNI specialist meeting on transient behaviour of high burnup fuel, September 12-14, 1995, Cadarache, France, pp. 433-443.
292. Nagase, F. and H. Uetsuka. Hydride morphology and hydrogen embrittlement of Zircaloy fuel cladding used in NSRR/HBO experiment, 1997. In: ANS topical meeting on light water reactor fuel performance, March 2-6, 1997, Portland, OR, USA: American Nuclear Society, pp. 677-684.
293. Forsberg, K. and A.R. Massih, *Redistribution of hydrogen in Zircaloy*. Journal of Nuclear Materials, 1990. 172: pp. 130-134.
294. Une, K. and S. Ishimoto, *Terminal solid solubility of hydrogen in unalloyed zirconium by differential scanning calorimetry*. Journal of Nuclear Science and Technology, 2004. 41(9): pp. 949-952.
295. Puls, M.P. *Effect of stress on hydride reorientation in zirconium alloys*, 1985. In: *Solute-defect interaction: Theory and experiment*, August 5-9, 1985, Kingston, Canada: S. Saimoto, G.R. Purdy, and G.V. Kidson, Editors, Pergamon Press, pp. 426-433.

296. Bai, J.B., C. Prioul, and D. Francois, *Effect of microstructure factors and cold work on the hydride precipitation in Zircaloy-4 sheet*. Journal of Advanced Science, 1991. 3(4): pp. 188-200.
297. Bai, J.B., *et al.*, Hydride embrittlement in Zircaloy-4 plate: Part II. Interaction between the tensile stress and the hydride morphology. Metallurgical and Materials Transactions A, 1994. 25A: pp. 1199-1208.
298. Sakamoto, K. and M. Nakatsuka, *Stress reorientation of hydrides in recrystallized Zircaloy-2 sheet*. Journal of Nuclear Science and Technology, 2006. 43: pp. 1136-1141.
299. Nagase, F. and T. Fuketa, *Influence of hydride re-orientation on BWR cladding rupture under accident conditions*. Journal of Nuclear Science and Technology, 2004. 41(12): pp. 1211-1217.
300. Chu, H.C., *et al.*, Effect of radial hydrides on the axial and hoop mechanical properties of Zircaloy-4 cladding. Journal of Nuclear Materials, 2007. 362: pp. 93-103.
301. Marshall, R.P. and M.R.J. Louthan, *Tensile properties of Zircaloy with oriented hydrides*. Transactions of the ASM, 1963. 56: pp. 693-700.
302. *IAEA Research Reactor Data Base (RRDB)*, International Atomic Energy Agency, Vienna, Austria: Available via internet at www.iaea.org/worldatom/rrdb/.
303. Kobayashi, S., *et al.*, *Experimental results of some cluster tests in NSRR*. Journal of Nuclear Science and Technology, 1978. 15(6): pp. 448-454.
304. Sugiyama, T., *et al.*, *Failure of high burnup fuels under reactivity-initiated accident conditions*. Annals of Nuclear Energy, 2009. 36: pp. 380-385.
305. CRISSE-S-WP2: Neutronics/thermal-hydraulics coupling in LWR technology, State-of-the-art report (REAC-SOAR), 2004, Report OECD/NEA-5436, OECD Nuclear Energy Agency, Paris, France.
306. Chadwick, M.B., *et al.*, ENDF/B-VII.0: Next generation evaluated nuclear data library for nuclear science and technology. Nuclear Data Sheets, 2006. 107: pp. 2931-3060.
307. *The JEFF-3.1 nuclear data library*, 2006, JEFF report 21, OECD Nuclear Energy Agency, Paris, France.
308. Watson, J. and K. Ivanov, Improved cross-section modeling methodology for coupled three-dimensional transient calculations. Annals of Nuclear Energy, 2002. 29: pp. 937-966.
309. Loubiere, S., *et al.* APOLLO2: Twelve years later, 1999. In: Mathematics and computation, reactor physics and environmental analysis in nuclear applications (M&C99), September 27-30, 1999, Madrid, Spain: American Nuclear Society.
310. Knott, D., B.H. Forssen, and M. Edenius, *CASMO-4: A fuel assembly burnup program – Methodology*, 1995, Report STUDSVIK/SOA-95/2, Studsvik of America, Inc.,
311. Stammli, R., *HELIOS-1.6 - Methods*, 2000, Report Studsvik Scandpower, Norway.
312. *TransFX computer software manuals*, 2001, Tranware Enterprises Inc., Sycamore, IL, USA.
313. Newton, T.D. and J.L. Hutton. *The next generation WIMS lattice code: WIMS9*, 2002. In: *PHYSOR 2002*, October 7-10, 2002, Seoul, Korea: American Nuclear Society.

314. Cho, N.Z., *Fundamentals and recent developments of reactor physics methods*. Nuclear Engineering and Technology, 2005. 37(1): pp. 25-78.
315. Sutton, T.M. and B.N. Aviles, *Diffusion theory methods for spatial kinetics calculations*. Progress in Nuclear Energy, 1996. 30(2): pp. 119-182.
316. Avvakumov, A. and V. Malofeev. Validation of an advanced heterogeneous model for LWR detailed pin-by-pin calculations, 1998. In: International conference on the physics of nuclear science and technology, October 5-8, 1998, Long Island, NY, USA.
317. Lautard, J.J., S. Loubiere, and C. Fedon-Magnaud. CRONOS2: A modular computational system for neutronic core calculations, 1993. In: IAEA specialists meeting on advanced calculational methods for power reactors and LWR core design parameters, September 10-14, 1990, Cadarache, France: International Atomic Energy Agency IAEA TECDOC-678.
318. Grundmann, U., *et al.*, DYN3D Version 3.2: Code for calculation of transients in light water reactors (LWR) with hexagonal or quadratic fuel elements - Description of models and methods, 2005, Report FZR-434, Forschungszentrum Rossendorf, Dresden, Germany.
319. Downar, T., *et al.*, PARCS V2.6: U.S. NRC core neutronics simulator - Theory manual, 2004, Report Purdue University, School of Engineering, West Lafayette, IN, USA.
320. *SIMULATE-3K: Models & methodology* 1998, Report SOA-98/13, Studsvik Scandpower,
321. Lahey, R.T. and F.J. Moody, *The thermal hydraulics of a boiling water nuclear reactor*. 1993, La Grange Park, IL, USA: American Nuclear Society.
322. Saha, P. and N. Zuber. Point of net vapor generation and vapor void fraction in subcooled boiling, 1974. In: Proceedings of the 5th international heat transfer conference, September 3, 1974, Tokyo, Japan: Scripta Book Co., Washington DC, USA, pp. 175-179.
323. Neutronics/thermal-hydraulics coupling in LWR technology, Vol 1. CRISSE-S-WP1: Data requirements and databases needed for transient simulations and qualification, 2004, Report OECD/NEA-4452, OECD Nuclear Energy Agency, Paris, France.
324. Austregesilo, H., *et al.*, *ATHLET Models and methods*, 2003, Report GRS-P-1/Vol. 4, Gesellschaft für Anlagen- und Reaktorsicherheit, Garching, Germany.
325. Toumi, I., *et al.*, FLICA4: A 3-D two-phase flow computer code with advanced numerical methods for nuclear applications. Nuclear Engineering and Design, 2000. 200(1-2): pp. 139-155.
326. *RELAP5/MOD3.2 Code manual*, 1995, Report NUREG/CR-5535, US Nuclear Regulatory Commission, Washington DC, USA.
327. Staudenmeier, J. TRACE: TRAC/RELAP Advanced Computational Engine 2004. In: Transactions of the 2004 nuclear safety research conference, NUREG/CP-0188, October 25-27, 2004, Washington DC, USA: US Nuclear Regulatory Commission pp. 65-66.
328. Suzuki, M., H. Saitou, and T. Fuketa, RANNS code analysis on the local mechanical conditions of cladding of high burnup fuel rods under PCMI in RIA simulated experiments in NSRR. Journal of Nuclear Science and Technology, 2006. 43(9): pp. 1097-1104.
329. Lassmann, K. and H. Blank, *Modelling of fuel rod behaviour and recent advances of the TRANSURANUS code*. Nuclear Engineering and Design, 1988. 106: pp. 291-313.

330. Lassmann, K. and P. Van Uffelen, *The structure of fuel rod codes*, 2004, Report EUR 21400 EN, European Commission, Directorate General JRC, Institute for Transuranium Elements (ITU), Karlsruhe, Germany.
331. Federici, E., *et al.* The SCANAIR code version 3.2: Main features and status of qualification, 2001. In: IAEA technical committee meeting on fuel behaviour under transient and LOCA conditions, September 10-14, 2001, Halden, Norway: International Atomic Energy Agency, IAEA-TECDOC-1320, pp. 88-101.
332. Suzuki, M., H. Saitou, and T. Fuketa, Analysis on pellet-clad mechanical interaction process of high burnup PWR fuel rods by RANNS code in reactivity-initiated accident conditions. *Nuclear Technology*, 2006. 155: pp. 282-292.
333. Pettersson, K., *Fuel behaviour under LOCA conditions*, 2007, (In preparation), OECD Nuclear Energy Agency, Paris, France.
334. Katanishi, S. and K. Ishijima, *Experimental study on the fuel behavior during reactivity accident at power operation conditions*. *Journal of Nuclear Science and Technology*, 1995. 32(11): pp. 1098-1107.
335. Fuketa, T., SOAR-RIA NSRR data correction, Personal communication (e-mail), April 17, 2009.
336. Fuketa, T., *et al.* Behavior of high burnup PWR fuel under a simulated RIA condition in the NSRR, 1995. In: CSNI specialist meeting on transient behaviour of high burnup fuel, September 12-14, 1995, Cadarache, France: OECD Nuclear Energy Agency, NEA/CSNI/R(95)22, pp. 59-85.
337. Ishijima, K., *et al.* Postulated mechanisms on the failure of 50 MWd/kgU PWR fuel in the NSRR experiment and the related research programs in JAERI, 1995. In: CSNI specialist meeting on transient behaviour of high burnup fuel, September 12-14, 1995, Cadarache, France: OECD Nuclear Energy Agency, NEA/CSNI/R(95)22, pp. 87-105.
338. Fuketa, T., *et al.*, *NSRR/RIA experiments with high-burnup PWR fuels*. *Nuclear Safety*, 1996. 37(4): pp. 328-342.
339. Fuketa, T. Experimental insights on high burnup PWR fuel behaviour during RIA, 1999. In: 23rd NSRR technical review meeting, November 11-12, 1999, Tokyo, Japan.
340. Sugiyama, T., *et al.* PWR fuel behavior in RIA-simulating experiment at high temperature, 2008. In: 2008 Water Reactor Fuel Performance Meeting, October 19-23, 2008, Seoul, Korea: Korean Nuclear Society.
341. Mardon, J.-P. and B. Dunn. Overview of the M5 alloy behavior under RIA and LOCA conditions, 2007. In: 2007 International LWR Fuel Performance Meeting, San Francisco, CA, USA: American Nuclear Society, pp. 496-514.
342. Fuketa, T., *et al.* JAEA studies on high burnup fuel behaviors during reactivity-initiated accident and loss-of-coolant accident, 2007. In: 2007 International LWR Fuel Performance Meeting, September 30 - October 3, 2007, San Francisco, CA, USA: American Nuclear Society, pp. 515-525.
343. Umeda, M. *MOX fuel behaviour during RIA*, 2007. In: *Fuel Safety Research Meeting*, May 16-17, 2007, Tokai, Japan.

344. Nam, C., Y.H. Jeong, and Y.H. Jung, A statistical approach to predict the failure enthalpy and reliability of irradiated PWR fuel rods during reactivity-initiated accidents. *Nuclear Technology*, 2001. 136: pp. 158-168.
345. Papin, J., *et al.* *IRSN R&D studies on high burn-up fuel behaviour under RIA and LOCA conditions*, 2006. In: *TopFuel-2006*, October 22-26, Salamanca, Spain: European Nuclear Society, pp. 274-278.
346. Yang, R.L. Resolving our understanding of REP-Na1: Microstructural analysis, 2004. In: 2004 international meeting on light water reactor fuel performance, September 19-22, 2004, Orlando, FL, USA: American Nuclear Society.
347. Papin, J., *et al.* *Synthesis of CABRI-RIA tests interpretation*, 2003. In: *Eurosafe Forum*, November 25-26, 2003, Paris, France.
348. Waeckel, N., C. Bernaudat, and B. Salles. *EDF proposed safety domain for rod ejection accidents in a PWR*, 2000. In: *ANS topical meeting on light water reactor fuel performance*, April 10-13, 2000, Park City, UT, USA: American Nuclear Society.
349. Summary and conclusions on what we learnt from the REP NA UO₂ tests interpretation (REP Na1 excluded), in Minutes of the fourteenth meeting of the technical advisory group of the IRSN-OECD CABRI water loop project. 2007: Aix-en-Provence, France.
350. Santamarina, A., *et al.*, *Advanced neutronic tools for BWR design calculations*. *Nuclear Engineering and Design*, 2008. 238: pp. 1965-1974.
351. Downar, T.J. *The US NRC spatial kinetics code PARCS*, 2004. In: *Transactions of the 2004 nuclear safety research conference, NUREG/CP-0188*, October 25-27, 2004, Washington DC, USA: US Nuclear Regulatory Commission pp. 71-72.
352. Xu, Y., *et al.* Multi-physics coupled code reactor analysis with the US NRC code system TRACE/PARCS, 2006. In: *ANS topical meeting on reactor physics*, September 10-14, 2006, Vancouver, BC, Canada: American Nuclear Society.
353. Rashid, Y.R., R.S. Dunham, and R.O. Montgomery, *Fuel analysis and licensing code: FALCON MOD01: Volume 1: Theoretical and numerical bases*, 2004, TR-1011307, Electric Power Research Institute,
354. Lyon, W.F., *et al.* Capabilities of the FALCON steady state and transient fuel performance code, 2004. In: 2004 international meeting on light water reactor fuel performance, September 19-22, 2004, Orlando, FL, USA: American Nuclear Society, pp. 678-699.
355. Motta, A.T., A review of the critical strain energy density (CSED) model to analyzing reactivity-initiated accidents (RIA) in high burnup fuel, 2004, ML041030260, US Nuclear Regulatory Commission,
356. Cunningham, M.E., *et al.*, *FRAPTRAN: A computer code for the transient analysis of oxide fuel rods*, 2001, Report NUREG/CR-6739, Vol. 1, US Nuclear Regulatory Commission, Washington DC, USA.
357. Berna, G.A., *et al.* (1997), *FRAPCON-3: A Computer Code for the Calculation of Steady-State, Thermal-Mechanical Behavior of Oxide Fuel Rods for High Burnup*, Report NUREG/CR-6534, Vol. 1, US Nuclear Regulatory Commission, Washington DC, USA.

358. Lamare, F. (2001), *The SCANAIR Code Version 3.2: Reference Documentation*, Report 01/37, Institut de Protection et de Sûreté Nucléaire, Cadarache, France.
359. Georgenthum, V. (2007), *Analysis of CIP0-1 and VA-2 Tests*, Fuel Safety Research Meeting, May 16-17, 2007, Tokai, Japan.
360. Lassmann, K., *TRANSURANUS: A fuel rod analysis code ready for use*. Journal of Nuclear Materials, 1992. 188: pp. 295-302.
361. Lassmann, K. (2001), *The TRANSURANUS Code – Past, Present and Future*, ITU Activity Report 2001 Institute for Transuranium Elements, Karlsruhe, Germany.
362. Hellwig, C., H. Wallin, and K. Lassmann (2002), *RIA modeling – A Comparison between TRANSURANUS and FREY*, 2002, Fuel Safety Research Specialist's Meeting, March 4-5, 2002, Tokai, Japan: Japan Atomic Energy Research Institute, JAERI Conf 2002-009, pp. 182-191.
363. Lassmann, K., J. van de Laar, and D. Elenkov (1999), *Analysis of RIA Accidents for WWER Reactors Employing the TRANSURANUS Code*, Third International Seminar on WWER Fuel Performance, Modelling and Experimental Support, October 4-8, 1999, Pamporovo, Bulgaria, p. 263.
364. Van Uffelen, P., *et al.*, Extending the application range of a fuel performance code from normal operating to design basis accident conditions. Journal of Nuclear Materials, 2008. 383: pp. 137-143.
365. Suzuki, M. and H. Saitou, *Light water reactor fuel analysis code FEMAXI-6 (Ver. 1) - Detailed structure and user's manual*, 2005, Report JAEA-Data/Code 2005-003, Japan Atomic Energy Agency, Tokai-mura, Japan.

OECD PUBLICATIONS, 2 rue André-Pascal, 75775 PARIS CEDEX 16
Printed in France.